

Masroor Bangesh

**THEORETICAL STUDIES ON STRUCTURE AND
MECHANISM OF VANADIUM HALOPEROXIDASES**

DISSERTATION

Theoretical Studies on Structure and Mechanism of Vanadium Haloperoxidases

DISSERTATION

zur Erlangung des akademischen Grades doctor rerum naturalium
(Dr. rer. nat.)

vorgelegt dem Rat der Chemisch-Geowissenschaftlichen Fakultät
der Friedrich-Schiller-Universität Jena



seit 1558

von M.Phil. Masroor Ahmad Khan Bangesh

geboren am 09.03.1971

in Balakot, Pakistan

Gutachter

1.

2.

Tag der öffentlichen Verteidigung:

*Knowledge brings power. And along it, more control in
the hands of powerful. The level of destruction which
modern militaries are able to inflict upon helpless
non-combatants is a testimony to this.* This humble work
is dedicated to the innocent victims of unethical use of
knowledge.

Acknowledgements

Gratitude is offered where it is due, and foremost is to my advisor Prof. Dr. Winfried Plass whose continued support and guidance in all the matters *scientific* put me in a position to present this work. Particular is the appreciation for his endless patience which helped me discover my own eccentricities.

I feel overwhelmingly indebted to BBG and all the members of our family for their patience during my long stay abroad. That I took so long to return is my failing. That they still own me is their magnanimity.

Greatly acknowledged are the contributions of my colleague Dr. Axel Buchholz towards my handling of matters of which I had little knowledge and no experience, i.e. living in Germany, understanding the *vogonic* poetry of German officialdom and moving from Siegen to Jena. Besides, his help in solving occasional computer hardware problems enabled my research work to run smoothly.

Special thanks to my former Rumanian colleague Dr. Simona Nica for giving the semblance of social existence to what was a secluded life in Siegen. During her stay in AG Plass, she was always kind and helpful. The memorable conversations we had, covered a wide range of topics from latest scandals (from anywhere) to Schopenhauer. Particularly, her aversion towards agreeing on almost anything made the conversations much more enjoyable (and explosive).

I am thankful to my many colleagues of past and present for maintaining a peaceful co-existence with me in our office (in case of Arne Roth, Dr. Manjola Manka, Eike Spielberg and Daniel Geibig), in the coffee-room (Anja Burkhardt and Lotte Neupert) and in the group (rest of group). I am specially thankful to Daniel Geibig and Rainer Wilcken for translating the abstract into German language. I highly regard Arne's deep understanding of the finer aspects of \LaTeX and tea, and his hitchhiking experiences in the distant parts of the galaxy. His readiness to share these is even more appreciated.

At different stages of my stay in Jena I was lucky enough to have the friendship of many wonderful people. My gratitude is to Dr. Altaf Ahmad, Dr. Mohammad Asim, Dr. Aurangzeb Jathol, Dr. Ijaz Hussain, Dr. Kamran Mirza, Krishna, Dr. Shaid Raja, Dr. Yogesh Tiwari, Waseem and Dr. Zafar Warraich for their nice company and light cricket. Where applicable, their respective better-halves are thanked for the hospitality I enjoyed at their homes. Special thanks to Dr. Jathol for the help he provided during my illness.

I am grateful to Jameel Butt Sahib, Ch. Abdulbasit Sahib and Baljinder Singh Sahib, for the undeserved level of love and respect I got from these extremely kind persons.

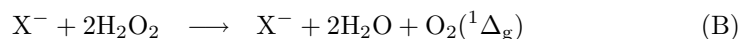
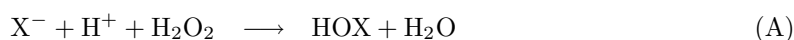
Maria, Benji, Carla, Sandra and Paulis are the loving friends I had the privilege to have in Jena. I am thankful to them for being the nice company during many stressful times.

Duly acknowledged are excellent supercomputing facilities provided by John von Neumann Institute for Computing (NIC) at the Forschungszentrum Jülich as without these, the numbers reported in this work would not have been obtained. Moreover, opportunities to attend the extraordinary scientific workshops and schools organised by NIC were great experience both in scientific and social terms.

After all is said and done, what should not remain unmentioned are the conducive research and personal conditions. Former were made possible due to smooth working of computing and other facilities in AG Plass. Later mainly because of uninterrupted provision of food, beverages and shelter. Money for both came from Deutsche Forschungsgemeinschaft and Friedrich-Schiller Universität Jena, which is duly acknowledged.

Abstract

Computational implementation of density functional theory was used to investigate the active site structure and haloperoxidative activity of vanadium containing haloperoxidases (VHPO). These enzymes utilise hydrogen peroxide and halide as cosubstrates and produce a reactive hypohalous species by two-electron oxidation of halide. Hypohalous species thus produced is responsible for halogenated organic substances found in the habitat of VHPO carrying organisms. For instance, the halogenated organic compounds isolated from sea water are attributed to haloperoxidative activity of VHPO found in sea weeds. The following two reactions describe the chemical transformation performed by VHPO,



i.e. either a hypohalous species is produced (Eq. A) which then goes on to halogenate the available organic substrates. Or in the absence of organic substrates, net disproportionation of two hydrogen peroxide molecules into water and molecular oxygen (in first excited state) is carried (Eq. B). VHPO enzymes are classified on the basis of whether they can oxidise chloride in addition to bromide and iodide, in which case VHPO is named vanadium chloroperoxidase (VCPO). The VHPO which catalyse the oxidation of only bromide and iodide are termed as vanadium bromoperoxidase (VBPO). The x-ray crystal structure of both type of enzymes reveal an identical active site characterised by a histidine residue coordinated to vanadate cofactor. Moreover, anionic oxygen atoms of vanadate are found to receive hydrogen bonds from the side chains of same set of amino acids. The VCPO sequence of these hydrogen bonding amino acids is Lys353, Arg360, Ser402, Gly403, His404 and Arg490. A comparison of active sites of VCPO and VBPO according to their x-ray crystal structures is shown in Fig. 1.1. Several questions regarding the structure and mechanism of VHPO pertained at the time when this investigation started. A summary of conclusions of this thesis is given in the following paragraphs.

Resting state of VHPO. The most fundamental question was regarding the geometry, electronic structure and protonation state of vanadate cofactor. In short, this could be neatly framed in following queries: Does vanadate cofactor has trigonal bipyramidal (TBP) geometry in the resting state of VHPO as was widely believed on the basis of its appearance in x-ray crystal structure? And whether vanadium(V) exists as VO^{3+} or VO_2^+ in the native VHPO active site? Fortunately, apart from the x-ray crystal structure, the *optical spectrum* of active site had been successfully utilised to monitor the enzyme turn-over. This provided an experimental hint about the electronic structure of vanadate cofactor. Time-dependent density functional theory (Chapter 2) was utilised to calculate the optical excitations of a variety of optimised structures modelled after the pentacoordinated vanadate cofactor (Chapter 3). These models (Fig. 3.1) included, pentacoordinated vanadate in trigonal bipyramidal (TBP) geometries and in monoanionic, neutral, and cationic protonation states. In addition, dianionic and monoanionic TBP structures enclosed in protein matrix (comprised of above listed active site residues), were also studied (Fig. 3.2). And finally, a pentacoordinated square

pyramidal geometry (SP) in monoanionic form was considered (Fig. 3.1). By comparing calculated electronic excitation energies/oscillator strengths of different structures with above mentioned experimental optical spectrum allowed us to conclude that vanadate in the resting state active site exists in distorted TBP geometry with most probably in monoanionic (diprotonated) protonation state.

Hydrogen bonding in VCPO and VBPO active sites. The confirmation of this conclusion, to be described shortly, again came under different context. The unequal catalytic performance of VCPO and VBPO in carrying chloroperoxidase activity appeared to be greatly puzzling in the view of the fact that both enzyme systems share an identical active site in terms of amino acid residues surrounding the vanadate cofactor. We hypothesised that observed crystallographic positions of active site amino acid side chains are dictated by secondary protein structure exterior to active site pocket. This would subtly determine the variation in pattern of hydrogen bonding between anionic oxygen atoms of vanadate and positively charged amino acid residues of active site. In order to substantiate this hypothesis, it was necessary to study the active site hydrogen bonding network in detail. The crystallographic positions of (non-hydrogen) atoms of active site residues were taken as carriers of all the effects of outer protein environment, and geometry of TBP vanadate was optimised in active site pockets of both VCPO and VBPO, while preserving the crystallographically determined orientations of hydrogen bonding residues of active site (Chapter 4). Furthermore, different variations on protonation states of TBP vanadate were also tried. Additionally, similar optimisations were done by utilising x-ray crystal structures of site mutated versions of VCPO enzyme in which Arg360 and His404 residues are replaced.

The energies of hydrogen bonding interaction between vanadate and active site residues in the structures obtained from above mentioned optimisations and some small model hydrogen bonded complexes, were calculated with supermolecular approach. Individual hydrogen bonds were also analysed with quantum theory of atoms in molecules (QTAIM). The resulting conclusions (Chapter 4) are listed below.

- The monoanionic (diprotonated) vanadate TBP structures were found to be energetically most stable in active site pockets derived both from VCPO and VBPO x-ray crystal structures (**CPO1** and **CPO2** in Fig. 4.9). This is the reconfirmation of earlier summarised conclusions drawn from TD-DFT studies. Moreover, the orientation of protonated oxygen atoms in active site pocket was also determined. It was found that apical oxygen atom of TBP vanadate structure and one equatorial oxygen atom oriented towards Ser residue were protonated.
- The model in which neutral His404 receives hydrogen bond from apical OH group of TBP vanadate was found to be unstable in comparison to the one in which positively charged His404 donates a hydrogen bond to apical OH group (**CPO1** vs. **CPO2** in Fig. 4.9).
- The potential energy surface for proton movement along mentioned His404...O_{ap} hydrogen bond was found to be sensitive to hydrogen bonding on equatorial oxyanionic sites of vanadate. The weakening of later resulted in proton transfer from His404 to apical oxygen atom of TBP vanadate, which can be then easily expelled as a water molecule as discussed in Chapter 5.
- The active site pocket derived from VCPO crystal structure was capable of stabilising the vanadate in both dianionic and monoanionic protonation states (**CPO1** and **CPO3** in Fig. 4.9). On the other hand, VBPO derived active site pocket was able to stabilise only monoanionic vanadate (**BPO1** and **BPO2** in Fig. 4.9)
- It was found that His404 and Lys353 have a similar level of hydrogen bonding interaction with vanadate in active site model based on VCPO crystal structure, while the VBPO active site model showed a weakened interaction between

His404 and vanadate. The supermolecular energy term for vanadate interaction with Ser402-Gly403-His404 fragment was found to be smaller in VBPO active site model. The same for Lys...vanadate interaction was found to be higher in VBPO active site model. This showed that negative charge on vanadate exhibits increased dependence on interaction with Lys for stabilisation in VBPO case.

On the basis of hydrogen bonding interactions in the TBP resting state geometry, we speculated that similar hydrogen bonding considerations would distinguish VCPO and VBPO also on another stage of catalytic cycle when cofactor assumes a TBP geometry. The TBP geometry is encountered again after the oxygen atom transfer step, with the formation of hypohalite species apically coordinated to vanadate (**3** in Fig. 6.1).

Formation of peroxovanadium species. The first step in catalytic cycle is the reaction of hydrogen peroxide with pentacoordinated vanadium. In fact this step is experimentally well founded because its outcome, an active site peroxovanadium species is shown to exist in the crystal structure of VCPO after its treatment with hydrogen peroxide. In Chapter 5, this step was studied with small model complexes in order to elucidate the involved mechanism. Among the detected reactive pathways, the energetically favourable one (Path B in Fig. 5.8) was found to proceed through following steps: First, the protonation of apical OH group of TBP vanadate, resulting into an apically coordinated water molecule which could be very easily expelled. Second, a proton transfer from hydrogen peroxide to one of the oxo oxygen atoms bonded to vanadium. This step is concerted with HOO-V bond formation. Third, η^2 coordination of peroxide to vanadium due to second peroxo-vanadium bond formation. This is accompanied by second proton transfer from the coordinated OOH group to coordinated OH group, and expulsion of a second water molecule.

Reaction of peroxovanadium species with halide. The second step in the catalytic cycle or reaction of peroxovanadium species with halide was considered in Chapter 6. The emphasis was laid on distinctions between VCPO and VBPO active site in order to understand the disparity in their catalytic activity. The x-ray crystal structure of peroxo form of VCPO shows Lys353 to be in the hydrogen bonding distance to one of oxygen atoms of metal coordinated peroxide, and have been thought to be crucial for catalysis. On the other hand, the crystal structure of VBPO shows the active site Lys341 residue closely neighboured by a histidine (His411) as a potential hydrogen bonding partner (Fig. 1.1). The different environment of active site Lys in VCPO and VBPO was considered to form the possible basis of differentiation in their catalytic behaviour. Three models of catalysis for the second step were constructed (Figs. 6.1 and 6.2) : The *non-enzymatic model* in which halide reacts with peroxovanadium species, the *VCPO catalytic model* which additionally includes a Lys residue hydrogen bonded to coordinated peroxide, and *VBPO catalytic model* with inclusion of His...Lys hydrogen bond to Lys in addition to Lys...peroxovanadium hydrogen bond.

Halide (X^-) was made to attack the apical oxygen atom (O3) of coordinated peroxide in (pseudo) TBP peroxovanadium species (Fig. 6.1). This led to X-O3 bond formation and O3-O4 dissociation resulting in a TBP vanadium species with apically coordinated hypohalite ion. In all three models, chloride was found to overcome greater energy barrier in the process, compared to bromide. In VCPO catalytic model the barrier height was reduced significantly below the one observed for non-enzymatic model. VBPO catalytic model operated in the same manner but the reduction in barrier height was lower than in VCPO catalytic model (Table 6.2). It was found that *proton transfer* from Lys353 to peroxide occurs before the halide attack in VCPO model. This remains inhibited in VBPO catalytic model until the halide attack, due to hydrogen bonding involvement of Lys with His in this model. This seems to be crucial in determining the oxidising power of VCPO and VBPO active sites. The electronic character of second

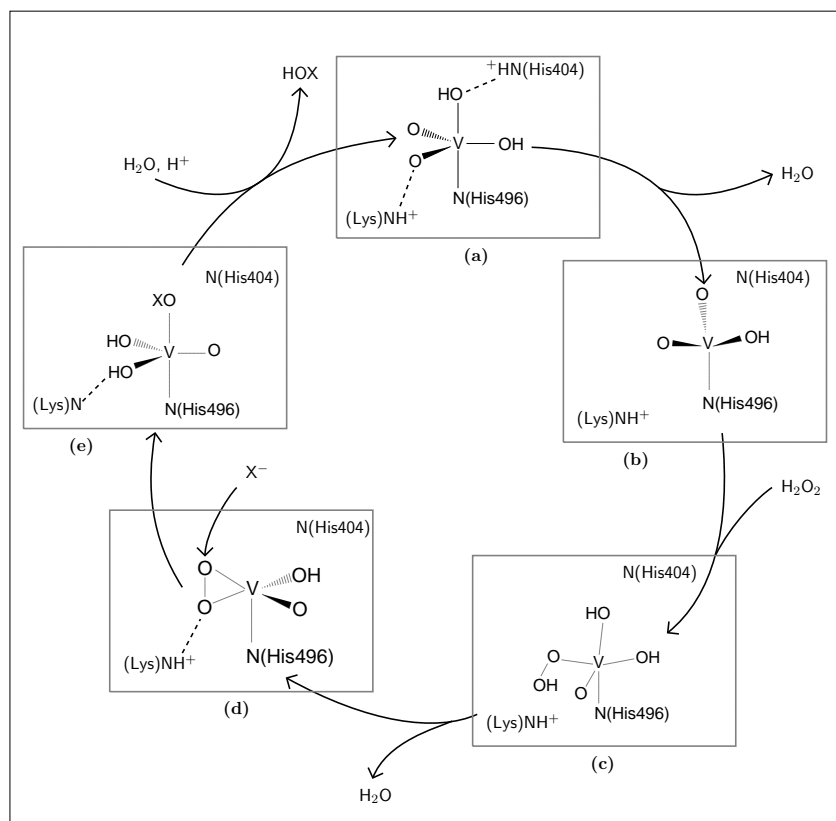


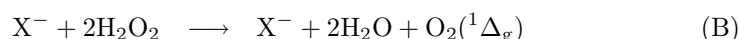
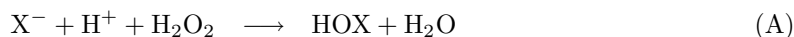
Figure A: The overview of VHPO catalytic cycle.

step was investigated by analysing the valence shell charge concentration (VSCC) region in the $\nabla^2\rho(\mathbf{r})$ distribution of metal bound peroxide during the halide attack. The catalytic power of VCPO and VBPO models was found to emanate from two factors: First, the usually attributed polarisation of O3–O4 bond due to involvement of one of peroxo oxygen atoms (O4 atom) in hydrogen bonding with Lys. Second, the weakening of O4–V bond because of proton transfer from Lys to O4 resulting in reduced charge donation from O4 to metal. This later factor enhances the Lewis acidity of vanadium, with increased preparedness of O3 atom for nucleophilic halide attack.

Overview of the catalytic cycle. The pieces of information presented in various chapters are gathered to build an overall picture of catalytic cycle in Fig. A. The resting state is described in panel (a) of this figure, and under some conditions a proton transfer can be induced from positively charged His404 residue followed by expulsion of water molecule to generate the structure in panel (b). The suitable circumstance for this to happen was found in Chapter 4 as curtailment of hydrogen bond donation to equatorial oxygen atoms of TBP structure. This may happen in the presence of hydrogen peroxide substrate, by its interference with active site hydrogen bond donors. The catalytic cycle proceeds through (c), (d) and (e), to finally regenerate the resting state. The introduction of proton in (e) at the cycle completion phase is done according to experimentally found stoichiometric condition, but this may as well happen at earlier phases by reprotonation of His404. In that case, protonated His404 would again be able to donate a hydrogen bond to oxygen atom of apically coordinated OX^- species. Obviously such a scenario has a role to play in release of HOX product. This along with the determination of exact stage in the cycle at which a proton is consumed, are proposed as future continuation of present investigations.

Abstract (German)

In dieser Arbeit wurde die computerchemische Methode der Dichtefunktionaltheorie genutzt, um die Struktur des aktiven Zentrums und die Reaktivität der vanadiumhaltigen Haloperoxidasen (VHPO) zu untersuchen. Diese Enzyme benutzen Wasserstoffperoxid und Halogenidionen als Co-Substrate und produzieren durch eine Zweielektronen-Oxidation des Halogenidions eine reaktive Hypohalogenid-Spezies. Die auf diesem Weg entstehenden Hypohalogenidionen sind für die Bildung halogener organischer Substanzen verantwortlich, die man im Habitat VHPO-haltiger Organismen findet. So wird zum Beispiel das Vorkommen dieser Verbindungen in Meerwasser der Haloperoxidase-Aktivität VHPO-haltiger Meeresalgen zugeschrieben. Die folgenden zwei Reaktionen beschreiben die von VHPO katalysierten Umwandlungen.



Demnach entsteht entweder eine hypohalogenige Säure (Gl. A), welche im weiteren Verlauf vorhandene organische Substrate halogeniert, oder es erfolgt bei Abwesenheit letzterer eine Disproportionierung zweier Wasserstoffperoxidmoleküle zu Wasser und Singulett-Sauerstoff (Gl. B). VHPO-Enzyme werden wie folgt klassifiziert: Ist das Enzym in der Lage, sowohl Iodid, Bromid als auch Chlorid zu oxidieren, spricht man von Vanadium-Chloroperoxidase (VCPO). Dagegen ist Vanadium-Bromoperoxidase (VBPO) auf die Oxidation von Iodid und Bromid beschränkt. Die Kristallstrukturen beider Enzyme zeigen ein identisches aktives Zentrum, welches durch einen an den Vanadat-Cofaktor koordinierten Histidinrest charakterisiert ist. Weiterhin fungieren die anionischen Sauerstoffatome des Vanadats als Akzeptoren für Wasserstoffbrückenbindungen, welche von verschiedenen Aminosäuren ausgehen. Diese sind in beiden Enzymen identisch und tragen in der VCPO-Sequenz die Bezeichnungen Lys353, Arg360, Ser402, Gly403, His404 und Arg490. Ein Vergleich der Kristallstruktur der aktiven Zentren von VCPO und VBPO ist in Fig. 1.1 dargestellt. Wesentliche Fragen bezüglich der Struktur und des Katalysiemechanismus der VHPO waren zu Beginn dieser Studien noch ungeklärt. Eine Zusammenfassung der Ergebnisse dieser Arbeit wird in den folgenden Abschnitten gegeben.

Ausgangszustand von VHPO. Die grundlegendsten Fragen betreffen die Geometrie, die elektronische Struktur und den Protonierungsgrad des Vanadat-Cofaktors. Folgende Fragestellungen beschreiben das Problem: Hat, wie weithin angenommen, der Vanadat-Cofaktor im Grundzustand der VHPO eine trigonal-bipyramidale Geometrie, wie dies auch aufgrund der vorhandenen Kristallstrukturen zu erwarten wäre? Existiert die Vanadium(V)-Spezies als VO^{3+} oder VO_2^+ im nativen Aktivzentrum der VHPO? Erfreulicherweise waren in vorangegangenen Arbeiten außer den Kristallstrukturen auch UV/VIS-Spektren des Aktivzentrums gemessen und mit Erfolg zur Beobachtung der Enzymaktivität herangezogen worden. Dies gab einen experimentellen Hinweis auf die elektronische Struktur des Vanadat-Cofaktors. Mittels zeitabhängiger Dichtefunktionaltheorie (TD-DFT, Kapitel 2) wurden die angeregten Zustände einer Vielzahl von op-

timierten Modellstrukturen, deren Geometrien vom Vanadat-Cofaktor abgeleitet sind, berechnet (Kapitel 3). Diese Modelle (Fig. 3.1) bestehen aus fünffach koordiniertem Vanadat in trigonal-bipyramidaler Geometrie, jeweils in Protonierungsgraden, die zu monoanionischen, neutralen und kationischen Gesamtladungen führen. Zusätzlich zu den genannten Modellen wurden dianionische und monoanionische trigonal-bipyramidale Strukturen in der Proteinmatrix (bestehend aus den o.g. Aminosäuresequenzen am Aktivzentrum) untersucht (Fig. 3.2). Schließlich wurde auch eine quadratisch-pyramidale Modellstruktur in monoanionischer Form betrachtet (Fig. 3.1). Durch Vergleich der berechneten elektronischen Anregungsenergien und Oszillatorenstärken verschiedener Strukturen mit dem oben genannten gemessenen Spektrum konnten wir schlussfolgern, dass der Vanadat-Cofaktor im Ausgangszustand des aktiven Zentrums als trigonal-bipyramidale Struktur im monoanionischen (zweifach protonierten) Zustand vorliegt.

Wasserstoffbrückenbindungen in den aktiven Zentren von VCPO und VBPO.

Die im letzten Abschnitt gezogene Schlussfolgerung wurde durch ein weiteres Ergebnis in einem anderen Kontext bestätigt. Die unterschiedliche katalytische Aktivität von VCPO gegenüber VBPO bezüglich der Chloroperoxidaseaktivität erschien in hohem Maße rätselhaft in Anbetracht der Tatsache, dass beide Enzyme ein identisches Aktivzentrum mit identischen Aminosäureliganden am Vanadat-Cofaktor besitzen. Wir vermuteten, dass die durch die Kristallstruktur aufgeklärten Positionen der Aminosäure-Seitenketten von der Proteinstruktur außerhalb der Enzymtasche des aktiven Zentrums bestimmt wird. Dies bedingt eine leichte Veränderung im Netzwerk der Wasserstoffbrückenbindungen zwischen den anionischen Sauerstoffatomen des Vanadats und den positiv geladenen Aminosäureresten des aktiven Zentrums. Um diese Hypothese zu erhärten, war es nötig, das Wasserstoffbrückenbindungs-Netzwerk um das aktive Zentrum im Detail zu untersuchen. Zur Modellierung der Proteinumgebung wurde das gesamte aktive Zentrum mit Ausnahme des Vanadat-Cofaktors auf den aus der Kristallstruktur entnommenen Atompositionen fixiert. Die Geometrie des trigonal-bipyridalen Vanadats wurde in der Enzymmatrix von VCPO und VBPO optimiert, während die kristallographisch bestimmten Orientierungen der Wasserstoffbrücken im Aktivzentrum beibehalten wurden (Kapitel 4). Darüber hinaus wurden Variationen des Protonierungsgrads des Vanadats untersucht. Zusätzlich wurden ähnliche Optimierungen auch unter Nutzung der Kristallstrukturen mutierter VCPO-Enzyme durchgeführt, in welchen die Arg360- und His404-Reste ersetzt sind.

Mit den oben aufgeführten optimierten Strukturen sowie einigen kleinen wasserstoffbrückegebundenen Systemen wurden die Energien der Interaktionen zwischen Vanadat und Resten am Aktivzentrum über Wasserstoffbrücken durch einen supermolekularen Ansatz berechnet. Einzelne Wasserstoffbrücken wurden auch mit der Quantentheorie *atoms in molecules* (QTAIM) untersucht. Die erhaltenen Ergebnisse (Kapitel 4) sind:

- Die monoanionischen (zweifach protonierten) trigonal-bipyridalen Vanadat-Modelle sind die energetisch stabilsten Strukturen in den aus den Kristallstrukturen entnommenen Aktivzentren von sowohl VCPO als auch VBPO (**CPO1** und **CPO2** in Fig. 4.9). Dies ist eine Bestätigung der vorher gezogenen Schlussfolgerungen aus TD-DFT-Rechnungen. Darüber hinaus wurde auch die Orientierung der protonierten Sauerstoffatome im Aktivzentrum aufgeklärt. Es wurde herausgefunden, dass sowohl das axiale Sauerstoffatom der Vanadat-Struktur als auch ein äquatoriales Sauerstoffatom, welches zur Serin-Seitenkette ausgerichtet ist, protoniert ist.
- Der Modellkomplex, in dem neutrales His404 durch eine Wasserstoffbrückenbindung

an die axiale OH-Gruppe des Vanadats gebunden ist, wurde als destabilisiert gegenüber der Struktur erkannt, bei der ein positiv geladenes His404 die Wasserstoffbrückenbindung zur axialen OH-Gruppe ausbildet. (**CPO1** vs. **CPO2** in Fig. 4.9)

- Bei der Untersuchung der Potentialhyperfläche für eine Protonenverschiebung entlang der o.g. $\text{His404} \cdots \text{O}_{ax}$ Wasserstoffbrückenbindung stellte sich heraus, dass diese empfindlich auf die Wasserstoffbrückenbindungen auf der äquatorialen oxoanionischen Seite des Vandats reagiert. Eine Schwächung der Letztgenannten führte zu einem Protonentransfer von His404 zum axialen Sauerstoffatom des Vanadats. Das entstehende Wassermolekül kann daraufhin leicht abgespalten werden. Dies wird in Kapitel 5 diskutiert.
- Das System des aus der VCPO-Kristallstruktur abgeleiteten Aktivzentrums war in der Lage, Vanadat in dianionischem und monoanionischem Protonierungsgrad zu stabilisieren (**CPO1** und **CPO3** in Fig. 4.9). Im Gegensatz dazu war das VBPO-Modellsystem nur in der Lage, monoanionisches Vanadat zu stabilisieren (**BPO1** und **BPO2** in Fig. 4.9).
- Es wurde herausgefunden, dass His404 und Lys353 im VCPO-Modellsystem eine vergleichbar starke Wasserstoffbrücken-Wechselwirkung mit Vanadat aufweisen, während im VBPO-Modellsystem die Wechselwirkung zwischen His404 und Vanadat geschwächt ist. Der supermolekulare Energieterm für die Interaktion zwischen Vanadat und dem Ser402-Gly403-His404-Fragment war im VBPO-Modellsystem kleiner, während der Energieterm für die Lysin \cdots Vanadat Wechselwirkung größer war. Dies zeigt, dass eine negative Ladung auf dem Vanadat im VBPO-Fall eine Stabilisierung über Lysin erfordert.

Auf der Basis der Wasserstoffbrücken-Wechselwirkungen im trigonal-bipyramidalen Grundzustand des Vanadats stellten wir die Vermutung an, dass ähnliche Unterschiede im Wasserstoffbrückenbindungs-Netzwerk zwischen VCPO und VBPO diese beiden Modellsysteme auch an anderen Stellen des Katalysekreislaufs unterscheiden würden, solange der Cofaktor eine trigonal-bipyramidale Geometrie aufweist. In der Tat wird die trigonal-bipyramidale Geometrie nach dem Sauerstoffatomtransfer mit der Bildung einer hypohalogenigen Spezies, die axial an das Vanadat koordiniert ist, wieder zurückgebildet (**3** in Fig. 6.1).

Bildung der Peroxovanadium-Spezies. Der erste Schritt im katalytischen Zyklus ist die Reaktion von Wasserstoffperoxid mit fünffach koordiniertem Vanadium. Dieser Schritt ist experimentell gut begründet, da durch Kristallstrukturanalyse bewiesen wurde, dass nach der Behandlung mit Wasserstoffperoxid eine Peroxovanadium-Spezies im aktiven Zentrum der VCPO vorliegt. In Kapitel 5 wurde dieser Schritt mit Hilfe kleiner Modellkomplexe untersucht, um den zugrunde liegenden Mechanismus aufzuklären. Es stellte sich heraus, dass der energetisch günstigste Reaktionspfad (Pfad B in Fig. 5.8) über folgende Stufen verläuft: Zunächst wird durch Protonierung der axialen OH-Gruppe des trigonal-bipyramidalen Vanadats ein Wassermolekül gebildet, welches sehr leicht abgespalten werden kann. Danach findet eine Protonentransferreaktion vom Wasserstoffperoxid zu einem der vanadiumgebundenen Oxoliganden statt, was mit der simultanen Bildung einer HOO–V Bindung einher geht. Durch eine zweite Peroxo–Vanadium Bindung ergibt sich schlussendlich eine η^2 -Koordination des Peroxoliganden. Diese wird von einem zweiten Protonentransfer von der koordinierten OOH-Gruppe zu einer koordinierten OH-Gruppe begleitet, was eine weitere Wasserabspaltung zur Folge hat.

Reaktion der Peroxovanadium-Spezies mit Halogenidionen. Der zweite Schritt im katalytischen Zyklus, die Reaktion der Peroxovanadium-Spezies mit Halogenidionen, wird in Kapitel 6 betrachtet. Der Schwerpunkt liegt dabei auf dem Unterschied der aktiven Zentren von VCPO und VBPO, um die unterschiedliche katalytische Aktivität zu verstehen. Wie die Kristallstruktur der Peroxoform von VCPO zeigt, befindet sich das Lys353 in einem Wasserstoffbrückenbindungsabstand zu einem der metall-kordinierten Peroxo-Sauerstoffatome. Darüber hinaus übt es vermutlich entscheidenden Einfluss auf den katalytischen Zyklus aus. Die Kristallstruktur von VBPO hingegen weist im aktiven Zentrum nahe des Lys341 ein Histidin (His411) als weiteren potentiellen Wasserstoffbrückenbindungspartner auf (Fig 1.1). Diese unterschiedliche Umgebung des Lysins in VCPO und VBPO wird als mögliche Ursache der verschiedenen katalytischen Aktivitäten der beiden Enzyme angenommen. Für den zweiten Schritt wurden drei Modellsysteme ausgearbeitet (Fig. 6.1 und 6.2): Das *nicht-enzymatische Modell*, bei welchem das Halogenidion mit einer Peroxovanadium-Spezies reagiert, das *VCPO-Modell*, welches einen mittels Wasserstoffbrückenbindung zum koordinierten Peroxoligand verbundenen Lysinrest einschließt, sowie das *VBPO-Modell*, welches zusätzlich eine His...Lys Wasserstoffbrückenbindung aufweist.

Der Angriff des Halogenidions auf das axiale Sauerstoffatom (O3) des Peroxoliganden der pseudo-trigonal-bipyramidalen Peroxovanadium-Spezies (Fig. 6.1) wurde modelliert. Dies führte zu einer X–O4 Bindungsbildung und einer O3–O4 Dissoziation und resultiert somit in einem trigonal-bipyramidalen Vanadiumkomplex mit axial koordiniertem Hypohalogenidion. Bei allen drei Modellsystemen zeigte sich, dass Chlorid eine größere Energiebarriere zu überwinden hat als Bromid. Bei dem VCPO-Modell ist die Energiebarriere im Vergleich zum nicht-enzymatischen Modell signifikant reduziert. Das VBPO-Modell verringerte die Energiebarriere ebenfalls, jedoch in kleinerem Ausmaß (Tab. 6.2). Es zeigte sich, dass im Falle des VCPO-Modells vor dem Angriff des Halogenidions ein Protonentransfer vom Lys353 zum Peroxid stattfindet. Dieser unterbleibt beim VBPO-Modell wegen der Wasserstoffbrückenbindung vom Lysin zum Histidin. Dies scheint ausschlaggebend für die unterschiedliche Oxidationskraft der beiden Enzyme zu sein. Durch Analyse der VSCC (valence shell charge concentration) der $\nabla^2\rho(\mathbf{r})$ -Verteilung des koordinierten Peroxids während des Halogenid-Angriffs wurde der elektronische Charakter des zweiten Schrittes untersucht.

Es konnte gezeigt werden, dass die Katalysatorstärke der VCPO und VBPO durch zwei Umstände bedingt ist: Zum Einen durch die Polarisierung der O3–O4 Bindung aufgrund der Ausbildung der Wasserstoffbrückenbindung eines der Sauerstoffatome (O4) zu Lysin. Zum Anderen führt die Schwächung der O4–V Bindung durch den Protonentransfer von Lysin zu O4 zu einer verminderten Ladungsübertragung vom O4 zum Metal. Letzteres verstärkt die Lewis-Acidität des Vanadiums und erhöht damit die Bereitschaft des O3 gegenüber dem nucleophilen Angriff des Halogenidions.

Überblick über den katalytischen Zyklus. Die einzelnen Informationen zum katalytischen Mechanismus, welche in den einzelnen Kapiteln dargestellt wurden, werden in Abb. A. A zusammengefasst. Der Ausgangszustand ist in Feld (a) der Abbildung zu sehen, welcher unter bestimmten Bedingungen durch einen vom positiv geladenen His404 ausgehenden Protonentransfer und unter Abspaltung eines Wassermoleküls in die Struktur in Feld (b) überführt werden kann. Durch eine Abnahme der Stärke der Wasserstoffbrückenbindungen zu den äquatorialen Sauerstoffatomen wird dieser Protonentransfer ermöglicht (siehe Kapitel 4). Dies könnte durch die Wechselwirkung von Wasserstoffperoxid mit Donoren der Wasserstoffbrückenbindungen im aktiven Zentrum ausgelöst werden. Der katalytische Zyklus verläuft über (c), (d) und (e) um schließlich den Ausgangszustand zurück zu bilden. Da experimentell ein stöchiometrischer Um-

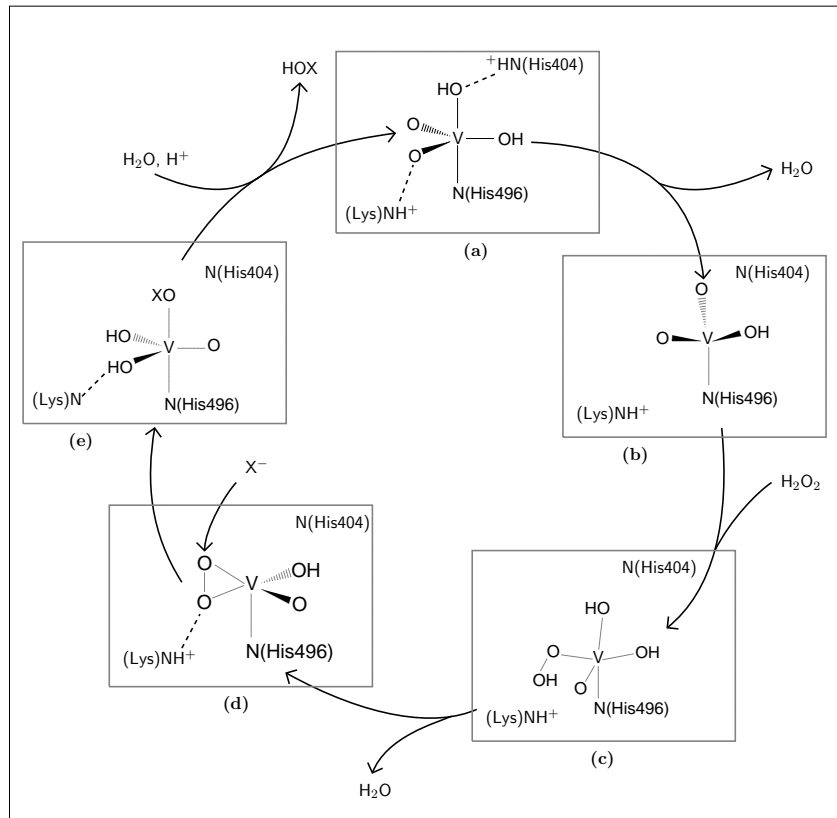


Figure A: Überblick über den katalytischen Zyklus der VCPO.

satz gefunden wurde, wird nach (e) ein Proton eingeführt, was jedoch auch schon in einer früheren Phase durch Protonierung von His404 geschehen könnte. In diesem Fall wäre das protonierte His404 wieder in der Lage eine Wasserstoffbrückenbindung zum Sauerstoffatom der axial gebundenen OX⁻ Spezies auszubilden, was Voraussetzung für die Abspaltung von HOX ist. Für weiterführende Untersuchungen wäre es denkbar, die genaue Stelle im Zyklus, an welcher ein Proton verbraucht wird, zu bestimmen.

Contents

Acknowledgements	vii
Abstract	ix
Abstract (German)	xiii
List of Figures	xxi
List of Tables	xxiii
1 Vanadium Haloperoxidases in Perspective	1
1.1 Introduction	1
1.2 Catalysis of Oxygen Atom Transfer	4
1.2.1 Background	4
1.2.2 Building Blocks of Catalyzed Peroxide Reduction	6
1.2.3 Theoretical studies of VHPO akin mechanisms	12
1.3 This Thesis	14
2 Time Independent and Dependent Density Functional Theory	15
2.1 Introduction: From Wave Function to Electron Density	15
2.2 DFT: From Electron Density to Wave Function	19
2.2.1 Hohenberg-Kohn Theorems	19
2.2.2 Kohn-Sham Method	22
2.3 Time Dependent Density Functional Theory	25
2.3.1 Runge-Gross Theorem	26
2.3.2 Kohn-Sham Linear Response Theory	28
3 TD-DFT Studies on the Electronic Structure of VHPO cofactor	33
3.1 Introduction	33
3.2 Computational Methods	35
3.2.1 Choice of geometrical structures	35
3.2.2 Optimisation of geometries	36
3.2.3 Calculation of excitations and oscillator strengths	37
3.3 Results and Discussion	38
3.3.1 Geometries	38
3.3.2 Excitations	41
3.3.3 Conclusions	50

4	Hydrogen Bonding in VHPO Active Site	51
4.1	Introduction	51
4.2	The Nature of Hydrogen Bond	52
4.2.1	Acid–Base equilibria and hydrogen bond	52
4.2.2	Approaches to characterisation	53
4.3	Computational Methods	58
4.4	Results and Discussion	59
4.4.1	Small model complexes	59
4.4.2	Effect of additional HB donors and implications for resting state . .	64
4.4.3	Analysis of protein-cofactor HB interactions	72
4.4.4	Outlook : Active Site and Catalytic Cycle	85
5	Reaction of Hydrogen Peroxide with Imidazole Bound Vanadate	87
5.1	Introduction	87
5.2	Computational Methods	89
5.2.1	Optimisation of stationary points	89
5.2.2	<i>ab initio</i> Molecular Dynamics simulations	89
5.2.3	Electron localisation function (ELF)	90
5.3	Results and Discussion	91
5.3.1	Peroxide attack on the anionic vanadate species I	91
5.3.2	Peroxide attack on the neutral vanadate species II	95
5.3.3	Formation of peroxovanadium species from tetrahedral vanadate . .	100
5.3.4	Electronic character of peroxo–vanadium bond formation	101
5.3.5	Summary and Conclusions	104
6	Reaction of Halide and Vanadium Bound Peroxide	107
6.1	Introduction	107
6.2	Computational Methods	108
6.3	Results and Discussion	108
6.3.1	Potential energy surface and catalysis	108
6.3.2	Hydrogen Bonding Geometries, QTAIM parameters and Energies . .	114
6.3.3	QTAIM Analysis of Reaction Step	121
6.3.4	The Mechanistic Outlook	133
	References	137
A	Supplement to Chapter 3	151
B	Supplement to Chapter 5	161
C	Supplement to Chapter 6	167

List of Figures

A	The overview of VHPO catalytic cycle.	xii
A	Überblick über den katalytischen Zyklus der VCPO.	xvii
1.1	VHPO active site structure	3
1.2	Vanadium species: standard electrode potentials	8
1.3	Metal catalysed oxidation of bromide	10
1.4	FeHPO and VHPO mechanisms	11
1.5	Mimoun and Sharpless mechanism	13
3.1	Protonated vanadate: optimised geometries	35
3.2	The VCPO active site: optimised geometry	36
3.3	LMCT spectrum of doubly protonated orthovanadate	43
3.4	Frontier energy levels for vanadate species	44
3.5	Diprotonated species: excitation energies	45
3.6	Various vanadate species: excitation energies	47
4.1	Types of HB on the basis of proton potential.	53
4.2	Perturbative interaction between n_V and σ_{X-H}^* orbitals	58
4.3	Optimised structures of small HB complexes	59
4.4	Optimised geometries of larger HB complexes	65
4.5	ADF-BP/TZ2P potential for HB proton in 2 and 7	70
4.6	ADF-BP/TZ2P potential for HB proton in 2 at different N...O distances	71
4.7	ADF-BP/TZ2P potential for HB proton of 2 and its complexes with additional guanidinium cations	71
4.8	Schematic number of atoms in active site of VHPO	73
4.9	Optimised structures of VHPO active site models	74
4.10	Properties at HB (3,-1) critical points at various theory levels	81
5.1	Schematic of starting TBP vanadate species in reaction with H_2O_2	88
5.2	Optimised stationary points: attack of H_2O_2 on monoanionic TBP vanadate	92
5.3	Energy profile for peroxide attack on monoanionic TBP vanadate	93
5.4	Optimised stationary points: attack of H_2O_2 on neutral TBP vanadate	96
5.5	Energy profile for peroxide attack on neutral TBP vanadate species	96
5.6	Optimised stationary points: attack of H_2O_2 on tetrahedral vanadate	100
5.7	The contour diagrams of $\eta(r)$ for sequence 2 — 9	104
5.8	Reactive channels for H_2O_2 attack on vanadate	105
6.1	Non-enzymatic model stationary points	109

6.2	VCPO and VBPO catalytic models stationary points	109
6.3	Optimised structures of HB complexes of peroxovanadate species.	115
6.4	Difference in QTAIM parameters between nono-enzymatic and enzymatic models	123
6.5	Simplified one-dimensional model for VSCC/VSCD	125
6.6	$\nabla^2\rho(\mathbf{r})$ function distribution in non-enzymatic and VCPO-catalyzed models for chloride oxidation	128
6.7	$\nabla^2\rho(\mathbf{r})$ function distribution for VBPO model of chloride oxidation	132
6.8	Schematic of charge flow in oxygen atom transfer to chloride ion	134
B.1	CPMD trajectories of atoms in vanadium coordination sphere with 4* as starting point	162
B.2	CPMD trajectories of atoms in vanadium coordination sphere with 21* as starting point	163
B.3	CPMD trajectories of atoms in vanadium coordination sphere with 24* as starting point	164
B.4	CPMD trajectories of atoms in vanadium coordination sphere with 30* as starting point	165
B.5	CPMD trajectories of atoms in vanadium coordination sphere with 32* as starting point	166

List of Tables

1.1	Standard reduction potentials for dioxygen	6
1.2	Properties of O–O bond	7
3.1	Optimised geometries (1 and 2), reference calculations	39
3.2	Optimised geometrical parameters (1–5), ADF-BP/TZ2P level	40
3.3	Optimised geometrical parameters(2 , 6–8), ADF-BP/TZ2P level	41
3.4	Vanadate species:excitation energies	42
4.1	Optimised HB geometrical parameters of complexes in Fig. 4.3	60
4.2	BSSE corrected HB energies at different theory levels	61
4.3	RMS of difference of topological properties at different theory levels from MP2/6-311++G** values	63
4.4	QTAIM parameters for Fig. 4.3 complexes	64
4.5	Optimised HB geometrical parameters for Fig. 4.4 complexes	65
4.6	ADF-PBE/TZ2P gas phase HB energies for Fig. 4.4 complexes	66
4.7	ADF-PBE/TZ2P aqueous phase HB energies for Fig. 4.4 complexes	68
4.8	QTAIM parameters for Fig. 4.4 complexes	69
4.9	Comparison of optimised HB geometries of CPO1 and BPO1	75
4.10	Comparison of optimised HB geometries of CPO1 and mutant models	76
4.11	Gas phase HB energies for VHPO active site models	78
4.12	Aqueous phase HB energies for VHPO active site models	79
4.13	QTAIM parameters for CPO1 and BPO1	82
4.14	QTAIM parameters for mutant models	83
4.15	HB Donor–acceptor interactions fro active site models	84
5.1	ELF basin populations in starting species of H ₂ O ₂ attack on vanadate.	102
5.2	Change in ELF basin populations leading to formation of 9	103
5.3	Gibbs Free energies for formation of peroxovanadium species	106
6.1	ADF/BP-TZ2P optimised geometries (1–7)	110
6.2	Energies for halide oxidation in three models	114
6.3	Calculated HB geometrical and QTAIM parameters for peroxovanadate com- plexes	116
6.4	Calculated HB (geometrical and QTAIM) parameters for PERCPO	117
6.5	ADF-PBE/TZ2P HB energies 4–7 , 9–11	119
6.6	ADF-PBE/TZ2P HB energies 8,10, 12,13	120
6.7	ADF-PBE/TZ2P HB energies PERCPO	121

6.8	Properties at extrema in $\nabla^2\rho(\mathbf{r})$ function distribution in Fig. 6.6	128
6.9	Properties at extrema in $\nabla^2\rho(\mathbf{r})$ function distribution in Fig. 6.7	132
6.10	NPA analysis for structures in three catalytic models	133
A.1	Structure 2	152
A.2	Structure 2	152
A.3	Structure 4	153
A.4	Structure 4	154
A.5	Structure HPO1	154
A.6	Structure HPO1	154
A.7	Structure 5	155
A.8	Structure 5	155
A.9	Structure 6	156
A.10	Structure 6	157
A.11	Structure 7	158
A.12	Structure 7	158
A.13	Structure 8	159
A.14	Structure 8	159
C.1	QTAIM parameters (a.u.) at bond critical points at ADF-BP/TZ2P level. .	168
C.2	QTAIM parameters (a.u.) at bond critical points at B3LYP/6-311G** level.	169

Chapter 1

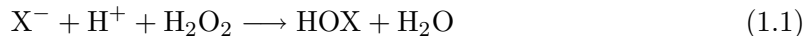
Vanadium Haloperoxidases in Perspective

1.1 Introduction

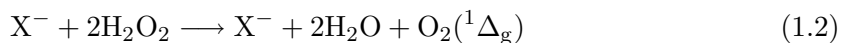
So important is the liason between dioxygen and metals in nature that various life forms depend on it for performing vital biochemical functions.¹⁻³ Three electronic incarnations of dioxygen i.e. molecular oxygen, superoxide and peroxide are since long known for their transition metal complexes,⁴ and one of the principle areas of interest in these complexes is defined by their role as efficient oxygen atom transfer agents. Since oxygen atom transfer is central not only to various biochemical pathways but also to many synthetic procedures in industry, it is needless to stress that more than pure scientific curiosity is at stake in our understanding of transition metal complexes of dioxygen. Complex ions of various metals, particularly in d^0 electronic configuration like those of Ti, V, Mo, W, and Re are able to bind peroxide which is thus activated to deliver oxygen atom to a large variety of substrates,⁵⁻¹³ including halides, alkenes and sulfur compounds, to mention only three. What is more important is that in many instances, after delivering oxygen atom, complex metal ions are catalytically regenerated to repeat the entire process. The adeptness of nature in using this catalytic function in various enzymes is an important lesson for bio-inorganic chemists in order to design effective catalytic schemes leading to production of ecologically and economically useful materials.

From this background present work derives its motivation, with scope limited to use of theoretical and numerical techniques to study a class of enzymes known as vanadium containing haloperoxidases (VHPO).¹⁴⁻¹⁶ These enzymes catalyse oxygen atom transfer particularly (but not only) to halide ions. It is worth pointing out that halogenated organic substances are part of industrially produced specialised and daily use commodities, and that halogenated organic species are important intermediates in organic synthesis. In this regard, use of non-selective and environmentally hazardous halogenating reagents as in elemental form, mineral acids or metal halides are desirable to be replaced by selective and clean reagents¹⁷⁻²¹ like catalytically generated hypohalous acid. The active site of VHPO enzymes uses halide ion and hydrogen peroxide as co-substrates and produces hypohalous acid (or hypohalite) ion as reactive halogenating species.

The active site of VHPO is characterised by presence of vanadate cofactor,^{22–24} which owing to its great propensity towards hydrogen peroxide, readily reacts with later producing peroxovanadium complex.²⁵ The vanadium bound peroxide inside VHPO active site is able to carry two electron oxidation of halide (iodide, bromide and chloride) giving reactive halogenating species HOX with subsequent regeneration of the original vanadate cofactor.^{26,27} The net two electron oxidation reaction is given by



while in the absence of appropriate organic target to halogenate, hydrogen peroxide undergoes halide assisted disproportionation into water and oxygen in first excited state.



In contrast to other classes of peroxidase enzymes (e.g. with haeme-iron cofactor), metal cofactor in VHPO maintains redox inertness as it remains in (+V) oxidation state during entire catalytic cycle.^{28,29}

The active site of two classes of VHPOs, bromoperoxidase (VBPO) and chloroperoxidase (VCPO), share a common structural motif but are differentiated on the basis of functionality i.e. whereas VBPO can oxidise I^- and Br^- , VCPO has the capability to oxidise I^- , Br^- , and Cl^- . Fluoride ion being too electronegative falls outside the oxidising range of these enzymes. Among the VHPO isolated from a variety of species, the VCPO from *Curvularia inaequalis* and VBPO from *Ascophyllum nodosum* remain the most studied representatives of their respective class. X-ray crystal structures of VCPO isolated from terrestrial *Curvularia inaequalis*²² and VBPO from sea algae *Ascophyllum nodosum*²³ (and also from *Corallina officinalis*²⁴) has been solved and their active site structure determined. Active sites of both enzymes contain vanadate cofactor surrounded by amino acid residues remarkably identical in terms of their identity, location and orientation in both systems (Fig. 1.1a). Using amino acid sequence for VCPO, common active site of these enzymes is described as follows. The Imidazole moiety of His496 residue lies within covalent bonding distance to vanadium at fifth coordination site of vanadate, thus turning otherwise tetrahedral vanadate into trigonal bipyramidal (TBP) structure. Five amino acid residues Lys353, Arg360, Ser402, Gly403 and Arg490 are located with their side chains in hydrogen bonding distance to three *exogenous* oxygen atoms of TBP equatorial plane. His404 lies in a position with its imidazole ring in hydrogen bonding distance to remaining exogenous oxygen atom at apical position of TBP structure. The distance of apical oxygen to vanadium being relatively longer than rest of O–V bonds confirms that apical oxygen atom belongs to OH group or possibly water molecule.

Hydrogen bond of apical oxygen with His404 has been postulated to be involved in acid-

base catalysis. The described residues define a cavity with cofactor enclosed in it, and precisely this cavity will be referred to as *active site* henceforth. The crystal structure, after treating VCPO with H_2O_2 , shows peroxo vanadate complex occupying the active site cavity.²⁵ As shown (Fig. 1.1b) peroxide is η^2 coordinated to metal and is oriented towards Lys353 residue within a distance to receive hydrogen bond from it. Since peroxide substitutes two water molecules from coordination sphere of vanadium, earlier mentioned acid base catalytic role of His404 may be important in expulsion of water.

The kinetic studies of formation of peroxo vanadate confirmed its status as the reactive intermediate responsible for oxygen atom transfer step.³⁰ In this regard, the hydrogen bond of Lys353 with η^2 peroxide is hypothesised to be vital for polarising O–O bond and hence preparing it to deliver oxygen atom during two electron oxidation of halide. It was found that VHPO loses catalytic activity on the loss of vanadate cofactor but regains after addition of vanadate,²⁸ that vanadate binds in active site more strongly in presence of H_2O_2 , and that peroxovanadate has greater affinity for active site than vanadate.³⁰ The structural similarity of the active site of *Curvularia inaequalis* VCPO in native form to that of *Ascohyllum nodosum* VBPO is shown in the overlay of crystallographic structures in Fig. 1.1c. The secondary protein shell i.e. amino acid sequence exterior to active site pocket, which is certainly responsible for dictating the spatial orientation of hydrogen bonding groups in active site, exhibits a number of variations in VCPO and VBPO systems. One particular variation in secondary protein shell is replacement of hydrophobic Phe397 in VCPO by hydrophobic His411 in VBPO (Fig. 1.1d). The closeness of these residues to Lys and the ability of His411 in VBPO to interfere with $\text{Lys} \cdots \text{vanadate}$ hydrogen bond may be crucial in determining the oxidising range of both enzymes. As was noted earlier, Lys353 in peroxo form of VCPO forms a hydrogen bond with vanadium bound peroxide, and possible disruption or modification of hydrogen bonding capability of Lys residue, due to a hydrogen bond from a residue like His411 from outer protein shell, can be among the factors to determine the oxidising power of active site peroxo group.

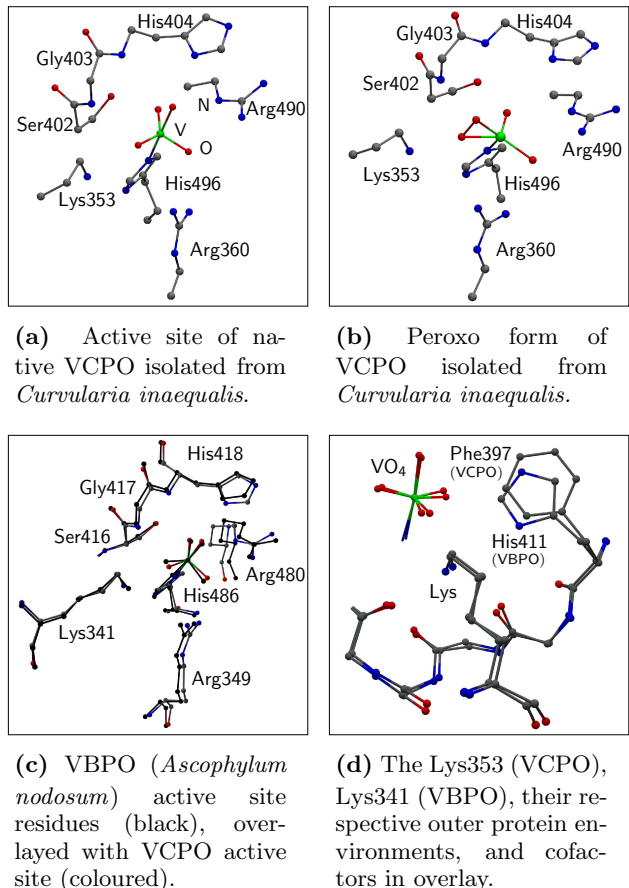


Figure 1.1

Numerous site directed mutagenesis of recombinant VCPO from *Curvularia inaequalis* has been performed to study the cruciality of each amino acid residue in haloperoxidative halogenation activity of VHPO. It was found by Hemrika *et al.*³¹ that mutation of His496, a residue which covalently binds with cofactor, to alanine renders VCPO completely inactive for both chlorination and bromination activities. Mutation of His404 resulted in complete loss of chlorinating activity but partially retained bromination.³² The residues which donate hydrogen bonds to equatorial oxygen atoms of TBP cofactor are Lys353, Arg360, and Arg490. Mutation of these residues again shows the trend that VCPO ceases to show chloroperoxidase activity while exhibiting much reduced level of bromoperoxidation.³¹ In another study existence of Ser402 was shown to be not crucial for both chloroperoxidase and bromoperoxidase activities, although its absence significantly reduced these activities.³³ Moreover, changing Phe397 to His diminished the rates of both bromide and chloride oxidation at acidic *pH*, although in medium close to neutral *pH*, bromide oxidation showed a slight enhancement.

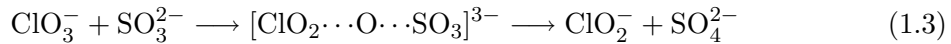
As noted earlier, loss of vanadate deactivates the VHPO, and in this regard crystal structure of apo form of VCPO shows a tetrahedral sulfate ion as cofactor analogue but without covalent bonding to His496 residue. Replacement of this with tungstate, as reported in crystal structure of tungstate derivative of VCPO,³⁴ results in tetrahedral tungstate ion *not* bonded to His496 residue ($W-N_{His496} \approx 255$ pm), which does *not* restore enzymatic activity of the apo enzyme. The molybdate is found to be covalently bonded to His189 ($Mo-N_{His189} \approx 204$ pm) in its complex as phosphate transition state analogue in acid phosphatase from *Escherichia blattae*.³⁵ It is to be stressed that protein environment of molybdate binding site in this acid phosphatase is identical to active site of VHPO systems. Despite this and the fact that peroxomolybdenum complexes are known for peroxidative halogenation activity in solution, molybdate was found to be unable to activate apo VCPO.³⁶ Similar failure is also reported to have been encountered with methyltrioxorhenium.³⁶ This provides grounds for the conclusion that VCPO active site is not optimised for catalytic role of cofactor analogues other than vanadate.

1.2 Catalysis of Oxygen Atom Transfer

1.2.1 Background

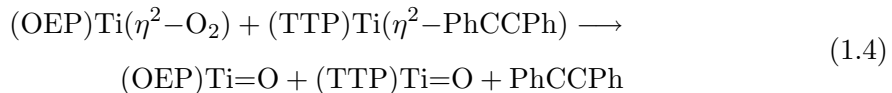
The atom transfer reactions resemble a more general class of redox processes known as *inner sphere* electron transfer.^{37–39} This resemblance is characterised by mediation of oxidation reaction through an atom bonded to one of the reacting species. This atom acts as a bridge in the intermediate activated complex and conclusion of redox process is distinguished by unambiguous transfer of bridging atom from one redox partner species to the other. For

illustration, an example of oxygen atom transfer reaction is given by,

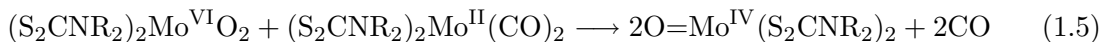


where transferred oxygen atoms was traced with ^{18}O labelling.⁴⁰ The formal redox change in such a reaction can often be, but not always, easily identified with valency of bridging atom i.e. transfer of univalent atom brings one electron and bivalent atom a two electron oxidation/reduction. Although reactions exemplified by Eq. 1.3 are commonplace for main group elements of periodic table, it is more often the case that either of atom donor and acceptor species or both are based on transition metals. In this regard, important distinction can be made in atom transfer reactions where one or two metal centres are involved.

Depending upon whether redox process is *metal centred* or *ligand centred*, atom transfer reactions are called *primary* or *secondary* respectively. For example following reaction⁴¹ has been labelled secondary atom transfer:⁴²



because peroxide ion, O_2^{2-} coordinated in η^2 fashion is reduced to 2O^{2-} by Ti(II) . Nomination of ligands: OEP (octaethylporphyrinato $^{2-}$), TTP (*meso*-tetraphenylporphyrinato $^{2-}$). This can be contrasted with an example of primary atom transfer reaction:^{42,43}



Another aspect emerging from these two reactions is the fact that both η^2 coordinated peroxo and terminal oxo group (M=O bond, $\text{M} = \text{metal}$) can act as oxygen atom transfer agent regardless of the source of transferred oxygen atom (dioxygen or otherwise). In Eq. 1.4, M=O bond is formed as a result of peroxo reduction while in Eq. 1.5, this is itself active oxidant. In fact it was observed that terminal metal oxo bond usually exists for the metals in high formal oxidation state ($\geq +\text{IV}$), and having four or fewer d electrons.⁴⁰ This probably is the reason for prominence enjoyed by complexes of group 4–8 transition metals as the catalysts for oxygen atom transfer reactions, because these metals form the stable terminal metal-oxo complexes.⁴⁴ Moreover, underlying *ligand* or *metal* centrality of redox step reflects an analogous dichotomy among the catalytic procedures involving these redox types. Put in other way this can be stated as, catalytic procedures for speeding oxygen atom transfer are analogously categorised in *ligand* centred and *metal* centred, depending upon whether the metal activates coordinated substrates by (Lewis) *acid-base* mechanism, or by active *redox* involvement. This distinction is important from the operational point of view in regard to haloperoxidase enzymes: while in haeme based haloperoxidases, metal centres

Table 1.1: Standard reduction potentials (mV) for dioxygen species in aqueous solution.⁴⁷ Reductions at left ($pH = 7$) and right ($pH = 0$).

\mathcal{E}^0		\mathcal{E}^0	
$O_2 + e^- \longrightarrow O_2^-$	-330.0	$O_2 + H^+ + e^- \longrightarrow HO_2$	-50.0
$O_2^- + e^- + 2H^+ \longrightarrow H_2O_2$	+890.0	$HO_2 + e^- + H^+ \longrightarrow H_2O_2$	+1440.0
$O_2 + 2H^+ + 2e^- \longrightarrow H_2O_2$	+281.0	$O_2 + 2H^+ + 2e^- \longrightarrow H_2O_2$	+695.0
$H_2O_2 + H^+ + e^- \longrightarrow H_2O + HO\cdot$	+380.0	$H_2O_2 + H^+ + e^- \longrightarrow H_2O + HO\cdot$	+800.0
$HO\cdot + H^+ + e^- \longrightarrow H_2O$	+231.0	$HO\cdot + H^+ + e^- \longrightarrow H_2O$	+272.0
$H_2O_2 + 2H^+ + 2e^- \longrightarrow 2H_2O$	+1349.0	$H_2O_2 + 2H^+ + 2e^- \longrightarrow 2H_2O$	+1763.0
$O_2 + H^+ + 4e^- \longrightarrow 2H_2O$	+815.0	$O_2 + H^+ + 4e^- \longrightarrow 2H_2O$	+1229.0

undergo complicated redox sequences, in non-haeme, vanadium dependent haloperoxidases (VHPO) vanadium cofactor remains in (+V) oxidation state during entire catalytic cycle. Interestingly a proposal was made⁴⁵ before the discovery of VHPO, to make use of secondary oxygen atom transfer to external substrate in a catalytic cycle, for the situations where changing the oxidation state of central metal is not desirable.

1.2.2 Building Blocks of Catalyzed Peroxide Reduction

As mentioned earlier, VHPO enzymes catalyse production of hypohalite ion by two electron oxidation of halide with hydrogen peroxide. Apparently the key feature of this catalysis is Lewis acid role of vanadium(+V) in activating the coordinated peroxide as nucleophile, which can then undergo O–O cleavage to deliver oxygen atom to halide. Essential building blocks of this catalysis, hence concern with the nature of peroxide co-substrate and its bonding to the vanadium metal. Present part of this section deal with the review of these issues, by considering basic chemistry of substrate–metal binding.

Nature of dioxygen oxidant

The molecular oxygen with paramagnetic ground state ($^3\Sigma_g^-$) has electronic configuration: $(1\sigma_g)^2(1\sigma_u^*)^2(2\sigma_g)^2(2\sigma_u^*)^2(2p\sigma_g)^2(2p\pi_u)^4(2p\pi_g^*)^2$, where two unpaired electrons occupy two degenerate π^* orbitals. The two lowest excited states ($^1\Delta_g$) and ($^1\Sigma_g^+$) lie respectively 22.5 , and 37.5 kcal mol⁻¹ above the ground state.⁴⁶ In the ground state, addition of one and two electrons in π_g^* orbitals produces superoxide (O_2^-) and peroxide ions respectively, while full four electron reduction leads to two water molecules. The role of dioxygen in life becomes obvious if enzymatic systems provided by nature to handle its chemistry are considered. Molecular oxygen (O_2) is unique in chemistry in the sense that it has a paramagnetic ground state and although its reactions with organic matter are thermodynamically exothermic, normally singlet ground states of organic species in cellular environment are

	ne_{π^*}	Bond order	ν_{O-O} (cm^{-1})	r_{O-O} (pm)
O_2^{2-}	4	1.0	802	149.0
O_2^-	3	1.5	1097	133.0
O_2	2	2.0	1580	121.0
O_2^+	1	2.5	1905	112.0

Table 1.2: Properties of O–O bond in dioxygen species.⁴ Number of π^* electrons ne_{π^*} , O–O stretching vibration ν_{O-O} , and O–O distance r_{O-O} .

kinetically disfavoured to react with (triplet) molecular oxygen under normal conditions. This kinetic barrier can be circumvented either by photochemically exciting O_2 to one of the singlet states, by thermally producing two free radicals in doublet state or by complexing it with paramagnetic metal ions. The last one is the method of choice in metalloenzymes which catalyse reactions of molecular oxygen for specialised physiological needs. On the other hand, one electron reduced form of dioxygen i.e. superoxide is often a toxic byproduct of biochemical activity and needs to be dismutated, and two-electron reduced form peroxide is either needed to be dismutated or utilised as useful oxidant. These functions are performed by some other specialised metalloenzymes. Interesting redox chemistry of dioxygen at neutral and acidic pH in terms of standard reduction potentials is produced in Table 1.1, while summary of physical properties of O–O bond is given in Table 1.2. An important feature emerging from data in Table 1.1 is thermodynamic preference (i.e. more positive reduction potentials) for two-electron processes, and the fact that proton drives \mathcal{E}^0 of dioxygen species towards (more) positive values by charge compensation i.e. disfavoured placement of extra electron in π^* orbital is stabilised by O–H bond formation. In DMF solvent it has been reported⁴⁸ that for one electron O_2 reduction, an endothermic $\mathcal{E}^0 = -600$ mV is changed to exothermic value of +120 mV. Thermodynamic favourability ensuing from O–H bond formation can be as well anticipated to occur with O–M bond formation on coordination of dioxygen to metal (M). The large exothermicity of reduction of hydrogen peroxide is in line with its powerful oxidising character, which can be tuned by pH and metal coordination to oxidise species otherwise not vulnerable to it.

The dioxygen chemistry sets the oxidising behaviour of metal bound peroxide in following terms. It was argued⁴⁹ that molecular oxygen is different in its coordination to metals from other ligands because of, first, molecular oxygen is observed to ligate metals already in reduced oxidation state and, second, there are readily accessible reduced oxidation states for dioxygen (superoxide and peroxide). These two factor determine that depending upon the stoichiometry and metal, none, one or two electrons can be easily transferred from metal to dioxygen on ligation.⁴⁹ By corollary, if peroxide is coordinated to a metal centre in d^0 electronic configuration, like vanadium(V), it suffices to restrict the metal to behave only as Lewis acid. Moreover, two electron reduction of hydrogen peroxide occurs at much larger positive value of \mathcal{E}^0 than that for its one electron reduction, making it a more powerful two electron oxidant or oxygen *atom* transfer agent.

Coordination chemistry of vanadium

Vanadium⁵⁰ (proton number 23) occupies an early place in first row transition elements, with $\approx 0.014\%$ abundance in nature. It is widespread in environment, some of its mineral deposits are *patronite* (a complex sulfide), *vanadinite* $[\text{Pb}(\text{VO}_4)_3\text{Cl}]$, and *carnotite* $[\text{K}(\text{UO}_2)\text{VO}_4 \cdot 3/2\text{H}_2\text{O}]$. Vanadium exists in various oxidation states with highest (+V) state corresponding to d^0 electrons. In oxidation states (II) to (V), the most well known species are $[\text{V}^{\text{II}}(\text{H}_2\text{O})_6]^{2+}$, $[\text{V}^{\text{III}}(\text{H}_2\text{O})_6]^{3+}$, $\text{V}^{\text{IV}}\text{O}^{2+}$, and $\text{V}^{\text{V}}\text{O}_2^+$. In many respects higher oxidation states of vanadium are dominated by oxo compounds, and in aqueous medium vanadium offers very rich and complicated chemistry (Fig. 1.2). Among numerous biological roles of vanadium (for a comprehensive review please refer to⁵¹), relatively recent (1984) discovery was rather surprising presence of vanadium cofactor instead of haeme iron, in then newly found VHPO.¹⁴ The aspects of coordination chemistry of vanadium concerning VHPO enzyme are of interest in present work. In VHPO vanadium(+V) is found in form of vanadate, the aqueous chemistry of which is highly dependent on $p\text{H}$. In this regard, at physiological $p\text{H}$ tetrahedral monoanionic $(\text{OH})_2\text{VO}_2^-$ is of prime dominance and is able to transform into trigonal bipyramidal (TBP) geometry with suitable supporting ligands. The VO_2^+ moiety in vanadate contains strong and polar $\text{V}=\text{O}$ bonds with strong oxygen to metal charge transfer. It is worth mentioning that long ago a triple bond character was attributed to metal-oxo bonds on the basis of theoretical arguments.^{52,53} The strength of $\text{V}=\text{O}$ bond is mainly due to σ donation from oxygen, and π interaction of oxygen p orbitals with relevant d orbitals of vanadium.

More importantly, due to presence of π back donation channel, charge can be easily shuttled between vanadium and oxo oxygen atoms, either induced by alterations in rest of coordination sphere of vanadium, or by controlling interaction of oxo oxygen atoms with environment, solvent etc. The hydroxyl ions (or water molecule) when coordinated to VO_2^+ , because of inductive effect of bound cation, is expected

to undergo enhancement in polarisation of O–H bond and hence a change in its acidity. This effect varies with effective nuclear charge on vanadium, a behaviour which carries significance if coordinated hydroxyl or water ligand is involved in *acid-base* catalysis.

Other important aspect of vanadium(+V) coordination chemistry relevant to present work is propensity of vanadate towards hydrogen peroxide. There is no better demonstration of this than classical spot test for vanadate which forms red peroxovanadium complex

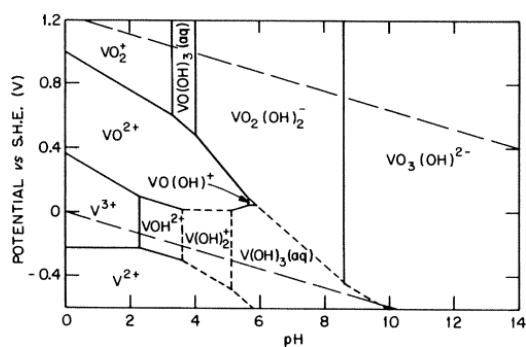
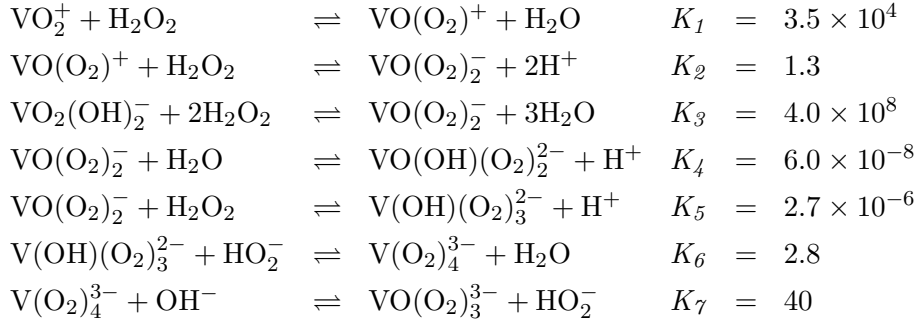


Figure 1.2: Standard electrode potential as a function of $p\text{H}$ for vanadium species. Reproduced from ref.⁵⁴

on addition of hydrogen peroxide. Peroxide coordinates in η^2 fashion to vanadium and monoperoxo, bisperoxo, trisperoxo and even tetraperoxo vanadium complexes are formed according to* :-



Bonding between peroxide and vanadium in η^2 coordination can be described as formation of (V–O_{peroxo}) coordinate bonds with donation from π type oxygen orbitals centred on peroxo group. The triangular bidentate peroxo–vanadium binding creates local C_{2v} symmetry giving rise to three Raman and IR active vibrational modes⁵⁸ : symmetric O–O stretch (880 cm^{-1}), symmetric vanadium–peroxo stretch (600 cm^{-1}), and asymmetric vanadium–peroxo stretch (500 cm^{-1}). Activation of peroxide coordinated in this fashion to many d⁰ metal ions, for oxidation of many substrates is well known and perxovanadium(+V) complexes being no exception, and following oxidations are carried by these: sulfoxidation and sulfonation of sulfides, epoxidation of alkenes, oxidation of primary and secondary alcohols to aldehydes and ketones, and hydroxylation of arenes and alkanes.

Haloperoxidase activity as oxygen atom transfer

The metal catalyzed oxygen atom transfer step involved in haloperoxidase activity (Eqs. 1.1, 1.2) is common in many enzymatic systems other than VHPO and in the (halo)peroxidative activity of non-enzymatic catalysis schemes involving metals including vanadium. Among the non-enzymatic catalytic analogues of VHPO are the systems involving V, Re, and Mo in highest oxidation state. Available experimental evidence indicates that vanadium metal in VHPO, and these high oxidation state metals in solution catalytic systems, do not undergo redox change during catalytic cycle, and that reactive intermediate is peroxide metal complex. In this respect several kinetic studies have been performed and foremost to the present concern is bromoperoxidative catalytic activity of *cis*-dioxovanadium(V) species VO_2^+ in acidic solutions.^{55,59,60} It was found that VO_2^+ reacts with hydrogen peroxide to give oxomonoperoxo-vanadium(V) $\text{VO}(\text{O}_2)^+$ and oxobisperoxo-vanadium(V) species $\text{VO}(\text{O}_2)_2^-$. These later two species were not found to oxidise bromide, but rather it was observed that these enter into equilibrium with a binuclear oxovanadium(V)-trisperoxo species,

* Equilibria (K_1 and K_2) in acidic solutions.⁵⁵ Equilibria (K_3 – K_7) results from ^{51}V NMR studies in near neutral solutions.^{56,57}

$(VO)_2(O_2)_3$, which was found to be responsible for bromide oxidation (Fig. 1.3a). Another aspect of this catalytic activity is suitable saturation of vanadium coordination sphere, which is crucial in determining the nature of reactive intermediate. For example, in case of coordination of hydroxyphenyl-salicylideneamine (H_2HPS), to hydroxo-oxovanadium(V), and subsequent reaction (Fig. 1.3b) of resulting complex with hydrogen peroxide generates a mononuclear oxo-monoperoxovanadium(V) species $(HPS)VO(O_2)^-$, which was found to oxidise bromide.⁶¹ Metals other than vanadium, known for catalysis of haloperoxidative activity of their peroxo complexes are Mo, W, and Re. Mo, and W complexes⁶² have been shown to catalyse oxygen atom transfer via a bisperoxo species (Fig. 1.3c), while Re complex^{63,64} follow a similar mechanism with the difference that both monoperoxo and bisperoxo Re complexes act as reactive intermediate. It was argued⁶⁵ that catalytic reactivity increases directly with Lewis acidity of the metals in their peroxo complexes in the order $WO(O_2)_2 > MoO(O_2)_2 > VO(O_2)_2$. In fact $VO(O_2)_2$ is unable to oxidise bromide, but a binuclear trisperoxo vanadium species is reactive species, as already mentioned. The Lewis acidity of high oxidation state metal centre is a direct consequence of low radius to charge ratio of metal cation, and a qualitative estimate can be made for these three metals.⁶⁶

For species VO_2^+ , MoO_2^+ and WO_2^+ ionic radii⁶⁷ in tetrahedral geometry are 50, 41 and 41 pm respectively, while (d shell) Z_{eff} ⁶⁸ in the same order is given as: 11.75, 12.75 and 12.75. It should be clear that catalytic power of metallo-enzyme which employs a scheme like in Fig. 1.3 emanates from modulation of metal Lewis acidity by the protein environment. The catalytic inactivity of tungstate complex with VCPO apoprotein, despite the fact that tungsten is the better Lewis acid than vanadium, is indicative that VCPO active site is not optimised for activating reactive peroxotungsten species. Among the metalloenzymes, Fe-haeme based haloperoxidases (FeHPO) share the functionality of peroxidative halogenation, and Fe-Haeme catalase that of hydrogen peroxide disproportionation (peroxide dismutation) with VHPO. Operative procedure for FeHPO is schematically depicted in Fig. 1.4a. As previously pointed out, oxygen atom transfer and their catalytic protocol is categorised into metal-centred or primary, and ligand-centred or secondary. While Fe metal in FeHPO and catalase systems acts as electron-transfer catalyst and belong to former category, VHPO and its non-enzymatic analogues fall into second category by em-

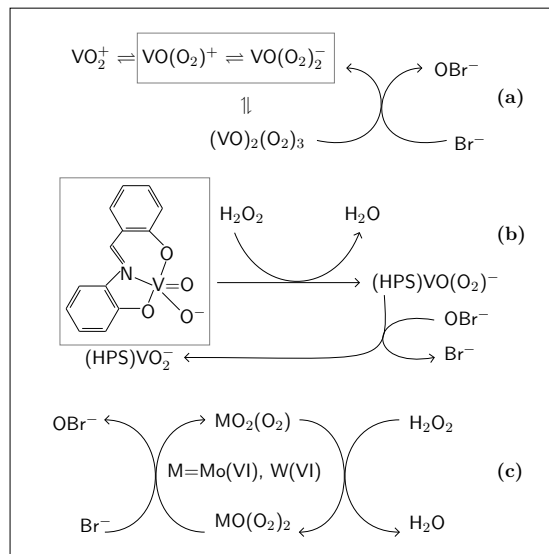


Figure 1.3

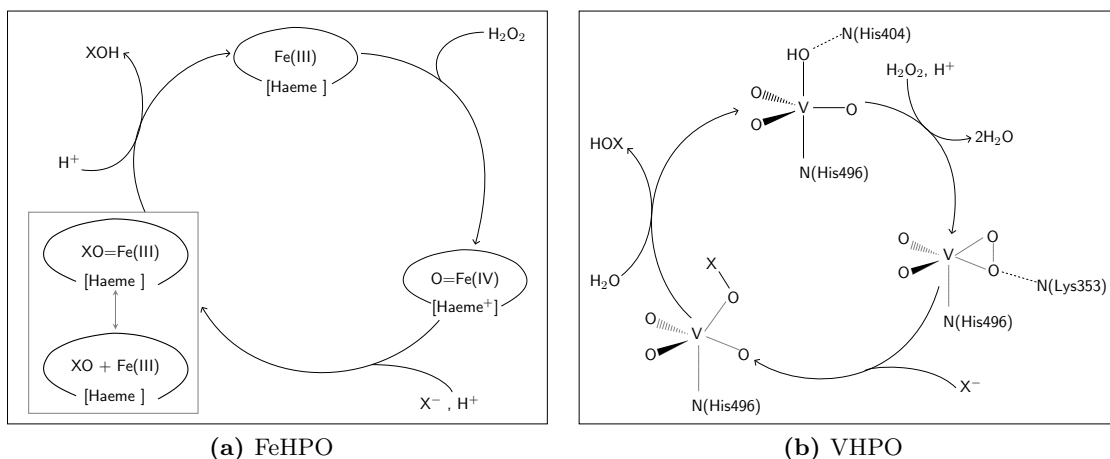


Figure 1.4: Outlines of FeHPO operation and proposed VHPO mechanism.

employing metal as Lewis acid catalyst. A reasonable VHPO mechanism proposal, based on crystallographic, and spectroscopic evidence and on the analogy to solution phase metallic Lewis acid catalysts (Fig. 1.3) is sketched in Fig. 1.4b. A related distinction between the two categories is the nature of transferable oxygen atom. In VHPO and its non-enzymatic analogues it originates from metal bound peroxide activated for heterolytic O–O cleavage. On the other hand in FeHPO (and catalase) transferable oxygen is two electron reduced form of peroxide (in fact an oxoferryl(IV) species) in what is termed by the biochemists as Compound 1, which is generated *after* the cleavage of O–O bond. Compound 1 delivers oxygen atom to halide substrate in FeHPO, while reacts with another hydrogen peroxide in catalase. The chemistry underlying these distinctions can be described in terms of metal redox character. Iron on one hand and vanadium, molybdenum, rhenium on the other are distinguished from the fact that highest oxidation state of former does not correspond to d^0 electronic configuration. FeHPO like mechanism in case of d^0 (V, Mo, Re) catalysts is not possible simply because these can not be oxidised beyond d^0 configuration.

It is important to note that reduction potential for $V(+V)/V(+IV)$ redox couple in the process $VO_2^+ \rightarrow VO^{2+}$ is reported⁶⁹ around 1000 mV, which is possible⁷⁰ for peroxide to carry out at appropriate pH if coupled with reactions where substrate is oxidised by one electron. Hence during catalysis of one-electron reduction where radical intermediates are involved, vanadium centre is no longer expected to maintain redox inertness. For example in the reaction of alcohols with hydrogen peroxide to give ketones, a net hydrogen atom abstraction, vanadium catalyst cycles between (+V) and (+IV) states.^{71,72} Similarly in hydroxylation of benzene with hydrogen peroxide, vanadium centre has been proposed to change from (V) to (IV) oxidation state and in the process initiating radical mechanism.⁷³

1.2.3 Theoretical studies of VHPO akin mechanisms

The epoxidation of alkenes by peroxo complexes of some second transition row metals in d^0 electronic configuration is akin to catalytic activity of peroxovanadium(+V) complexes and VHPO enzyme. Considerable efforts have been invested into study of olefin epoxidation by Mimoun's type oxobisperoxo Mo(VI) complexes,^{8,9,73,74} Hermann's type methyloxobisperoxo Re(VII) complexes,^{10,12} and Venturello's peroxotungstate system.¹¹ Incidentally it is also one of the extensively studied mechanisms at theoretical level and knowledge generated by these studies in recent years is of prime relevance to present work. Some of the issues decided by these studies are of current concern in this part of the chapter.

Mimoun and Sharpless mechanism

One of the earliest mechanistic controversies was about the proposals regarding the nature of energy barrier during olefin attack on Mo(VI) bound peroxide. Mimoun⁹ hypothesised a three step mechanism in which (1) Olefin is coordinated to Mo in oxobisperoxomolybdenum(VI) complex (suggested by the observation that higher coordination saturation by other ligands seemed to block epoxidation), (2) coordinated olefin is inserted into Mo–O_{peroxo} bond forming a five membered ring and (3) epoxide is formed by inversion of the ring. On the other hand Sharpless⁷⁵ suggested a concerted one-step mechanism in which a three-membered ring is formed in transition state due to direct attack of olefin on oxygen atoms of peroxo group. Mimoun's proposal implied that olefin is made electrophilic by loss of charge to metal and peroxo group acts as nucleophile. Sharpless proposal on the other hand assigns electrophilic character to peroxo group. It is well established that organic analogues of peroxometal complexes i.e. dioxiranes and peracids, in stoichiometric epoxidation depend upon electrophilic character of their peroxo functional group.^{76–82} The computational verdict with evidence in favour of Sharpless mechanism has been reviewed (Fig. 1.5).⁸³ The investigation by Frenking *et al.* demonstrated that formation of five-membered ring intermediate for epoxidation of olefin by oxobisproxomolybdenum complex would result in carbonyl product rather than epoxide.⁸⁴ Rösch *et al.* in their computational study of olefin epoxidation by bisperoxo complex of [Re(VII)O(O₂)₂Me] showed that Re coordinated olefin complex is *not* formed, and that formation of five membered ring has to surpass a significantly higher activation barrier in comparison to one for concerted oxygen atom transfer.⁸⁵ Sensato *et al.* reported Sharpless like mechanism for sulfoxidation by oxobisperoxomolybdenum(VI)⁸⁶. Similar results have been obtained for epoxidation by peroxocomplexes of Cr⁸⁷, W⁸⁷, and V.⁸⁸

Peroxo complexes of different d^0 metals

In the computational studies cited above, reactivity of complexes of different metals also came under investigation and some interesting outcome is reproduced here. It was found

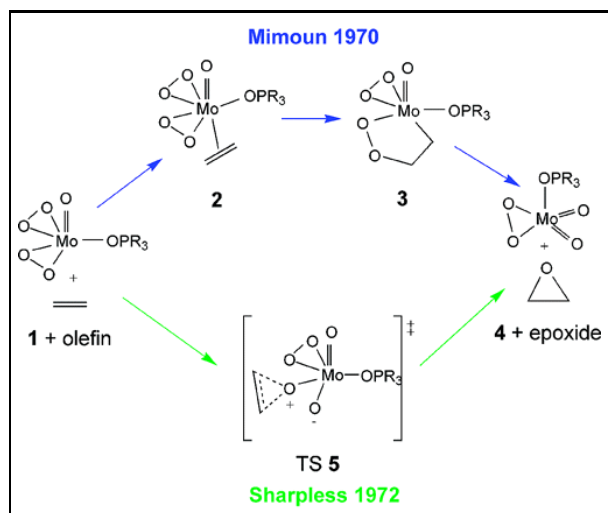


Figure 1.5: Sketch of Mimoun and Sharpless mechanistic proposals for olefin epoxidation by Mimoun's type complexes, reproduced from ref.⁸³ *Mimoun's mechanism*, $1 \rightarrow 2$:- Olefin coordination to metal, $2 \rightarrow 3$:- 5-membered metallocycle formation, $3 \rightarrow 4$:- Insertion into Mo-O bond. *Sharpless mechanism*, $1 \rightarrow \text{TS } 5$:- Concerted nucleophilic attack of olefin. Sharpless type mechanism is supported for a number of metals by computational studies.

that in the complexes of triad (Cr, Mo, W), activity decreases in the order $W > Mo > Cr$. It was further found^{87,89} that bisperoxo complexes of Cr and Mo are more reactive compared to monoperoxo complexes.^{87,89,90} However, reactivity difference between mono- and bisperoxo complexes of Mo, in terms of activation barrier is only 2–3 kcal mol⁻¹, which cautions not to underestimate the reactivity of monoperoxo complexes of this metal. It is relevant to cite an argument forwarded in case of peroxidative halogenation by bisperoxo complexes of Mo in which lack of experimental evidence for reactive monoperoxo intermediates was argued, not on behalf of any inherent lack of reactivity of monoperoxo complexes, but thermodynamic equilibrium which is greatly favourable towards bisperoxo species.⁶⁴ The peroxo complexes of tungsten in computational studies were found to be activationally indifferent towards mono- or bis- coordination of peroxo species.⁸⁹ The ligation of metal centre by an additional N-base (e.g ammonia) raised the activation energy considerably for all of three metals due to consequentially diminished electrophilicity of peroxo group,^{87,90,91} while adding electron releasing substituents on C=C double bond in olefin substrate reduced the activation barrier.⁸⁹

Another observation was that in case of Ti(IV), hydroperoxo and alkylperoxo coordinated end on (μ^1),⁹² while to Mo(VI) hydroperoxo group coordinated in side on (η^2) fashion.⁹³ For reactions of both Ti and Mo hydroperoxo complexes, transition states of olefin attack show side on metal coordination (i.e. involving both α and β peroxygen atoms) of hydroperoxo functionality. For both metals these complexes showed higher reactivity in comparison to respective peroxo complexes.^{92,93} The base effect of additional ammonia ligand was found to be helpful in raising activation energy of side on complexes, but for hydroperoxo complex this effect was negligible. In contrast, Re(VII) shows opposite behaviour as hydroperoxo functionality coordinated to it is activationally more demanding than coordinated peroxo functionality.⁸⁵

1.3 This Thesis

Answer to some structural and mechanistic questions regarding VHPO have been attempted in this thesis, the outline of which is produced here. By the time of start of this work several perplexities marred the extensive wealth of experimental findings, and answers from computational side were rather scarce. Outcome of present work makes a contribution which is overlapped in certain aspects by findings meanwhile reported by other groups, and in some other aspects offers a fresh perspective.

- Chapter 2 reviews the theoretical basis of computational approaches used to study the VHPO systems.
- Chapter 3 takes the question of resting state of VHPO with the help of optical excitations calculated with time dependent density functional theory. The geometry and protonation state of vanadate cofactor is determined on the basis of comparison between experimental and theoretical electronic excitations in vanadate cofactor in gas and protein environments.
- Chapter 4 presents detailed comparative studies on hydrogen bonding patterns between cofactor and protein environment in otherwise identical VCPO and VBPO active sites. The implications for functional disparity between the two enzyme systems is discussed.
- Chapter 5 presents the results about first step in vanadium haloperoxidative halogenation: i.e. reaction of hydrogen peroxide with imidazole bound vanadate to give reactive peroxovanadium species. In this respect results about role of His404 are also presented.
- Chapter 6 presents the results about the second step: the reaction of peroxovanadium species with halide to produce reactive halogenating species. The role of Lys353 residue, and influence of VCPO and VBPO environment on it is also discussed.
- And finally the abstract (along with its German translation, given in the beginning of the thesis) summarises the findings reported in present work.

Chapter 2

Time Independent and Dependent Density Functional Theory

To obtain useful knowledge about the VHPO active site by computing relevant parts of potential energy surface of active site models is of primary concern in this thesis. Such computations are based on the theory of matter at atomic and molecular level. In particular, density functional theory (DFT) of electronic structure has permitted a very useful computational access to quantum description of chemical systems. Present chapter briefly outlines the formal foundations on which computational work of this thesis rests and in this regard the description of DFT in its static and time-dependent forms is given.

2.1 Introduction: From Wave Function to Electron Density

The information about a system at atomic level is obtainable from a state vector $|\Psi\rangle$ in Hilbert space and the extraction of this information is closely linked to representation of state vector. Of special interest in quantum chemistry is the representation in *position* space (or coordinate space) as wave function $\Psi(\mathbf{r})$. In principle the information about an N -electron system carried by its state vector $|\Psi_N\rangle$ can be obtained by density operator,

$$\hat{\gamma}_N = |\Psi_N\rangle\langle\Psi_N| \quad (2.1)$$

If space coordinate \mathbf{r}_i and spin coordinate s_i of i th particle are combined in a single coordinate $\mathbf{x}_i = \mathbf{r}_i s_i$, and Hilbert space is comprised of coordinate basis $|\mathbf{x}_i\rangle$, the coordinate representation of density operator (Eq. 2.1) given as,

$$\begin{aligned} \gamma_N(\mathbf{x}'_1 \mathbf{x}'_2 \cdots \mathbf{x}'_N, \mathbf{x}_1 \mathbf{x}_2 \cdots \mathbf{x}_N) &= \langle \mathbf{x}'_1 \mathbf{x}'_2 \cdots \mathbf{x}'_N | \hat{\gamma}_N | \mathbf{x}_1 \mathbf{x}_2 \cdots \mathbf{x}_N \rangle \\ &= \Psi(\mathbf{x}'_1 \mathbf{x}'_2 \cdots \mathbf{x}'_N) \Psi^*(\mathbf{x}_1 \mathbf{x}_2 \cdots \mathbf{x}_N) \end{aligned} \quad (2.2)$$

defines a density matrix. The quantity Ψ_N is wave function and with simplified notation of coordinate variables according to $(\mathbf{x}_1 \mathbf{x}_2 \cdots \mathbf{x}_N) = (\mathbf{x}^N)$, the diagonal elements $(\mathbf{x}'_i = \mathbf{x}_i)$ of

above defined density matrix give the following trace for normalised Ψ_N ,

$$\text{tr}(\hat{\gamma}_N) = \int \Psi(\mathbf{x}^N) \Psi^*(\mathbf{x}^N) d\mathbf{x}^N = 1 \quad (2.3)$$

the integrand in Eq. 2.3 is interpreted as probability of finding the system in a state in which N th particle with spin between s_N and ds_N , is present at position in the range r_N to dr_N . The integration of this over all space and spin coordinates gives unit probability. This description of a quantum system is important in the view that any observable associated with an operator \hat{A} can be obtained as:

$$\langle \hat{A} \rangle = \text{tr}(\hat{A} \hat{\gamma}_N) \quad (2.4)$$

For describing the systems of chemical interest, it is useful to write density matrix in terms of one-electron and two-electron descriptors by integrating $\hat{\gamma}_N$ over coordinates of all but one, and two electrons respectively. This gives rise to first-order (γ_1) and second-order (γ_2) reduced density matrices,

$$\gamma_1(\mathbf{x}'_1, \mathbf{x}_1) = N \int \cdots \int \Psi(\mathbf{x}'_1 \mathbf{x}_2 \mathbf{x}_3 \cdots \mathbf{x}_N) \Psi^*(\mathbf{x}_1 \mathbf{x}_2 \mathbf{x}_3 \cdots \mathbf{x}_N) d\mathbf{x}_2 \cdots d\mathbf{x}_N \quad (2.5)$$

$$\gamma_2(\mathbf{x}'_1 \mathbf{x}'_2, \mathbf{x}_1 \mathbf{x}_2) = \frac{N(N-1)}{2} \int \cdots \int \Psi(\mathbf{x}'_1 \mathbf{x}'_2 \mathbf{x}_3 \cdots \mathbf{x}_N) \Psi^*(\mathbf{x}_1 \mathbf{x}_2 \mathbf{x}_3 \cdots \mathbf{x}_N) d\mathbf{x}_3 \cdots d\mathbf{x}_N \quad (2.6)$$

The factors N in Eq. 2.5 and $\frac{N(N-1)}{2}$ in Eq. 2.6 are normalisation constants and it is obvious that γ_1 and γ_2 normalise respectively to number of electrons and number of distinct electron pairs according to:

$$\text{tr} \gamma_1(\mathbf{x}'_1, \mathbf{x}_1) = N \quad (2.7)$$

$$\text{tr} \gamma_2(\mathbf{x}'_1 \mathbf{x}'_2, \mathbf{x}_1 \mathbf{x}_2) = \frac{N(N-1)}{2} \quad (2.8)$$

It is possible to further simplify reduced density matrices by taking out spin coordinate from \mathbf{x}_1 in $\gamma_1(\mathbf{x}'_1, \mathbf{x}_1)$ and from \mathbf{x}_1 and \mathbf{x}_2 (both primed and unprimed) in $\gamma_2(\mathbf{x}'_1 \mathbf{x}'_2, \mathbf{x}_1 \mathbf{x}_2)$ to produce spinless reduced density matrices. The spinless first order and second order density matrices are given by:

$$\rho_1(r'_1, r_1) = N \int \cdots \int \Psi(r'_1 s_1 \mathbf{x}_2 \cdots \mathbf{x}_N) \Psi^*(r_1 s_1 \mathbf{x}_2 \cdots \mathbf{x}_N) ds_1 d\mathbf{x}_2 \cdots d\mathbf{x}_N \quad (2.9)$$

$$\rho_2(r'_1 r'_2, r_1 r_2) = \frac{N(N-1)}{2} \int \cdots \int \Psi(r'_1 s_1 r'_2 s_2 \mathbf{x}_3 \cdots \mathbf{x}_N) \Psi^*(r_1 s_1 r_2 s_2 \mathbf{x}_3 \cdots \mathbf{x}_N) ds_1 ds_2 d\mathbf{x}_3 \cdots d\mathbf{x}_N \quad (2.10)$$

The diagonal elements of $\rho_1(r'_1, r_1)$ and $\rho_2(r'_1 r'_2, r_1 r_2)$ define useful functions from chemical point of view, which in case of former is electron density,

$$\rho(r_1, r_1) = \rho(r_1) = N \int \cdots \int \Psi_N(x_1 \cdots x_N) \Psi_N^*(x_1 \cdots x_N) ds_1 dx_2 \cdots dx_N \quad (2.11)$$

and describes the probability of finding any electron of any spin, at position r_1 while all other electrons take arbitrary positions in space. This quantity integrates to N or total number of electrons as

$$\int \rho(r) dr = N \quad (2.12)$$

As will be seen later in this chapter, electron density is starting point in journey towards ground state properties of N -electron system in DFT. Diagonalisation of first-order density matrix produces *natural orbitals* as eigen functions, and *occupation numbers* as eigen values of this matrix. Likewise, the diagonal element of second order reduced spinless density matrix $\rho_2(r'_1 r'_2, r_1 r_2)$ in Eq. 2.10 gives a function called electron-pair density written as:

$$\rho(r_1 r_2, r_1 r_2) = \rho(r_1, r_2) = \frac{N(N-1)}{2} \int \cdots \int \Psi_N(x_1 \cdots x_N) \Psi_N^*(x_1 \cdots x_N) ds_1 ds_2 dx_3 \cdots dx_N \quad (2.13)$$

This is probability of finding one electron of any spin at position r_1 , and simultaneously another of any spin at position r_2 , while the remaining particles take arbitrary positions in space. Moreover analogously to Eq. 2.12, pair density integrates to total number of distinct electron pairs $\frac{N(N-1)}{2}$.

Importance of second order reduced density matrix in electronic structure theory and corresponding pair density becomes evident by the fact that these carry all the information about pair correlations, i.e. correlated movement of any two electrons. This is an important issue in regard to post Hartree-Fock *ab initio* level of accuracy in quantum-chemical prediction of molecular properties. This can be shown by considering many body electronic Hamiltonian,

$$\hat{\mathcal{H}} = - \sum_{i=1}^N \frac{1}{2} \nabla^2 + \sum_{i=1}^N v(r_i) + \sum_{i<j}^N \frac{1}{r_{ij}} \quad (2.14)$$

of which the first term is one electron kinetic energy term, $v(r_i) = \sum_{\alpha} \frac{Z_{\alpha}}{r_{i\alpha}}$, is the sum of all interaction potentials between i th electron and α th nucleus, and final term is sum of all two electron interactions. Of these only the third term involves two electrons and is of present concern with respect to its operation in concert with second order (two-electron) reduced density matrix. Any two electron operator $\hat{\mathcal{O}}_2$, in space only (i.e. not including

spin) coordinate representation, can be written as a sum over representations of all pairs as in Eq. 2.15

$$\hat{\mathcal{O}}_2 = \sum_{i < j}^N O_2(\mathbf{r}'_i \mathbf{r}'_j, \mathbf{r}_i \mathbf{r}_j) \quad (2.15)$$

$$\hat{V}_{ee} = \sum_{i < j}^N \frac{1}{r_{ij}} \quad (2.16)$$

and since two-electron terms in Eq. 2.16 (interelectronic interaction part of Hamiltonian, Eq. 2.14) are local in the sense that these involve no primed space coordinates, its representation as in Eq. 2.15 needs only diagonal terms $O_2(\mathbf{r}_i \mathbf{r}_j)$ to be considered. With this consideration and using formula in Eq. 2.4 for expectation value of $\hat{\mathcal{O}}_2$ in terms of second order reduced density matrix is given as

$$\begin{aligned} \langle \hat{\mathcal{O}}_2 \rangle &= \text{tr}[\hat{\mathcal{O}}(\mathbf{r}'_1 \mathbf{r}'_2, \mathbf{r}_1 \mathbf{r}_2) \rho_2(\mathbf{r}'_1 \mathbf{r}'_2, \mathbf{r}_1 \mathbf{r}_2)] \\ &= \int \int [O_2(\mathbf{r}'_1 \mathbf{r}'_2, \mathbf{r}_1 \mathbf{r}_2) \rho_2(\mathbf{r}'_1 \mathbf{r}'_2, \mathbf{r}_1 \mathbf{r}_2)]_{\mathbf{r}'_1 = \mathbf{r}_1, \mathbf{r}'_2 = \mathbf{r}_2} d\mathbf{r}_1 d\mathbf{r}_2 \\ &= \int \int \frac{1}{r_{12}} \rho_2(\mathbf{r}_1, \mathbf{r}_2) d\mathbf{r}_1 d\mathbf{r}_2 \end{aligned} \quad (2.17)$$

Writing the interelectronic energy in terms of pair density opens the way to look into quantum mechanical nature of correlation between electrons. If expectation value of interelectronic interaction energy (Eq. 2.17) was solely due to Coulombic repulsion between electron density distribution at two points it would have been sufficient to simply write it as following.

$$J[\rho] = \frac{1}{2} \int \int \frac{1}{r_{12}} \rho(\mathbf{r}_1) \rho(\mathbf{r}_2) d\mathbf{r}_1 d\mathbf{r}_2 \quad (2.18)$$

This is a manifestation that pair density carries both classical (Coulombic) and quantum-mechanical interaction, thus suggesting to rewrite it in view of Eq. 2.17 and 2.18

$$\rho_2(\mathbf{r}_1, \mathbf{r}_2) = \frac{1}{2} \rho(\mathbf{r}_1) \rho(\mathbf{r}_2) [1 + h(\mathbf{r}_1, \mathbf{r}_2)] \quad (2.19)$$

where expression $h(\mathbf{r}_1, \mathbf{r}_2)$ is a pair-correlation function, addition of which to Coulombic term incorporates all quantum-mechanical interactions to give pair density. With $h = 0$ completely uncorrelated picture of electrons is given, in which case pair density is just simple product of densities at two points. A little rearrangement of Eq. 2.19 allows to have more closer look at role of pair-correlation function :

$$\frac{1}{2} \rho(\mathbf{r}_2) h(\mathbf{r}_1, \mathbf{r}_2) = \frac{\rho(\mathbf{r}_1, \mathbf{r}_2)}{\rho(\mathbf{r}_1)} - \frac{1}{2} \rho(\mathbf{r}_2) \quad (2.20)$$

The first term on right hand side is *conditional* probability of finding an electron at a point r_2 , if another is already present at point r_1 . The quantity $\rho(r_2)h(r_1, r_2)$ is termed as *exchange-correlation hole*, and it can be seen from Eq. 2.20 that it is conditional density at point r_2 minus the density at the same point i.e. a hole dug into surrounding of an electron at position r_1 . This carries negative sign and is denoted here by ρ_{xc} . Since electron density can be written in terms of pair density (comparison of Eq. 2.11 and 2.13) as,

$$\rho(r_1) = \frac{2}{N-1} \int \rho_2(r_1, r_2) dr_2 \quad (2.21)$$

inserting Eq. 2.19 in Eq. 2.20 results into :

$$\int \rho(r_2)h(r_1, r_2) dr_2 = \int \rho_{xc} dr_2 = -1 \quad (2.22)$$

Exchange-correlation hole is result of summing both *exchange* effects , and *correlation* effects and hence it can also be decomposed into *Fermi hole*, arising from exchange effects due to interaction between same spin particles, and *correlation hole* arising from repulsion between same charge of the particles. In the motion of an electron, exchange-correlation hole can be imagined to occupy a region surrounding the electron from which other electrons are excluded. It is commented in passing that particular form of exchange-correlation hole in Eq. 2.20 incorporates the normalisation of γ_2 to $\frac{N(N-1)}{2}$ *distinct* number of electron pairs, as opposed to $N(N-1)$ number of *non-distinct* pairs.

2.2 DFT: From Electron Density to Wave Function

While electron density was described as arising from interpretation of wave function in previous section, the reverse process of obtaining the observable properties associated with (unknown) ground state wave function from known ground state electron density is domain of density functional theory (DFT). Present section describes DFT formalism, first as existence-of-proof (Hohenberg-Kohn theorems), and then as implementation to calculate ground state energy of N electron system (Kohn-Sham method).

2.2.1 Hohenberg-Kohn Theorems

The fundamental tenet of DFT is derived from proofs provided by Hohenberg and Kohn (HK) that ground state electron density of a system completely determines all the ground state properties.⁹⁴ In this regard it is illuminating to reconsider the Hamiltonian (Eq. 2.14), the ground state expectation value of which is given as:

$$\langle \Psi_0 | \hat{\mathcal{H}} | \Psi_0 \rangle = \langle \Psi_0 | - \sum_{i=1}^N \frac{1}{2} \nabla^2 | \Psi_0 \rangle + \langle \Psi_0 | \sum_{i=1}^N v(r_i) | \Psi_0 \rangle + \langle \Psi_0 | \sum_{i<j}^N \frac{1}{r_{ij}} | \Psi_0 \rangle \quad (2.23)$$

The second term describes nuclear–electronic interaction and can be recasted as $\int \rho(\mathbf{r})v(\mathbf{r})d\mathbf{r}$. It can be seen that for an N electron system, Hamiltonian is completely determined if external potential $v(\mathbf{r})$ is fixed. In other words, N (total number of electrons) and $v(\mathbf{r})$ determine all the properties of ground state. Furthermore $\rho(\mathbf{r})$ integrates over the all space to N , and if it is proved that $v(\mathbf{r})$ is also determined by $\rho(\mathbf{r})$ in some manner, then all ground state properties can be determined solely by $\rho(\mathbf{r})$. This proof, along with another for variational principle of DFT were provided by HK.

First HK theorem

With the consideration of non-degenerate ground state, this theorem states that external potential “ $v(\mathbf{r})$ is a unique functional of $\rho(\mathbf{r})$, apart from a trivial additive constant”.⁹⁴ This statement provides a basis for one-to-one mapping between external potential(s) and electron density distribution(s). Its proof was given by *reductio ad absurdum*, by first assuming that there exist two external potentials v and v' differing by more than an additive constant (and hence two Hamiltonians $\hat{\mathcal{H}}$ and $\hat{\mathcal{H}}'$), each giving the same ρ for the ground state of an N electron system, even if corresponding wave functions Ψ and Ψ' are different. By applying variational principle ($E_0 \leq \langle \Psi | \hat{\mathcal{H}} | \Psi \rangle$, where E_0 is the true ground state energy and Ψ a trial wave function) to both Ψ and Ψ' of this statement leads to a contradiction which becomes obvious by considering the following.

$$\begin{aligned} E_0 &< \langle \Psi' | \hat{\mathcal{H}} | \Psi' \rangle = \langle \Psi' | \hat{\mathcal{H}}' | \Psi' \rangle + \langle \Psi' | \hat{\mathcal{H}} - \hat{\mathcal{H}}' | \Psi' \rangle \\ &= E'_0 + \int \rho(\mathbf{r})[v(\mathbf{r}) - v'(\mathbf{r})]d\mathbf{r} \end{aligned} \quad (2.24)$$

$$\begin{aligned} E'_0 &< \langle \Psi' | \hat{\mathcal{H}}' | \Psi' \rangle = \langle \Psi' | \hat{\mathcal{H}} | \Psi' \rangle + \langle \Psi' | \hat{\mathcal{H}}' - \hat{\mathcal{H}} | \Psi' \rangle \\ &= E_0 - \int \rho(\mathbf{r})[v(\mathbf{r}) - v'(\mathbf{r})]d\mathbf{r} \end{aligned} \quad (2.25)$$

Adding these two equations gives rises to the contradiction: $E'_0 + E_0 < E_0 + E'_0$, resulting in disproval of initial assumption while uniqueness of $v(\mathbf{r})$ for each $\rho(\mathbf{r})$ is proven.

Second HK theorem

Since first theorem proves that electron density $\rho(\mathbf{r})$ uniquely determines the external potential $v(\mathbf{r})$, and N the number of electrons, hence ground state energy E_v and all other properties are also determined. This allows us to write the ground state energy of N electrons in presence of external potential $v(\mathbf{r})$ as:

$$E_v[\rho] = T[\rho] + V_{ee}[\rho] + V_{ne}[\rho] = F_{hk}[\rho] + \int \rho(\mathbf{r})v(\mathbf{r})d\mathbf{r} \quad (2.26)$$

According to second theorem, $E_v[\rho]$ assumes its minimum value for the correct $\rho(\mathbf{r})$, if the admissible functions are restricted by the condition $N \equiv \int \rho(\mathbf{r}) d\mathbf{r}$.⁹⁴ If $\tilde{\rho}(\mathbf{r})$ is a trial density, $E_v[\tilde{\rho}]$ is the energy arising from it and E_0 true ground state energy, this theorem can be restated as:

$$E_0 \leq E_v[\tilde{\rho}] \quad (2.27)$$

This is the DFT counterpart of variational principle for trial wave functions and is proven as follows. The Hamiltonian is fixed because of the fact that both external potential and total number of electrons are determined by trial density $\tilde{\rho}$. This implies that wave function $\tilde{\Psi}$ is also determined and hence expectation value of Hamiltonian can be written in conjunction with Eq. 2.26 as :

$$\langle \tilde{\Psi} | \hat{\mathcal{H}} | \tilde{\Psi} \rangle = [F_{hk}[\rho] + \int \tilde{\rho}(\mathbf{r}) v(\mathbf{r}) d\mathbf{r}] \geq E_v[\rho] \quad (2.28)$$

For any density to obey the second HK theorem, the energy functional $E_v[\rho]$ associated with it must be stationary under the constraint $\int \rho(\mathbf{r}) d\mathbf{r} = N$ according to following Euler-Lagrange equation:

$$\frac{\delta E_v[\rho]}{\delta \rho(\mathbf{r})} = v(\mathbf{r}) + \frac{F_{hk}[\rho]}{\delta \rho(\mathbf{r})} \quad (2.29)$$

Since functional $F_{hk}[\rho]$ is independent of external potential $v(\mathbf{r})$, it is said to be universal functional of electron density and HK theorems allow exact calculation of ground state properties if this functional is known.

Extension to HK theorems

The first HK theorem is originally limited only to the case of non-degenerate ground state and besides, there are other problems which needed to be considered. One of these is that HK theorems applies only to what is called *v-representable* electron densities, i.e. ground state energy can be obtained from a trial density only if later maps onto an external potential $v(\mathbf{r})$ corresponding to an N electron Hamiltonian. The conditions for a trial density to be *v-representable* remain unknown. Another problem is that ground state density $\rho_0(\mathbf{r})$ must correspond to an antisymmetric ground state wave function, but there exist infinite number of antisymmetric wave functions which can be normalised to give same density, and issue is how to distinguish a density corresponding to ground state wave function. These limitations are removed if Hilbert space of N particle system is *constrained* to allow only those wave functions which are variationally minimised, and by quadrature,

give density ρ_0 . Consider the true ground state energy which is stated as

$$E_0 = \langle \Psi_0 | \hat{\mathcal{H}} | \Psi_0 \rangle \leq \langle \Psi_{\rho_0} | \hat{\mathcal{H}} | \Psi_{\rho_0} \rangle \quad (2.30)$$

If both Ψ_0 and Ψ_{ρ_0} give the same density $\rho_0(\mathbf{r})$ then Eq. 2.30 can be rewritten in view of Eq. 2.26,

$$\begin{aligned} \langle \Psi_0 | \hat{T} + \hat{V}_{ee} | \Psi_0 \rangle + \int \rho_0(\mathbf{r}) v(\mathbf{r}) d\mathbf{r} &\leq \langle \Psi_{\rho_0} | \hat{T} + \hat{V}_{ee} | \Psi_{\rho_0} \rangle + \int \rho_0(\mathbf{r}) v(\mathbf{r}) d\mathbf{r}, \\ \langle \Psi_0 | \hat{T} + \hat{V}_{ee} | \Psi_0 \rangle + \int \rho_0(\mathbf{r}) v(\mathbf{r}) d\mathbf{r} &\leq F_{hk}[\rho_0] + \int \rho_0(\mathbf{r}) v(\mathbf{r}) d\mathbf{r} \\ \implies F_{hk}[\rho_0] &= \langle \Psi_0 | \hat{T} + \hat{V}_{ee} | \Psi_0 \rangle \end{aligned} \quad (2.31)$$

Since Ψ_0 is a true ground state wave function, any trial wave function which can be variationally made stationary to yield ground state expectation value of operator $\hat{T} + \hat{V}_{ee}$, can give density ρ_0 of which $F_{hk}[\rho_0]$ will be a universal functional in accordance with HK theorems. This suggests, due to Levy,⁹⁵ a two step conformation to HK theorems,

$$E_0 = \min_{\{\rho\}} \left\{ \min_{\{\Psi \rightarrow \rho\}} \langle \Psi | \hat{\mathcal{H}} | \Psi \rangle \right\} = \min_{\{\rho\}} \left\{ F[\rho] + \int \rho(\mathbf{r}) v(\mathbf{r}) d\mathbf{r} \right\} = \min_{\{\rho\}} E[\rho] \quad (2.32)$$

Densities arising from such wave functions also allow degenerate states to obey HK first theorem. Choosing an N electron antisymmetric wave function converts v -representability problem to N -representability problem. And finally, as already noted, out of densities belonging to different wave functions, only those which conform to Eq. 2.32 obey the HK theorems.

2.2.2 Kohn-Sham Method

In the formulation by Kohn and Sham⁹⁶ to arrive at ground state energy of a system in accordance with Hohenberg-Kohn theorems, a reference system of *non-interacting* electrons with electron density identical to that of *interacting* system is considered. The energy functional $F[\rho]$ of Eq. 2.26 is rearranged to give

$$F[\rho] = T_s[\rho] + J[\rho] + E_{xc}[\rho] \quad (2.33)$$

Where $T_s[\rho]$ is the kinetic energy of non-interacting system, and $E_{xc}[\rho]$ carries the correction term to kinetic energy for interacting system, besides of non-classical correction to Coulomb term $J[\rho]$ according to

$$E_{xc}[\rho] = T[\rho] - T_s[\rho] + V_{ee}[\rho] - J[\rho] \quad (2.34)$$

The variational minimisation of total energy functional $E[\rho] = F[\rho] + \int \rho(\mathbf{r})v(\mathbf{r})d(\mathbf{r})$ subject to constraint $\int \rho(\mathbf{r})d\mathbf{r} = N$ refurnishes the Euler-Lagrange equation (Eq. 2.29) as

$$\frac{\delta E_v[\rho]}{\delta \rho(\mathbf{r})} = v_e(\mathbf{r}) + \frac{T_s[\rho]}{\delta \rho(\mathbf{r})} \quad (2.35)$$

with $v_e(\mathbf{r})$ being the effective potential

$$\begin{aligned} v_e(\mathbf{r}) &= v(\mathbf{r}) + \frac{\delta J[\rho]}{\delta \rho(\mathbf{r})} + \frac{\delta E_{xc}[\rho]}{\delta \rho(\mathbf{r})} \\ &= v(\mathbf{r}) + \frac{\int \rho(\mathbf{r}')}{|\mathbf{r} - \mathbf{r}'|} d\mathbf{r}' + v_{xc}(\mathbf{r}) \end{aligned} \quad (2.36)$$

The terms in Eq. 2.36 are external, Coulomb (also called Hartree potential), and exchange-correlation potentials respectively.

The issue of determining exact $T_s[\rho]$ and corresponding density is described as follows. The exact kinetic energy for a system of interacting electrons is expectation value

$$T = \sum_i^N n_i \langle \psi_i | -\frac{1}{2} \nabla^2 | \psi_i \rangle \quad (2.37)$$

with natural orbitals ψ_i , occupation numbers $0 \leq n_i \leq 1$, and total electron density

$$\rho(\mathbf{r}) = \sum_i^N n_i \sum_s |\psi_i(\mathbf{r}, s)|^2 \quad (2.38)$$

There are infinite number of terms in last two equations, and Kohn-Sham replaced these two equations for reference non-interacting system with following two equations,

$$T_s[\rho] = \sum_i^N \langle \psi_i | -\frac{1}{2} \nabla^2 | \psi_i \rangle \quad (2.39)$$

$$\rho(\mathbf{r}) = \sum_i^N \sum_s |\psi_i(\mathbf{r}, s)|^2 \quad (2.40)$$

by restricting the summation only to occupied N orbitals with occupation number $n_i = 1$. It can be easily seen that kinetic energy and density given in Eq. 2.38 and 2.39 describe a system of non-interacting electrons whose total energy is expectation value of following Hamiltonian with external potential v_s (acting in the absence of inter-electronic repulsive terms).

$$\hat{\mathcal{H}}_s = \sum_i^N \left(-\frac{1}{2} \nabla_i^2 \right) + \sum_i^N v_s(\mathbf{r}) \quad (2.41)$$

The exact ground state of this system of non-interacting electrons is given by a Slater determinant of N (lowest energy) one-electron eigen states arising from one-electron eigen problem

$$\hat{h}_s \psi_i = [-\frac{1}{2}\nabla^2 + v_s(\mathbf{r})]\psi_i = \varepsilon_i \psi_i \quad (2.42)$$

In order to arrive at *true* ground state energy from the density (Eq. 2.40) of non-interacting electrons, total energy functional is written as

$$\begin{aligned} E[\rho] &= T_s[\rho] + J[\rho] + E_{xc}[\rho] + \int \rho(\mathbf{r})v(\mathbf{r})d\mathbf{r} \\ &= \sum_i^N \langle \psi_i | -\frac{1}{2}\nabla^2 | \psi_i \rangle + J[\rho] + E_{xc}[\rho] + \int \rho(\mathbf{r})v(\mathbf{r})d\mathbf{r} \end{aligned} \quad (2.43)$$

and variational minimisation of this functional, under the orthonormality constraint: $\langle \psi_i | \psi_j \rangle - \delta_{ij} = 0$, requires that functional Λ (of set of orbitals $\{\psi_i\}$) becomes stationary according to

$$\delta\Lambda[\{\psi_i\}] = \delta E[\rho] - \sum_i^N \sum_j^N \varepsilon_{ij} \delta\{\langle \psi_i | \psi_j \rangle - \delta_{ij}\} = 0 \quad (2.44)$$

with set $\{\varepsilon_{ij}\}$ of Lagrange multipliers. The orthonormality constraint is necessary if kinetic energy expression (Eq. 2.39) is to hold true, and density described by Eq. 2.40 is to normalise correctly according to Eq. 2.12. Finding the $\{\psi_i\}$ by making Λ stationary according to Eq. 2.44, gives N equations of the form

$$\hat{h}_e \psi_i = [-\frac{1}{2}\nabla^2 + v_e]\psi_i = \sum_j^N \varepsilon_{ij} \psi_j \quad (2.45)$$

along with the density determined by set $\{\psi_i\}$. In these equations v_e is effective potential which was earlier given in Eq. 2.36, and matrix comprised of elements ε_{ij} can be diagonalised by unitary transformation to give canonical *Kohn-Sham* equations:

$$\hat{h}_e \psi_i = [-\frac{1}{2}\nabla^2 + v_e]\psi_i = \varepsilon_i \psi_i \quad (2.46)$$

In a manner analogous to canonical Hartree-Fock equations, ε_i values can be interpreted as expectation values of Hamiltonian \hat{h}_e , i.e. energies of orbitals ψ_i , although interpreting Kohn-Sham orbitals in the same manner as Hartree-Fock orbitals has questionable justification. This is because of auxiliary nature of Kohn-Sham orbitals, which are basically deployed only to compute the true ground state electron density and corresponding electronic kinetic energy. Determination of this density and subsequent calculation of ground state energy by using Eq. 2.43, is subject to knowledge of *exchange-correlation* functional $E_{xc}[\rho]$.

The explicit form of $E_{xc}[\rho]$ is a matter of constant improvement, as its exact nature remains unknown. Historically, the most fundamental approximation to this energy term comes from assumption of a uniform electron gas, which is reasonable for the crystalline metallic systems. According to this approach, termed as *local density approximation* (LDA), $E_{xc}[\rho]$ is given as

$$E_{xc}^{LDA}[\rho] = \int \rho(\mathbf{r}) \varepsilon_{xc}(\rho) d\mathbf{r} \quad (2.47)$$

where $\varepsilon_{xc}(\rho)$ is exchange and correlation energy per particle of a uniform (or very slowly varying) electron gas of density ρ . As was mentioned previously that exchange correlation hole can be split into exchange and correlation holes, so can be done with ε_{xc} according to

$$\varepsilon_{xc} = \varepsilon_x + \varepsilon_c \quad (2.48)$$

The ε_x and E_x^{LDA} are given by Dirac formula

$$\varepsilon_x(\rho) = C_x \rho^{\frac{1}{3}}, \quad E_x^{LDA}[\rho] = C_x \int \rho^{\frac{4}{3}}(\mathbf{r}) d\mathbf{r}, \quad C_x = \frac{3}{4} \left(\frac{3}{\pi} \right)^{\frac{1}{3}} \quad (2.49)$$

The values for correlation energy for a uniform electron gas has been accurately determined by quantum Monte Carlo simulations by Ceperley and Alder, and an analytical form has been derived from this data by Vosko, Wilk, and Nusair. An improvement over LDA approach should consider corrections arising from *non-uniform* nature of electron density as is practically found in molecular systems of interest in chemistry. In other words, exchange and correlation energies should be described not only as density dependent functionals, but first derivative of density should also be included as independent variable. The methods derived from this improved approximation are categorised as *generalised gradient approximation* and further inclusion of higher order gradient of density as independent variable leads to meta-GGA functionals.

2.3 Time Dependent Density Functional Theory

Density functional theory in its original Hohenberg-Kohn context is essentially a ground state theory and not applicable to situations where matter is interacting with time-dependent fields. The exact reformulation of time-dependent quantum mechanics in terms of density (as opposed to many-body wave function) gives rise to time dependent density functional theory (TD-DFT), and three major areas of its applications have been described by Burke *et al.*⁹⁷ Of particular interest to chemical problems is linear response to spatially uniform electric field, or the optical response of molecules in the dipole approximation, which allows calculations of electronic excitations both in terms of their energy and oscillator strength.

Central to time dependent version of DFT is Runge-Gross theorem,⁹⁸ which gives the formal proof of one-to-one correspondence between time-dependent external potentials and time-dependent densities. Armed with this theorem, time-dependent Kohn-Sham (TD-KS) equations can be easily constructed. And finally, relevant to optical excitations frequently encountered in chemistry, (linear response) perturbative solution of TD-KS equations yields excitation frequencies and oscillator strengths.

2.3.1 Runge-Gross Theorem

A simple statement of time-dependent analogue of first HK theorem, or Runge-Gross (RG) theorem proclaims that⁹⁹ “*Two densities $\rho(\mathbf{r}, t)$ and $\rho'(\mathbf{r}, t)$ evolving from a common initial state $\Psi_0 = \Psi(t_0)$ under the influence of two potentials $v(\mathbf{r}, t)$ and $v'(\mathbf{r}, t)$ are always different provided that the potentials differ by more than a purely time-dependent function (Eq. 2.50)*”. The condition of applicability of this statement is given by,

$$\begin{aligned} v(\mathbf{r}, t) &\neq v'(\mathbf{r}, t) + c(t) \\ \Delta v_k(\mathbf{r})|_{t=t_0} &= \frac{\partial^k}{\partial t^k} \{v(\mathbf{r}, t) - v'(\mathbf{r}, t)\} \Big|_{t=t_0} \neq \text{constant} \end{aligned} \quad (2.50)$$

The two lines in Eq. 2.50 are equivalent. The first line states that two potentials differ by more than a purely time dependent function, and the second line establishes that Taylor expansion about $t = 0$ of difference between two potentials is spatially not uniform for some order $k \geq 0$.

The proof of this theorem is much more involved¹⁰⁰ than first HK theorem and is accomplished in two steps. In the first step, notated here as RG1, equation of motion for current density are shown to dictate that potentials v and v' which are compliant with condition (Eq. 2.50) generate different respective current densities \mathbf{j} and \mathbf{j}' . In the second step or RG2, continuity equation is used to demonstrate that two systems with different current densities also have different densities i.e. $\mathbf{j} \neq \mathbf{j}' \Rightarrow \rho \neq \rho'$.

The RG1 step is performed as follows. Consider the Hamiltonian in Eq. 2.14 in following time-dependent form:

$$\hat{\mathcal{H}} = \hat{T} + \mathcal{V}_{ee} + \sum_{i=1}^N v(\mathbf{r}_i, t) \quad (2.51)$$

and a ground state $|\Psi_0(t_0)\rangle$ which remains in the same stationary state until some time dependent external potential is switched on at $t > t_0$. After this time state evolves as $|\Psi(t)\rangle$ if external potential is $v(\mathbf{r}, t)$ or as $|\Psi(t)\rangle'$ if external potential is $v'(\mathbf{r}, t)$, whereas two potentials differ by more than time-dependent function according to Eq. 2.50. The quantum mechanical equations of motion for current densities corresponding to wave functions of two

states are

$$\begin{aligned}\frac{\partial}{\partial t}\mathbf{j}(\mathbf{r}, t) &= -i\langle\Psi(t)|[\hat{\mathbf{j}}(\mathbf{r}), \hat{\mathcal{H}}(t)]|\Psi(t)\rangle \\ \frac{\partial}{\partial t}\mathbf{j}'(\mathbf{r}, t) &= -i\langle\Psi'(t)|[\hat{\mathbf{j}}(\mathbf{r}), \hat{\mathcal{H}}'(t)]|\Psi'(t)\rangle\end{aligned}\quad (2.52)$$

where $\hat{\mathbf{j}}(\mathbf{r})$ is current-density operator. Since two wave functions evolve from same initial state $|\Psi_0(t_0)\rangle$ (and corresponding initial density $\rho_0(\mathbf{r}, t_0)$), the equation of motion for difference of above two current densities given by

$$\left.\frac{\partial\Delta\mathbf{j}(\mathbf{r}, t)}{\partial t}\right|_{t=t_0} = -\rho_0(\mathbf{r}, t_0)\nabla\{v(\mathbf{r}, t_0) - v'(\mathbf{r}, t_0)\} \quad (2.53)$$

tells that evolution of $\Delta\mathbf{j}$ is non zero if Eq. 2.50 holds for $k = 0$, or if it also holds when k is infinitesimally greater than zero in which case comparison of Eq. 2.50 and 2.53 gives

$$\left.\frac{\partial^{k+1}\Delta\mathbf{j}(\mathbf{r}, t)}{\partial t^{k+1}}\right|_{t=t_0} = -\rho_0(\mathbf{r}, t_0)\nabla\{\Delta v_k(\mathbf{r})|_{t=t_0}\} \neq 0 \quad (2.54)$$

In other words for time-dependent external potentials which differ according to Eq. 2.50, current densities corresponding to them diverge at times after t_0 .

In RG2 step continuity equation is used, which for the difference between densities is given by

$$\frac{\partial\Delta\rho(\mathbf{r}, t)}{\partial t} = \frac{\partial}{\partial t}\{\rho(\mathbf{r}, t) - \rho'(\mathbf{r}, t)\} = -\nabla \cdot \Delta\mathbf{j}(\mathbf{r}, t) \quad (2.55)$$

which in view of Eq. 2.54 becomes

$$\left.\frac{\partial^{k+2}\Delta\rho(\mathbf{r}, t)}{\partial t^{k+2}}\right|_{t=t_0} = \nabla \cdot \rho_0(\mathbf{r}, t_0)\nabla\{\Delta v_k(\mathbf{r})|_{t=t_0}\} \quad (2.56)$$

Content enclosed in the curly brackets ($u(\mathbf{r}) = \Delta v_k(\mathbf{r})|_{t=t_0}$) on the right hand side of above equation are non-constant under the condition of Eq. 2.50, and in order for densities $\rho(\mathbf{r}, t)$ and $\rho'(\mathbf{r}, t)$ to differ at times greater than t_0 , the right hand side of Eq. 2.56 should be shown to obey

$$\nabla \cdot \{\rho_0(\mathbf{r})\nabla u(\mathbf{r})\} \neq 0 \quad \text{if} \quad u(\mathbf{r}) \neq \text{constant} \quad (2.57)$$

This is done by *reductio ad absurdum*. First it is assumed that $\nabla \cdot \{\rho_0(\mathbf{r})\nabla u(\mathbf{r})\} = 0$ and then divergence theorem is used to write the surface integral

$$\oint \rho_0(\mathbf{r})u(\mathbf{r})\nabla u(\mathbf{r}) \cdot d\mathbf{S} = \int \rho_0(\mathbf{r})|\nabla u(\mathbf{r})|^2 d\mathbf{r} + \int u(\mathbf{r})\nabla \cdot \{\rho_0(\mathbf{r})\nabla u(\mathbf{r})\} d\mathbf{r} \quad (2.58)$$

which should vanish for all physically realistic potentials due to the fact that for such potentials $u(r)$ falls off at least as inverse distance, and density decays exponentially. If our assumption of $\nabla \cdot \{\rho_0(r)\nabla u(r)\} = 0$ is correct than integrand in first term of right hand side of Eq. 2.58 should be simultaneously zero, which is in contradiction with $u(r) \neq \text{constant}$. Hence it is proven that right hand side of Eq. 2.56 is non zero and two densities evolved from same initial density $\rho_0(r)$ under the influence of two potentials obeying Eq. 2.50 must be finitely different at a time infinitesimally later than t_0 .

2.3.2 Kohn-Sham Linear Response Theory

On the basis of RG theorem, the time-dependent Kohn-Sham scheme can be easily built,^{100–102} under which Kohn-Sham orbitals obey the following time-dependent Schrödinger equation, and give rise to an *interacting* time-dependent density $\rho(r, t)$, to represent *non-interacting* Kohn-Sham electrons.

$$i\frac{\partial\psi_i(r, t)}{\partial t} = \hat{\mathcal{H}}_{KS}(r, t)\psi_i(r, t), \quad \hat{\mathcal{H}}_{KS} = -\frac{1}{2}\nabla^2 + v_e[\rho](r, t) \quad \text{and} \\ \rho(r, t) = \sum_i^N |\psi_i(r, t)|^2 \quad (2.59)$$

The effective potential $v_e(r, t)$ has similar components like in static case $v_e(r)$,

$$v_e[\rho](r, t) = v_{\text{ex}}[\rho](r, t) + v_H[\rho](r, t) + v_{xc}[\rho](r, t) \quad (2.60)$$

where v_{ex} is external potential, v_H Hartree potential, and v_{xc} is exchange-correlation potential. The v_{xc} commonly used in practical TD-DFT calculations is the LDA potential combined with adiabatic approximation (i.e. the static LDA potential determined from time dependent density while ignoring the time dependence of potential), $v_{xc}^{\text{ALDA}}(r, t)$ given as

$$v_{xc}^{\text{ALDA}}[\rho](r, t) = v_{\text{LDA}}^0[\rho](r)|_{\rho=\rho(r, t)} \quad (2.61)$$

whereas $v_{\text{LDA}}^0(r)$ is static LDA potential like the one employed for description of ground state. In other words density at every time t determines the exchange-correlation potential at that time by using local density approximation. It should be noted that $v_{xc}^{\text{ALDA}}(r, t)$ carries all the shortcomings of static LDA potential, and adiabatic approximation is expected to work better for system which deviates slightly from ground state. In principle, GGA potentials may be expected to improve the description of time-dependent systems, but more severe problem with all such approximate XC potentials including those with GGA correction, is their inability to reproduce the $(-\frac{1}{r})$ dependence of exact XC potential.

Consider a system of interacting electrons which remains in ground state with density

$\rho_0(\mathbf{r})$ under the influence of external potential $v_{ex}^{(0)}(\mathbf{r})$ at time $t \leq t_0$, and assumes a density $\rho(\mathbf{r}, t) = \rho_0(\mathbf{r}) + \delta\rho(\mathbf{r}, t)$ when a time-dependent potential $v_{ex}(\mathbf{r}, t) = v_{ex}^{(0)}(\mathbf{r}) + v^{(1)}(\mathbf{r}, t)$ is switched on for the times $t > t_0$. The density response of the system to perturbation $v^{(1)}(\mathbf{r}, t)$ is

$$\delta\rho(\mathbf{r}, t) = \rho^{(1)}(\mathbf{r}, t) + \rho^{(2)}(\mathbf{r}, t) + \rho^{(3)}(\mathbf{r}, t) + \dots \quad (2.62)$$

and since we are concerned here only to linear response, following description is restricted to first order density change $\rho^{(1)}(\mathbf{r}, t)$, which is written exactly as integrated first order term in Taylor expansion of density around $v_{ex}^{(0)}$

$$\begin{aligned} \rho^{(1)}(\mathbf{r}, t) &= \int dt' \int d\mathbf{r}' \chi(\mathbf{r}, \mathbf{r}', t, t') v^{(1)}(\mathbf{r}', t') \\ \chi(\mathbf{r}, \mathbf{r}', t, t') &= \left. \frac{\delta\rho(\mathbf{r}, t)}{\delta v_{ex}(\mathbf{r}', t')} \right|_{v_{ex}^{(0)}} \end{aligned} \quad (2.63)$$

where $\chi(\mathbf{r}, \mathbf{r}', t, t')$ is called density-density response function of the interacting system. Calculation of this function requires the knowledge of complete set of wave functions corresponding to ground state and excited states. Instead a non-interacting system is considered for which Eqs. 2.63 are rewritten:

$$\begin{aligned} \rho_s^{(1)}(\mathbf{r}, t) &= \int dt' \int d\mathbf{r}' \chi_s(\mathbf{r}, \mathbf{r}', t, t') v_e^{(1)}(\mathbf{r}', t') \\ \chi_s(\mathbf{r}, \mathbf{r}', t, t') &= \left. \frac{\delta\rho(\mathbf{r}, t)}{\delta v_e(\mathbf{r}', t')} \right|_{v_e[\rho_0]} \end{aligned} \quad (2.64)$$

with $v_e^{(1)}$ the first-order linear response of Kohn-Sham potential, caused by density response to perturbation $v^{(1)}$ after time t_0 . This is given as $v^{(1)}(\mathbf{r}, t)$ plus the linear responses of Hartree and XC potentials (first-order terms in Taylor expansion of v_H and v_{xc} , respectively around ρ_0).

$$\begin{aligned} v_e^{(1)}(\mathbf{r}, t) &= v^{(1)}(\mathbf{r}, t) + v_H^{(1)}(\mathbf{r}, t) + v_{xc}^{(1)}(\mathbf{r}, t) \\ &= v^{(1r)}(\mathbf{r}) \times v^{(1t)}(t) + \int d\mathbf{r}' \frac{\rho^{(1)}(\mathbf{r}', t')}{|\mathbf{r} - \mathbf{r}'|} + \int dt' \int d\mathbf{r}' f_{xc}(\mathbf{r}, \mathbf{r}', t, t') \rho^{(1)}(\mathbf{r}', t') \end{aligned} \quad (2.65)$$

In the second line of above equation, $v^{(1)}(\mathbf{r}, t)$ is rewritten as a product of functions after space and time separation of variables, and quantity f_{xc} , known as XC kernel, is given by $\left. \frac{\delta v_{xc}(\mathbf{r}, t)}{\delta \rho(\mathbf{r}', t')} \right|_{\rho_0}$. For periodic potentials it is useful to perform Fourier transform from time to frequency domain according to $f(\omega) = \int e^{i\omega t} f(t)$. By introducing above expression for first-order KS potential into expression for first-order density of non-interacting system

(Eq. 2.64), and performing requisite Fourier transform yields following:

$$\rho^{(1)}(\mathbf{r}, \omega) = \int d\mathbf{r}' \chi_s(\mathbf{r}, \mathbf{r}', \omega) \left[v^{(1r)}(\mathbf{r}') v^{(1t)}(\omega) + \int d\mathbf{r}'' \frac{\rho^{(1)}(\mathbf{r}'', \omega)}{|\mathbf{r}' - \mathbf{r}''|} + \int d\mathbf{r}'' f_{xc}(\mathbf{r}', \mathbf{r}'', \omega) \rho^{(1)}(\mathbf{r}'', \omega) \right] \quad (2.66)$$

The frequency-dependent density-density response function $\chi_s(\mathbf{r}, \mathbf{r}', \omega)$

$$\chi_s(\mathbf{r}, \mathbf{r}', \omega) = \sum_{ph} \left(\frac{\psi_p(\mathbf{r}) \psi_h^*(\mathbf{r}) \psi_p^*(\mathbf{r}') \psi_h(\mathbf{r}')}{\omega - (\varepsilon_h - \varepsilon_p)} - \frac{\psi_p^*(\mathbf{r}) \psi_h(\mathbf{r}) \psi_p(\mathbf{r}') \psi_h^*(\mathbf{r}')}{\omega + (\varepsilon_h - \varepsilon_p)} \right) \quad (2.67)$$

of the Kohn-Sham non-interacting ground state contains KS orbitals ψ_i (from converged ground state determinant) and their energies ε_i , with indices $i = \{p, h\}$ referring to “particle” (occupied) and “hole” (virtual) orbitals respectively. For solution of Eq. 2.64, the first-order density $\rho_s^{(1)}$ and first-order KS potential $v_e^{(1)}$ are to be determined self-consistently, and for this purpose following parametrised expression for first-order density is introduced after inserting χ_s from Eq. 2.67 into (Fourier transformed) Eq. 2.64.

$$\rho^{(1)}(\mathbf{r}, \omega) = \sum_{ph\sigma} [P_{ph}^\sigma(\omega) \psi_{p\sigma}(\mathbf{r}) \psi_{h\sigma}^*(\mathbf{r}) + P_{hp}^\sigma(\omega) \psi_{p\sigma}^*(\mathbf{r}) \psi_{h\sigma}(\mathbf{r})] \quad (2.68)$$

It should be noted that decomposition of first-order density is done into spin $\sigma = \{\alpha, \beta\}$ components. Furthermore, in analogy to zeroth-order density (the ground state density) which was introduced as summation over products of occupied KS orbitals (Eq. 2.59), the first order density in above equation is introduced as summation over products of occupied and virtual KS orbitals. Finally the expansion coefficients P_{ph} carry the meaning of linear response of density matrix. Determination of so called P-matrix described by elements P_{ph}^σ and P_{hp}^σ ,

$$P_{ph}^\sigma(\omega) = \frac{\int \psi_{p\sigma}^*(\mathbf{r}') v_e^{(1)}(\mathbf{r}', \omega) \psi_{h\sigma}(\mathbf{r}')}{(\varepsilon_h - \varepsilon_p) + \omega}, \quad P_{hp}^\sigma(\omega) = \frac{\int \psi_{p\sigma}(\mathbf{r}') v_e^{(1)}(\mathbf{r}', \omega) \psi_{h\sigma}^*(\mathbf{r}')}{(\varepsilon_h - \varepsilon_p) - \omega} \quad (2.69)$$

and substitution of these matrix elements into Eq. 2.68 allows determination of excitations and their oscillator strengths, the detail of which will not be further touched in present outline. However it is interesting to see in a simplified manner that how the linear response of non-interacting KS electrons, uniquely determines energies of electronic excitation. This can be done by rearranging Eq. 2.66 and writing it in a form in which a first-order density

is acted upon by an integral operator:

$$\begin{aligned} \int d\mathbf{r}'' \left[\delta(\mathbf{r} - \mathbf{r}'') - \int d\mathbf{r}' \chi_s(\mathbf{r}, \mathbf{r}', \omega) \left(\frac{1}{|\mathbf{r}' - \mathbf{r}''|} + f_{xc}(\mathbf{r}', \mathbf{r}'', \omega) \right) \right] \rho^{(1)}(\mathbf{r}'', \omega) \\ = \int d\mathbf{r}' \chi_s(\mathbf{r}, \mathbf{r}', \omega) v^{(1)}(\mathbf{r}', \omega) \end{aligned} \quad (2.70)$$

shows that first-order density appears only on left hand side. Since terms in response function χ_s contain $\varepsilon_h - \varepsilon_p + \omega$ in its denominator, and true excitation energy is generally not equal to excitation from an occupied to virtual (KS) orbital, at ω corresponding to true excitation energy Ω , χ_s and right hand side of above equation has a finite value in general. On the other hand at ω corresponding to Ω , first-order density and hence the right hand side of Eq. 2.70 becomes infinite. This leads to a contradiction unless it is realised that integral operator at the right hand of this equation has all eigen values equalling zero at frequencies corresponding to true excitation energy, and hence whole (Ω) spectrum can be rigorously determined. Moreover, relationship between $\varepsilon_h - \varepsilon_p$ and true excitation energy is given by

$$\begin{aligned} \Omega = \varepsilon_h - \varepsilon_p + K_{hp,hp} \\ K_{hp,hp} = \int d\mathbf{r} \int d\mathbf{r}' \psi_p^*(\mathbf{r}) \psi_h(\mathbf{r}) \left(\frac{1}{|\mathbf{r} - \mathbf{r}'|} + f_{xc}(\mathbf{r}, \mathbf{r}') \right) \psi_h^*(\mathbf{r}') \psi_p(\mathbf{r}') \end{aligned} \quad (2.71)$$

whereas correction to simple KS orbital excitation is given in second line of equation as diagonal element of coupling-matrix \mathbf{K} , a matrix arising from self-consistent determination of first-order density by expansion (Eq. 2.68).

Chapter 3

TD-DFT Studies on the Electronic Structure of VHPO cofactor

3.1 Introduction

Enzyme architecture specialised for certain chemical process provides an appropriate environment which is energetically difficult to achieve in solution phase. Reactions facilitated in enzymatic environment take advantage of factors which have been attributed to stabilisation of transition state due to preconfigured electrostatics,^{103–105} preorganisation of active-site to form what is termed as near attack configuration (NAC)^{106–109} and dynamic motions¹¹⁰ of protein during turnover. These factors sum up to the effect that activation barrier is lowered or even new reactive channels are brought forth.^{111,112} Later may possibly involve replacing a high energy barrier with several low energy barriers. In the context of studying vanadium containing haloperoxidases (VHPO) in order to elucidate their catalytic power, obtaining the detailed knowledge of their active site is the necessary first step.

Crystal structures of vanadium containing chloroperoxidase (VCPO)²² and bromoperoxidases (VBPO)^{23,24} has been determined showing an orthovanadate in covalent bonding distance to one histidine residue and surrounded by several other amino acid residues forming hydrogen bonds to its anionic oxygens (Chapter 1). The insight gained by these crystal structures along with some kinetic studies^{30,113} has given rise to genuinely legitimate speculations about possible mechanism^{114–116} of these enzymes. Despite this, very little is definitively known about the mechanism. In our attempt to understand the operation of VHPO's, present chapter reports the results of studies on the electronic structure of the active site of these enzymes. The motivation behind the work of present chapter was our belief that before embarking in search of mechanistic channels, some structural questions need to be settled. This is due for two reasons: First, vanadate is known to occur in different protonation states and at physiological *pH* value it is in the form of $[\text{VO}_2(\text{OH})_2]^-$.⁵¹ Different protonation states give rise to different electronic structure around the metal centre (e.g. VO^{3+} or VO_2^+), which in turn may profoundly effect the mechanism in terms of

availability^{53,117} of metal d_π orbitals not involved in V=O double bond(s). While preference of one of these protonation states is easier to make in the bulk solution phase and decided by the pH value, a discreet vanadate entrapped in a small cavity of the enzyme active site leaves this question far from unambiguous. Second, electronic structure and coordination chemistry of most of transition metals including vanadium is formulated in terms of idealised point group geometries (e.g. O_h , T_d or C_{4v}), which is reasonable for stable species in solution. But for intermediates and in enzymes, a coordination observed other than what is in stable solution species, leads to lower or no symmetry and becomes more important in two ways: (1) it rearranges electronic density and hence alters reactivity to meet electrophilic/nucleophilic encounter, (2) initially equivalent bonds, say in tetrahedral field, now split into distinctly weaker and stronger bonds.^{118,119} For example vanadate is transformed to pentacoordination^{22–24} in VHPO active site where the fifth position is occupied by the complexing histidine residue, and also in the enzymes where it acts as transition state analogue to phosphate.⁵¹ Now pentacoordination around the metal centre can form geometries ranging from trigonal bipyramidal (TBP) to square pyramidal (SP) structures depending upon the nature of substitution at the coordination sites and in case of VHPO, as suggested by x-ray crystal structure, a distorted trigonal bipyramid is obtained. While these structural differences might seem inconsequential from the overall energetic point of view, these can be important in context of intramolecular rearrangement of electron density and of one-electron energy levels in the frontier regions. Our laboratory is engaged in synthetically modelling the active site of VHPOs^{120–126} followed by characterisation of products for any catalytic activity which is customary to perform via monitoring the chemical change with physical techniques. Recently we have performed such experiments¹²⁷ with newly synthesised model compounds^{128,129} on the basis of optical absorption spectroscopy for relevant catalytic reactions. Such studies have also been done directly on VCPO³⁰ from *Curvularia inaequalis* giving useful kinetic information. Interestingly, this optical behaviour during the turnover is relevant from another perspective as well, i.e. what structural changes the metal center undergoes during the catalytic cycle. From this point of view, results of these studies, seen in a wider theoretical picture, lend themselves for detailed analysis of the nature of chemical change. We present here a picture for the electronic structure of pentacoordinated vanadium centres, by modelling pentacoordination as shown in Fig. 3.1 and also by modelling the active site of VCPO (Fig. 3.2, cf. 22). Moreover, we look into ligand-to-metal charge transfer (LMCT) electronic transitions using time dependent density functional theory (TD-DFT). In conjunction with the electronic spectrum observed for VCPO³⁰ from *Curvularia inaequalis* we examine the issues of preferred protonation state and geometry of the vanadate in the enzyme.

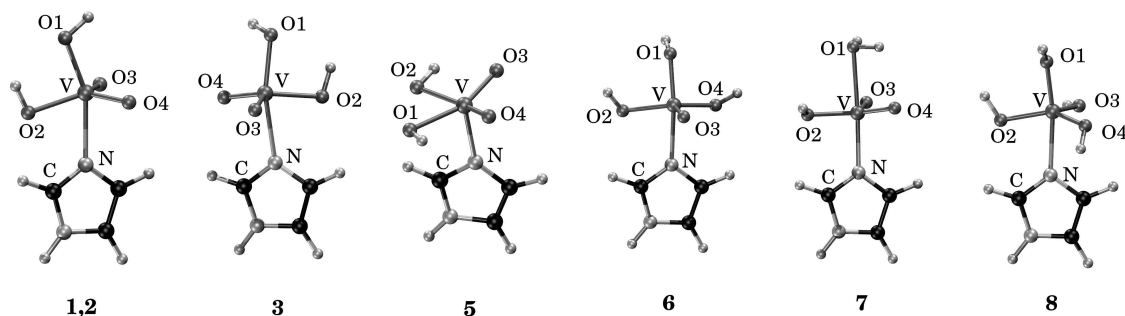


Figure 3.1: Optimised structures of doubly protonated vanadate species $[\text{VO}_2(\text{OH})_2\text{Im}]^-$ (with a coordinated imidazole ligand) and its higher protonation states (see text for details).

3.2 Computational Methods

3.2.1 Choice of geometrical structures

This section describes the details concerning the chosen structures shown in Figs. 3.1, and 3.2. Structures modelling the cofactor of the VCPO enzyme are depicted in Fig. 3.1. In these structures the coordinated histidine residue, the group covalently anchoring the vanadate to the active site pocket, is approximated by an imidazole moiety. The structures **1,2** and **3** are trigonal bipyramidal (TBP) geometries, containing vanadate species $[\text{VO}_2(\text{OH})_2\text{Im}]^-$ protonated at the apical and at one of the equatorial oxygen atoms while the vanadium centre is coordinated by imidazole at the other apex of TBP in different orientations.

In structure **1** the imidazole aligns with the equatorial OH group of the vanadate in a fashion which defines a C_s plane of symmetry. **2** and **3** are the same structures with C_s constraint removed, but they are distinguished among themselves by the fact that in **3** equatorial OH group is *trans* to the protonated nitrogen of the imidazole ring. Structure **4** is an analogous species with the frozen geometry taken from an optimised structure (denoted as **HPO1**) including the first protein shell at the active site of the enzyme (see Fig. 3.2). To explore another possibility of pentacoordination, the doubly protonated structure **5** was selected with imidazole coordinated at the top of a square pyramid (SP). Additional protons in TBP geometry gives the species $[\text{VO}(\text{OH})_3\text{Im}]$ (**6**), $[\text{VO}_2(\text{OH})(\text{H}_2\text{O})\text{Im}]$ (**7**) and $[\text{V}(\text{OH})_4\text{Im}]^+$ (**8**) shown in Fig. 3.1.

The structures **HPO1** and **HPO2** include a model matrix representing the primary protein shell at the active site of the enzyme, that has been taken from the x-ray crystal structure of the enzyme,²² and is comprised of Lys353, Arg360, Ser402, Gly403, His404, Arg490 and His496 as depicted in Fig. 3.2 (for optimisation of these structures see vide infra). **HPO1** and **HPO2** differ in the protonation at the equatorial oxygen atom O2. In **HPO1** this oxygen atom is protonated and donates a hydrogen bond to the oxygen atom

O5 of the neighbouring Ser402 residue as shown by the dotted line in Fig. 3.2. **HPO2** is the same basic structure with O3 remaining unprotonated while receiving a hydrogen bond from the hydroxy group of O5 of Ser402. The apical oxygen atom O1 is protonated in both structures.

3.2.2 Optimisation of geometries

Geometries were optimised, using Becke exchange and Perdew correlation (BP) functionals. Repeated optimisations were performed, starting from Slater type basis sets of double zeta quality (DZ). Final geometries of all structures reported here (except **4** and the protein models **HPO1** and **HPO2**), which have been used in excitation calculations, were obtained with basis sets of triple zeta quality added with two polarisation functions (TZ2P; with 1s frozen for O, N, C and up to 2p frozen for V), and have been found to reproduce the results from those optimised with only one polarisation function (TZP level).

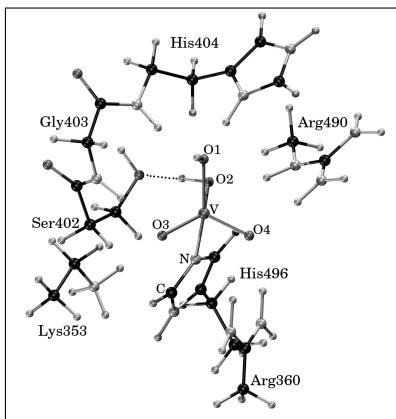


Figure 3.2: Optimised geometry of the model matrix **HPO1** representing the primary protein shell at the active site of the VCPO enzyme including vanadate as the cofactor, the latter represents structure **4**; **HPO2** is represented by the same basic structure, it only differs in the protonation state at oxygen atom O2 (see text for details).

Structures **HPO1** and **HPO2** were obtained with the following procedure: First the coordinates of amino acid residues shown in Fig. 3.2 were obtained from the crystal structure of the enzyme²² and then terminated at appropriate points so as to adequately include the necessary portions of side chains. Then protons were added where needed. Since the orientation of the side chains of the residues that establish the vanadate binding pocket is determined by the outer protein shell, all their heavy atoms were fixed at crystallographic positions. Then the coordinates of all added protons, vanadate and of the imidazole moiety representing His496 starting from C_β were optimised using BP functionals and Slater type orbitals (TZP basis sets; with 1s frozen for C, N, O and up to 3p frozen for V). The ADF

package of programs^{130–132} was used to perform all these calculations. For structures **1** and **2** (with and without C_s symmetry, respectively), optimisations were also performed with the B3LYP functional and Hay-Wachters basis^{133,134} for vanadium augmented with two diffuse functions and 6-311G* basis set for all other atoms (henceforth denoted as basis1). This was done to establish the accuracy of our method as the aforementioned level of theory for vanadium is well tested.^{88,135–137} The Gaussian package G03¹³⁸ was used for these reference calculations.

3.2.3 Calculation of excitations and oscillator strengths

Though density functional theory (DFT) in its original form provides a theoretical basis for calculation of ground state properties,¹³⁹ its time-dependent version^{98,140} (TD-DFT) is now also been successfully used for predictions involving excitations and response properties. Particularly for calculations of excitation energies and oscillator-strengths, the advantage of TD-DFT over its Hartree-Fock counterpart (TDHF) is the achievement of a reliable level of accuracy by inclusion of correlation energy. On the other hand traditional *ab initio* based accurate methods like CASPT2¹⁴¹ are still computationally expensive to cover an affordable but realistic range of electron active spaces. This puts TD-DFT in an ideal situation and its further growth is expected in application fields. In the present work the EXCITATION program^{101,142,143} of the RESPONSE^{144,145} module of the ADF package^{130–132} was used to calculate $d \leftarrow n$ excitation energies and oscillator strengths. This implementation¹⁴² involves in addition to the usual Kohn-Sham potential $\nu_s(\mathbf{r})$ (an exchange-correlation potential ν_{xc} , together with Hartree potential, ν_h and external potential, ν_{ext}), which defines Kohn-Sham orbitals and the electron density, the exchange-correlation kernels f_{xc} and g_{xc} . The later two quantities are necessary for determining time evolution and spatial response of ν_{xc} to perturbation $\delta\nu_{ext}(\mathbf{r}, t)$, and for their calculation adiabatic local density approximation (ALDA)¹⁴² was employed. This approximation makes use only of response of local (as opposed to gradient-corrected) exchange-correlation potential and also neglects the frequency dependence of exchange-correlation kernels. It has been shown that not this approximation but inaccuracies in model exchange-correlation (XC) potential ν_{xc} can prove detrimental to accuracy of results.^{142,146–148} It is because potentials calculated by commonly used functionals are unable to depict correctly the one electron energy levels. To circumvent this, the statistical average of the orbital model exchange-correlation potential (SAOP)^{148,149} was used in addition to calculations which employed the Becke-Perdew (BP) potential. SAOP was specially devised to model correctly both inner and outer electronic regions for use in accurate response properties. Excitation calculations were repeated with two different sets of all electron Slater type functions (STO) as available in ADF database: First, with a basis set of triple-zeta quality augmented by two polarisation functions (TZ2P) and second with a large basis set of even tempered quadruple-zeta functions augmented by three polarisation functions and one diffuse function (ET-QZ3P-1D) for each angular momentum.

It should be noted at this point that although structure **4** represents a part of the optimised protein model **HPO1** with the geometry given in Table 3.2, both structures are different with respect to there electronic structure and, hence, there behaviour as electronic excitations are concerned. Actually, the comparison of **4** and **HPO1** allows for a analysis of the influence of the protein environment on the excitation behaviour of the cofactor of VHPO enzymes. In addition to this the large size of **HPO1** and **HPO2** can not afford

the use of large basis set ET-QZ3P-1D, which also include a set of s, p, d and f diffuse Slater type functions. The one-electron energy levels in the frontier regions can be very sensitive toward diffuse functions, rather diffuse functions are required for correct depiction of frontier region in excited states. We have followed a procedure in which effect of these large basis set is reasonably made clear in case of small structures **1-8** and the same trend is understood to extrapolate to structures **HPO1** and **HPO2**, in which cases direct calculations with ET-QZ3P-1D are very expensive.

3.3 Results and Discussion

3.3.1 Geometries

Tables 3.1, 3.2 and 3.3 summarise the selected bond distances, bond angles and dihedral angles calculated with the methods described in the previous section. The results of reference calculations to compare ADF-BP/TZ2P and B3LYP/basis1 levels of theory for structures **1** and **2** are given in Table 3.1. It can be seen that geometries obtained from these two methods are in good agreement. With C_s constraint bond distances and bond angles totally agree. The dihedral angle V–O3–O4–O2, which is actually an out of plane torsion of the vanadium atom, slightly differs in both cases. Some minor differences between bond lengths can be seen when the C_s constraint is removed i.e V–O bond distances obtained from B3LYP/basis1 tend to be shorter by 2 pm, whereas the V–N bond distance is about 1 pm longer than corresponding values at the ADF-BP/TZ2P level. Another, apparently considerable, deviation of 4.8° is found for the dihedral angle O2–V–N–C. This dihedral angle corresponds to a free rotation of vanadate against the imidazole ring. Taking into account that rather flat energy surfaces are associated with dihedral angles this difference is insignificant.

The obtained geometrical parameters of various doubly protonated vanadate species $[\text{VO}_2(\text{OH})_2\text{Im}]^-$ (**1-5** and **HPO1**), calculated at the ADF-BP/TZ2P level are given in Table 3.2. The reason to include in present work the species **5**, which is a square pyramid (SP) with imidazole at the top, was to make an understanding of contrast between this and other trigonal bipyramidal (TBP) structures. Due to the reason that in enzyme active site tetrahedral vanadate is considered to be transformed into a distorted TBP geometry, which may be considered a halfway to other perfect extreme of SP structure, it was worth looking as to how much the behaviour of vanadate in enzyme varies from a perfect TBP or SP geometry. The later can be quantified by the so called τ parameter (cf. Table 3.2), which for an ideal tetragonal pyramid (SP structure) leads to $\tau = 0$, whereas for an ideal trigonal bipyramid (TBP structure) gives a value of $\tau = 1$. Consistent with the SP geometry for structure **5** a τ value of 0 is observed, whereas for the so called TBP structures **1-4** τ values between 0.4 to 0.65 are found indicating a distortion of the ideal TBP structure. It

Table 3.1: Optimised geometrical parameters for structures **1** and **2** from reference calculations with pure (ADF-BP/TZ2P basis) and hybrid (B3LYP/basis 1) density functionals; all bond lengths are given in pm and angles in degrees; for notation of atoms see Fig. 3.1.

	1 / C_s		2 / C_1	
	ADF-BP/TZ2P	B3LYP/basis1	ADF-BP/TZ2P	B3LYP/basis1
V–O1	192.0	192.0	191.4	189.9
V–O2	196.5	196.5	196.6	194.4
V–O3	165.0	165.0	165.3	163.5
V–O4	165.0	165.0	164.7	162.7
V–N	229.5	229.5	233.8	234.7
O3–V–O4	109.4	109.3	111.7	112.1
O1–V–N	159.2	159.3	162.2	161.6
O2–V–N	75.5	75.6	74.9	74.6
V–O3–O4–O2	13.3	15.1	15.1	14.9
O2–V–N–C	0.0	0.0	1.2	6.0

is important to mention that, all attempts to put the imidazole at an equatorial position of a SP arrangement failed. Similarly no TBP structure could be found in which the imidazole ring can be placed at a *trans* position to one of the oxo groups. A comparison can be made between the structures of SP and other TBP geometries. One striking difference is that the SP structure has the shortest V–N bond, implying that coordination of imidazole is more pronounced in SP compared to all other TBP structures. This is also accompanied by the fact that **5** is the only structure listed in Table 3.2 which has a negative value of the dihedral angle V–O3–O4–O2. In practical terms this means that the out of the plane projection of the vanadium atom is flipped towards the imidazole side. The second observation which can be made is that, this enhanced V–N bonding occurs at the expense of V–OH bonding, which is evident from the elongated V–O bonds of the oxygen atoms of the OH groups in the SP structure. These observations are in line with the earlier understanding that in TBP structures, axial bonds are weaker than equatorial ones and this order is reversed in SP structures. And finally, the *cis*-dioxo VO₂ group seems to retain its basic character, because the V=O bond distances are almost the same for all structures. Moreover, the bond angle of the *cis*-VO₂ group (O3–V–O4) closely resembles the value observed in experimental structures.^{124–126}

Some interesting variations can also be observed within the group of TBP structures listed in Table 3.2. First, that imposition of C_s constraint (as in structure **1**) causes the V–N bond to shorten by 5 – 6 pm. Second, with a value of 219.5 pm the shortest V–N bond distance among the TBP structures is observed for **4**, which – as it is taken from the optimised protein model **HPO1** – allows engagement of the vanadate oxygen atoms in hydrogen bonding with neighbouring positively charged amino acid residues. It is

Table 3.2: Calculated geometrical parameters for structures **1-5** at the ADF-BP/TZ2P level of theory; all bond lengths are given in pm and angles in degrees; for notation of atoms see Fig. 3.1 and 3.2.

	1	2	3	4^a	5
V–O1	192.0	191.4	190.7	193.8	202.4
V–O2	196.5	196.6	194.7	189.4	202.4
V–O3	165.0	165.3	164.4	170.2	166.6
V–O4	165.0	164.7	166.3	168.3	166.6
V–N	229.5	233.8	234.5	219.5	210.2
O3–V–O4	109.4	111.7	112.0	111.5	105.4
O1–V–N	159.2	162.2	162.9	159.1	91.4
O2–V–N	75.6	74.9	74.7	78.9	91.4
V–O3–O4–O2	13.3	15.1	16.4	9.6	-12.9
O2–V–N–C	0.0	1.2	156.7	142.7	142.4
τ^b	0.61	0.65	0.64	0.43	0.0

^a Structure **4** corresponds to the cofactor of the protein model **HPO1**; the geometry given here is taken from the optimised structure of **HPO1** at the BP/TZP level, see section Computational Methods for details.

^b $\tau = (\alpha - \beta)/60$ (α and β are the two largest angles at the vanadium atom) ; for an ideal tetragonal pyramid $\tau = 0$ and for an ideal trigonal bipyramid $\tau = 1$.

worth comparing geometrical parameters of **HPO1** with those obtained from the protein crystal structure. The x-ray crystal structure of the protein (at 2.19 Å resolution), has given a V–N distance of 225 pm, which is about 5 pm longer than the calculated value of **HPO1**. The V–O distances from the crystal structure are as follows, with the values for **HPO1** given in parenthesis: 165 (168), 165 (170), 165 (189), 197 pm (194 pm) (cf. Table 3.2 and²²). Moreover, **HPO1** also has the lowest value of the dihedral angle V–O3–O4–O2 which is another manifestation for a reduces V–O bonding of the equatorial oxygens atoms, that are involved in hydrogen bonding to the neighbouring amino acids residues. This is consistent with the decreased V–N bond as compared to the non hydrogen bonded structures **2** and **3**. It is not surprising that the geometry found for the structure **HPO2** rather closely resembles the equivalence of the equatorial V–O bond distances as suggested by the crystal structure, albeit somewhat longer distances are obtained in our calculations. As shown by the results of the reference calculations, ADF-BP/TZ2P level of theory does give about 3 pm longer bond distances as compared to B3LYP/basis1 level of theory and, therefore, overestimate the bond distances accordingly. This combined with the limit of resolution in the x-ray crystallography could perhaps reconcile these bond lengths. But a closer comparison between the bond distances in **HPO1** and those for the similar doubly protonated species **2**, **3**, reveals that hydrogen bonding also plays an important role in determining the V–O bond distances. For example the equatorial V–O3 bond in **HPO1** is shortened, as compared to the corresponding values for **2** and **3**, due to the donating

Table 3.3: Calculated geometrical parameters for structures **2** and **6-8** at the ADF-BP/TZ2P level as well as **HPO2** at the BP/TZP level of theory; all bond lengths are given in pm and angles in degrees; for notation of atoms see Fig. 3.1 and 3.2.

	HPO2	2	6	7	8
V–O1	197.1	191.4	182.9	235.1	176.5
V–O2	173.2	196.6	186.6	185.5	179.0
V–O3	177.5	165.3	159.4	163.3	176.4
V–O4	172.6	164.7	184.4	163.6	174.5
V–N	227.1	233.8	224.0	210.8	219.0
O3–V–O4	114.8	111.7	112.8	113.2	109.5
O1–V–N	164.8	162.2	165.3	175.8	168.9
O2–V–N	79.5	74.9	77.0	90.2	78.1
V–O3–O4–O2	12.5	15.1	12.8	-9.9	12.6
O2–V–N–C	138.2	1.2	29.1	11.1	1.5

hydrogen bond of the OH group (O3) towards the side chain oxygen atom O5 of Ser402. Conversely all other V–O bonds are elongated, since the corresponding oxygen atoms are receiving hydrogen bonds.

The structures **6** to **8** and **HPO2** shown in Figs. 3.1 and 3.2, respectively, correspond to species with TBP geometry with successively added protons, starting from the doubly protonated situation as found in structures **1** to **4**. The geometrical parameters for the minima of these structures are given in Table 3.3 along with those of **2** for comparison. All these species are TBP structures with the apical oxygen atom protonated, and successive addition of protons at the equatorial oxygen sites of vanadate. Excluding **7**, where the additional third proton goes to the apical oxygen atom O1, this constitutes a continuous series of proton addition from left to right in Table 3.3. Each additional proton in this series decreases the apical V–O bond distance at the oxygen atom O1, starting from 197.1 pm in the monoprotonated species **HPO2** to 176.5 pm in **8** where all oxygen atoms are protonated. In structure **7** the opposite occurs as the apical OH group is converted to a coordinated water molecule. This species may carry some relevance as it provides a situation resembling the role of the apical oxygen atom prior to or during peroxide attack in conjunction with the His404 residue in the proposed acid-base catalytic step.²⁵ It is interesting to note that the values of the equatorial V–O bond distances in **HPO2** and **8** closely match each other, despite the fact that in the former the oxo groups are engaged only in hydrogen bonds, while in later all positions are explicitly protonated.

3.3.2 Excitations

Orthovanadate and dihydrogen orthovanadate

In Table 3.4 the excitation energies and respective oscillator strengths for the $[\text{VO}_2(\text{OH})_2]^-$ species calculated with two different model exchange-correlation potentials (BP and SAOP,

see Computational Methods section) are summarised. The reason for the choice of this dioxo species as the basis for the discussion of imidazole coordination is that it is the dominant species at relevant physiological pH values. The geometry of $[\text{VO}_2(\text{OH})_2]^-$ was optimised at the ADF-BP/TZ2P level of theory. Since LMCT excitations for tetrahedral vanadate are well understood, the $[\text{VO}_2(\text{OH})_2]^-$ species can provide a basis for discussion of the calculated excitations (oscillator strengths) for the structures given in Fig. 3.1. The two lowest energy absorptions for trianionic vanadate $[\text{VO}_4]^{3-}$ were experimentally observed at 4.58 and 5.58 eV¹⁵⁰ (with oscillator strengths of 0.15 and 0.12, respectively) and calculations by Ziegler *et al.* employing the Hartree-Fock discrete variation method (DVM) produced the values of 4.51 and 5.71 eV¹⁵¹ (respective oscillator strengths, 0.22 and 0.12). The two transitions have been assigned as $(t_2^2 t_1^2 e^0 \rightarrow t_2^2 t_1^1 e^1)$ and $(t_2^2 t_1^2 e^0 \rightarrow t_2^1 t_1^2 e^1)$, respectively. Based on this experimental and theoretical background, it should be noted that LMCT excitation behaviour of vanadate may alter in two ways: First, if some of the anionic oxygens atoms are substituted by e.g. OH^- , which corresponds to a protonation of the oxygen atoms. As a result the energy and degeneracy of the highest occupied molecular orbitals (which are non-bonded oxygen orbitals) are altered along with their electron donating ability. Second, by changing the tetra- to pentacoordination and, hence, perturbing the energy and degeneracy of the lowest unoccupied molecular orbitals, which are to a large extent empty metal d orbitals. While the results arising from the later consideration are discussed in next section, the multitude of transitions listed in Table 3.4 have to be seen in the context that two oxygen atoms of the vanadate moiety are replaced by hydroxy groups. Indeed it is known for many metal oxo anions that the substitution of oxo with hydroxy groups or other substituent leads to the splitting of, at least, the lowest energy absorption band into a red shifted and a higher energy band.¹⁵² For vanadate it has been observed that protonation leads to a decrease in absorption intensity for the lowest energy band accompanied by a blue shift.¹⁵³ At the same time absorption intensity at approximately 4.00 eV

Table 3.4: Calculated excitation energies in eV for $[\text{VO}_2(\text{OH})_2]^-$ at different levels of theory; oscillator strengths are given in parenthesis. The energy levels are labelled according to their position relative to highest occupied and lowest unoccupied molecular orbitals (*homo* and *lumo* respectively).

		BP/TZ2P	SAOP/TZ2P	SAOP/ET-QZ3P1D
(1)	$\varepsilon_{homo \rightarrow lumo}$	3.93 (0.0034)	4.34 (0.0033)	4.29 (0.0041)
(2)	$\varepsilon_{homo \rightarrow lumo+1}$	4.05 (0.0000)	4.45 (0.0002)	4.41 (0.0001)
(3)	$\varepsilon_{homo \rightarrow lumo+2}$	4.73 (0.0029)	5.10 (0.0021)	5.06 (0.0022)
(4)	$\varepsilon_{homo \rightarrow lumo+3}$	4.68 (0.0086)	5.35 (0.0062)	5.31 (0.0052)
(5)	$\varepsilon_{homo-1 \rightarrow lumo}$	4.49 (0.0099)	4.88 (0.0097)	4.83 (0.0102)
(6)	$\varepsilon_{homo-1 \rightarrow lumo+1}$	4.63 (0.0003)	5.07 (0.0034)	5.01 (0.0054)
(7)	$\varepsilon_{homo-2 \rightarrow lumo}$	4.98 (0.0029)	5.34 (0.0028)	5.29 (0.0037)
(8)	$\varepsilon_{homo-2 \rightarrow lumo+1}$	5.00 (0.0011)	5.35 (0.0013)	5.30 (0.0015)
(9)	$\varepsilon_{homo-3 \rightarrow lumo}$	5.21 (0.0058)	5.52 (0.0031)	5.47 (0.0041)
(10)	$\varepsilon_{homo-3 \rightarrow lumo+1}$	5.26 (0.0004)	5.63 (0.0003)	5.57 (0.0003)

(310 nm) shapes into an intense band. For doubly protonated (monoanionic) vanadate, two low intensity bands at ≈ 4.77 eV (260 nm) and ≈ 4.00 eV (310 nm) replace the lowest energy band observed for the unprotonated trianionic vanadate (cf.¹⁵³). Now comparing these values with our calculated bands for monoanionic vanadate $[\text{VO}_2(\text{OH})_2]^-$ in Table 3.4: transition (1) in Table 3.4 corresponds to the low energy tail, with calculated values of 3.93 and 4.34 eV based on BP and SAOP model potentials, respectively, and TZ2P basis set. Using the higher level basis set ET-QZ3P1D at the SAOP level gives a value of 4.29 eV. For the higher energy tail, calculated values are 4.49 eV at ADF-BP/TZ2P, 4.88 eV at ADF-SAOP/TZ2P and 4.83 eV at the ADF-SAOP/ET-QZ3P1D level (transition (5), Table 3.4). It is worth mentioning that the two potentials used not only give different energy spacing between the levels but also different ordering of the orbitals. Although, the value of 3.93 eV calculated at the BP level for low energy tail is incidentally close to the experimental value of 4.00 eV, the BP potential seems to underestimate transition energies as the calculated energy of the high energy tail (4.49 eV) is even lower than that of the original band observed for unprotonated trianionic vanadate (4.58 eV, ref.¹⁵⁰). On the other hand SAOP reproduces the splitting correctly centred on the original band, albeit both branches of the band are shifted to somewhat higher energies, a trend which is more distinct for the lower energy tail. Moreover, the calculations with the BP potential also turned out to be heavily dependent on the basis set used. With ET-QZ3P1D basis set it failed to reproduce even the correct composition of orbitals. As expected, SAOP on the other hand remained stable with both basis sets as it is obvious from the values in Table 3.4. To conclude about the validity of the methods used, SAOP gives better agreement with the experiment and use of larger basis set tends to correct the overestimation of transition energies. The spectra simulated with bands taken from Table 3.4 are shown in Fig. 3.3. The highest energy band in Fig. 3.3 corresponds to the transition (9) in Table 3.4. The position of this maximum at 5.21, 5.52 and 5.47 eV calculated at ADF-BP/TZ2P, ADF-SAOP/TZ2P and ADF-SAOP/QZ3P1D level, respectively, is close to the higher energy

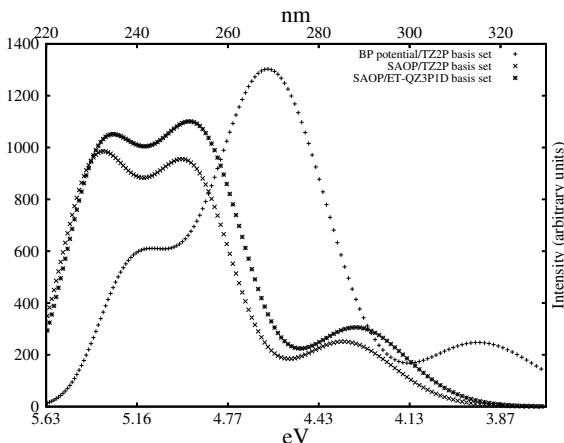


Figure 3.3: LMCT spectrum of doubly protonated orthovanadate $[\text{VO}_2(\text{OH})_2]^-$ simulated with the program swizard¹⁵⁴ utilising a 1/2 bandwidth of 3000 cm^{-1} , bands were calculated with TD-DFT at different levels of theory: ADF-BP/TZ2P, ADF-SAOP/TZ2P and ADF-SAOP/ET-QZ3P1D (see text for details).

transition (5.58 eV) observed for unprotonated trianionic vanadate (ref.¹⁵⁰) Nevertheless, it is unclear whether or not it corresponds to the same transition as observed in trianionic vanadate, which might be somewhat affected by protonation.

Imidazole coordination to dihydrogen orthovanadate

For the tetrahedral geometry of vanadate the highest occupied molecular orbitals (HOMO) are mainly non-bonded p orbitals of the oxygen atoms and the lowest unoccupied molecular orbitals (LUMO) are comprised mainly of d orbitals centred on vanadium atom. It was mentioned in the previous subsection that LMCT excitation behaviour of tetrahedral orthovanadate changes upon substitution of oxo with OH^- groups, i.e. protonation, and by extending the coordination sphere, here by addition of an imidazole ligand. While the former is expected to work through perturbing the degeneracy of oxygen atom centred HOMOs, the latter alters the energies of vanadium atom centred LUMOs. Coordination by imidazole may possibly also cause additional $\pi(\text{imidazole}) \rightarrow d(\text{vanadium})$ LMCT in addition to disturbing the existing $p(\text{oxygen}) \rightarrow d(\text{vanadium})$ LMCT. Fig. 3.4a gives a comparison of energy levels in the frontier region of structures **1–5** with those for dihydrogen orthovanadate. It can be seen that coordination by imidazole reduces the gap between occupied and virtual orbitals, an effect which is most pronounced for the SP geometry of **5**. The energy pattern of the orbitals of **4** somewhat resembles that of **5** in the occupied region and that of **1**, **2** and **3** in the region of the virtual orbitals. The Figs. 3.5a and 3.5b present the excitation behaviour of the structures **2** and **3** with C_1 symmetry as well as those of the structures **1** and **5** with C_s symmetry. The transitions obtained with the ET-QZ3P1D basis set are shifted to slightly lower energies in most cases with respect to

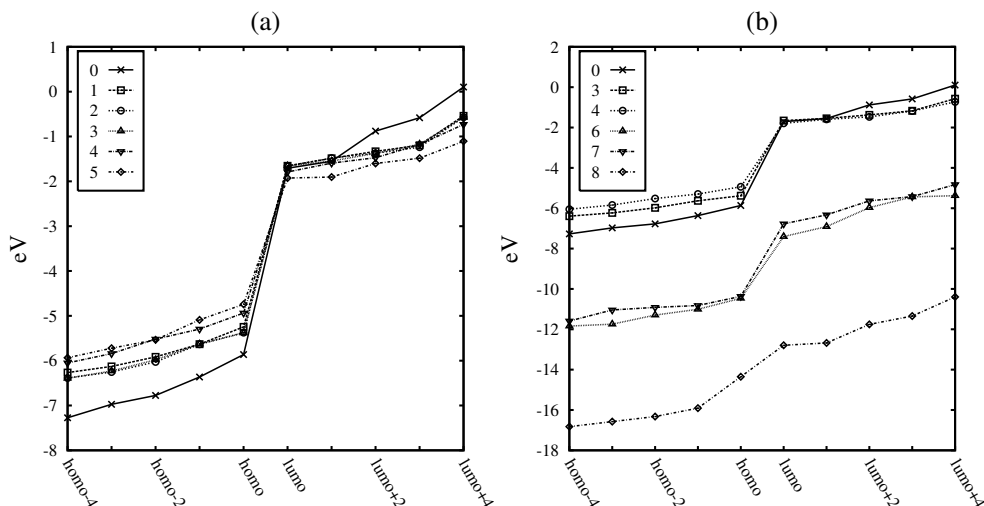


Figure 3.4: Calculated energy levels in the frontier region for dihydrogen orthovanadate (structure donated as **0**) and the corresponding pentacoordinate models with imidazole ligand **1–8**.

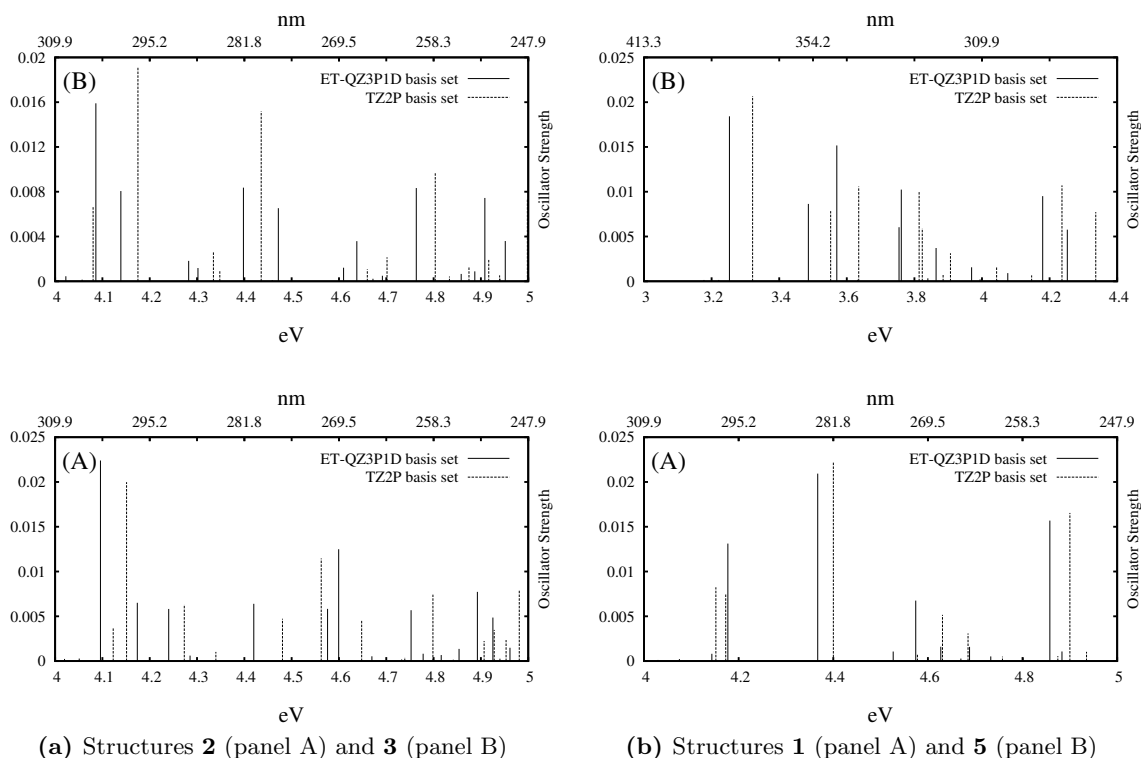


Figure 3.5: Calculated excitation energies for structures **1**, **2**, **3**, and **5** using SAOP with TZ2P and ET-QZ3P1D basis sets.

the TZ2P basis set. Similarly oscillator strengths also change with basis sets, but generally similar looking patterns can be easily recognised for both cases. The strongest transitions for the TBP structures **2** and **3** occur in the region 4.1 – 4.2 eV, nevertheless these two geometries differ in the details of their bands in the regions of 4.4 – 4.7 eV. The C_s geometry **1** differs from both **2** and **3** in the fact, that it has markedly dropped oscillator strength for transitions in the 4.1 – 4.2 eV region, while the other bands are stronger compared to corresponding bands for **2** and **3**. Fig. 3.5b reveals structure **5** as the one exhibiting a radically different excitation behaviour. The whole spectrum is observed within a much lower energy region, and the strongest excitation occurs at around 3.2 eV. A detailed look on the origin of excitations expressed in Figs. 3.5a and 3.5b revealed that excited electrons originate from the orbitals mainly centred on oxygen atoms without any exception. The nature of the highest singly occupied molecular orbitals in the excited state strongly differ for all these structures. It was found that the mixing of π orbitals of the imidazole ring with empty vanadium d orbitals, to varying extents in virtual orbitals regions, is responsible for the differences in the excitation behaviour of the different geometrical arrangements. For excitations at 4.58 eV in **1**, 4.17, 4.57 and 4.89 eV in **2** and at 4.13, 4.47, 4.76 and 4.9 eV in **3**, the excited electron ends up in a virtual orbital which has a varying predominant contribution from the imidazole ring in addition to some d character from the vanadium atom (e.g. see Tables A.1 and A.2 for structure **2**). All other excitations for these structures

are oxygen→vanadium LMCT in character and there is no evidence of any LMCT from imidazole to vanadium. The difference in the details between the spectra of structures **2** and **3** arises due to the fact that the oxygen atoms of vanadate are oriented differently with respect to the imidazole ring in both structures. This causes a variation in the transition dipole moments for certain transitions because the charge on oxygen atoms is assigned differently with respect to some virtual orbitals with predominant imidazole contribution. The excitation behaviour of SP structure **5** is not only quantitatively different as obvious from its spectrum, but also qualitatively, due to the reason that from all the excitations only those at 3.75 eV and at 3.48 eV are oxygen→vanadium LMCT in character. All the other structures have very strong mixing of imidazole character in the highest singly occupied molecular orbital (cf. Tables A.7, A.8).

Effect of protonation on excitations of imidazole-vanadate species

Fig. 3.4b shows the energy range of levels in the frontier region for structures **6**, **7** and **8** in comparison with that of different doubly protonated species including dihydrogen orthovanadate. It can be seen that additional protons shift the energy levels to lower values and that this change is most pronounced for **8**. The spectra for these species are shown in Fig. 3.6a which also show a variation from excitation behaviour discussed in last subsection. The site of the third protonation makes a difference as can be seen from the comparisons of panels (A) and (C) of Fig. 3.6a. The species **6** and **7** show bands of comparable strength in the region 4.2 – 4.7 eV. Whereas both structures differ in the fact that **6** also shows an excitation at 3.95 eV along with several peaks between 5.0 and 5.5 eV. In comparison, structure **7** undergoes one very strong excitation (oscillator strength 0.05) at 5.62 eV and another comparatively weaker excitation at 5.53 eV. Finally, for species **8**, where all the oxygen atoms of vanadate are protonated, the spectrum given in Fig. 3.6a (B) differs markedly as the lowest energy excitation occurs at 1.62 eV along with additional excitations between 3.2 – 5.0 eV. The nature of excitations of these species in higher protonation states have been found to differ from those discussed earlier in the fact that additional protonation causes strong imidazole→vanadium LMCT along with oxygen→vanadium LMCT. Thus, excitations at 5.13 eV for **6** to a lesser extent, and at 4.58 eV (structure **7**), 1.62, 1.69, 3.20 and 3.28 eV (structure **8**), to predominant extent are caused by imidazole to vanadium LMCT (Tables A.9 — A.14).

The inclusion of protein environment of active site of VCPO

The effects of the protein environment on the excitation behaviour of TBP vanadate species is discussed in this section. These effects can be divided into two types: First, the orientation of vanadate oxygen atoms to achieve the maximum stabilisation by forming hydrogen bonds with the surrounding amino acid residues modifies the TBP geometry, which in turn

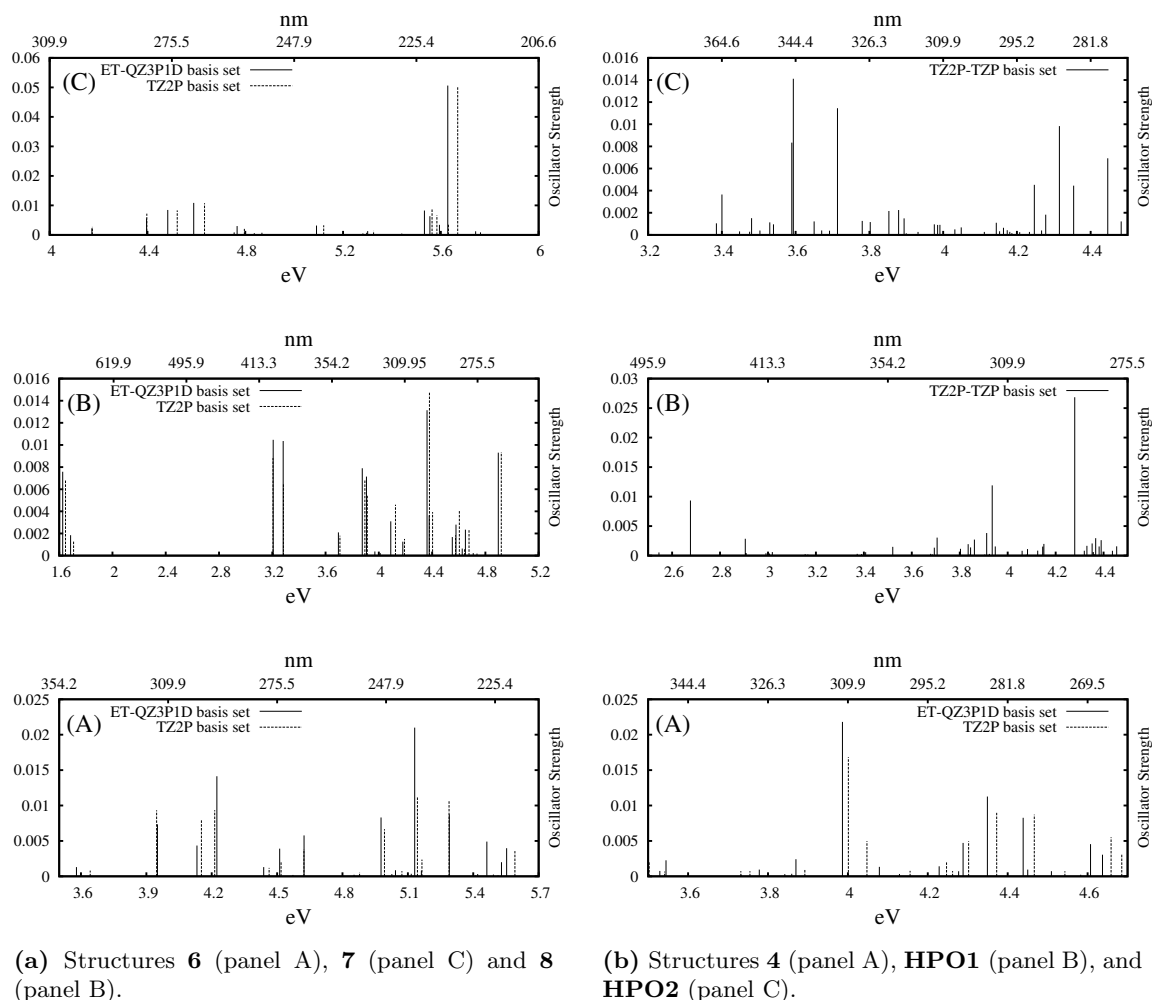


Figure 3.6: Calculated excitation energies for structures **4**, **6**, **7**, **8**, **HPO1** and **HPO2** using SAOP. Both TZ2P and ET-QZ3P1D basis sets were used for structures **4**, **6**, **7** and **8**. For **HPO1** and **HPO2**, TZ2P basis were used for the atoms of the vanadate and His496 moieties and TZP basis for all the other atoms.

may affect the excitation behaviour. This is manifested in the spectrum of structure **4** shown in Fig. 3.6b (A), which shows just another variation of effects of differences in geometry already explained while discussing the spectra of structures **1**, **2**, **3** and **5** depicted in Figs. 3.5a and 3.5b. Second, the engagement of vanadate oxygen atoms in hydrogen bonds alters the charge distribution on these oxygen atoms, which on the one hand allows the imidazole moiety to closely approach the coordination sphere of the vanadium atom, simply because the ligand-ligand repulsion between imidazole and oxygen atoms (equatorial) is reduced. On the other hand this may also affect the oxygen→vanadium LMCT. The fact that His404 is more strongly bound to doubly protonated vanadate inside the protein environment is evident from the decreased V–N bond distance in structure **4** as compared to structures **2** and **3**. Another evidence comes from the origin of the peaks in Fig. 3.6b

(A). The excitation pattern of the spectrum of structure **4** matches those shown in Fig. 3.5a for structures **2** and **3**, with the difference that highest singly occupied molecular orbital in the excited states of structure **4**, which corresponds to all these transitions, has a strong mixing of imidazole orbitals with those of empty vanadium *d* orbitals (cf. Tables A.3, A.4). In this respect these transitions resemble those observed for the SP species **5**.

The calculated excitation energies for the full structures **HPO1** and **HPO2** (cf. Fig. 3.2) are shown in Figs. 3.6b (B) and 3.6b (C). Unfortunately, calculations for a monoprotonated imidazole-vanadate species could be successfully performed only inside a protein model environment like in **HPO2**. Therefore a direct comparison with the excitation behaviour of a corresponding isolated monoprotonated species is prevented. A comparison of the panels (B) and (C) in Fig. 3.6b shows that **HPO1** and **HPO2** exhibit a markedly different transition behaviour. At the higher energy end **HPO2** shows several peaks while **HPO1** shows only two at 3.93 eV and at 4.28 eV. Similarly, towards the low energy end **HPO1** shows only one transition at a very low energy of 2.6 eV, while **HPO2** again has several peaks in the region of 3.4 – 3.8 eV. The composition of these transition is comparatively simple in the case of **HPO1** (Tables A.5, A.6), where the one at 2.67 eV is due to a His496→vanadium LMCT, and that at 4.28 eV is a mixture of several excitations, which are predominantly of oxygen→vanadium LMCT character. Moreover, the transition lying between these two at 3.93 eV is attributed to the protein structure, and apparently has nothing to do with the vanadium centre. On the other hand in the case of **HPO2**, the transition at 4.44 eV is the only one which is solely of oxygen→vanadium LMCT character. Some oxygen→vanadium LMCT character is also found for the transition at 4.32 eV, whereas the one at 3.71 eV is attributed to excitations within the protein environment. The two closely spaced strong transitions at around 3.59 eV are a mixture of a His496→vanadium LMCT and some excitations attributed to the protein environment. Interestingly, in the region of 4.2 – 4.5 eV structures **4** and **HPO2** exhibit similarities. Of the two strongest peaks observed for **HPO2** in this region, the one at 4.32 eV has a partial, while that at 4.44 eV has pure oxygen→vanadium LMCT character. The corresponding peaks in the spectrum of **4** lie at 4.35 and 4.43 eV and are both of oxygen→vanadium LMCT in character. Although the geometry of structure **4** is taken from **HPO1** and therefore the same, all oxygen→vanadium LMCT bands except the very strong one at 4.28 eV disappear in **HPO1**. On the other hand two additional transitions with different composition appear, not observed in **4**.

Recently Borowski *et al.* published the results of TD-DFT calculations on the active site of VCPO using B3LYP hybrid density functional.¹⁵⁵ Although their model system of the active site of VCPO has a major difference with respect to our protein model structures **HPO1** and **HPO2** by the fact that they did not include the amino acid residues Ser402 and Gly403 in their description of protein environment, their results for the doubly proto-

nated imidazole-vanadate species are fairly comparable. They have reported a transition at 3.95 eV with an oscillator strength of about 0.01 due to a His496→vanadium charge transfer excitation. Our calculations for **HPO1** also show a transition at 3.93 eV with an oscillator strength of about 0.012. But our findings disagree, regarding the origin of this transition, as our calculations attribute this transition to an internal excitation within the protein environment and not to a His496→vanadium charge transfer band. For structure **4** the transition closest to the reported values of Borowski *et al.* is found at 3.98 eV, but with a much higher oscillator strength (0.025) and attributed to an oxygen to metal charge transfer excitation. The second transition reported by Borowski *et al.* occurs at 4.3 eV with an oscillator strength of about 0.018. This is consistent with our findings, as for **HPO2** we observe a transition at 4.28 eV with an oscillator strength of 0.027. In this case both results agree with respect to the origin of the transition, which is assigned as oxygen to metal charge transfer.

Renirie *et al.*³⁰ observed a transition at 3.93 eV (315 nm) for the recombinant form of VCPO at pH values of 8.3 and 5.0. Similarly, Ray *et al.* have shown that complexed vanadate in phosphoglucosyltransferase shows a band at 3.97 eV (312 nm).¹⁵³ Our results for **HPO1** and **HPO2** can be compared with the reported data in order to identify the experimentally observed transition. Both protein model structures **HPO1** and **HPO2** exhibit an oxygen to metal charge transfer transition at the higher energy end of their respective spectra. The energy of this transition is 4.28 eV for **HPO1** and 4.44 eV for **HPO2**. As shown in an earlier subsection, SAOP overestimates the energy of the lowest energy band observed for dihydrogen orthovanadate by 0.34 eV with TZ2P and by 0.29 eV with ET-QZ3P1D basis sets. Applying this correction, we are left with values of 3.94 eV for **HPO1** and 4.10 eV for **HPO2**.

The former not only matches the experimentally observed transition, it also has a high oscillator strength (0.026) as compared to the other transitions in the spectrum of **HPO1** as well as all the transitions observed in the spectrum of **HPO2**. This puts the protein model structure **HPO1** as an eligible candidate for the structure of the active site of the resting state of VCPO at physiological pH values. This is supported by recent calculations of Zampella *et al.*,¹⁵⁶ which suggest that a hydroxy group along with two oxo groups in equatorial position and another hydroxy group at the axial position of a TBP arrangement is the energetically favourable structure for the resting state of the active site of VCPO. Nevertheless, there is a significant difference with respect to the orientation of the equatorial hydroxy group, which in the case of Zampella *et al.* is suggested at the position near the Lys353 residue (corresponds to O4 in Fig. 3.2). Whereas in our protein model structure **HPO1** the equatorial hydroxy group is hydrogen bonded towards the Ser402 residue, which itself is found to be hydrogen bonded in the crystal structure towards a nearby water molecule.²²

3.3.3 Conclusions

We have used time dependent density functional theory to calculate electronic excitations for monoanionic vanadate and vanadate coordinated by imidazole in different geometries and protonation states and, moreover, also for structures which incorporate the protein environment of VCPO. Two different exchange-correlation model potentials were utilised, one generated by the Becke-Perdew functional and the other by the statistical average of the orbital model exchange-correlation potential (SAOP). Our results allow for the following conclusions:

1. It is found that the SAOP approach produces one electron energy levels in the frontier region for which the excitations behaviour is in agreement with the experimentally determined optical absorptions for dianionic vanadate. Moreover, although results obtained with TZ2P and ET-QZ3P1D basis sets are basically similar, the ET-QZ3P1D basis leads to values for the excitation energies which are in better agreement with the experiment.
2. Calculations at the SAOP/ET-QZ3P1D level on monoanionic vanadate coordinated by an imidazole show that the excitation behaviour is strongly dependent of the actual geometry of the resulting species.
3. The protonation of vanadate causes the imidazole fragment orbitals to contribute to the highest occupied molecular orbital region, thus leading to excitations with LMCT character originating from the imidazole ligand.
4. While the excitation energies obtained for different protonation states indicate that a doubly protonated monoanionic species is the likely structure of enzyme active site in the resting state, higher protonation states will show varied reactivity due to participation of imidazole within the frontier orbital region.
5. The energy calculated for the most intense band of the doubly protonated vanadate species as model for the protein resting state is in good agreement with the experiment. Moreover, the character assigned to this excitation is predominantly of oxygen to vanadium LMCT.

These results of the theoretical calculations connect two experimental findings: The geometry of the VCPO active site obtained by x-ray crystallography and the optical absorption spectra observed for vanadate located within the enzyme active site.

Chapter 4

Hydrogen Bonding in VHPO Active Site

4.1 Introduction

Hydrogen bonding (HB) is strongest among all weak interactions and ubiquitously responsible for working of numerous sub molecular phenomenon in biological systems.^{157,158} The biological catalysts of nature, the so called enzymes, heavily depend upon HB interactions¹⁵⁹ for electrostatically stabilising intermediates and transition structures and thus carrying (otherwise) complicated chemistry of cellular environment at ambient temperatures. This becomes possible because enzymes fine tune the arrangement of hydrogen bonds between different motifs in active sites, in a way to extract maximum possible kinetic benefit. It is well known that hydrogen bonds are capable of acting in cooperative fashion^{157,158,160,161} and thus of imparting extra stability to supramolecular adducts. These cooperative effects apparently owe their origin to the fact that acceptance (or donation) of a hydrogen bond by an electronegative atom modifies its ability to accept (donate) another hydrogen bond so that combined effect of more than one hydrogen bond is different than sum of an equal number of isolated hydrogen bonds. In context of present work, comparative chloroperoxidase activity^{65,162} in VCPO and VBPO poses a perplexing question, as catalytic efficiency of these otherwise identical active sites^{22,23,25} in oxidising chloride is in stark contrast. The elusive answer to this question may be found in details of extensive hydrogen bonding network found in the active site of these enzymes. It may be the case that steric constraints imposed by secondary protein structure on the active site cavity of both enzymes, fine tunes the hydrogen bonds of active site amino acids with cofactor in a fashion, such that combined effect of these hydrogen bonds operates differently in both systems. It is intended in present chapter to explore the hydrogen bonding details in active site of these enzymes. For this purpose crystal structure atomic positions of VCPO^{22,25} and VBPO²³ active site cavities are borrowed to optimise the cofactor geometry in them and then hydrogen bonding patterns are studied in each. Following section of this chapter is dedicated to conceptual framework of hydrogen bonding studies, utilised later in the chapter. After this a description of computational procedure is given and then results are discussed.

4.2 The Nature of Hydrogen Bond

Hydrogen bond (HB) is an attractive interaction between two atoms bridged by a hydrogen atom covalently bonded to one of these atoms. Starting with the proposal originated by Linus Pauling,¹⁶³ HB is traditionally viewed as an electrostatic interaction between two electronegative atoms ($\overset{-\delta}{\text{X}}-\overset{+\delta}{\text{H}}\cdots\overset{-\delta}{\text{Y}}$) mediated by a proton. Despite having well recognised role in biomolecules,¹⁶⁴ crystal engineering^{165,166} and vast range of chemical phenomenon, and having enjoyed a variety of respectable experimental methods ranging from IR spectroscopy to x-ray diffraction, neutron diffraction and ^1H NMR spectroscopy for its detection and characterisation,^{159,167,168} accurate definition of hydrogen bond is still a hotly debated issue among theoreticians. The inability to predict the properties of HB with simplified rules and models is rather frustrating in different fields of chemistry, a discipline which is traditionally known for efficient use of such rules and models. This is partly due to relatively wide operative range of HB energies and to varied spectrum of physical origins of HB interactions. The inclusion under HB semantic umbrella of weak attractive forces in which condition of electronegativity for HB donor atom is no longer considered strictly necessary,¹⁶⁹ like carbon atom in C–H, and the ability of commentators to distinguish such hydrogen bonds from other weak interactions¹⁷⁰ has further complicated the issue. On the other end of spectrum the attribution of covalent character to strong hydrogen bonds,¹⁷¹ has not helped the matter either. Roughly, hydrogen bond energies range¹⁷² between a fraction of kcal mole⁻¹ for donors like C–H to 40 kcal mol⁻¹ for $[\text{F}\cdots\text{H}\cdots\text{F}]^{-1}$ system.

4.2.1 Acid–Base equilibria and hydrogen bond

Broadly speaking, HB donor and acceptor atoms can be viewed as competing bases (or acids), the relative basicity (acidity) of which determines the hydrogen bond strength. As a general rule in the equilibrium



smaller the value of ΔpK_a , i.e. the pK_a difference between XH and Y^+H groups (or ΔPA , the proton affinity difference between atoms X and Y in gas phase) the greater is the strength of hydrogen bond.^{173–176} The strongest hydrogen bonds are formed between homonuclear donor acceptor pairs and those involving heteronuclear atoms are, as a rule weaker than former ones.¹⁷⁷ Hydrogen bonding strength can be altered by changing the proton affinity of donor or acceptor atoms with change in environment or substitutions on these atoms. In this context, a classification of hydrogen bonds can be made on the basis of potentials for proton motion along the line between donor–acceptor atoms^{159,167,168} as

conceptually demonstrated in Fig. 4.1.

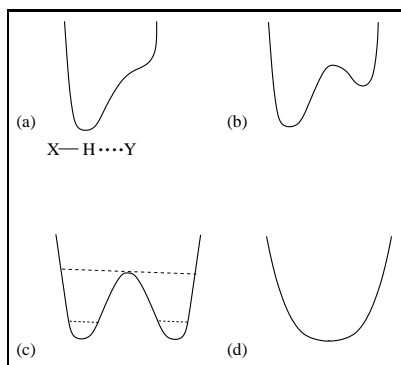


Figure 4.1: Types of HB on the basis of proton potential.

out controversy.¹⁸³ For the hydrogen bonds with potentials (c) and (d), the proton lies at equal distance from both heavy atoms (i.e. donor and acceptor atoms), and bonding energy is claimed to have strong contribution from covalent interactions. It is worth mentioning that sufficient alteration of relative proton affinities of X and Y atoms can lead to symmetry reversal of potential (a) and (b), a situation corresponding to ion-pair formation on the right side of equilibrium (Eq. 4.1).

4.2.2 Approaches to characterisation

Hydrogen bond is characterised in a number of ways, both phenomenological and theoretical. Among the former, most widely used are geometrical parameters (obtained from x-ray and neutron diffraction, or from quantum chemical computations), intermolecular vibrational frequencies (for van der Waal's complexes these are typically around 100 cm^{-1} and hydrogen-bonded intermolecular stretch is in the region 200 cm^{-1}),¹⁸⁴ and red shifting of X-H bond stretching frequency.^{159, 184} This category should also include the complexation energies calculated with supermolecular approach.¹⁸⁵ However energies calculated with symmetry adapted perturbation theory (SAPT)¹⁸⁶ aim at investigating the underlying physical origins of interactions, and hence this method operates at more fundamental level. Other methods at theoretical level are mostly *post facto* in nature involving an analysis of previously calculated wave function. In following part of this section, a brief description of methods relevant to present chapter is given.

Geometrical criteria and supermolecular energies

Geometrical parameters are a convenient and simple way of predicting the presence and quality of a hydrogen bond.^{157, 167–169, 185, 187, 188} In principle this criterion nicely differentiates a hydrogen bond from other weaker attractions like van der Waals interactions. A typical van der Waals attraction between two monomers A and B operates at interatomic

distance with an equilibrium value which is close to sum of van der Waals radii of contact atoms. On the other hand in $X-H\cdots Y$ hydrogen bond, the proton penetrates into electronic cloud of Y atom, far beyond the limit imposed by sum of van der Waals radii of H and Y . For example it was reviewed¹⁶⁸ that $H\cdots O$ distance is frequently in the range of 160 to 220 pm for $O-H\cdots O$ systems, whereas the sum of van der Waals radii of H and O are nearly 270 pm. Moreover in $O-H\cdots O$ hydrogen bonds, the distance between oxygen atoms often goes well below 300 pm, the approximate sum of van der Waals radii of two oxygen atoms. However, this criterion along with the condition of high electronegativity of donor and acceptor atoms, excludes the so called “weak hydrogen bond”. It has been argued¹⁷⁰ that electrostatic interaction in hydrogen bond, being a long range force should retain its ability to act at distances longer than van der Waals cutoff. Another aspect of geometrical criterion is directionality of hydrogen bonds and hydrogen bonds tend to retain a linear XHY angle,^{157,169} which obviously offers a line of maximum interaction between donor and acceptor atoms. Moreover directionality of $X-H$ vector, towards acceptor atom Y , has been found¹⁸⁸ to preferentially orient in directions associated with lone pairs of acceptor atom on the basis of sp^2 and sp^3 hybridisation.

The HB energy is commonly obtained through quantum-mechanical calculations on hydrogen bonded intermolecular complex and its component molecular fragments, in what is known as supermolecular approach.^{185,189,190} The bonding energy of a hydrogen bond between A and B is given as

$$\Delta E^{A,B} = E_{A+B} - E_A - E_B \quad (4.2)$$

whereas E_{A+B} is calculated as the energy of optimised supramolecular adduct of A and B , and other two terms on right hand side are energies of fragments A and B with their geometries frozen as in optimised supramolecular adduct.

For the supramolecular complexes composed of more than two molecules, the total interaction energy between all complexing molecules can be calculated by subtracting the sum of all individual molecular energies from that of supramolecular adduct in a fashion similar to Eq. 4.2. For such complexes, interaction energy between any two component molecules can be related to total interaction energy by expressing the latter in terms arising from interaction within the fragments composed of two, three, ..., many molecules. These so called two-body, ..., many-body etc. terms are again calculated by the approach employed in Eq. 4.2.

It is to be noted that interaction energy expressed in this way does not include the energy change involving geometrical deformation of molecules (or fragments composed of any number of molecules) caused by complexation. If inclusion of this effect is also desired than e.g., E_A and E_B are to be calculated with fully optimised geometries of A and B in calculation of $\Delta E^{A,B}$. In literature one can find examples of $\Delta E^{A,B}$ calculated both with

deformed or optimised geometries of A and B . For true HB energy, the error introduced by use of *partial* basis set for calculating E_A and E_B (relative to *full* basis used for calculation of E_{A+B}) should be cancelled. The cancellation of this error, or basis set superposition error (BSSE) is normally done by counterpoise method.¹⁹¹

Charge and resonance assistance to HB

On the theoretical front, one of the oldest quantum mechanical picture of hydrogen bond was provided with its valence-bond treatment by Coulson.^{192–194} A hydrogen bond between a homonuclear donor, acceptor pair was formulated as a mixture of following resonance structures :-

1. Ψ_I No charge-transfer state $(X-H \cdots X)$
2. Ψ_{II} Charge-transfer state $(X^- \cdots H-X^+)$
3. Ψ_{III} Ionic state $(X^- \cdots H^+ \cdots X)$

In case of heteronuclear hydrogen bond, state Ψ_I has to be replaced with two for ground states $(X-H \cdots Y)$ and $(X \cdots H-Y)$. It is to be pointed out that Ψ_I represents interaction which is commonly interpreted as electrostatic in hydrogen bonds and Ψ_{II} , with charge transfer implies shared electron or covalent interaction. Evidently, contribution from Ψ_{II} will enhance hydrogen bond strength, but becoming possible only if energies of Ψ_{II} and Ψ_I lie close to each other. Taking the example of $[O-H \cdots O=]$ system Gilli and Gilli¹⁷⁷ collected crystal structure data for systems with $O \cdots O$ distance ≤ 270 pm, and analysed available IR (O–H) stretching frequencies, 1H chemical shifts and thermodynamic data for gas phase HB energies. In a masterly display of inferential skill and theoretical insight they argued that Ψ_I and Ψ_{II} can be mixed by making them isoenergetic through:-

1. Connecting $=O$ acceptor and $O-H$ through π -conjugated chain,
2. Adding a negative charge: $[O-H \cdots O=] + e^- \longrightarrow [^-O \cdots H \cdots O=]$
3. Removing a negative charge: $[O-H \cdots O=] - e^- \longrightarrow [=O \cdots H \cdots O=]^+$

The charged hydrogen bonding systems in (2) and (3) get stabilisation from two resonance structures with charge localised on either of oxygen atoms. With this in view, strong hydrogen bond was said to be actually *three centre four electron* covalent bond. On the basis of this framework, the surveyed hydrogen bonds from literature were classified into:

1. Strong negative charge assisted hydrogen bond or (–)CAHB: $[^-O \cdots H \cdots O=]^-$
2. Strong positive charge assisted hydrogen bond or (+)CAHB: $[=O \cdots H \cdots O=]^+$
3. Strong resonance assisted hydrogen bond or RAHB: $[O-H \cdots O=]$
4. Moderate polarisation assisted hydrogen bond (PAHB), in which substituents on oxygen atoms play role in hydrogen bond strength.
5. Weak isolated hydrogen bonds.

By extending this classification to heteronuclear hydrogen bonds, another class of strong hydrogen bonds was added,

6. Positive/negative charge assisted hydrogen bonds or (\pm)CAHB for (O,N) pairs. In this last class which is also relevant to present work, HB strength and location of proton in HB was found to be dependent over Δ PA (for donor and acceptor atoms) as was discussed in Sec. 4.2.1.

Bader's theory and Popelier criteria

As explained above, a charged hydrogen bond system can achieve additional strength due to contributions from charge transfer canonical states i.e. by furnishing some covalent character. Characterisation of such systems should account for this possibility. Besides, there are systems like intramolecular hydrogen bonds and multiple hydrogen bonds in supramolecular assemblies, where scrutinising individual hydrogen bonds is not possible because system cannot be fragmented in a suitable way for supermolecular approach to predict the strength of individual hydrogen bonds in the system. Geometrical criteria is of help in such cases, but is not sufficient for complete description of the system. Bader's Quantum theory of Atoms in Molecules (QTAIM)^{195,196} provides a rigorous way to describe interactions between chemical entities, and for last few years is increasingly being used for describing hydrogen bonds. Starting with proposals of Koch and Popelier,¹⁸⁷ and with subsequent reports of many workers,^{197–200} certain QTAIM based topological characteristics of electron density in hydrogen bonded complexes have become accepted measure of existence and strength of hydrogen bonds. It is interesting to note that this kind of application of QTAIM is no way limited to theoretically calculated electron density, but has also been carried out with experimentally determined electron density.^{201–203} Of Popelier criteria,¹⁸⁷ those employing QTAIM parameters are listed as follows:–

1. The most primary requirement is *existence of bond critical point* (BCP) for $H \cdots Y$ contact.
2. *Electron density at these BCP* (ρ_C), with a value an order of magnitude less than that for covalent bonds and typically in a range 0.002 – 0.040 a.u. Connected to this requirement is the property that stronger hydrogen bonds show a greater value of ρ_C . Indeed it has been shown¹⁸⁷ that there exists a linear relationship between ρ_C and hydrogen bond energy.
3. A *positive value of Laplacian of $\rho(r)$ at BCP* ($\nabla^2 \rho_C$) in the range 0.024 – 0.140 a.u. The 3×3 matrix of second partial derivatives of electron density with respect to coordinates, after diagonalisation yields three eigen values. The sum of these eigen values is Laplacian $\nabla^2 \rho(\mathbf{r})$.

With regard to last two conditions, it is important to note that closed shell interactions like ionic bonds, van der Waals interactions, and hydrogen bonds are characterised by positive $\nabla^2\rho_C$ and low ρ_C . This is the consequence of contraction of charge away from interatomic surface towards nuclei. It was pointed out¹⁶⁸ that above proposed ranges for ρ_C and $\nabla^2\rho_C$ are good for distinguishing weak and very weak hydrogen bonds from van der Waals interactions, but strong hydrogen bonds would show values of these properties well above the upper limit of mentioned ranges.

To quantify the concept of what is termed “partial covalent character” of hydrogen bonds, the electronic kinetic energy density $G(r)$, potential energy density $V(r)$, and their sum, the total electronic energy density at hydrogen bond BCP have found a useful application. In the description of these QTAIM parameters, it would be useful to summarise their relation to nature of interaction. The Lagrangian kinetic energy density $G(r)$, and potential energy density $V(r)$ are connected to $\nabla^2\rho(r)$ by local version of virial theorem.

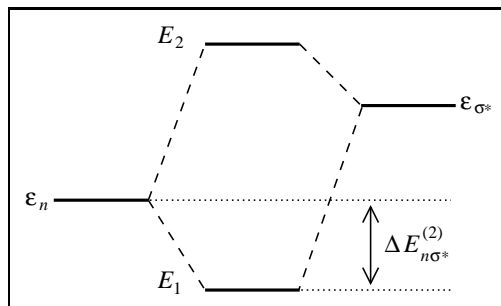
$$(\hbar^2/4m)\nabla^2\rho(r) = 2G(r) + V(r) \quad (4.3)$$

For bound states, $V(r)$ is always negative while $G(r)$ is always positive so $|V(r)| > 2G(r)$ ($\nabla^2\rho(\mathbf{r}) < 0$) indicates an accumulation of electronic density at r , and $2G(r) > V(r)$ ($\nabla^2\rho(\mathbf{r}) > 0$) implies depletion of electronic density at that point. This is another way of stating that sign of $\nabla^2\rho(\mathbf{r})$ at a point in space is determined by local excess of either $2G(r)$ or $V(r)$ at that point, over average quantities of the whole system which should always be related by $2\int G(r)dr = -\int V(r)dr$, the virial condition. Of special interest are these quantities at BCP, which for shared electron interactions like covalent bonds mean a negative $\nabla^2\rho_C$. A positive $\nabla^2\rho_C$ is characteristic of closed shell interactions as already mentioned. In the later case, the possible occurrence of $|G_C| < |V_C|$ despite having $2G_C > V_C$, has been attributed to “partial covalent” character^{204,205} of hydrogen bond. This situation may arise for strong hydrogen bonds, where the close proximity of proton to acceptor atom²⁰⁶ does not permit the ruling out of short range interactions.

Interactions between natural bond orbitals of donor and acceptors

Koch and Popelier also reported the net charge transfer from HB acceptor to HB donating monomers on complexation. This can be quantified by using any of charge partitioning schemes commonly used. We use the natural atomic charges^{207,208} for this purpose. It has been reported by Hobza¹⁸⁴ that charge transfer from HB acceptor to HB donor is very small, but its overall contribution to stabilisation is significant. Hobza also gave a rough estimation that transfer of 0.001 a.u charge corresponds to stabilisation by 1 kcal mol⁻¹. Such a stabilisation can be predicted with the concept of interaction between natural bond orbitals centred on interacting HB donor and acceptor. In this scheme²⁰⁹ (natural) bond orbitals

Figure 4.2: Perturbative interaction between occupied n_Y and empty σ_{X-H}^* orbitals in $X-H \cdots Y$ hydrogen bond according to Eq. 4.4.



(σ , π) and non-bonding orbitals (n) interact with antibonding orbitals (σ^* , π^*) resulting in net transfer of electron occupancy from the former to the later. In present context of hydrogen bonding entities, important interactions are (Fig. 4.2) between n orbitals of Y with σ^* orbital of $X-H$ bond in a $X-H \cdots Y$ hydrogen bond. Stabilisation arising from such interaction has been described by second order energy

$$\Delta E_{n\sigma^*}^{(2)} = -2 \frac{\langle n | \hat{F} | \sigma^* \rangle^2}{\varepsilon_{\sigma^*} - \varepsilon_{\sigma_n}} \quad (4.4)$$

where \hat{F} is the Fock operator and ε in denominator refers to energies of orbitals. This energy lowering has been taken as a measure of delocalisation of charge in occupied non-bonding natural orbital of (HB) acceptor over antibonding natural orbital of (HB) donor.

4.3 Computational Methods

Geometries (structures in Figs. 4.3 and 4.4) were optimised using Becke and Perdew (BP) combination of exchange and correlation functionals and a basis set of Slater type functions of triple zeta quality augmented with two sets polarisation functions (TZ2P). For some structures (**2**, **7**, **8**, **9** ; Fig. 4.3) the orientation of imidazole ring with respect to vanadate species was constrained in order for imidazole \cdots vanadate hydrogen bond to resemble the His404 \cdots vanadate hydrogen bond in VCPO. For large model structures of enzyme active site based on crystal structure (Fig. 4.9), crystallographic positions of amino acid atoms defining active site pocket were fixed and saturated with protons. The coordinates of pentacoordinated vanadate and all the protons were optimised by using TZP basis. These calculations were performed with ADF package of programs. These methods are henceforth mentioned as ADF-BP/TZP or ADF-BP/TZ2P. Hydrogen bonding energies at these geometries were calculated with supermolecular approach.¹⁸⁵ For small model complexes some benchmark calculations were done at a variety of theoretical levels including MP2/6311++G**, B3LYP/6-311++G**, ADF-BP/TZ2P and ADF-PBE/TZ2P levels. HB energies for large enzymatic systems were calculated at ADF-PBE/TZ2P level. MP2 and B3LYP calculations were done with Gaussian *G03* package of programs. HB energies were corrected for basis set superposition error (BSSE). The calculation of HB energies was repeated after placing the hydrogen bonded complexes into aqueous solvation medium (dielectric constant = 78.34) with conductor like screening model (COSMO) approach²¹⁰⁻²¹³

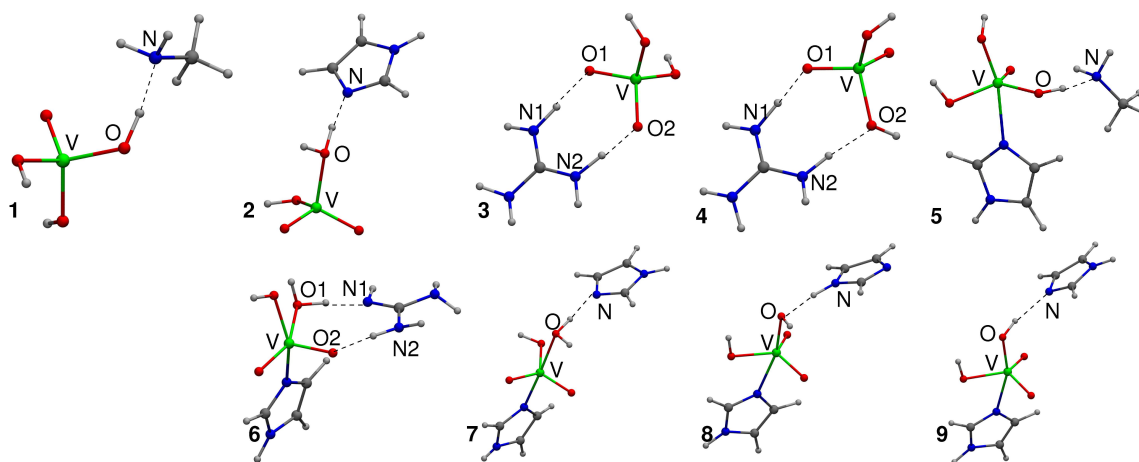


Figure 4.3: Optimised structures of small model complexes, each showing one of the individual HB interactions present in VHPO active site. See Table 4.1 for optimised HB geometrical parameters.

HB interactions were also characterised by topological analysis of electron density, by using Bader’s theory with software XAIM.²¹⁴ Natural bond orbital analysis was done with NBO program.²¹⁵

4.4 Results and Discussion

4.4.1 Small model complexes

Since full enzymatic active site involves multiple interactions between vanadate cofactor and many amino acid residues, in order to make an understanding of component interactions, it was deemed necessary to first analyse (1:1) model complexes of vanadate with groups representing side chains of lysine, histidine and arginine. Fig. 4.3 represents the optimised geometries of small model complexes, with either tetrahedral or TBP hydrogen bonded vanadate. This section describes the hydrogen bonding in these structures.

Geometries of small model complexes

The HB geometries of complexes in Fig. 4.3 are summarised in Table 4.1 and following parameters are listed: the distance between donor and acceptor atoms $R_{O...N}$, distance of proton to donor/acceptors atoms, $r_{O...H}$ and $r_{N...H}$ and hydrogen bond angle, \angle_{OHN} . Among the various optimised HB complexes, the donor–acceptor distances are generally smaller for complexes of tetrahedral vanadate than those of TBP vanadate species due to steric changes which accompany the increase in vanadium coordination number and transformation from tetrahedral to TBP geometry. The $R_{O...N}$ values for complexes of tetrahedral vanadate fall in the range of strong hydrogen bonds as it was reported¹⁷⁷ that $R_{O...N}$ in the range 250 –265 pm are typical of strong hydrogen bonds. The values reported here for tetrahedral

Table 4.1: Hydrogen bond geometrical parameters of complexes in Fig. 4.3. Optimisations were performed at ADF-BP/TZ2P level of theory. All distances in pm and angles in degrees.

		$R_{O\cdots N}$	$r_{O\cdots H}$	$r_{N\cdots H}$	\angle_{OHN}
1		264.8	104.8	160.5	172.0
2		255.3	107.8	148.0	172.4
3	(N1,O1)	265.2	158.0	107.2	178.4
3	(N2,O2)	258.2	148.5	109.6	179.2
4	(N1,O1)	254.3	142.9	111.4	178.5
4	(N2,O2)	270.1	165.1	105.8	174.6
5		275.8	101.8	175.6	167.1
6	(N1,O1)	262.1	104.6	157.6	176.2
6	(N2,O2)	277.4	173.4	104.3	174.6
7		271.1	101.9	169.6	172.6
8		278.8	175.6	105.1	166.5
9		301.1	98.0	204.8	166.5

vanadate complexes are in accordance with hydrogen bonds involving inorganic acids and nitrogen bases, as found in a survey¹⁷⁷ of Cambridge Crystallographic Database. Moreover the calculated values listed in Table 4.1 are reflective of strong hydrogen bonds between heteronuclear donor-acceptor pairs, termed as $\pm(\text{CAHB})$ by Gilli and Gilli.¹⁷⁷ Among complexes of tetrahedral vanadate species, the nearest approach between HB donor and acceptor atoms is found for imidazole-vanadate adduct (complex **2**), followed by one of the dual hydrogen bonds with guanidinium ion (complexes **3** and **4**), and then hydrogen bond with methylamine species (complex **1**). In the complexes of TBP vanadate species, the closest O-N distance is for one of hydrogen bonds with guanidine (262.1 pm ; complex **6**). All other heavy atom distances range between 271.1 pm (complex **7**) and 278.8 pm (complex **8**), except for complex **9** where O-N distance of 301.1 pm of indicates much weaker hydrogen bond between anionic TBP vanadate species and imidazole. It is worth mentioning that although $R_{O\cdots N}$ distance in HB complexes of TBP vanadate is longer than that in complexes of tetrahedral vanadate, the former still satisfy van der Waals radii cutoff criteria of hydrogen bonds.

There are other aspects of hydrogen bonding geometry. The X-H and H \cdots Y distances closely follow the trend of X \cdots Y distances, i.e. the shorter the distance between donor and acceptor atoms the longer is the X-H distance and shorter the H \cdots Y one. The linearity of HB is manifested in X-H \cdots Y angle. It can be seen that values of this angle are larger than 170° for majority of the hydrogen bonds. Only cases of relatively lower linearity of hydrogen bonds are for complexes **5**, **8** and **9**. It would not be without conceptual benefit, if we mention at this point the well known fact that hydrogen bond strength is directly related to linearity of its angle, and vast majority of examples in crystal structure data show that X,Y pairs tend to align themselves in linear fashion.

More interesting in these optimised structures is location of proton involved in hydrogen

bond. These hydrogen bonds are an aspect of acid-base equilibrium:



The position of proton is certainly dependent on ΔpK_a , the difference of pK_a values of donor and acceptor atoms in solution phase, or ΔPA , the difference of proton affinities of the same in gas phase.^{173–177} These values are zero in case of strong and symmetrical hydrogen bonds between homonuclear donor–acceptor pairs, but more usually like in present case, proton lies closer to more basic atom of the pair. Because of their anionic nature, vanadate oxygen atoms can be anticipated to have higher basicity, so in complexes of vanadate with imidazole and methylamine, HB proton is covalently bonded to vanadate oxygen atom, resulting into neutral hydrogen bonded species. On the other hand for complexes of tetrahedral vanadate species (**3** and **4**), nitrogen atoms of guanidinium cation prove to be too basic to let the HB proton covalently bond with oxygen atoms of vanadate. For the adduct of guanidine with TBP vanadate (**6**) this is not the case, and one of HB proton prefers to form covalent bond with oxygen atom of vanadate. Interestingly, proton from guanidinium is transferred to oxygen atom of V–OH rather than V=O entity.

Benchmarks on energies of small model complexes

In order to calculate HB energies with supermolecular approach while using DFT, it is always necessary to compare the performance of DFT method with more reliable *ab initio* methods. Although these days hybrid functionals like B3LYP are increasingly being relied upon for calculation of HB energies, the MP2 level of theory remains the true benchmark. In order to test the pure density functionals with Slater type basis functions as implemented in ADF, we performed calculations for a number of selected complexes at MP2/6311++G** and B3LYP/6-311++G** levels of theory. The HB energies at different levels of theory are listed in Table 4.2. and in general, DFT tends to overestimate the HB strength compared

Table 4.2: BSSE corrected HB energies (kcal mol^{−1}) for selected complexes at different DFT and *ab initio* levels of theory. Aqueous dielectric constant of 78.34 used for COSMO effects.

	MP2	B3LYP	ADF-BP	ADF-PBE	ADF-BP	ADF-PBE
	6-311++G**	6-311++G**	TZ2P	TZ2P	TZ2P(COSMO)	TZ2P(COSMO)
1	−14.3	−15.7	−16.0	−17.1	−14.6	−15.7
2	−23.5	−26.7	−26.6	−27.6	−19.6	−20.5
3	−104.5	−114.0	−117.3	−118.7	−9.3	−10.8
4	−109.6	−112.6	−114.6	−116.2	−9.0	−10.6
5	−9.8	−10.5	−10.4	−11.9	−8.5	−10.1
6	−22.6	−27.8	−28.6	−30.1	−14.5	−16.1
7	−9.4	−10.0	−10.0	−11.2	−8.4	−9.6

to MP2 energies, a trend which is minimal for hybrid B3LYP functional. It was satisfying for us to find that mainstay of our calculations, the pure functionals with Slater type basis functions (ADF) predict the HB energies not far from MP2/6-311++G** energies. Among the pure functionals we heed to Hobza’s advice¹⁸⁴ and choose PBE functional for the study of larger systems. As for actual HB strengths of complexes listed in Table 4.2, the energies of all the complexes except **3** and **4** lie in typical HB energies range, of 3-40 kcal mole⁻¹. The large HB energies for complexes **3** and **4** are partly due to the fact that there are two hydrogen bonds involved, but even with this consideration average HB energy per hydrogen bond exceeds the commonly accepted limit for strongest of hydrogen bonds. This clearly indicates towards large ionic interactions involved in the ion pair of guanidinium cation and vanadate anion. Similar high HB energies have been reported in literature for (guanidinium : sulfate) complexes.²¹⁶

The solvent effect of water is evaluated by use of COSMO (dielectric constant=78.39) in conjunction with supermolecular approach to HB energies for these complexes. Resulting values given in Table 4.2 show an interesting outcome. Since COSMO solvent environment stabilises individual HB partners more than HB adducts, the HB energies are in general slightly lower. This is in line with commonly held view that polar environment reduces hydrogen bond strengths. But this effect is dramatically high in case of ion pair complexes **3** and **4**, where aforementioned unusually high HB energies are reduced to those typical of ordinary hydrogen bonds. This may be the result of neutralising of charges on HB partners in presence of dielectric environment and thus removal of excessive ionic interaction between them in their HB adducts.

For both gas phase values and those in presence of dielectric medium, the tetrahedral vanadate shows a contrast in O–H···N hydrogen bond formed with CH₃NH₂ and imidazole (complexes **1** and **2** respectively) in terms of complexation energy. The (imidazole : vanadate) complex (structure **2**) shows around 10 kcal mol⁻¹ and 5 kcal mol⁻¹ stronger complexation in gas and dielectric media respectively, in comparison to (CH₃NH₂ : vanadate) complex (structure **1**). The effects due to formal charge should be similar as complexing components and their adduct are neutral in both cases. Apparent difference between two hydrogen bonds are: One, N acceptor atom in **2** is part of aromatic system while in **1** a methyl group is attached to it. Two, hydrogen bond donating oxygen atom in **2** belongs to a coordinated water molecule, while in **1** it is coordinated hydroxyl group. The transformation of vanadate monomer into TBP geometry (**5** and **7**) equalises its interaction with CH₃NH₂ and imidazole acceptors as seen by HB energies for **5** and **7**.

Since dielectric medium cancels ionic interactions, as seem to be present in **3** and **4**, the HB energies with inclusion of COSMO effects allows to compare the behaviour of guanidinium in these complexes with CH₃NH₂ and imidazole. It turns out that two hydrogen bonds of guanidinium with tetrahedral vanadate are weaker than the single hydrogen bonds

	$\delta\rho_C$	$\delta\nabla_C^2$	δG_C	δV_C
B3LYP/6-311G**	0.0019	0.0036	0.0011	0.0019
B3LYP/6-31+G**	0.0011	0.0084	0.0058	0.0114
B3LYP/6-311++G**	0.0016	0.0053	0.0015	0.0019
ADF-BP/TZP	0.0023	0.0176	0.0053	0.0064

Table 4.3: Root mean square ($\delta^p = \sqrt{\frac{1}{n} \sum_i^n \Delta(p_i)^2}$) of difference (Δp) of topological properties (a.u.) from MP2/6-311++G** values at different levels of theory.

in **1** and **2**, in presence of COSMO environment. On the other hand TBP vanadate interacts strongly with guanidine (**6**) in comparison with CH_3NH_2 (**5**) and imidazole (**7**) both in presence and absence of COSMO environment.

QTAIM analysis

The analysis of hydrogen bonds in small complexes between two HB partners in terms of Bader’s QTAIM approach is produced here. The bond critical points (BCP) for hydrogen bonds are located and four local quantities at these points are reported. These are: electron density at BCP (ρ_C), Laplacian of electron density at BCP ($\nabla^2\rho_C$), (electronic) Lagrangian kinetic energy density at BCP (G_C) and electronic potential energy density at BCP (V_C). The values of these quantities for small systems by using DFT electron density at different levels of theory were benchmarked against those calculated with electron density derived from MP2/6-311++G** wave function. The root mean square difference between DFT and MP2 values of these quantities for ten hydrogen bonds in complexes (**1** to **7**) are listed in Table 4.3 and agreement of DFT values is acceptably good with MP2 values. The QTAIM parameters for complexes in Fig. 4.3 calculated with electron density obtained at B3LYP/6-311G** level of theory are listed in Table 4.4. The values of ρ_C are higher than Popelier criteria range and are indicative of the strength of interaction. The Laplacian of electron density at BCP ($\nabla^2\rho_C$) being positive for all listed hydrogen bonds, confirms that these interactions are essentially electrostatic in nature. For complexes **3** and **4**, $\nabla^2\rho_C$ values are higher than suggested by Popelier criteria, showing that depletion of electronic density at BCP is atypically high. It has to be kept in mind that **3** and **4** are ion pairs and (\pm)CAHB is expected to be in play. Finally, despite having a positive Laplacian at BCP, the total electronic density at BCP ($H_C = G_C + V_C$) is dominated by potential energy and its sign is invariably negative for all listed hydrogen bonds, indicating that covalent character is present without exception. On the basis of ρ_C values, imidazole- $\text{N}\cdots\text{H}-\text{O}$ bond in **2** appears to be strongest with a value 0.092 a.u. In comparison, $\text{CH}_3\text{NH}_2\cdots\text{H}-\text{O}$ bond in **1** has a value of ρ_C equalling 0.072 a.u. This is in line with respective strengths of these hydrogen bonds as seen by their HB energies and geometrical parameters. Values of $\nabla^2\rho_C$ for these two complexes show similar behaviour in reverse order: i.e. $\nabla^2\rho_C$ for **1** is higher than that for **2** indicating a stronger electrostatic pull of nuclei on HB BCP in case of **1**. Now looking at values of H_C for these, it is -0.04 a.u for **2** while -0.022 a.u. for

Table 4.4: QTAIM parameters (a.u) calculated by using electron density obtained at B3LYP/6-311G** level, for structures in Fig. 4.3.

		ρ_C	$\nabla^2\rho_C$	G_C	V_C	H_C
1		0.070	0.094	0.045	-0.067	-0.022
2		0.092	0.066	0.056	-0.096	-0.040
3	(N1,O1)	0.061	0.148	0.050	-0.062	-0.013
3	(N2,O2)	0.078	0.148	0.061	-0.086	-0.024
4	(N1,O1)	0.089	0.143	0.069	-0.102	-0.033
4	(N2,O2)	0.052	0.144	0.043	-0.050	-0.007
5		0.048	0.101	0.033	-0.041	-0.008
6	(N1,O1)	0.072	0.099	0.048	-0.071	-0.023
6	(N2,O2)	0.040	0.129	0.034	-0.036	-0.002
7		0.053	0.107	0.038	-0.048	-0.011

1. In other words covalent character is stronger in **2**, and perhaps this interplay between electrostatic and covalent interactions tilts favourably towards **2** which shows larger HB energy as discussed previously. In case of **3** and **4**, both the values of $\nabla^2\rho_C$ and H_C for both hydrogen bonds show strong electrostatic pull and presence of covalent character.

The complexes of TBP vanadate show the HB QTAIM parameters indicative of relatively weaker hydrogen bonds as their ρ_C values are reduced in comparison to those for complexes of tetrahedral vanadate. HB interaction in complexes **5** and **7** in comparison to corresponding hydrogen bonds in tetrahedral vanadate category (**1** and **2** respectively) present an interesting situation. The ρ_C values are lower while $\nabla^2\rho_C$ values are higher in TBP case which can be interpreted as increase in electrostatic attraction. On the other hand covalent character in terms of negative H_C is relatively reduced in TBP case, and recalling from the discussion of geometrical parameters where it was shown that in TBP case donor-acceptor atoms lie at longer distances, it makes sense to infer that elongation of donor-acceptor distance is accompanied by decrease in covalent character, but electrostatic pull is maintained as it is able to operate at longer distances. The two hydrogen bonds in **6** not only maintain a high $\nabla^2\rho_C$, but one involving (N1,O1) pair also shows H_C equalling -0.023 a.u., the most negative value of this quantity in TBP category.

4.4.2 Effect of additional HB donors and implications for resting state

Geometries

In order to move systematically from small model complexes discussed in previous subsections to more complex systems resembling enzyme active site, a few more HB adducts were optimised with added number of HB partners. Resulting geometries are presented in Fig. 4.4 and corresponding HB geometrical parameters are listed in Table 4.5. The cooperative effects of additional HB interactions are clearly demonstrated by proton transfer along certain hydrogen bonds. The O1-H...N1 hydrogen in **6** (Fig. 4.3) is transformed

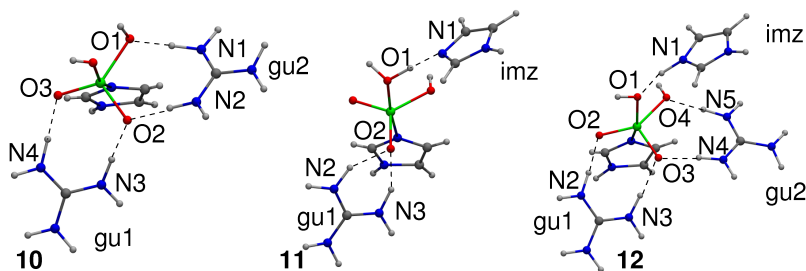


Figure 4.4: Optimised structures of some more model HB complexes, with increased complexity. See Table 4.5 for optimised HB geometrical parameters.

into $O1 \cdots H-N1$ in **10** (Fig. 4.4). Similarly the hydrogen bond between nitrogen atom of imidazole and apical oxygen atom of TBP vanadate moiety ($O-H \cdots N$) in **7** is gradually transformed into $O1 \cdots H-N1$ in **12** through **11** (Please note the gradual shifting of protonic distance from N and O atoms in the sequence **7**, **11**, **12** ; Tables 4.1 and 4.5). This is a demonstration of sufficient neutralisation of negative charge on oxygen atom and resulting modification of relative proton affinities of donor and acceptor atoms due to donation of additional hydrogen bonds by the guanidinium cations, so that acid–base equilibrium (Eq. 4.5) in section 4.4.1 is shifted towards the right side. The transformation along the sequence **7**, **11**, **12** is accompanied by shortening of $N \cdots O$ distance ($N1 \cdots O1$ in **11** and **12**), which is found as 271.1 pm for **7**, 256.6 pm for **11** and 255.9 pm for **12**. It is worth mentioning that in actual VCPO active site this distance is dictated by the limited flexibility of imidazol(ium) moiety of His496. Interestingly similar change of heavy atom distance does not occur in proton transfer involving complexes **6** and **10**.

The effect of hydrogen bond between imidazolium and apical oxygen atom on the hydrogen bonds with guanidinium cations in equatorial plane of TBP can be observed by comparison of calculated geometrical parameters of **10** with those of **12**. The $O \cdots N$ distances for hydrogen bonds in equatorial plane are elongated in **12**, and consequently proton

		$R_{O \cdots N}$	$r_{O \cdots H}$	$r_{N \cdots H}$	\angle_{OHN}
10	(N1,O1)	262.9	154.4	108.6	177.7
10	(N2,O2)	274.8	169.8	105.1	177.2
10	(N3,O2)	272.1	166.3	105.8	178.6
10	(N4,O3)	269.0	163.1	106.1	177.2
11	(N1,O1)	256.6	107.4	149.5	174.1
11	(N2,O2)	276.3	182.8	104.3	147.2
11	(N3,O2)	264.7	167.0	105.2	152.3
12	(N1,O1)	255.9	146.5	110.8	167.6
12	(N2,O2)	276.4	171.9	104.6	176.5
12	(N3,O3)	281.7	177.6	104.1	178.8
12	(N4,O3)	276.3	171.9	104.6	175.1
12	(N5,O4)	271.6	165.6	106.0	176.7

Table 4.5: Hydrogen bond geometrical parameters of complexes in Fig. 4.4, optimised at ADF-BP/TZ2P level. All distances in pm and angles in degrees.

Table 4.6: Gas phase supermolecular energies at ADF-PBE/TZ2P level (kcal mol⁻¹) and its decomposition in two-body/many-body terms (Eq. 4.6) for complexes in Fig. 4.4.

	$\Delta E^{V,X}$	BSSE	i	$\Delta E^{V,i}$	$\Delta E^{V+i,X-i}$	$\Delta E^{i,X-i}$	BSSE ^{V,i}
10	-223.9	1.6	gu1	-119.2	-55.5	49.2	0.8
			gu2	-122.4	-52.3	49.2	0.9
			imz	-17.2	-49.1	-3.4	0.6
11	-62.9	1.1	gu1	-39.6	-26.7	-3.4	0.5
			imz	-116.5	-101.5	95.3	0.6
			gu1	-114.9	-109.6	88.8	0.7
12	-313.3	2.1	gu2	-118.0	-89.9	105.4	0.8

to acceptor (H···O) distances also exhibit elongation, while H–N distances shrink slightly for these hydrogen bonds.

The main lesson from this discussion is that combined interactions of several HB donors with vanadate species are markedly in contrast with cases where only individual interactions exist. Specially, the protonation state of vanadate can be easily manipulated by the extent to which multiple interactions are available. At physiological *pH*, vanadate is known to exist in monoanionic form (i.e. diprotonated), and as shown above — its TBP geometry can easily gain additional proton to form neutral species (**6** and **7**), but in presence of more of strong HB donors its ability to do so is severely curtailed. This means that in such cases relatively higher hydronium ion concentrations in aqueous solution would be necessary to form neutral vanadate species.

Gas phase HB energies

The cooperativity of hydrogen bonds reported in previous subsection is considered here from energetical point of view. The HB interaction strengths for oligomers **10**, **11** and **12** are reported as total interaction energy, $\Delta E^{V,X}$, between vanadate V and collective fragment X which is composed of all other HB partners $i = \text{gu1, gu2, imz}$ (as may be the case for each structure in Fig. 4.4). The major concern is to evaluate the individual contribution to $\Delta E^{V,X}$ from i th HB partner of vanadate. Unfortunately in supermolecular approach, it is not possible to write $\Delta E^{V,X}$ unambiguously as the sum of i additive terms $\Delta E^{V,i}$ i.e. two-body interaction terms for all (V, i) pairs. However the standard way of writing interaction energy of supramolecular adduct (Eq. 4.2) does allow to suitably split it into terms involving one-body, many-body etc. fragments,¹⁸⁹ which for present purpose is given as :

$$\Delta E^{V,X} = E_{V+X} - E_V - E_X = \Delta E^{V,i} + \Delta E^{V+i,X-i} - \Delta E^{i,X-i} \quad (4.6)$$

It is important to note that this equation is another form of Eq. 4.2 for complexes with more than two interacting molecules and total interaction energy of vanadate with the

rest of adduct is expressed in terms of interaction within appropriate subsystems of the total adduct (cf. page 54). The notations used for superscripts in respective subsystem interaction terms relates to the way in which whole adduct is decomposed into hydrogen bonding fragments, i.e. whole adduct is composed of vanadate (V), and the collection (X) of remaining fragments. The subsystem X is composed of all the non-vanadate fragments i . $V+i$ stands for the fragment composed of V and a particular i , and $X-i$ for X after the exclusion of that particular i . The calculated values of $\Delta E^{V,X}$ and its fragmental terms according to Eq. 4.6 are listed in Table 4.6 for **10**, **11** and **12**. Each complex is fragmented in all possible ways so that interaction in each pair (V, i) has the chance to appear in one of the sums. In this fashion, $\Delta E^{V,i}$ is taken as a measure of i th (V, i) contribution to total interaction with vanadate $\Delta E^{V,X}$. Please note how the fragmental terms sum up to same $\Delta E^{V,X}$ for every individual HB partner i . The BSSE to $\Delta E^{V,X}$ and two-body term $\Delta E^{V,i}$ are also tabulated.

As noted before in case of (1:1) complexes, the two-body terms in present case can also be categorised into those arising from ion-pair like interaction with very high values, and the others with the values falling into normal range of energies typical of hydrogen bonds. It would be useful to invoke at this point the Gilli's terminology, in which one of the classes of strong hydrogen bonds involving charged HB partners are named as charge assisted hydrogen bonds (CAHB). Coming to investigate the HB cooperativity, comparison of HB energies in small (1:1) complexes (Table 4.2) to relevant two-body terms in oligomers is presented and it can be easily seen that the changes in the HB geometry due to additional hydrogen bonds as described in previous subsection are also accompanied by changes in HB energy.

The ADF-PBE/TZ2P HB energy for **6** is $-30.1 \text{ kcal mol}^{-1}$ while the $\Delta E^{V,X}$ value for **10** is $-222.3 \text{ kcal mol}^{-1}$ after BSSE correction. In other words, about seven fold stabilisation is gained by the interactions of one additional guanidinium cation, but if we also consider the repulsive term $\Delta E^{i,X-i}$, this gain is reduced to nearly six fold. The sum of ADF-PBE/TZ2P HB energies of **6** and **7** is $-41.3 \text{ kcal mol}^{-1}$ whereas the value of $\Delta E^{V,X}$ for **11** is $-61.8 \text{ kcal mol}^{-1}$ after BSSE correction. This amounts to about 20 kcal mol^{-1} gain of stabilisation. Finally, the phenomenon of very high supramolecular stabilisation of **12** reflected in its much larger $\Delta E^{V,X}$ value compared to the average $\Delta E^{V,X}$ for **10** and **11** is again due to its ion-pair character.

On the other hand, the (BSSE corrected) two-body term $\Delta E^{V,i}$ in **10** is $-118.4 \text{ kcal mol}^{-1}$ for HB partner labelled as gu1 and $-121.5 \text{ kcal mol}^{-1}$ for gu2, compared to $-30.1 \text{ kcal mol}^{-1}$ for guanidine in **6** (Table 4.2). This high stabilisation is indicative of (\pm) charge assistance to hydrogen bonds after ion-pair formation. This effect is far less pronounced for contribution from gu1 if we go from **6** to **11**, where no ion-pair formation occurs and only charge assistance arises from +CAHB due to guanidinium cation in **11**. Furthermore,

cooperative stabilisation imparted by +CAHB from gu1 cation is larger than that by simple hydrogen bond from neutral imidazole (imz) in **11** (Table 4.6) over the interaction energies for (1:1) complexes **6** and **7** respectively (Table 4.2). In comparison, charge assistance to two-body terms for gu1, gu2 and imz is again very high in **12** because of ion-pair like interaction. Another factor apart from lack of ion-pair formation contributing to less pronounced cooperativity of gu1 in **11** would be the fact that gu1 in **11** is not forming perfectly linear hydrogen bonds as reflected by the \angle_{OHN} values for this complex in Table 4.5.

Aqueous (COSMO) effects on HB energies

The inclusion of aqueous solvent effects through COSMO methodology causes the calculated supermolecular interaction energies to loose all the charge assistance observed in gas phase. This is seen in COSMO energy values produced in Table 4.7 in comparison to similar quantities in Table 4.6. It should not come as surprise as high dielectric medium is expected to better solvate the charged species and hence the consequent loss of higher electrostatic interaction between opposite charges. For instance the two-body term for neutral imidazole ($\Delta E^{\text{V},i}$, $i = \text{imz}$) in **11** is $-17.2 \text{ kcal mol}^{-1}$ and $-15.9 \text{ kcal mol}^{-1}$, without and with COSMO effects respectively. The similar values for charged HB partners in all complexes show a decrease in their two-body terms by an order of magnitude due to solvation by COSMO. The COSMO data also gives an opportunity to look if any cooperative effects exist which are clean of any contribution from charge assistance. This is done by comparing COSMO interaction energies for (1:1) adducts reported in Table 4.2 and relevant values in Table 4.7. First taking the comparison of **6** and **10**, it appears that there is actually anti-cooperativity at work in presence of solvation, as $\Delta E^{\text{V},\text{X}}$ for **10** is less than double of ADF-PBE-COSMO/TZ2P interaction energy for **6**. Similarly the sum of interaction energies for **6** and **7** is greater than $\Delta E^{\text{V},\text{X}}$ for **11**. Similar consideration holds for **12** in relation to individual interactions in corresponding (1:1) complexes. In connection with our discussion in Sec. 4.4.2 about combined effect of several HB donors over protonation state of vanadate, question may be raised that observed offsetting of cooperativity by solvent

Table 4.7: COSMO (aqueous phase) supermolecular energies (kcal mol^{-1}) and its decomposition in two-body/many-body terms (Eq. 4.6) for complexes in Fig. 4.4.

	$\Delta E^{\text{V},\text{X}}$	BSSE	i	$\Delta E^{\text{V},i}$	$\Delta E^{\text{V}+i,\text{X}} - i$	$\Delta E^{i,\text{X}-i}$	BSSE $^{\text{V},i}$
10	-22.3	0.9	gu1	-11.3	-11.3	-0.3	0.5
			gu2	-13.6	-8.9	-0.3	0.6
			imz	-15.9	-6.4	-1.2	0.6
11	-21.1	1.0	gu1	-5.7	-16.5	-1.2	0.3
			imz	-13.4	-18.1	1.8	0.4
			gu1	-10.3	-22.7	0.3	0.5
12	-33.3	1.3	gu2	-12.6	-18.0	2.3	0.6

Table 4.8: QTAIM parameters (a.u.) calculated by using electron density obtained at B3LYP/6-311G** level, for oligomeric structures in Fig. 4.4.

		ρ_C	$\nabla^2\rho_C$	G_C	V_C	H_C
10	(N1,O1)	0.069	0.147	0.054	-0.072	-0.018
10	(N2,O2)	0.045	0.133	0.038	-0.042	-0.004
10	(N3,O2)	0.049	0.138	0.041	-0.047	-0.006
10	(N4,O3)	0.053	0.144	0.044	-0.052	-0.008
11	(N1,O1)	0.088	0.071	0.055	-0.092	-0.037
11	(N2,O2)	0.035	0.113	0.029	-0.029	-0.001
11	(N3,O2)	0.049	0.146	0.042	-0.047	-0.005
12	(N1,O1)	0.083	0.149	0.064	-0.091	-0.027
12	(N2,O2)	0.042	0.131	0.035	-0.038	-0.003
12	(N3,O3)	0.037	0.120	0.031	-0.032	-0.001
12	(N4,O3)	0.042	0.131	0.036	-0.038	-0.003
12	(N5,O4)	0.051	0.140	0.042	-0.049	-0.007

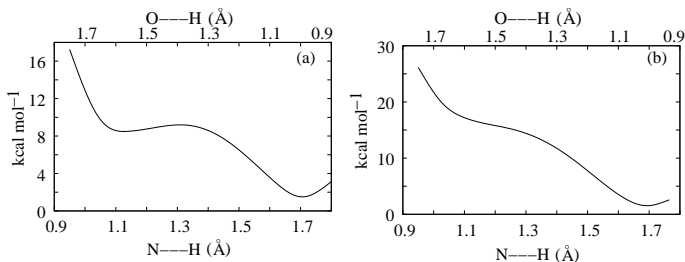
can also reverse the reported combined HB effect on protonation state. We want to point towards the possibility that hydrogen bonding of solvent molecules with oxoanionic acceptor sites on vanadate, in their competition with other donors for HB donation, may rather join hands to reduce the basicity of oxoanionic sites and fix its protonation state. However, the suitable alteration in pH can always shift the position of protons involved in HB, thus also changing the protonation state of vanadate.

QTAIM analysis of oligomers

The effect of additional HB partners in terms of QTAIM parameters is performed in this subsection. This is done by comparison of values for oligomeric structures in Table 4.8 with those for analogous hydrogen bonds in (1:1) complexes in Table 4.4. To start with, the structures **6** and **10** are compared. By keeping in mind that gu2 is analogous to guanidine in **6** in its orientation with respect to TBP vanadate moiety, the effects of additional HB partner gu1 can be seen on interaction of gu2. The (N1,O1) hydrogen bond in **6** and **10** (gu2) differ in the fact that nitrogen and oxygen atoms has a switched donor/acceptor role in two structures. This results in an increase of 0.048 a.u. in $\nabla^2\rho_C$ value for **10**. It is also accompanied by slight change in H_C (from -0.023 a.u. to -0.018 a.u.). These changes manifest increase in electrostatic attraction and slight decrease in covalent character. The (N2,O2) hydrogen bond donated by gu2, also shows slight gain of strength and electrostatic character in comparison to (N2,O2) bond in **6**.

To see the behaviour of imidazole-N \cdots H-O hydrogen bond, the QTAIM parameters for N1 \cdots O1 hydrogen bond can be compared in **7**, **11**, and **12**. In going from **7** to **11**, N1 \cdots H-O1 hydrogen bond witnesses an increase of 0.035 a.u. in ρ_C , a reduction of 0.036 a.u. in $\nabla^2\rho_C$ and change of H_C from -0.01 a.u. to -0.037 a.u. These are significant changes in

Figure 4.5: ADF-BP/TZ2P potential for HB proton in **2** (a) and **7** (b) at $N\cdots O$ of 2.7 Å. The placement of ordinate origin at zero is arbitrary.



terms of increase in strength and covalent character of hydrogen bond, which should not be surprising as geometrical parameters for this hydrogen bond in **11** (Table 4.5) show short $N\cdots O$ (256.6 pm) and $H\cdots N$ distances (149.5 pm) compared to respective values of 271.1 pm and 169.6 pm for **7** (Table 4.1). The transition from **11** to **12** and accompanying proton transfer in (N1,O1) hydrogen bond, witnesses a large increase of $\nabla^2\rho_C$ by 0.078 a.u., signifying electrostatic interaction between positively charged imidazolium and negative vanadate. Covalent character is also maintained albeit with a decrease of 0.01 a.u. in $|H_C|$ compared to that in **11**.

The effect of imidazolium- $NH\cdots O$ hydrogen bond on interaction of two guanidinium cations can be seen by comparison of relative QTAIM parameters in **10** and **12**. It is obvious that absolute values of all the quantities decrease for each of guanidinium- $\cdots O$ hydrogen bond implying a weakened interaction in presence of apical imidazolium- $NH\cdots O$ interaction in TBP geometry. This is probably because neutralisation of vanadate charge by imidazolium leads to decreased electrostatic attraction between vanadate and guanidinium cations.

Potential energy surface of im- $N\cdots O$ hydrogen bond

The proton transfer along the imidazole- \cdots oxygen HB induced by additional hydrogen bonds on the other acceptor sites on vanadate species as observed in sequence of complexes **7**, **11** and **12** requires more closer attention because such ease in proton shift manipulation signals implications for role of analogous hydrogen bond involving His404 in VCPO active site. In this respect the protonation state of (A,B) pair in $A-H\cdots B$ hydrogen bond involving apical oxygen atom and imidazole in **7** may have repercussions for its enzymatic analogue. To this end the ADF-BP/TZ2P total energies of **7**, **8** and **9** are first presented. It was found that formation of **8** and a free proton starting from **7** is 329.1 kcal mol⁻¹ endothermic while formation of a free proton and **9** starting from **7** is endothermic by 353.5 kcal mol⁻¹. This points towards strong favourability for **7** in contrary to some of proposals²¹⁷ which suggest an *active site resting state* akin to **9**. Taking **7** as preferred model for active site, the ADF-BP/TZ2P potential for proton movement along the $O\cdots N$ hydrogen bond at a fixed heavy atom distance (i.e. $N\cdots O$ distance) of 2.7 Å, along with that for **2** is given in Fig. 4.5. This reveals the effects of TBP and tetrahedral vanadate geometries

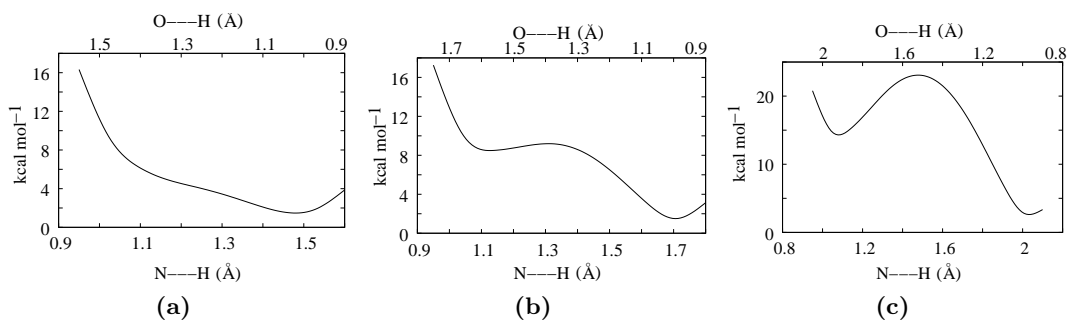


Figure 4.6: ADF-BP/TZ2P potential for HB proton in **2** at $\text{N}\cdots\text{O}$ distances (a) 2.55 Å, (b) 2.7 Å, (c) 3.05 Å. The placement of ordinate origin at zero is arbitrary.

on the hydrogen bond under consideration. Complex **2** shows an unsymmetrical two-well potential, while the potential for **7** exhibits position of low lying potential-well i.e. close to oxygen atom, similar to that for **2**. Somewhat flatter potential towards nitrogen end for **7** does not pass through any minimum. Moreover the depth of low lying potential-well for **7** is double in comparison to that for **2**. Both these observations indicate that TBP geometry of vanadate makes apical oxygen atom more basic compared to nitrogen atom of (hydrogen bonding) imidazole, so that oxygen atom preferably retains the proton. With this difference between **2** and **7** in consideration, and taking advantage of smaller size of former structure, further analysis of this potential is carried.

In Fig. 4.6 the effect of fixed heavy atom (i.e. N, O) distance for **2** is reported and is expectedly observed that at shortest heavy atom distance the barrier between the potential-wells vanishes, while at longest distance it rises considerably. The $\text{N}\cdots\text{O}$ distance of 2.7 Å is important in the fact that it is close to the value observed for ($\text{N}_{\text{His404}}\cdots\text{O}_{\text{van}}$) contact in x-ray crystal structure of VCPO. The effect of additional hydrogen bonds donated to remaining HB acceptor oxygen atoms of vanadate, were considered by adding more HB donor guanidinium cations to structure **2**. The potential for HB proton in imidazole \cdots vanadate hydrogen bond, calculated at fixed heavy atom distance of 2.7 Å for resulting structures is

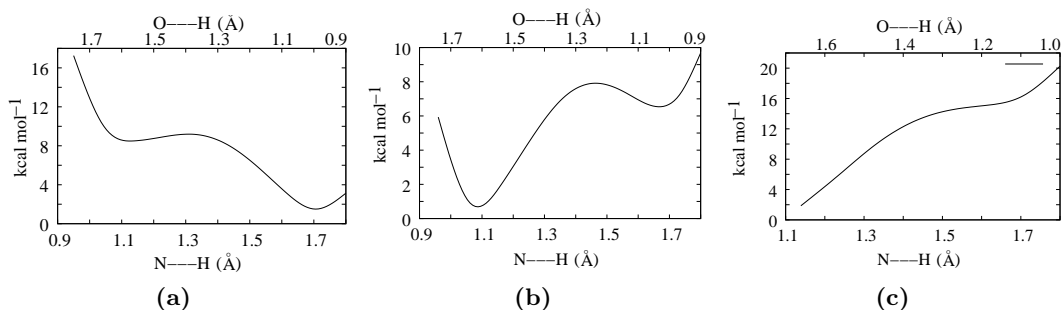


Figure 4.7: ADF-BP/TZ2P potential for HB proton in (a) complex **2**, (b) **2** with one and (c) two additional guanidinium HB donors at $\text{N}\cdots\text{O}$ distance of 2.7 Å. The placement of ordinate origin at zero is arbitrary.

produced in Fig. 4.7b, c. The corresponding potential for **2** is also given for comparison (Fig. 4.7a). With one additional guanidinium cation, the symmetry of double-well potential is reversed and role of N (imidazole) and O is exchanged to that of donor and acceptor respectively. With two additional guanidinium cations as HB donors, this effect receives further enhancement and the potential-well lying towards oxygen end becomes flattened (i.e. a definitely complete proton transfer from O to N). This is a clear indication that in the presence of additional hydrogen bond donors, vanadate oxygen atom can not retain its basicity sufficiently enough to deprotonate the imidazolium HB donor. This behaviour of tetrahedral vanadate (**2**) is expected to extrapolate to TBP vanadate (**7**) after taking their differences (Fig. 4.5) into account. The shallowness of potential for **7** at positions near the nitrogen atom (Fig. 4.5b) means that basicity of O relative to N is higher in TBP geometry than in tetrahedral one. In other words, for TBP geometry more of additional hydrogen bonds would be needed to induce the proton transfer from vanadate to imidazole. In enzyme active site hydrogen bonds are abundantly donated to oxygen atoms of TBP vanadate, with the implication that resting state is expected to have an apically coordinated hydroxyl which receives hydrogen bond from positively charged His404. Moreover, any disruption in hydrogen bonding network of active site can easily induce proton transfer from His404-H⁺ to apical oxygen atom of vanadate.

4.4.3 Analysis of protein-cofactor HB interactions

In this section the methodology employed to study the HB complexes as described so far is extended to x-ray crystal structure based (Fig. 4.8) *optimised geometries* of active site as detailed in Fig. 4.9. The name of each structure self evidently denotes the (enzyme) x-ray crystal structure from which the positions of heavy atoms of hydrogen bonding amino acids are derived. In this case the CPO refers to crystal structure of VCPO isolated from *C. Inaequalis*,²² BPO to crystal structure of VBPO isolated from *A. Nodosum*,²³ and CPOM360, CPOM404 refer respectively to Arg360Ala and His404Ala mutants of VCPO²¹⁸ derived from *C. Inaequalis*. Since the positions of active site amino acids are largely dictated by secondary protein structure in immediate vicinity to active site pocket, by freezing the heavy atoms of side chains of hydrogen bonding residues we ensured that essential information from individual crystal structures was retained while optimising the positions of all the other atoms (i.e. all the added protons, and atoms belonging to vanadate and imidazole moiety of His496). The side chains of arginine and lysine residues are respectively approximated as guanidinium cations and methylamine/ammonium groups. The whole polypeptidal chain from Ser402 to His404 (as numbered in VCPO, but this assertion also refers to corresponding residues in VBPO), was included while truncating on the ends not relevant to active site. Other distinctions between the structures are different number of protons as should be evident from Fig. 4.9.

Protonation state of calculated active site structures

The total energies show that in full active site (i.e. one involving all the active site amino acid residues in native enzyme as opposed to mutated varieties), prefer a monoanionic vanadate cofactor. This can be observed from total energies of dissociating a proton from **CPO1**, **BPO1**. Formation of **CPO2** and a free proton from **CPO1** is endothermic by $155.0 \text{ kcal mol}^{-1}$, while formation of **CPO3** and free proton from **CPO1** is endothermic by $159.1 \text{ kcal mol}^{-1}$. Similarly formation of **CPO4** and a proton from **CPO1** is endothermic by $158.8 \text{ kcal mol}^{-1}$. The same energy relation holds for **BPO1** \rightarrow **BPO2** + H^+ with a value of $+150.1 \text{ kcal mol}^{-1}$. The fact that **CPO2** is much higher in energy than **CPO1** is confirmation inside the active site, of a result already computationally observed for bare species **7** and **9** (Sec. 4.4.2). This again goes contrary to active site proposal in favour of **CPO2**.²¹⁷ It is desirable to mention that attempts to optimise **CPO1** with proton from imidazolium moiety of His404 transferred to (apical) hydroxyl oxygen atom of TBP cofactor always resulted back into structure **CPO1**. It is interesting to note that optimised geometries derived from VBPO crystal structure (**BPO1** and its conjugate **BPO2**), both have a monoanionic vanadate species, as the proton transfer from Lys to O3 accompanies the proton dissociation process **BPO1** \rightarrow **BPO2**.

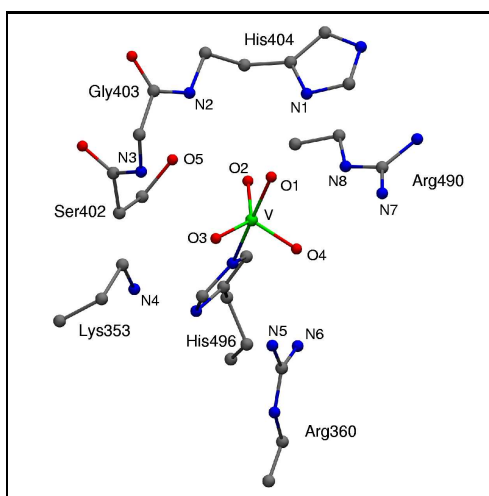


Figure 4.8: Active site of VCPO as revealed by x-ray crystal structure, and schematic numbering of HB donor/acceptor atoms used in discussion of the optimised structures presented in Fig. 4.9.

On the other hand corresponding VCPO active site pocket is able to contain a dianionic vanadate species (**CPO3**), although an isoelectronic species (**CPO4**) arising as a result of proton transfer from His is isoenergetic to it. With considerable curtailment of hydrogen bonds to vanadate, as in **CPOM404-1**, and **CPOM404-2**, vanadate species favours a neutral state, either as a result of proton transfer from Lys or if apical oxygen atom is doubly protonated, in which case proton transfer from Lys is also prevented. The former scenario (proton transfer from Lys) may be reasonable to assume in basic medium where Lys may be acting as a local source of proton for vanadate. The later case (doubly protonated apical oxygen atom of vana-

date) may be typical of acidic medium. Moreover the proton dissociation from **CPOM404-2** to produce **CPOM404-1** and a proton is endothermic by $183.2 \text{ kcal mol}^{-1}$. An important contrast between **CPOM404** and **CPOM360** models is lack of proton transfer in later, either from His or Lys, signifying the extent of curtailment of HB environment sufficient for inducing proton transfer.

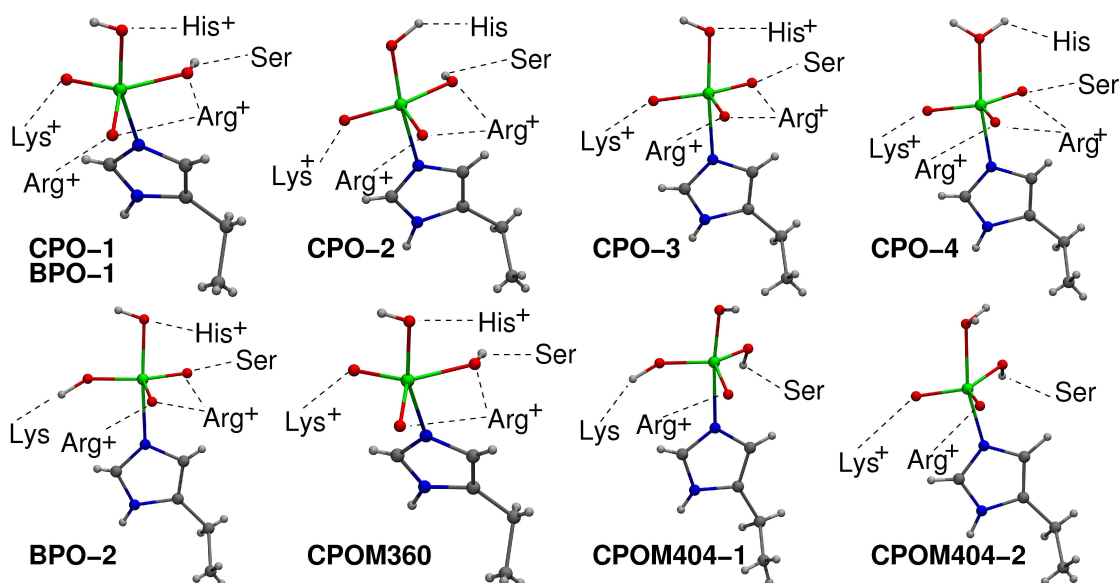


Figure 4.9: Representation of optimised structures of various models of VHPO active site (Fig. 4.8). These structures are variations on the basic structure in Fig. 4.8 showing the coordinated cofactor in relation to amino acids schematically. Gly and its peptidal linkage to His (404 in case of VCPO) and Ser are present in all optimised structures (except in **CPOM404** structures where His404 is absent) but not mentioned here for clarity. Moreover, in structures **CPOM404-1** and **CPOM404-2** residue Arg490 is not part of the model, as it was found not to be in HB distance from cofactor in x-ray crystal structure on which these models are based. See the text for nomenclature.

HB geometries

In description of hydrogen bonding in enzymatic active site the atom numbering scheme presented in Fig. 4.8 will be used. This is started with comparison of HB geometries in VCPO and VBPO crystallographic active site pockets, by using their most stable, isoelectronic optimised structures (Table 4.9). In doing so the amino acids sequence nomenclature for VCPO crystal structure is used which in present discussion applies to corresponding amino acids in VBPO crystal structure also, however the distinction should always be clear from the context.

The parameters of interest listed are usually employed as criteria of HB strengths, and these do reveal the differences between the hydrogen bonds within a structure, and between the analogous hydrogen bonds in two different structures. On the basis of parameter $R_{A...B}$ for **CPO1** the distances between donor/acceptor pair N1,O1 and N4,O3 (i.e. His and Lys donors, respectively) emerge as the shortest ones, followed in shortness by others in this order: Ser \cdots O (O2,O5), Arg490 \cdots O (N8,O4), Arg360 \cdots O (N6,O4), Arg490 \cdots O (N7,O4), Gly \cdots O (N3,O3), Arg360 \cdots O (N5,O4) and finally the longest ones N2,O1 and N2,O2. The two heavy atom pairs with closest N \cdots O distance in above list (N1,O1 and N4,O3), also share a proton with shortest $r_{H...B}$ distance, and a relatively elongated $r_{A...H}$ distance compared to other donor/acceptor pairs. Add to this the fact that these two pairs also exhibit near linear hydrogen bonding angle \angle_{AHB} , and the primacy of these two

Table 4.9: Comparison of optimised hydrogen bond geometrical parameters for **CPO1** and **BPO1**. All distances in pm and angles in degrees.

	$R_{A...B}$		$r_{H...B}$		$r_{A...H}$		\angle_{OHN}	
	CPO1	BPO1	CPO1	BPO1	CPO1	BPO1	CPO1	BPO1
N1,O1	275.7	281.8	169.7	178.5	106.4	105.5	174.6	165.3
N2,O1	332.7	361.8	238.2	303.2	101.9	101.8	153.7	117.7
N2,O2	360.9	381.1	272.6	289.2	-	-	145.1	150.4
N3,O3	307.6	307.0	205.9	205.5	102.2	102.2	172.6	172.1
N4,O3	277.9	261.4	170.6	151.3	107.9	110.2	172.3	176.5
N5,O4	323.8	313.8	238.2	219.6	102.3	102.9	140.6	151.3
N6,O4	286.8	300.2	186.8	203.3	103.5	102.9	161.6	155.7
N7,O4	301.1	296.9	198.3	193.9	103.4	103.3	172.2	174.4
N8,O2	283.4	282.3	179.2	178.0	104.7	104.4	172.7	176.9
O5,O2	283.3	291.2	183.1	192.6	100.5	99.6	175.5	169.7

hydrogen bonds in VCPO active site is instantly recognised. The values of $r_{H...B}$ distances for other A,B pairs in **CPO1** follow nearly similar trend as described for $R_{A...B}$ above. With regard to HB angle parameter \angle_{AHB} , the A,B pairs involving Arg360 (N5,O4 and N6,O4) and N atom of His-Gly peptide linkage (N2,O1 and N2,O2) show the largest deviations from linear 180° value.

Now coming to comparison of these trends in **CPO1** to those in **BPO1**, the striking contrast between the two systems is that positive charges provided by His⁺ and Lys⁺ to stabilise anionic cofactor have more balanced placement relative to respective oxygen acceptor atoms in **CPO1** while in case of **BPO1** a more polarised situation is encountered. This assertion is based on following observations: The difference between the $R_{A...B}$ for His...O HB and Lys...O HB is only 2.2 pm for **CPO1** but 20.4 pm for **BPO1**. Moreover His...O HB in **CPO1** is 6.1 pm shorter than one in **BPO1** while this relation between two systems is reversed for Lys...O HB which is 16.5 pm shorter in **BPO1** compared to that in **CPO1**. This trend is also manifested in values of $r_{H...O}$ for these hydrogen bonds in both systems, which show that for **BPO1**, proton in Lys...O bond lies 27.2 pm closer to acceptor atom compared to the proton in His...O hydrogen bond. Relatively weaker His...O bond in **BPO1** is indicated by loss of linearity in N-H...O angle as reflected by values of this angle.

Other important differences do exist between both structures, one being stronger interaction between Ser and cofactor (O2,O5) in **CPO1** compared to that in **BPO1** as suggested by geometrical parameters for this hydrogen bond given in Table 4.9. Moreover there is closer vicinity of atom N2 to cofactor oxygen atoms O1 and O2 in **CPO1**. However, since N...O distances are too long for these, and NHO angles relatively far from linearity, geometrical criteria alone can not decide the existence of hydrogen bonds between N2 and O1 or O2. All this discussion suggests that in structure **BPO1**, stabilisation of cofactor negative charge by protein environment is heavily dependent upon Lys residue, while stronger

Table 4.10: Comparison of hydrogen bond geometrical parameters for **CPO1** and mutant models **CPOM360**, **CPOM404-1**, and **CPOM404-2** (**CPO** prefix omitted for mutant models in column headings). All distances in pm and angles in degrees.

	CPO1	M360	M404-1	M404-2	CPO1	M360	M404-1	M404-2
	$R_{A...B}$				$r_{H...B}$			
N1,O1	275.7	271.1	-	-	169.7	162.3	-	-
N2,O1	332.7	309.5	447.2	419.9	238.2	212.6	359.5	336.6
N2,O2	360.9	337.6	336.6	330.4	272.6	256.2	236.7	230.8
N3,O3	307.6	295.0	295.0	304.2	205.9	192.9	195.0	203.8
N4,O3	277.9	276.6	251.8	255.5	170.6	170.7	144.2	146.3
N5,O4	323.8	-	288.5	303.9	238.2	-	196.9	213.5
N6,O4	286.8	-	272.2	283.6	186.8	-	175.1	187.4
N7,O4	301.1	280.0	-	-	198.3	176.1	-	-
N8,O2	283.4	275.7	-	-	179.2	171.6	-	-
O5,O2	283.3	276.4	332.2	308.6	183.5	177.2	238.7	209.0
	$r_{A...H}$				\angle_{AHB}			
N1,O1	106.4	108.8	-	-	174.6	176.5	-	-
N2,O1	101.9	102.6	102.1	101.8	153.7	157.0	145.2	140.1
N2,O2	-	-	-	-	145.1	136.0	165.9	165.4
N3,O3	102.2	102.7	102.2	101.9	172.6	171.6	165.3	167.3
N4,O3	107.9	108.8	109.5	110.5	172.3	162.8	165.9	168.1
N5,O4	102.3	-	103.6	103.0	140.6	-	145.7	145.3
N6,O4	103.5	-	104.6	103.5	161.6	-	152.5	153.1
N7,O4	103.4	104.7	-	-	172.2	170.1	-	-
N8,O2	104.7	105.4	-	-	172.7	168.7	-	-
O5,O2	100.5	100.2	98.6	99.7	175.5	170.1	157.9	176.4

contributions from His404 and Ser in **CPO1** compared to their counterparts in **BPO1**, make **CPO1** less reliant on Lys. Perhaps this is the reason that cofactor could be optimised as dianionic species in VCPO pocket (structure **CPO3**), while in VBPO pocket (**BPO2**) this could not be achieved as proton transfer from Lys to atom O4 inevitably happens.

The absence of certain amino acid HB donors, as in crystal structures of site mutated VCPO enzyme can possibly shed light on how these modify the interactions of other residues. The structural changes arising from absence of Arg360 (**CPOM360**) and of His404 and Arg490 (**CPOM404-1** and **CPOM404-2**) are presented in Table 4.10.

In case of **CPOM360**, it might be interesting to see the locations where compensations are made to loss of interactions arising from absence of Arg360. It turns out that hydrogen bonding geometrical parameters for donor atoms belonging to Ser, Gly and His residues in **CPOM360** indicate a strengthened interaction with cofactor, while those for Lys remains virtually unchanged. Specially the N2,O1 donor, acceptor pair shows much closer approach, about 23.2 pm shorter in mutant system. Also the shared proton in this pair is located 25.6 pm closer to acceptor atoms compared to its analogue in **CPO1**. Similarly other donor atoms in Ser–Gly–His chain show closer interaction. Perhaps a more efficient cofactor stabilisation by these three residues is permanent characteristic of VCPO systems, given

into consideration our comparison of **CPO1** and **BPO1** above. It is interesting to note that in the absence of Arg360, cofactor is not increasingly attracted towards Lys, although it is pulled towards Arg490 a residue which also shows improved interactions with cofactor along with Ser, Gly and His.

From this point of view, heavy dependence on Lys residue in VBPO active site for stabilisation of cofactor might have consequences at certain stage of catalytic cycle as HB donating capability of Lys in VBPO is expected to be crippled by a His411 residue in its external protein environment. This His residue is replaced by Phen397 in VCPO (Fig. 1.1).

The combined effect of absence of two residues His404 and Arg490 is rather drastic on interactions of remaining residues in **CPOM404** structures. The interactions with Ser occurs at longer interatomic acceptor donor distance, and that with Arg360 and Lys at closer values of this distance. Because of diminished neutralising of anionic oxygen atoms, a proton transfer from Lys to atom O4 is induced (**CPOM404-1**), which can be prevented due to presence of additional proton on apical O1 atom (**CPOM404-2**). Moreover the pair (N2,O2) also closes up and assumes an HB angle more linear compared to in other structures.

Interaction energies: CPO1 and BPO1

The interaction energy of cofactor with protein environment is analysed according to Eq. 4.6, with i = Lys353, Arg360, Arg490, SGH (the polypeptidial chain of three amino acids Ser402, Gly403, and His404) taken as individual protein fragments which interact with TBP vanadate species. The values of $\Delta E^{V,X}$, and its fragmentation into two-body and many-body terms are given in Table 4.11 for cofactor structure optimised in VCPO and VBPO (crystallographic) active site pockets. Reader is to be reminded that amino acid sequence nomenclature used here is that from VCPO crystal structure, but is also used for structures based on VBPO crystal structure to denote the analogous residues. It can be seen that absolute values of $\Delta E^{V,X}$ for **CPO1** and **BPO1** differ by only 3.1 kcal mole⁻¹ but decomposition of this quantity into two-body, many-body etc. fragmentation varies to a larger extent in both structures. The largest differences between the two structures in terms of absolute values of two-body term $\Delta E^{V,i}$ occur for fragments SGH and Lys353. The term for SGH is larger than that for Lys353 in both systems, but the value for later is by 8.1 kcal mol⁻¹ larger in **BPO1** while that for the former by 10.1 kcal greater mol⁻¹ in **CPO1**. This is a reconfirmation of results previously discussed in regard to optimised HB geometrical data (Table 4.9) of these systems. The stabilisation of a TBP vanadate structure with different capabilities of SGH and Lys to this end in both systems may have consequences for relative catalytic efficiency of VCPO and VBPO enzymes, at least during the stages of catalytic cycle at which cofactor moiety assumes TBP geometry. These include the resting state as in present discussion (**CPO1** and **BPO1**) and active hypohalite

Table 4.11: Gas phase supermolecular energies $\Delta E^{V,X}$ in kcal mol⁻¹ (corresponding BSSE in parenthesis.), and its decomposition in two-body/many-body terms (Eq. 4.6) for **CPO1** and **BPO1**, **CPOM360**, and **CPOM404-2**. SGH refers to fragment composed of Ser402, Gly402, and His404 residues.

CPO1					BPO1			
$\Delta E^{V,X}$	-386.7 (3.6)				-383.6 (3.5)			
i	SGH	Lys353	Arg360	Arg490	SGH	Lys353	Arg360	Arg490
$\Delta E^{V,i}$	-129.5	-106.1	-101.7	-111.0	-119.4	-114.2	-100.2	-113.3
$\Delta E^{V+i,X-i}$	-109.7	-146.9	-142.6	-123.8	-119.4	-131.1	-140.6	-118.7
$\Delta E^{i,X-i}$	147.5	133.7	142.4	151.9	144.8	138.3	142.8	151.6
BSSE ^{V,i}	1.8	0.6	0.8	1.1	1.7	0.7	0.7	0.7
CPOM360					CPOM404-2			
$\Delta E^{V,X}$	-321.4 (3.1)				-75.8 (2.0)			
i	SGH	Lys353	Arg360	Arg490	SGH	Lys353	Arg360	Arg490
$\Delta E^{V,i}$	-139.0	-109.2	-	-114.2	-14.6	-40.6	-31.7	-
$\Delta E^{V+i,X-i}$	-73.0	-129.4	-	-103.3	-54.7	24.2	14.4	-
$\Delta E^{i,X-i}$	109.4	82.8	-	103.9	6.5	59.4	58.5	-
BSSE ^{V,i}	1.9	0.6	-	0.8	1.0	0.5	0.5	-

complex of vanadium in the final stages of cycle (See Chapter 6, Fig. 6.1). Specially in TBP hypohalite complex, the oxygen atom of hypohalite ion is coordinated to vanadium centre at apical position and is expected to be involved in hydrogen bonding interaction with His404, a residue which is part of SGH fragment, and which was also reported in previous section to have closer HB interaction with apical oxygen atom in **CPO1**. The energy terms for Arg360 and Arg490 differ only marginally in the two structures.

The interaction energies in aqueous (COSMO) phase are listed in Table 4.12, showing a behaviour already discussed for small model HB complexes, i.e. reduction in HB energies due to solvation of complexing entities and their charges.

Interaction energies: mutant versions

Comparison of site mutated structures to **CPO1** presents an interesting scenario which can only be explained on the basis of electronic or orientational cooperation. By electronic cooperation it is meant that HB strength is modified because of change in accepting capability due to other hydrogen bonds. By orientational cooperation it is meant that in full active site (like **CPO1** model) the interaction of amino acids help cofactor assuming an orientation in which it can take maximum stabilising benefit of interaction with each amino acid. This simply means that each hydrogen bond is able to assume a geometry corresponding to a point on its HB potential energy surface with possibly best donor-acceptor interaction. To start with **CPOM360**, it was observed while discussing its HB geometrical parameters that enhanced interactions of cofactor with SGH and Arg490 are expected compared to those in **CPO1** while those with Lys are expected to remain unchanged. The value of $\Delta E^{V,X}$ for this structure in gas phase shows total loss of 65.3 kcal mol⁻¹ compared to **CPO1** because

Table 4.12: Aqueous phase (COSMO) supermolecular energies $\Delta E^{V,X}$ in kcal mol⁻¹ (corresponding BSSE in parenthesis.), and its decomposition in two-body/many-body terms (Eq. 4.6) for **CPO1** and **BPO1**, **CPOM360**, and **CPOM404-2**. SGH refers to fragment composed of Ser402, Gly402, and His404 residues.

CPO1					BPO1			
$\Delta E^{V,X}$	-40.3 (2.9)				-37.8 (3.4)			
i	SGH	Lys353	Arg360	Arg490	SGH	Lys353	Arg360	Arg490
$\Delta E^{V,i}$	-17.3	-9.1	-4.3	-10.1	-13.7	-10.9	-4.0	-9.1
$\Delta E^{V+i,X-i}$	-11.4	-24.6	-32.1	-22.2	-13.0	-21.3	-30.8	-20.6
$\Delta E^{i,X-i}$	11.5	6.6	3.9	8.0	10.8	5.3	2.7	7.8
BSSE ^{V,i}	1.5	0.5	0.5	0.5	1.3	0.5	0.3	0.5
CPOM360					CPOM404-2			
$\Delta E^{V,X}$	-40.9 (2.4)				-10.9 (1.7)			
i	SGH	Lys353	Arg360	Arg490	SGH	Lys353	Arg360	Arg490
$\Delta E^{V,i}$	-20.1	-9.0	-	-10.0	-4.9	-6.4	-2.8	-
$\Delta E^{V+i,X-i}$	-9.3	-27.7	-	-24.1	-2.8	1.2	-6.6	-
$\Delta E^{i,X-i}$	11.5	4.3	-	6.9	3.1	5.6	1.4	-
BSSE ^{V,i}	1.5	0.4	-	0.5	1.1	0.4	0.4	-

of absence of Arg360 (Table 4.11) and splitting of $\Delta E^{V,X}$ shows that two-body terms for all three fragments SGH, Lys353 and Arg490 exhibit an enhanced hydrogen bonding with them. The later two fragments show an increase in $\Delta E^{V,i}$ of about 3 kcal mol⁻¹ while SGH shows an increase of 9.5 kcal mol⁻¹ compared to its values in **CPO1**. This certainly reflects that loss of Arg360 in mutant version of VCPO does not adversely effect the orientation of cofactor in relation to other amino acids. On the other hand interaction energies for **CPOM404-2** show these adverse effects. The $\Delta E^{V,X}$ for this structure is reduced by 310.9 kcal mol⁻¹ compared to that in **CPO1** and individual two-body terms for fragments SGH, Lys353 and Arg360 also show drastically reduced values. It is to be remembered that SGH fragment in this case does not contain His404 part, and interaction of this fragment is comprised of that due to only Ser and Gly. Moreover Arg490 is also not present because it is found at non-interactive distance in crystal structure. It was reported in a previous subsection that in **CPOM404-2**, interatomic acceptor-donor distance for Ser...O is far apart while those for Lys and Arg360 are closer compared to those in **CPO1**. Despite geometrically closer interaction, the reduction in the values of two-body energy terms for these two cationic residues in comparison to **CPO1** is due to the fact that now interaction of cationic residues is not with anionic but neutral cofactor entity.

Interestingly, the aqueous (COSMO) phase interaction energies (Table 4.12) show that hydrogen bonding interaction in **CPOM360** is stronger compared to that in **BPO1**, while similar to that in **CPO1** in aqueous phase. The comparative look at aqueous phase HB energies for **CPO1** and **CPOM360** makes it clear that while SHG in later is strongly complexed, other residues maintain similar level of interaction with cofactor in both structures. The comparison of **BPO1** and **CPOM360** shows that all residues (with the exception

of Lys) are strongly complexed with cofactor in later structure. Moreover, the repulsive terms $\Delta E^{i,X-i}$, have smaller positive values in **CPOM360**, contributing to larger aqueous phase total interaction energy for this structure ($-40.9 \text{ kcal mol}^{-1}$) compared to $-37.8 \text{ kcal mol}^{-1}$ for **BPO1**.

QTAIM parameters for 12 and CPO1

While analysing present systems with QTAIM, it would be interesting to see how the hydrogen bonds between same donor-acceptor pairs behave in different supramolecular structures. One such hydrogen bond is imidazole-NH \cdots O in **12** and **CPO1**. Obvious difference between the two systems is extensiveness of hydrogen bonding network in later structure. The values of ρ_C for (N1,O1) hydrogen bond in **12** and **CPO1** are 0.083 a.u. (Table 4.8) and 0.045 a.u. (Table 4.13) respectively. Similar reduction in other properties in going from **12** to **CPO1** is observed, given in this order in a.u. :- $\nabla^2\rho_C$ (0.149 and 0.131), G_C (0.064 and 0.037), V_C (-0.091 and -0.041), and H_C (-0.027 and -0.001). This shows that imidazole-NH \cdots O hydrogen bond, in presence of active site constraints and more extensive hydrogen bonds on oxygenic sites of vanadate, is somewhat weaker in comparison to one in **12** both in terms of electrostatic pull (lower $\nabla^2\rho_C$), and covalent interactions (less negative H_C). Similarly the comparative look at interaction of gu2 in **12** and Arg490 in **CPO1** shows weakening of both hydrogen bonds donated by Arg490 in **CPO1**. This is reflected by reduced electron density at BCP and smaller values of $\nabla^2\rho_C$. Covalent character of these hydrogen bonds in **CPO1** is also diminished (Tables 4.8 and 4.13).

Previously it was discussed that cumulative effect of several hydrogen bond fixes the optimum protonation state of vanadate, and now QTAIM comparison of hydrogen bonds in **12** and **CPO1** show that in active site environment several hydrogen bonds also adjust their individual characteristics in order to achieve maximum stabilisation of whole supramolecular adduct.

QTAIM: Comparison of CPO1 and BPO1

Our purpose was to elucidate the contrasts between hydrogen bonding patterns in active site cavities from reported crystal structure and the lowest energy isoelectronic structures **CPO1** and **BPO1** were taken to serve as representative of resting states of VCPO and VBPO. Doing this with use of QTAIM criteria is specially useful for systems with multiple hydrogen bonds not distinguishable from each other in supermolecular approach. B3LYP electron densities with 6-311G** and 6-31+G* basis, and ADF-BP/TZP electron density were used for locating HB BCP and calculating BCP properties. Results presented in Fig. 4.10 show that three levels of theory faithfully reproduce the trends in calculated properties. The BCP electron density or ρ_C is indistinguishably close for all levels of theory,

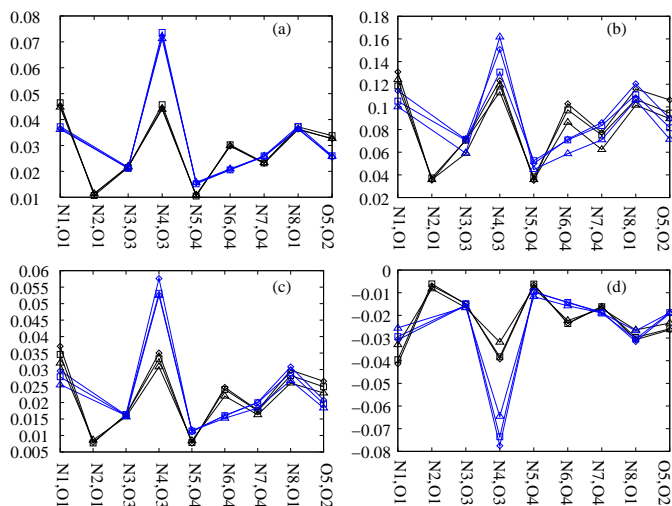


Figure 4.10: Calculated values of some local properties at HB (3,-1) critical points in a.u. (data in Table 4.13) (a) ρ_C (b) ∇_C^2 (c) G_C (d) V_C . Black lines : **CPO1**, Blue lines : **BPO1**. diamonds: B3LYP/6-311G**, triangles: B3LYP/6-31+dp, squares: ADF-BP/TZP.

while scatter for Laplacian at BCP $\nabla^2\rho_C$ is largest. This scatter, however, does not affect the general trend i.e. comparative picture of two structures produced at each theory level remains similar. In order to have a quantitative focus on differences between two structures, the B3LYP/6-311G** values are tabulated (Table 4.13). It can be seen that **BPO1** lacks one hydrogen bond, as absence of (3,-1) BCP for pair N2,O1 implies. For **CPO1** this BCP exists and the listed values of QTAIM parameters at its location lie within the range accepted for hydrogen bonds. This is in line with supermolecular energetic observation discussed previously, which showed that two-body interaction term for SGH fragment is larger in **CPO1** than **BPO1**. The extra (N2,O1) hydrogen bond in SGH fragment of **CPO1** may be one of the contributors to this difference.

As observed while discussing geometrical parameters, the His...O (N1,O1) and Lys...O (N4,O3) again stand out distinctively in view of their listed QTAIM quantities for both structures. First, they have large values of ρ_C , signifying a strong HB. Secondly values of $\nabla^2\rho_C$ are also about an order of magnitude higher compared to those for majority of other listed hydrogen bonds. This implies a stronger attraction between electron density at HB BCP and nuclei connected to it, so that a larger curvature of bound atomic surfaces around BCP is resulted. Third, the total energy density at BCP or $H_C = G_C + V_C$ is negative showing net local excess of attractive forces at BCP which imparts partial covalent character to these hydrogen bonds. These two hydrogen bonds are also the starkest point of contrast between the systems **CPO1** and **BPO1**. As can be seen, the two hydrogen bonds accommodate an equal amount of electron density at BCP for **CPO1** as shown by values of ρ_C for this structure. On the other hand **BPO1** has much larger value of this quantity for Lys...O (N4,O3) compared to that for His...O (N1,O1). The difference for the two HB in **BPO1** of about 0.035 a.u. is in fact larger than the actual ρ_C values for most of hydrogen bonds listed in Table 4.14. A similar imbalance between these two HBs for **BPO1** (but not for **CPO1**), is also reflected in $\nabla^2\rho_C$ values. These are manifestations

Table 4.13: QTAIM parameters (a.u.) for **CPO1** and **BPO1** calculated by using density obtained at B3LYP/6-311G** level.

	CPO1					BPO1				
	ρ_C	$\nabla^2\rho_C$	G_C	V_C	H_C	ρ_C	$\nabla^2\rho_C$	G_C	V_C	H_C
N1,O1	0.045	0.131	0.037	-0.041	-0.004	0.037	0.114	0.030	-0.031	-0.001
N2,O1	0.011	0.035	0.008	-0.007	0.001	-	-	-	-	-
N3,O3	0.022	0.071	0.016	-0.015	0.001	0.021	0.072	0.016	-0.015	0.002
N4,O3	0.044	0.123	0.035	-0.039	-0.004	0.072	0.151	0.058	-0.078	-0.020
N5,O4	0.011	0.035	0.008	-0.007	0.001	0.016	0.050	0.011	-0.010	0.001
N6,O4	0.030	0.103	0.025	-0.023	0.001	0.021	0.072	0.016	-0.014	0.002
N7,O4	0.023	0.077	0.018	-0.016	0.002	0.026	0.086	0.020	-0.019	0.001
N8,O2	0.036	0.116	0.030	-0.031	-0.001	0.037	0.120	0.031	-0.032	-0.001
O5,O2	0.033	0.106	0.026	-0.026	0.000	0.025	0.090	0.021	-0.019	0.002

that while His \cdots O hydrogen bond is weakened, Lys \cdots O gets stronger in **BPO1** compared to structure **CPO1**. The final QTAIM parameter to be looked for these two interactions in the two systems is H_C . In **CPO1** two hydrogen bonds show an equal extent of covalent character, as the values of H_C for both are -0.004 a.u., but going to **BPO1** it is observed that H_C for His \cdots O is changed to -0.001 a.u while that for Lys \cdots O, with much enhanced negative value of -0.02 a.u. is dominated by potential energy density. In other words **BPO1** shows a much larger covalent contribution present in Lys \cdots O HB, while the same in His \cdots O is reduced. The hydrogen bond involving (N3,O3) pair in SGH backbone is very identical in both structures in terms of listed QTAIM quantities. The Ser \cdots O HB (O5,O2) is clearly stronger in **CPO1** as its ρ_C is 0.008 a.u greater than corresponding **BPO1** value. Specially V_C plays a dominant role in **CPO1** as it is exactly balancing G_C to give a zero H_C , while in **BPO1** total energy density at BCP has a net positive value of 0.002 a.u.

Of the two hydrogen bonds donated by Arg360, the one involving (N5,O4) pair is weaker in terms of QTAIM parameters, expectedly as geometrical parameters for two HBs were previously shown to be relatively far from optimum values, and more so in case of N5,O4. However QTAIM parameters of N5,O4 HB for **BPO1** predict a slightly stronger HB than those for **CPO1**. The other stronger hydrogen bond between atoms (N6,O4) turns out to be weaker in **BPO1** with lower values of ρ_C , $\nabla^2\rho_C$ and V_C . By revisiting the two-body interaction term for Arg360-cofactor pair in Table 4.11, its slightly higher value for **CPO1** allows us to conclude that two hydrogen bonds donated by Arg360, despite having different QTAIM picture in **CPO1** and **BPO1**, give the same total interaction of Arg360 with atom O4. In other words overall energy term for interaction of Arg360 seems to be no different in two structures, but in directional terms of individual hydrogen bond, (N6,O4) HB appears to be better tuned in **CPO1**. The residue Arg490 with its two hydrogen bonds involving pairs (N7,O4) and (N8,O2) give very identical QTAIM parameters for the two structures with slight inclinations of increased strength in **BPO1**. Moreover in both structures small negative values of H_C for (N8,O2) HB show a trace of shared interaction.

Table 4.14: QTAIM parameters (a.u.) for **CPOM360** and **CPOM404-2** calculated by using density obtained at B3LYP/6-311G** level.

	CPOM360					CPOM404-2				
	ρ_C	$\nabla^2\rho_C$	G_C	V_C	H_C	ρ_C	$\nabla^2\rho_C$	G_C	V_C	H_C
N1,O1	0.056	0.133	0.043	-0.053	-0.010	-	-	-	-	-
N2,O1	0.019	0.063	0.014	-0.013	0.001	-	-	-	-	-
N2,O2	-	-	-	-	-	0.012	0.039	0.009	-0.007	0.001
N3,O3	0.028	0.094	0.022	-0.022	0.001	0.022	0.076	0.017	-0.016	0.002
N4,O3	0.045	0.120	0.035	-0.039	-0.005	0.082	0.158	0.066	-0.093	-0.027
N5,O4	-	-	-	-	-	0.018	0.059	0.013	-0.012	0.002
N6,O4	-	-	-	-	-	0.029	0.103	0.024	-0.023	0.002
N7,O4	0.038	0.119	0.031	-0.033	-0.001	-	-	-	-	-
N8,O2	0.044	0.131	0.037	-0.041	-0.004	-	-	-	-	-
O5,O2	0.038	0.123	0.032	-0.033	-0.001	0.018	0.058	0.013	-0.011	0.002

QTAIM: Comparison of CPO1 with mutant variants

The structure **CPOM360** shows significant changes in QTAIM parameters in comparison to those for **CPO1**. These are in line with similar changes in geometrical and supermolecular energetic context as all listed QTAIM parameters in Table 4.14 show HB interactions with considerable enhancement over their counterparts in **CPO1**.

To start with His \cdots O (N1,O1) HB, ρ_C is increased in **CPOM360** by 0.011 a.u. over its value in **CPO1**. The value of $\nabla^2\rho_C$ remains virtually unchanged but covalent character is increased as reflected by H_C value of -0.01 compared to -0.004 in **CPO1**. Similarly HB involving (N2,O1) and (N3,O3) undergo an increasement in values of QTAIM parameters but to a lesser extent. The HB Lys \cdots O (N4,O3) remains virtually unchanged, but interactions of cofactor with Ser and Arg490 are considerably transformed. First considering the two hydrogen bonds of Arg490, the one involving (N7,O4) exhibits 0.015 a.u. increase in ρ_C compared to its counterpart in **CPO1** and increase of 0.04 a.u. in $\nabla^2\rho_C$. The G_C and V_C are also increased in a manner that their sum (H_C) reports a tiny value with negative sign. The HBs between the atoms of the pairs N8,O2 and N5,O2 (Ser \cdots O HB) record the same trend in all quantities.

The mutagenesis of His404 residue, the resulting crystal structure data of which is basis of **CPOM404-2** optimised structure causes the loss of interactions with cofactor of not only His404 but also of Arg490. The effects on listed QTAIM parameters (Table 4.14) are summarised here. Notably the HB in atoms pair (N2,O1) is replaced by one involving (N2,O2) pair. The values of listed quantities for new HB are comparable to those for (N2,O1) in **CPO1**. Similarly parameters for (N3,O3) are also comparable to its counterpart in **CPO1**. The Lys \cdots O (N4,O3) interaction is enhanced with the change in quantities ρ_C , $\nabla^2\rho_C$, and H_C , in this order, by 0.038 a.u., 0.035 a.u., and -0.023 a.u. over their respective values in **CPO1**. Hydrogen bond (N5,O4) donated by Arg360 is strengthened by changes in ρ_C (0.007 a.u.), $\nabla^2\rho_C$ (0.024 a.u.), and G_C (0.001 a.u.). Other hydrogen bond donated

Table 4.15: Donor–acceptor (charge transfer and natural bond orbital) interactions for **CPO1**, **BPO1**, **CPOM360**, and **CPOM402-2**, prefix **CPO** dropped from the column headings of last two structures. *Upper block:* Vanadate→protein charge transfer (natural charges). *Lower block:* Second order donor–acceptor natural orbital interaction energies ($E^{(2)}$, Eq. 4.4). First line of each entry gives interaction between n_Y and σ_{X-H}^* orbitals in $X-H\cdots Y$ hydrogen bond, and second line gives total interaction of all natural molecular orbitals centred on X with those on Y.

	CPO1	BPO1	M360	M404-2
Charge transfer (a.u.) from TBP vanadate moiety				
Van→SGH	0.05	0.04	0.09	−0.08
Van→Lys	0.08	0.12	0.08	0.13
Van→Arg360	0.04	0.04	-	0.05
Van→Arg490	0.08	0.08	0.13	-
$E^{(2)}$ for donor–acceptor interaction (kcal mol ^{−1}).				
N1,O1	22.3	15.0	36.0	-
	28.3	18.3	42.6	-
N2,O1	1.4	-	3.8	-
	2.5	-	5.1	-
N2,O2	-	-	-	2.2
	-	-	-	3.1
N3,O3	4.7	4.6	8.7	5.1
	6.4	8.2	13.0	5.9
N4,O3	15.3	41.8	14.4	37.1
	21.3	51.3	22.2	52.4
N5,O4	1.4	0.4	-	3.8
	2.5	4.9	-	4.4
N6,O4	5.5	1.7	-	4.1
	12.8	11.0	-	11.7
N7,O4	7.2	1.6	5.6	-
	9.2	13.8	21.3	-
N8,O2	14.7	14.1	22.4	-
	17.8	16.8	25.6	-
O5,O2	15.3	9.6	19.2	6.0
	16.8	11.4	21.5	6.8

by Arg360 (O6,O4) shows no significant changes. On the other hand Ser \cdots O (O5,O2) HB considerably loses stabilisation as reflected in following changes: ρ_C (−0.015 a.u.), $\nabla^2\rho_C$ (−0.048 a.u.) and H_C (0.002 a.u.).

Natural Bond Orbital Analysis

As reported, hydrogen bonding may also accompany charge transfer (CT) from HB acceptor to HB donor. This is important for active site of enzyme under consideration as neutralisation of negative charge of cofactor oxygen atoms is vital for catalytic cycle. The net charge transfer in terms of natural electronic population from vanadate moiety to HB partners is listed in Table 4.15. The amount of CT in **CPO1** and **BPO1** is 0.25 a.u. and 0.28 a.u. respectively, and in case of later structure, Lys residue receives larger share from vanadate than its counterpart in **CPO1**. This is in line with earlier discussion regarding closer interaction of Lys in **BPO1**. For **CPOM360** the total loss of negative charge from

vanadate is 0.30 a.u., larger than corresponding values for **CPO1** and **BPO1**. It turns out that absence of Arg360 in this structure results in enhanced CT to Arg490 as reflected by its value 0.13 a.u. compared to 0.08 a.u. in both **CPO1** and **BPO1**. Similar enhanced CT to smaller extent, is also observed to SGH fragment for **CPOM360**. On the other hand the net loss of charge on vanadate in **CPOM404-2** is only 0.10 a.u., distinguished by gain of negative charge from SGH fragment and larger loss to Lys by vanadate.

The perturbative stabilisation, $\Delta E_{n\sigma^*}^{(2)}$ arising from interaction of n_Y orbitals (lone pairs) with σ_{X-H}^* in $X-H \cdots Y$ hydrogen bonds according to Eq. 4.4 are listed again in Table 4.15. The values for interactions of all natural orbitals on X with those on Y are also listed, and it can be seen that for large majority of cases, $n_Y \rightarrow \sigma_{X-H}^*$ is highly dominant in these electron donor-acceptor interactions. Moreover, HB donor-acceptor pairs for His (N1,O1) and Lys (N4,O3), and to smaller extent for Ser (O5,O2), become the contrasting point between **CPO1** and **BPO1**. It is notable that vanadate in **CPOM360** shows an increased interaction of SGH fragment and Arg490 but maintains identical interaction with Lys in terms of $\Delta E_{n\sigma^*}^{(2)}$ values, when compared with **CPO1**. On the other hand **CPOM404-2** for which interaction of vanadate with curtailed SGH is much lower, and that with Arg490 completely absent, exhibits a markedly enhanced interaction of vanadate and Lys. Looking at the trends for **BPO1** it can be safely concluded that any weakness of vanadate interactions with SGH fragment and/or Arg490 results in increased reliance on Lys hydrogen bond for stabilisation.

4.4.4 Outlook : Active Site and Catalytic Cycle

In this chapter hydrogen bonding of vanadate with analogues of VHPO active site residues were studied with a number of theoretical methods. Starting with small model complexes, the question of differences between x-ray crystallographic active sites of VCPO and VBPO and two site mutated versions of VCPO was addressed.

The studies on small (1:1) and larger oligomeric complexes of vanadate with moieties representing active site residues furnished the charge assisted character of hydrogen bonds. The charge assistance to HB strength was found to diminish in aqueous dielectric medium. Moreover, the protonation state of vanadate was observed to be dependent on number of hydrogen bonds donated on its oxygen atoms.

Regarding the resting state of VHPO active site, the result obtained in Chapter 3 is reconfirmed, i.e. a diprotonated vanadate species is energetically favourable in active site environment. Furthermore, positively charged His404 residue donating a hydrogen bond to apical oxygen atom of TBP vanadate is found to be energetically favourable compared to a neutral His404 receiving a hydrogen bond from same oxygen atom.

The combined effect of residues, Lys, Arg360, Ser, Gly, His404 and Arg490 was found to be vital in fixing the protonation state of cofactor. The crystallographic active site

cavities of VCPO and VBPO were found to interact with vanadate cofactor in different ways. In this regard the hydrogen bonds of Lys, Ser, Gly and His404 were determined to show a contrasting behaviour in both systems. Whereas VCPO active site pocket offers a balanced interaction of cofactor with Lys on one hand and fragment Ser-Gly-His (SGH) on the other, the VBPO active site pocket with relatively weak interaction of cofactor with SGH fragment, gains a level of stabilisation similar to **CPO1** by depending more on interaction of cofactor with Lys. This can be important at the stages of catalytic cycle, when cofactor assumes trigonal bipyramidal geometry. Two such stages can be easily conjectured: first, the resting state, and second, formation of TBP vanadate species with apically coordinated hypohalite ion (please see Chapter 6, Fig. 6.1). At these stages, VBPO active site is expected to stabilise TBP structure differently in comparison to VCPO due to following reasons:

1. As mentioned VBPO active site has relatively weak interactions with SGH fragment, and so has to depend on Lys residue to compensate for this.
2. On the other hand Lys may not be able to fully compensate for the loss of interaction with SGH fragment. This is because the protein shell in immediate exterior to active site contains a number of HB acceptors surrounding the terminus of Lys side chain. These include two carbonyl oxygen atoms belonging to protein backbone in case of both VCPO and VBPO, and an additional His in case of VBPO (Fig. 1.1). These HB acceptors may compete with oxygen atoms belonging to cofactor for making hydrogen bond with Lys, and hence may reduce the effectiveness of Lys residue.

The study on models based on site mutated versions of VCPO showed that absence of His404 (and Arg490) in structures **CPOM404-1,2** altered the cofactor interaction with active site protein environment in a fundamental way, characterised by significantly enhanced (cofactor \cdots Lys) interaction. On the other hand, absence of Arg360 in **CPOM360** did not change (cofactor \cdots Lys) interaction, while showing increased interaction of cofactor with SGH fragment.

Chapter 5

Reaction of Hydrogen Peroxide with Imidazole Bound Vanadate

5.1 Introduction

Hydrogen peroxide is an important oxygen atom donor for the reactions involving oxygen atom transfer mediated on the metal centres.^{21,40,74} Peroxo complexes of early transition metals, Ti, V, Mo, W and Re are well known as reactive intermediates^{219–222} in a variety of oxygen transfer reactions, including the oxidation of halides, the primary step *en route* to halogenation of organic substrates.⁶ This reaction is best performed in vanadium containing haloperoxidases (VHPO),^{26,114,115,223} and it has been found that mode of action of these enzymes operates in two steps. In the first step the pentacoordinated vanadate in the active site is attacked by hydrogen peroxide and metal coordination is transformed from dioxo to peroxo vanadium species. In the second step peroxovanadium species transfers an oxygen to the halide substrate while completing the catalytic cycle by formation of dioxo species. The second step is experimentally found to surpass a higher energy barrier. The role of enzymatic environment in bringing down this barrier is rightly emphasised but there is no reason to overlook the enzymatic capability to facilitate the events leading to formation of peroxo species and their proper placement in the enzyme environment. X-ray diffraction crystallographic structures of both the native form²² of vanadium containing chloroperoxidase (VCPO) and its reactive peroxide form²⁵ (see Fig. 1.1) amply show the outcome of first step of catalytic cycle, a pentacoordinated, monoperoxovanadium species involved in hydrogen bonding with amino acid residues. The peroxide in solution, on the other hand, is known to form a variety of peroxovanadium complexes with different stoichiometry of protons and peroxide itself.^{65,224–227} Moreover, the stability and catalytic activity of peroxo species in solution is sensitive to choice of ligands in synthesised complexes.^{120–128,228,229} Therefore the fact that particular architecture of the active site of VHPOs has the ability to carry out the first catalytic step to form most reactive peroxo species can not be overemphasised. The subject of present chapter is the investigation carried out about the peroxide attack on pentacoordinated dioxo vanadium modelled after

the VHPO active site. Previous computational work by us (Chapter 3,²³⁰ Chapter 4) and others,^{156,231} has indicated that in VHPO, vanadium forms a monoanionic species with distorted trigonal bipyramid (TBP) in which two apices are occupied by hydroxyl group and a histidine residue. For modelling peroxide attack on such species, cofactor bound to active site is considered as a dihydrogen orthovanadate bound to an imidazole and two starting scenarios are envisaged (Fig. 5.1) in present context.

One, the reaction of imidazole bound, pentacoordinated dihydrogen orthovanadate species in monoanionic form (**I**) and the other in which the same species has taken a proton to form a neutral species with coordinated water at the apex (**II**). This later variation (**II**) was considered necessary to study, because the apical oxygen which is located at the mouth of active site cavity, facing a channel of water molecules leading into the active site as found in crystal structure, thus giving rise to the possibility of protonation. Moreover apical oxygen atoms receives a hydrogen bond from a histidine residue in VHPO (His404 in vanadium chloroperoxidase).²² This residue has been hypothesised to be involved in acid-base catalysis, so apical oxygen atom is also prone to proton transfer from His404 (see e.g. Chapter 4).

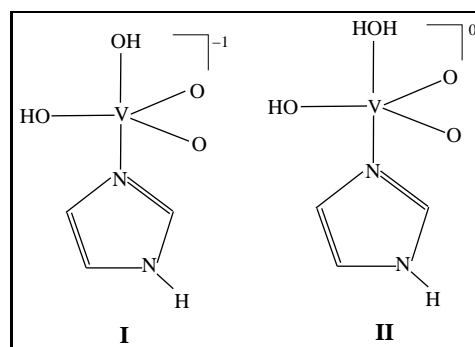


Figure 5.1: Schematic representation of TBP vanadate species used as starting point for reactions studied in present work.

Before starting the discussion of our results in a later section, it would be useful to point out some features of starting points of reactions studied here and reactive paths ensuing from these. First, as already mentioned, there may be protonation of oxygen atom of apical hydroxyl group due to proton transfer either from His404 or from solvent, prior to peroxide attack. Second, the starting configuration of reactants (hydrogen peroxide and vanadate species) can be considered as a hydrogen bonded complex, and during the course of reaction, oxygen atom belonging to hydrogen peroxide seeks to bind with vanadium while transferring a proton to an oxygen atom on vanadate moiety. Since in these starting complexes of reactants oxygen belonging to peroxide can be neighboured by different oxygen atoms of vanadate moiety, the proton transfer to different oxo/hydroxo positions on vanadate can be anticipated to lead to different intermediates and reactive channels. Further, the incoming hydrogen peroxide may attack an axial or equatorial position on the TBP vanadate species. In fact it is reasonable to envision the trigonal bipyramid as having a potential to transform into octahedral structure by making room for a fourth vertex in equatorial plane, and so incoming peroxide oxygen may occupy this vacant site in intermediate structures. Finally in carrying out these changes enzyme active sight can be thought to take different roles.

Since HOOH transfers a proton to oxygen atom on vanadate, and a HOO–V bond is formed, these two processes may or may not be concerted. In any case stabilisation of free HOO[−] species in appropriate orientation can be performed by positively charged hydrogen bond donating amino acid residues of active site. Furthermore, orientation of cofactor is forced by the protein environment of active site, and each oxygen atom on vanadate moiety is extended towards different but definite hydrogen bonding partner(s) among the surrounding positively charged amino acids. Because of this, incoming hydrogen peroxide may find it possible to bond with vanadium only from certain specific positions in active site pocket.

5.2 Computational Methods

5.2.1 Optimisation of stationary points

To appropriately sample over the potential energy surface, constrained geometry optimisations were performed along the anticipated reaction coordinates by letting the system traverse over the so called ‘linear transit’. The method involves stepwise optimisations of all internal degrees of freedoms except the one associated with reaction coordinate, which is kept frozen but is gradually varied in each linear transit step. Number of steps was chosen to be enough for smooth transition of the system from one step to the next. The energy profile thus obtained along the reaction coordinate allowed the choice of suitable guess for stationary points to be investigated. Such guess points were then calculated for second derivatives of energy by numerical differentiation of energy gradients,^{232,233} and depending upon whether this resulted in one negative eigen value of Hessian matrix, the internal degrees of freedom of each of such geometries were fully optimised with a quasi-Newtonian approach^{234–236} either for minimum or saddle point. The Hessian update in optimisation steps was done by Broyden-Fletcher-Goldfarb-Shanno (BFGS) method for search of minima and with Powell method for that of saddle points. For thus located stationary points, the second derivatives of energy were again calculated analytically,^{237–239} to perform vibrational zero-point corrections to their energies and to determine their thermodynamic properties. Computations were performed with ADF package of programs,^{130–132} using Becke-Perdew (BP) combination of exchange and correlation functionals and a basis set of Slater type functions of triple zeta quality augmented with two sets of polarisation functions (TZ2P).

5.2.2 *ab initio* Molecular Dynamics simulations

In order to confirm that optimised transition states (TS) connect the minima corresponding to reactants and products, the evolution of reaction coordinate starting from TS geometry

was monitored with *ab initio* molecular dynamics. Car Parinello molecular dynamics^{240,241} simulations were performed on some optimised transition states using CPMD package^{242,243} at 300 K for a duration of 0.7 ps. A fictitious wave function mass of 400 a.u. and timestep of 0.12 fs was used. Using BP functional, Kohn-Sham orbitals for valence electrons were expanded in plane wave basis with energy cutoff of 90 Ry, and core electrons were represented by pseudopotentials of Goedecker type.²⁴⁴ In order to check the suitability of this combination of plane wave cutoff and pseudopotentials, geometry of sample system optimised with this method and by using standard BP/TZ2P method described in previous subsection were compared. These were found to be in good agreement. Additionally, this method was also used to reproduce some of the reported trends⁸⁸ of simulations performed with Troullier-Martin pseudopotentials²⁴⁵ on peroxovanadium species. This showed that for systems studied here, our method gives reliable results. Purpose of these simulations was not to calculate average quantities but to observe the evolution of *transitional* degrees of freedom (those with imaginary frequencies) into nearest reactant/product basins by following the trajectories of atoms involved in bond making or breaking. This was achieved in two steps:

1. To sample over possible trajectories initiated from TS stationary points, short pre-equilibration runs of different time durations were performed while keeping the transitional degrees of freedom fixed and equilibrating all other degrees of freedom. The different duration of such pre-equilibration determines the velocities and forces on frozen atoms, and would lead them to follow different trajectories. Initial configurations were attained by such runs of durations 60 fs, 84 fs, 108 fs, 132 fs.
2. Starting with these initial configurations, production runs of upto 0.7 ps were performed, while keeping all the degrees of freedom relaxed. These resulted in different final configurations giving information about possible basins to which starting TS may settle.

5.2.3 Calculation of electron localisation function (ELF) and its basin populations

In order to make an assessment of electronic changes occurring along the reaction coordinate it is necessary to determine the electronic charges on reacting atoms at each reaction step. In this respect the choice of method to assign electronic populations to individual atoms is crucial, as traditional methods utilising projection of wave function give varying results. It has therefore increasingly become attractive in recent years to rely on information extracted from electron density in direct space. The point of vital importance in such methods is the way in which molecular space is partitioned, and for our purpose we found it insightful to use the the zero flux surfaces of gradient vector field¹⁹⁶ of electron localisation function

$$(\text{ELF})^{246-248} \eta(r),$$

$$\nabla \cdot \eta(r) = 0 \quad (5.1)$$

as these define subdomains within an atom which can be ascribed to core, bonded valence, and non-bonded valence electrons. We summarise here the definition of ELF and terminology used in ELF analysis to make the later discussion of results useful. ELF as originally defined is given by²⁴⁹

$$\eta(r) = \frac{1}{1 + \left(\frac{D_\sigma}{D_\sigma^0}\right)^2} \quad (5.2)$$

where D_σ represent the conditioned pair probability of finding an electron in a region around the reference point where an electron of same spin is already present. D_σ^0 is the same quantity for homogeneous electron gas of same electron density as actual system. Value of D_σ gives the extra local kinetic energy and is smaller in the regions where Pauli repulsion is small, i.e. electrons are either unpaired or form antiparallel spin pairs. The value of $\eta(r)$ ranges from 0 to 1 and a value of 1 indicates very weak Pauli repulsion and so complete localisation in the region while a value of 0.5 gives a homogeneous electron gas like situation. In the regions where same spin conditional pair density is high, $\eta(r)$ closes to zero. The regions bounded by the surfaces obeying Eq. 5.1 contain the attractor or maximum in $\eta(r)$ and are classified as $C(X)$, $V(X)$, $V(X,Y)$ or core, non-bonded valence, and bonded valence basins respectively, whereas X,Y are atoms near which they are found. $V(X)$ and $V(X,Y)$ are differentiated on the basis of their "synaptic order", or the number of atomic nuclei to whose core basin ($C(X)$) these are connected. So $V(X)$ with synaptic order of 1 corresponds to non bonded valence electrons while $V(X,Y)$ with synaptic order of 2 relates to two-centre chemical bond. The electron density integrated over the volumes of these basins gives the number of electrons populated therein. The calculation of ELF and integration of density over basins was done with DGrid and Basin programmes²⁵⁰ using the electron density calculated at TZ2P/BP level with ADF.

5.3 Results and Discussion

5.3.1 Peroxide attack on the anionic vanadate species **I** with apically coordinated hydroxyl ion

In this section we discuss the peroxide attack on pentacoordinated vanadate species in anionic form **I** (Fig. 5.1), and energy minima corresponding to starting configuration of reactants are shown as **1**, **2** and **3** in Fig. 5.2. In these structures hydrogen peroxide donates two hydrogen bonds, one to apical oxygen atom of TBP and second to another oxygen atom in equatorial plane. Structures **1** and **2** are similar in that both hydrogen bonds are received by hydroxyl groups of vanadate moiety, and equatorial hydroxyl group is aligned closer to plane of imidazole ring in both structures. However alignment of equatorial hydroxyl group

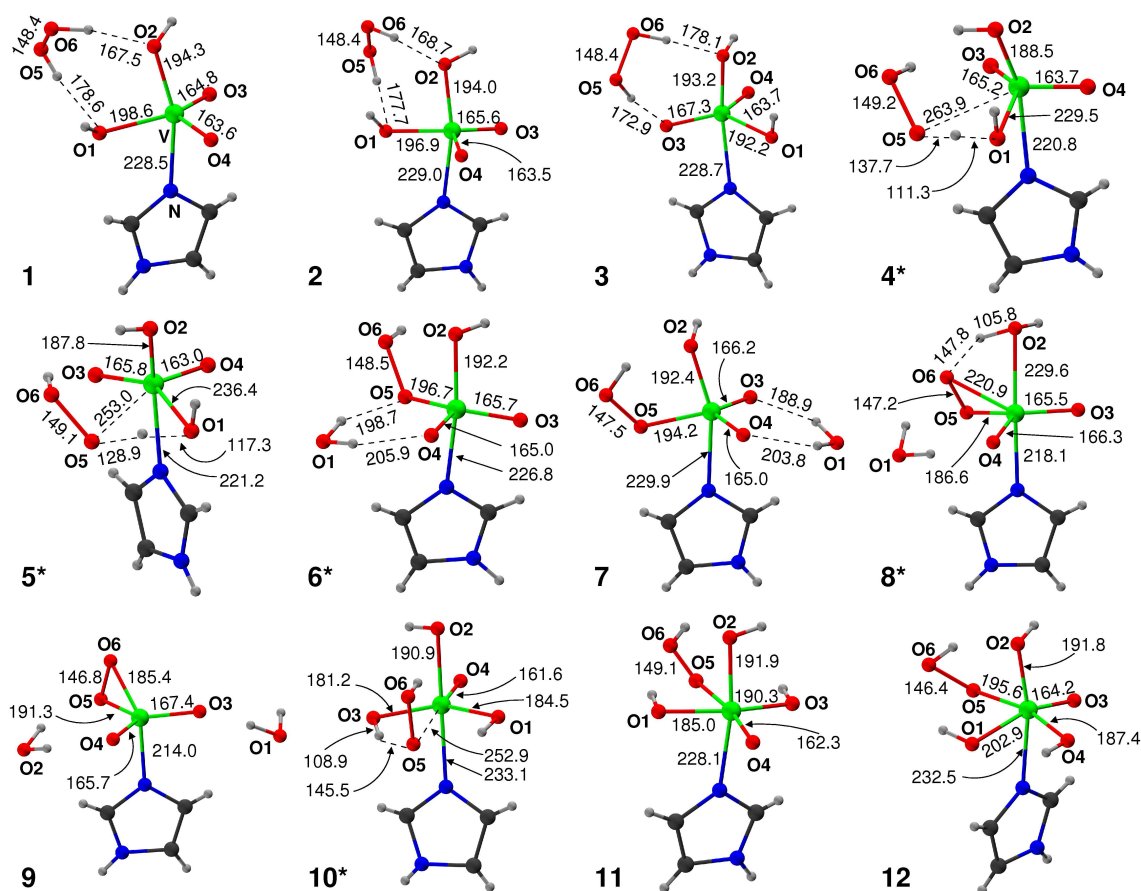


Figure 5.2: Representation of optimised stationary points along the reaction coordinate for attack of peroxide on monoanionic pentacoordinated dihydrogen orthovanadate (**I** in Fig. 5.1). All distances in pm. Structures with * denote a saddle point.

in one structure is out of phase from other by close to 145° . In **3** an equatorial oxo oxygen atom lies closer to imidazole plane and receives a hydrogen bond. In the initial phase of reaction, peroxide oxygen atom moves towards vanadium to form a bond with vanadium while transferring a proton to the vanadate oxygen atom to which it is hydrogen bonded. Following subsections describe the sequence of events following this initial phase.

Proton transfer to apical oxygen

With none of the above mentioned starting structures, peroxide–vanadium bond could be formed at apical position of TBP with the following outcome — A proton transfer from hydrogen peroxide to apical oxygen of TBP could not be sustained, as in all calculations transferred proton swiftly returns to hydrogen peroxide without formation of peroxide–vanadium bond. Forcing a proton transfer by freezing the coordinates of transferred proton in a position bonded to apical oxygen while trying to make a V–OOH bond results in cleaving of imidazole–vanadium bond without leading to any stationary point with intact imidazole–vanadium bond. In this regard our findings are in contrast with an earlier

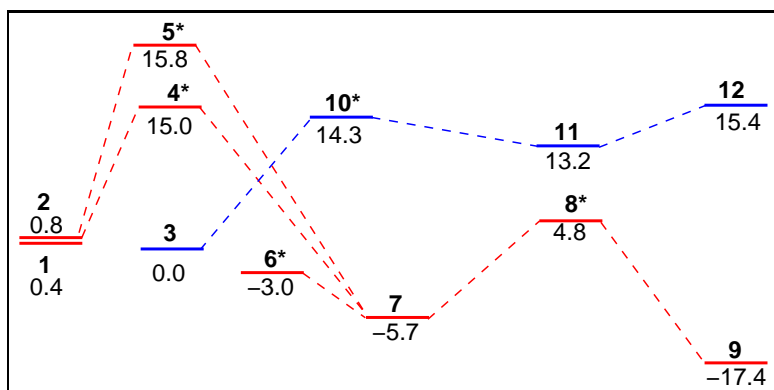


Figure 5.3: Energy profile for peroxide attack on monoanionic TBP vanadate species. All values in kcal mol⁻¹, and show difference of energy from 0.0 kcal mol⁻¹.

report,²³¹ where a transition state was proposed in which hydrogen peroxide transfers a proton to apical OH with simultaneous V–OOH bond formation. It can be said that proton transfer to apical position, at least in gas phase calculations, does not accompany simultaneous peroxide–vanadium bond formation. Moreover even with forced proton transfer, expulsion of apical water molecule concerted with V–OOH bond formation does not occur, and instead HO₂⁻ species replaces imidazole. We would like to add that stabilisation of free HO₂⁻ by enzyme environment may make formation of apical peroxide–vanadium bond possible after the expulsion of water molecule from apex.

Water expulsion from equatorial plane

A proton transfer from hydrogen peroxide to one of equatorial oxygen atoms of TBP vanadate results in formation of vanadium–peroxide bond leading to different products. Fig. 5.2 shows various stationary points encountered during the formation of vanadium bound peroxide species **9**, **11**, and **12** starting from hydrogen bonded complexes **1**, **2** and **3**. Energy profile of these changes is presented in Fig. 5.3. It is clear that formation of peroxovanadium species **9** occurs in two steps (red lined route), each involving eviction of a water molecule from the metal centre. The first water expulsion occurs in the equatorial plane and corresponds to saddle points **4*** and **5***, which are almost equal in energy but different in orientation of imidazole ring with respect to vanadate. Other water expulsion undergoes through saddle point **8***. In **4***, O5 atom of peroxide approaches the metal at a distance of 263.9 pm and aligns itself near O1 in the equatorial plane (bond angles O5–V–O1 = 59.0°, O5–V–O3 = 82.3°, O3–V–O4 = 110.1°, and dihedral O5–V–O1–O4 = 164.0°). An underway proton transfer from peroxide O5 to O1 is nearly complete as shown by the distances of proton to these oxygen atoms. Moreover O1–V distance in **4*** is elongated in comparison to that in **2** by 32.6 pm. This transition state sinks into a minimum **7**, but before that evicted water molecule has to be removed or transferred to a position as in **7** so that ligands in equatorial plane can freely rotate to align newly bonded peroxide (O5–O6) in energy minimum position i.e. in the plane of imidazole ring. This is achieved by crossing a local energy maximum **6***, as the imaginary frequency associated with **6*** reveals that

this saddle point corresponds to conformational rotation of equatorial plane around V–N bond.

CPMD trajectories of atoms in vanadium coordination shell for **4*** are shown in Fig. B.1 (see Appendix). Bond distances V–O3, and V–O4 were found to be stable and are not shown. Fig. B.1(A) shows decomposition of **4*** into reactant basin. At about 0.1 ps deprotonation of O1 occurs as proton goes back to O5, shown by divergence of H–O1 and H–O5 bond distances. This is closely followed at 0.15 ps by V–O1 distance reaching an average value of 200 pm, which is very close to V–O1 bond distance in **1**, **2** and **3**. About simultaneously O5 breaks away. Another feature is a weak V–N bond which gradually breaks at the simulation temperature beyond 0.2 ps reaching a value of 350 pm at 0.7 ps.

Trajectories for reverse process are shown in Fig. B.1(B), where protonation of O1 becomes permanent at 0.15 ps, which then breaks away from metal centre as a water molecule, while O5 simultaneously closes in to vanadium, ultimately reaching an average (V–O5) distance of 200 pm by the end of simulation. V–N bond again shows the same decomposition trend showing that species similar to **6*** and **7** may not last longer than necessary to proceed along the reactive path. Role of enzyme active site in neutralising negative charge on anionic oxygen atoms around vanadium may be important for maintaining a stable V–N bond.

Another saddle point **5*** (Fig. 5.2), similar to **4*** but with a different conformation of imidazole ring with respect to metal centre lies close in energy to **4***. In this structure O5 atom approaches the metal by about 11 pm closer than in **4***. Besides, O1–V distance is about 6 pm longer in comparison to that in **4*** and position of proton between O5 and O1 is also slightly shifted. Other geometric parameters for **5*** are: O5–V–O1 = 58.9°, O5–V–O3 = 84.8°, O3–V–O4 = 109.6°, and O5–V–O1–O4 = 166.8°.

Second water expulsion from apex

Next step involves closure of peroxo ring in **7** via **8*** with simultaneous proton transfer from O6 to apical O2, before finally achieving bidentate ligation of peroxide as seen in energy minimum **9**. The saddle point **8*** is characterised by loosely bonded oxygen atoms O2 and O6, and leads to **9** by expulsion of O2 as water molecule.

The bond angle O6–O5–V as an indicator of side-on coordination of peroxide assumes values 114.3°, 81.3°, and 64.9°, in the same order along the sequence **7**, **8***, and **9**. Moreover, alignment of O5–O6 axis with V–N bond, as indicated by O6–O5–V–N dihedral, shows how the O5–O6 bond changes orientation while η^2 coordination develops along the same sequence of structures. The value of this dihedral are 161.0°, 137.6° and 175.8° for **7**, **8*** and **9** respectively. It is obvious that presence of apical water molecule in **8*** forces the partially η^2 coordinated peroxide to remain (relatively) close to a perpendicular orientation with respect to V–N axis. After the expulsion of apical water molecule, completely side-on

coordinated peroxide aligns parallel to V–N axis in **9**. It is interesting to note that dioxo angle O3–V–O4, in structures **1** to **9** is almost preserved, the values of which in order are: 111.0°, 111.1°, 111.8°, 110.1°, 109.6°, 113.7°, 110.2°, 114.8°, 114.4°.

Energetically, first water expulsion requires to surpass a barrier, about 15.0 kcal mol^{−1} higher from the lowest energy starting structure, while second water expulsion offers a barrier of 10.5 kcal mol^{−1} measured as energy difference between **7** and **8*** (Fig. 5.3).

Endothermic formation of octahedral species

Other reactive route in Fig. 5.3 (blue lined) does not result in any of water dissociations, but rather in formation of octahedral peroxo species **11**. The saddle point **10*** is characterised by peroxide atom O5 approaching vanadium at a distance of 252.9 pm and angle O5–V–O3 with a value of 65.5° while simultaneously transferring proton to O3. The values 168.2° for dihedral O5–V–O1–O4, and 169.1° for O5–V–O3–O4 show that atoms O1, O3, O4, and O5 are arranged in a coplanar fashion. This saddle point offers a barrier isoenergetic to one discussed before (**4***) for water expulsion from equatorial plane. The product **11** lies higher in energy than any of reactant species **2**, **3**, or **1**. Another octahedral minimum **12** was also found which is slightly less stable compared to its isomer **11**. Attempts were made to transfer a proton from O6 to O1 or O2 to evict a water molecule in both **11** and **12**, and to see if this leads to bidentate ligation of metal by peroxide. This, however, always leads to cleaving of V–N bond without leading to any fruitful results.

5.3.2 Peroxide attack on the neutral vanadate species II with apically coordinated water

It has been found that catalytic cycle of VHPO involves consumption of a proton. It was further postulated that this occurs as protonation of one of oxygen atoms belonging to vanadate prior to peroxide attack. The fact that apical oxygen of vanadate lies in hydrogen bonding distance to His404, leads to speculation about acid-base catalytic role of this residue. In fact a recent report²⁵¹ suggests that protonation of apical OH group of vanadate, forming an apically coordinated water, is energetically viable. Moreover, the results in Sec. 4.4.2 suggest that apical OH group in TBP vanadate can be protonated due to proton transfer from imidazolium cation hydrogen bonded to it. Does such prior protonation lead to kinetic advantage in formation of peroxovanadium species? This section attempts to answer this question while discussing peroxide attack on the neutral pentacoordinated vanadate species (**II** in Fig. 5.1). Energy minima for starting structures are given as **13**, **17**, **19** and **20** (Fig. 5.4). In these structures hydrogen peroxide is hydrogen bonded to neutral vanadate species in different orientations. In structures **13** and **20**, hydrogen peroxide lies in equatorial plane to donate two hydrogen bonds to oxygen atoms in equatorial plane of

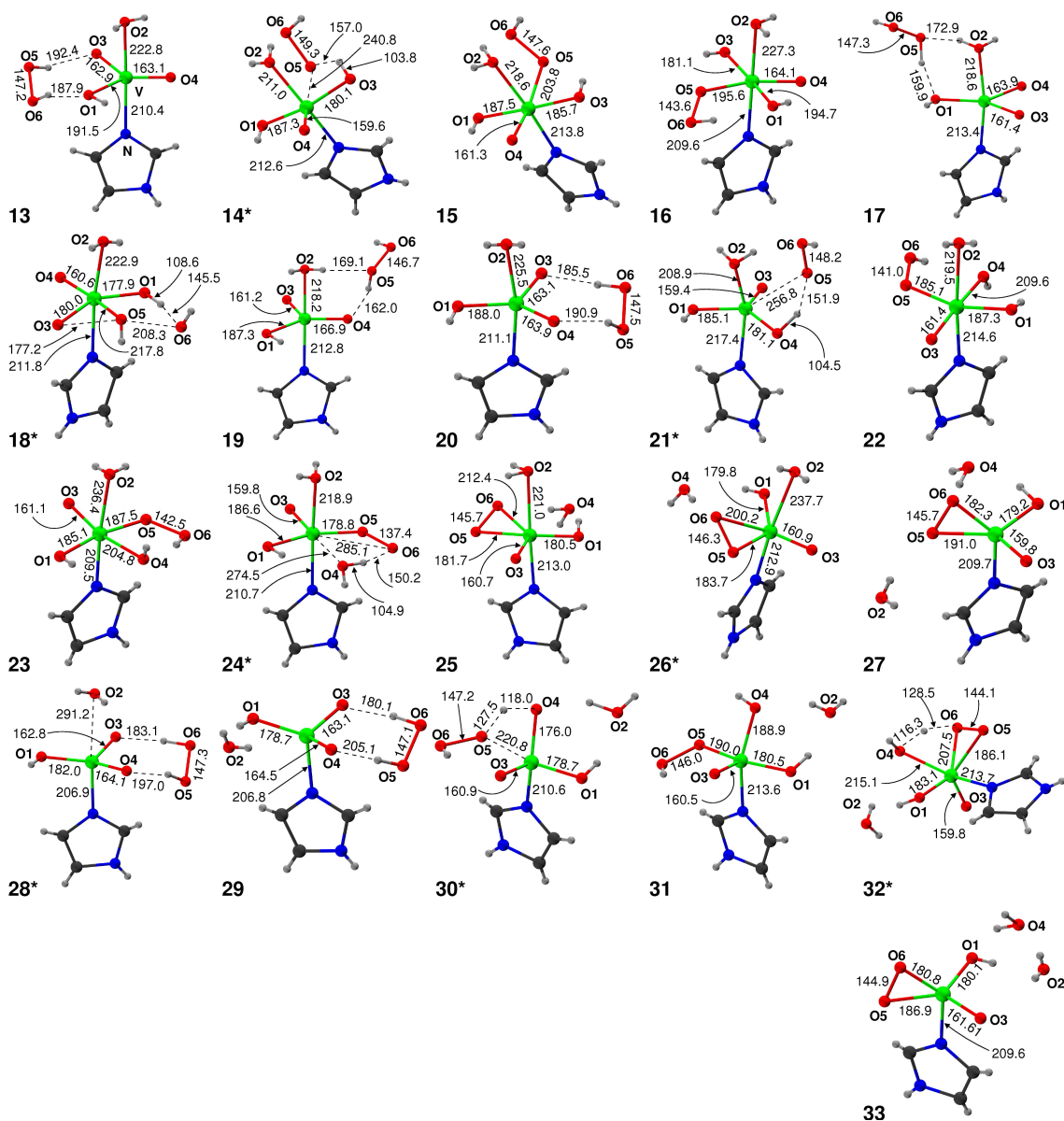
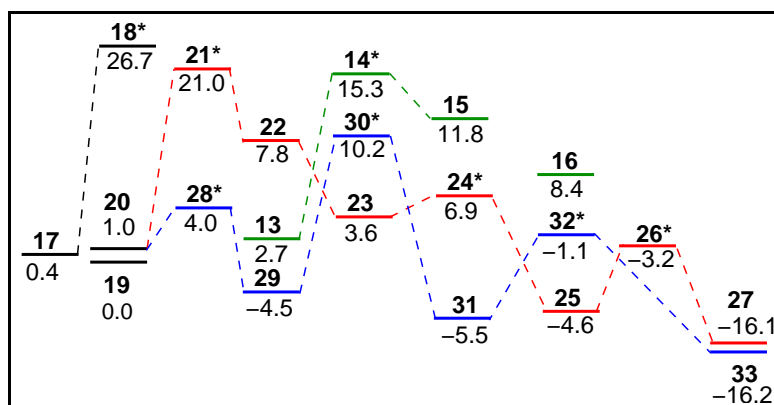


Figure 5.4: Representation of optimised stationary points along the reaction coordinate for attack of peroxide on neutral pentacoordinated dihydrogen orthovanadate ((II) in Fig. 5.1). All distances in pm. Structures with * denote a saddle point.

Figure 5.5: Energy profile for peroxide attack on neutral TBP vanadate species. All values in kcal mol^{-1} , and show difference of energy from $0.0 \text{ kcal mol}^{-1}$.



vanadate species. On the other hand **17** and **19**, have hydrogen peroxide in an orientation where it donates one hydrogen bond to oxygen atom in equatorial plane while receiving a hydrogen bond from coordinated water at the apex. As seen in discussion in previous section, formation of peroxovanadium bond accompanies proton transfer from hydrogen peroxide to a vanadate oxygen atom. This is again the case for reactive channels discussed in this section, and depending upon the oxygen atom to which proton is transferred, different possibilities arise. Optimised stationary points for this discussion are presented in Fig. 5.4 and their energy profile in Fig. 5.5.

Endothermic formation of octahedral monodentate peroxovanadium species 15 and 16

Proton transfer from O5 to O3 in **13**, Fig. 5.4 gives rise to reactive channel in Fig. 5.5 connecting structures **13**, **14***, **15** and **16**. The saddle point **14*** offers an energy barrier 15.34 kcal mol⁻¹ above the zero in Fig. 5.5. Height of this barrier is not very different than those encountered for peroxide attack on anionic vanadate discussed in previous section. It shows alignment of peroxide at a distance of 240.8 pm from vanadium and with a value 69.4° of angle O5–V–O3. The values for dihedrals O5–V–O1–O4 and O5–V–O3–O4 are 175.8° and 175.4° respectively, indicating the formation of equatorial plane of octahedron. The octahedral products **15** and **16** do not lead to desired bidentate peroxovanadium species as all attempts to close the peroxo ring (O5–O6–V), starting from these structures failed and lead to cleavage of V–N bond.

Formation of bidentate peroxovanadium species via octahedral intermediate species

An interesting but high energy saddle point **18*** (Fig. 5.4) is observed. Starting from energy minimum **17** hydrogen peroxide aligns laterally in equatorial plane of TBP between O3 and O1. In **18***, peroxide O5–O6 bond cleaves homolytically, while O5 forms bonds with V and O3, and O6 receives proton from O1. Such a transition state may ultimately end up in bidentate peroxovanadium species, where O5 remains protonated but obviously O–O cleavage makes **18** much higher in energy compared to other reactive paths discussed below. Because of this reason, this path was not further pursued.

The reactive channel connecting **20**, **21***, **22**, **23**, **24***, **25**, **26***, and **27** in Fig. 5.5 arises due to proton transfer from O5 to O4 in **19** or **20** (Fig. 5.4). The saddle point **21*** is 21.03 kcal mol⁻¹ above the zero (Fig. 5.5) and O5 atom of incoming peroxide approaches V at a distance of 256.8 pm but not quite in equatorial plane of TBP as dihedrals O5–V–O4–O1 and O5–V–O3–O1 have the values 149.1° and 149.2° respectively. This structure converts to minimum **22** in octahedral geometry, which further loses energy to form relatively stable octahedral conformer **23**. It is worth noting that apart from different orienta-

tion of imidazole ring around apical axis, **22** also differs from **23** in O2–V distance which is 219.5 pm for the former, but in later O2 is only very loosely bound to V at 236.4 pm. It may be anticipated that apical water molecule can be easily lost from **23** giving rise to a structure resembling more stable **31** (Fig. 5.4), and hence diversion of this reactive path to one to be discussed in next subsection. An internal proton transfer from O6 to O4 in **23** undergoes through a barrier corresponding to **24*** causing breakage of V–O4 bond (bond distance 274.5 pm). Saddle point **24*** is only 3.31 kcal mol^{−1} above **23** in energy and it shows apical water again becoming strongly coordinated to V with V–O2 distance of 218.9 pm. The ultimate breakaway of water (H–O4–H) affords closure of O5–V–O6 ring by formation of V–O6 bond in **25**. The minimum **25** is stabilised by 11.55 kcal mol^{−1} compared to **24*** with O5–V–O6 ring still being closer to equatorial plane as exhibited by dihedrals O6–O5–V–N (110.5°), O6–O5–V–O3 (152.7°) and O5–O6–V–O1 (162.1). Change of these values in the same order to 131.1°, 134.8°, and 146.9° respectively (i.e. relative straightening up of peroxo ring) and elongation of V–O2 to a value of 237.7 pm, results in saddle point **26*** which is only 1.42 kcal mol^{−1} higher above **25** in energy. Completion of this process is culminated in bidentate peroxovanadium species **27** where peroxo ring is completely coplanar with V–N bond with a value of 179.0° for dihedral O6–O5–V–N and apical water molecule is completely eliminated.

Picture emerging from above discussion is also supported by CPMD trajectories of atoms in vanadium coordination shell for **21*** (Fig. B.2) and **24*** (Fig. B.3). For **21***, trajectories for falling back to reactant basin, Fig B.2(A), show deprotonation of O4 and onset of O5 breakaway in 0.1 ps. In contrast to anionic species, in this case apical water molecule makes a difference and V–N bond remains stable in the duration of simulation. Interestingly, apical water molecule is not evicted but remains coordinated to metal as shown by stable V–O2 distance. In Fig. B.2(B), the forward process of formation of species like **22** and **23** is shown. Within 0.1 ps protonation to O4 becomes permanent and O5 closes in to vanadium: by 0.2 ps it reaches the average value close to V–O5 distance in **22** and **23**. V–N bond also remains stable. So is V–O2 but it tends to dissociate by the end of simulation as its average value resembles more like V–O2 distance in **23**. Fig. B.3 shows the movements of atoms in vanadium coordination shell for **24***. In Fig. B.3(A) falling back of **24*** to octahedral species like **23** is seen. Proton between O6 and O4 reaches a point equidistant to both O4 and O6 by 0.2 ps, from which point trajectories for H–O4, and H–O6 diverge. After fluctuating periodically until at around 0.5 ps proton remains permanently attached to O6. At about 0.1 ps O4 closes in to vanadium, until maintaining a stable average bond distance till the end of simulation. All other bond distance remain stable including V–O6. The forward process is shown in Fig. B.3(B). Proton remains bonded to O4, which is expelled as water molecule at about 0.1 ps, while O6 gradually bonds to vanadium thus closing peroxo ring. In the duration between 0.1 ps to 0.4 ps, bond distances show similarity to

species **25** and **26***. From 0.4 ps on, apical water molecule is expelled as seen by gradually widening V–O2 distance and stable species **27** is formed.

Formation of bidentate peroxovanadium species via tetrahedral intermediate species

For attack of peroxide on vanadium, after elimination of apical water, reactive channel connecting **20**, **28*** through **33** (Fig. 5.4) is presented in Fig. 5.5. It is obvious that apical water molecule can be easily expelled as **28*** offers a small barrier of 3.96 kcal mol⁻¹ above the zero, and more stable tetrahedral species **29** may be readily formed. Transition of TBP to tetrahedral geometry can be readily seen by inspection of angles O1–V–N, O3–V–N, O4–V–N, with values in same order for: **20** (89.6°, 95.2°, 96.9°), **28*** (98.4°, 100.2°, 102.8°), and **29** (105.9°, 105.3°, 107.0°). We would like to add that another TBP isomer of **29** was found in which hydrogen peroxide occupies the apex of TBP with one of its oxygen atoms located at 229.2 pm from vanadium. This structure was found to be 3.10 kcal mol⁻¹ higher in energy than **29**. Formation of peroxo–vanadium bond is carried through **30***, where at V–O5 distance of 220.8 pm, proton transfer from O5 to O4 is underway. Barrier height of **30*** from **29** is 14.68 kcal mol⁻¹, not very different from the one calculated for peroxo–vanadium bond formation (and water expulsion) for anionic species **I** in Fig. 5.1 (Sec. 5.3.1). Completion of V–O5 bond formation and proton transfer to O4 is seen in **31**, which is a pseudo square pyramid with either imidazole ring or O3 can be variously ascribed as occupying the apex. Comparison of angles O1–V–N, O3–V–N, O4–V–N, and O5–V–N in **30*** and **31** is given in this order as: **30*** (91.3°, 106.9°, 128.9°, 79.657°), **31** (86.2°, 104.4°, 136.7°, 84.8°). Other angles, O1–V–O3, O4–V–O3, O5–V–O3 are for **30***:- 110.0°, 113.4°, 92.3° and for **31** :- 107.1°, 118.3° and 98.0°. Closure of peroxo ring (O5–O6–V) is carried through **32*** with an internal proton transfer from O6 to O4 and expulsion of water molecule, resulting in final bidentate peroxovanadium species **33**. This process has to surpass a small energy barrier of 4.39 kcal mol⁻¹. In structure **32***, peroxo ring is neither coplanar with V–N bond nor perpendicular to it, while in **33** it is coplanar with V–N bond as shown by O6–O5–V–N dihedral which has a value of 156.9° for the former and 178.1° for the later.

Connection between these stationary points as described above is supported by CPMD trajectories of atoms in **30*** and **32***. These are presented for **30*** in Fig. B.4. In Fig. B.4(A) bond distances show conversion of **30*** to **29** as proton gets attached permanently to O5 followed by breaking away of V–O5 connection. Opposite and forward process of conversion from **30*** to **31** is shown in Fig. B.4(B) where protonation of O4 becomes complete before 0.1 ps, while at 0.1 ps O5 forms bond with vanadium. All other distances, including V–N remains stable throughout simulation in both reverse and forward trajectories. Similar data for **32*** is presented in Fig. B.5. Part A of the figure shows taking

back of proton by O6, and opening of peroxo ring at 0.1 ps as shown by H–O6 and V–O6 distances. Inspection of same distances in part B of the figure depicts forward process of water eviction and formation of bidentate peroxovanadium species.

5.3.3 Formation of peroxovanadium species from tetrahedral vanadate

As shown in Sec. 5.3.1, attempts to make an attack of hydrogen peroxide on the apical position of anionic trigonal bipyramidal vanadate structures resulted in cleavage of adducts at imidazole–vanadate bond. This prompted us to look at the possibility of peroxide attack on tetrahedral vanadate i.e. without fifth coordination by imidazole, the product of which may later simply cap over the imidazole ring to form pentacoordinated peroxovanadium species. The resulting stationary points are presented in Fig. 5.6. Formation of peroxovanadium bond and expulsion of water molecule i.e. formation of **35*** from **34**, requires overcoming of barrier of 19.89 kcal mol^{−1}. The saddle point **35*** is characterised by partial proton transfer from peroxo oxygen atom O5 to OH group of vanadate and formation of V–O5 bond. Energy for this saddle point when compared to similar barriers with reaction of pentacoordinated vanadate (previous sections) shows that imidazole coordination to vanadate reduces the height by about 5 kcal mol^{−1}. Closure of O5–V–O6 ring in **36** by internal proton transfer from O6 to O2 and expulsion of another water molecule could not be detected.

Capping of peroxo-vanadate moiety in **36** over imidazole ring to produce **37**, passes through a saddle point which is 8.9 kcal mol^{−1} higher in comparison to sum of the energies of individual optimised structures of reactants (end-on peroxovanadate moiety of **36** and imidazole). The **37** is however only 0.6 kcal mol^{−1} stable compared to this saddle point indicating that **37** would cleave almost barrierlessly at vanadium–imidazole bond.

Attempts to close the peroxo ring in **37** resulted in cleavage of imidazole–metal bond without forming any desired (bidentate) peroxovanadium species. Similarly capping of end-on peroxovanadium moiety of **36** on imidazole in a lateral form, to give an end-on bound

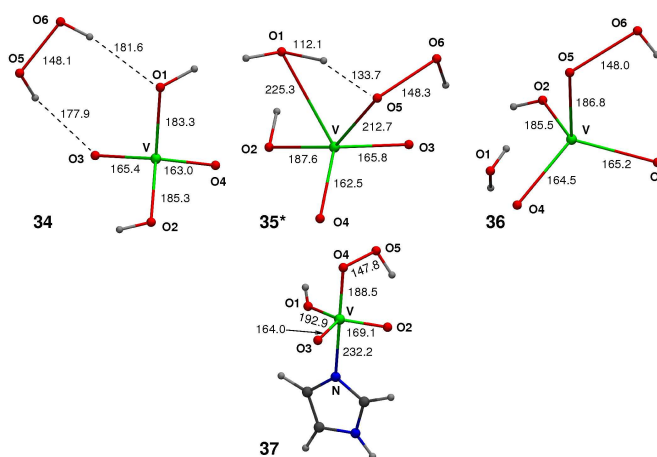


Figure 5.6: Representation of optimised stationary points for reaction of hydrogen peroxide with tetrahedral dihydrogen orthovanadate, distances in pm.

peroxo group like in **7** occurred with a barrier of 10.1 kcal mol⁻¹, and decomposition of capped structure backwards occurs with much ease as it is stable only by 1.5 kcal mol⁻¹ compared to the barrier.

5.3.4 Electronic character of peroxo–vanadium bond formation

As the results in previous sections show, peroxo–vanadium bond formation involves proton transfer from hydrogen peroxide to oxygen atom already bonded to metal centre and this proton accepting oxygen atom may be expected to be identified as nucleophilic centre on account of change in its negative charge that accompanies the formation of corresponding transition state. However since this also involves alteration in coordination to metal centre, it would be interesting to know if vanadium atom participates in change of electronic interactions over the reaction barrier. This may be expected as charge is free to flow between all metal bonded oxygen atoms because of resonance and inductive effect across the vanadium centre. The results in present section i.e. the investigation into electronic populations of ELF basins show that structural features characterising transition state does not affect the electronic character of metal centre and all the changes occur in outer sphere. This is primarily because, ELF description of metal–oxygen bonds in present systems show their highly ionic nature.

ELF basin populations for starting species

Table 5.1 summarises the basin population for the atoms in vanadium coordination shell of starting structures. It is notably evident that similarity of chemical composition of these structures is reflected in nearly constant number of electrons in corresponding basins. Population in vanadium core (close to 20.30) show the diminishing extent of positive charge on metal cation relative to formal oxidation state (+V) of vanadium because of coordination by oxygen atoms and imidazole. Similarly the sum of basin populations on each coordinated oxygen atom show high negative charge on them, implying the highly polarised nature of V–O bond. This is in agreement with earlier works which have reported the vanadium core population of 20.45 for vanadium (V) oxide,²⁵² and 21.0 for vanadium (III) oxide.²⁵³ More strikingly absence of any bisynaptic $V(O,V)$ basins indicates the ionic nature of V–O bonds, a confirmation of earlier findings on vanadium oxide systems.²⁵⁴ Only covalent bond involving vanadium atom is V–N bond with a $V(N,V)$ basin containing electronic population greater than 2. Moreover the position of ELF attractor in this basin lies closer to N atom, with distance range of 66 to 69 pm from N atom and above 143 pm from V atom in all the listed structures, indicating a donor-acceptor nature of this bond. The anionic (**2**, **3**, **1**) and neutral species (**13**, **17**, **19**, **20**) can be contrasted by the fact that population in $V(N,V)$ is slightly increased, and the position of ELF attractor in this basin is drawn closer to vanadium atom by upto 35 pm for the neutral species. Besides this, the

Table 5.1: Population in ELF basins for starting species. *C*, and *V* denote the core or valance basins. Each basin is located closest to the atom(s) enclosed in parenthesis.

	1	2	3	13	17	19	20
<i>C</i> (V)	20.27	20.31	20.30	20.30	20.33	20.31	20.31
<i>C</i> (O1)	2.19	2.18	2.19	2.18	2.19	2.18	2.17
<i>V</i> (O1)	5.93	5.94	5.93	5.89	5.89	5.86	5.87
<i>V</i> (O1,H)	1.68	1.70	1.70	1.70	1.71	1.70	1.70
<i>C</i> (O2)	2.19	2.18	2.18	2.17	2.17	2.17	2.18
<i>V</i> (O2)	5.89	5.89	5.89	4.32	4.34	4.34	4.33
<i>V</i> (O2,H)	1.71	1.71	1.71	1.75	1.77	1.77	1.75
<i>V</i> (O2,H)				1.75	1.75	1.76	1.75
<i>C</i> (O3)	2.18	2.18	2.18	2.19	2.17	2.19	2.18
<i>V</i> (O3)	7.06	6.99	7.01	6.93	6.90	6.89	6.93
<i>C</i> (O4)	2.16	2.19	2.19	2.19	2.19	2.17	2.18
<i>V</i> (O4)	6.98	6.97	6.97	6.94	6.95	7.05	6.97
<i>C</i> (N)	2.15	2.16	2.16	2.16	2.17	2.17	2.17
<i>V</i> (N,V)	2.76	2.77	2.77	2.83	2.82	2.82	2.84
<i>C</i> (O5)	2.17	2.18	2.18	2.18	2.18	2.18	2.18
<i>V</i> (O5)	4.95	4.95	4.94	4.92	4.86	4.84	4.90
<i>V</i> (O5,H)	1.71	1.72	1.73	1.72	1.77	1.77	1.75
<i>C</i> (O6)	2.19	2.19	2.17	2.17	2.18	2.18	2.19
<i>V</i> (O6)	4.94	4.94	4.95	4.90	4.92	4.90	4.92
<i>V</i> (O6,H)	1.72	1.72	1.73	1.75	1.70	1.72	1.72
<i>V</i> (O5,O6)	0.48	0.48	0.48	0.49	0.49	0.51	0.49

presence of an extra proton at atom O2, redistributes the valence population of this atom for neutral species as shown by its value in *V*(O2) basins. It should be remembered that a bound proton lies in the basin of its bond to heavy atom and its own valence basin is indistinguishable.

ELF description of peroxo–vanadium bond formation

As a typical case, the successive changes in ELF basins for events leading to formation of peroxo–vanadium species **9**, starting from anionic species **2** are reflected in values of change in basin population as listed in Table 5.2. Remarkably the vanadium core basin population remains unperturbed during ligand substitution in its coordination sphere as shown by the magnitude of change which remains insignificant within the margin of numerical error. This clearly shows that chemical change is affected by charge migrations in coordination sphere atoms as obvious from changes in valence basins of oxygen atoms involved in proton transfer.

The data in Table 5.2 should be seen in conjunction with $\eta(r)$ contours depicted in Fig. 5.7. Upper panel in the figure shows the contours in plane containing O5–O6 (peroxide) bond, while in lower panel contours are drawn in equatorial plane of TBP. The concerted event of first (O5 to O1) proton transfer and V–O1 cleavage can be clearly seen from

Table 5.2: Change in populations of ELF basins along reaction coordinate for formation of peroxo-vanadium species **9**. *C*, and *V* denote the core or valence basins. Each basin is located closest to the atom(s) enclosed in parenthesis.

	2 → 4*	2 → 5*	4* → 7	5* → 7	7 → 8*	8* → 9
<i>C</i> (V)	0.02	0.02	−0.03	−0.02	0.06	−0.03
<i>V</i> (O1)	−1.44	−1.35	0.03	−0.06		
<i>V</i> (O1,H)	0.05	0.04	−0.06	−0.05		
<i>V</i> (O2)	−0.04	−0.04	0.03	0.01	−1.43	
<i>V</i> (O2,H)	−0.01	0.00	−0.06	0.00	0.05	
<i>V</i> (O5)	1.47	1.44	−0.04	−0.01	−0.03	0.03
<i>V</i> (H5)	0.52	0.43				
<i>V</i> (O1,H5)	1.17	1.21	0.52	0.48		
<i>V</i> (O6)	−0.01	−0.02	0.00	0.01	1.44	−0.06
<i>V</i> (O6,H6)	0.03	0.03	−0.03	−0.03		
<i>V</i> (O2,H6)					1.72	
<i>V</i> (O5,O6)	−0.03	−0.03	0.03	0.02	−0.08	−0.21

topological changes in $\eta(r)$ that occur while going from **2** to **5***. In **2**, the valence basins *V*(O5,H5) and *V*(O1) are in contact in a hydrogen bonding situation but in **5*** proton breaks free of O5. As a result *V*(O5,H5) vanishes and two new basins are created: an independent *V*(H5) basin and *V*(O1,H5). The population in vanished basin is distributed among *V*(O5) and new *V*(H5). The other newly formed *V*(O1,H5) populates at the expense of *V*(O1), while overall population in *all* valence basins of O1 decreases showing that some density is migrated to *V*(H5). In other words proton H5 draws negative charge from both oxygen atoms. However this proton leaves behind considerably large negative charge in valence basins of O5, which may immediately feel the electrostatic pull from metal centre, thus leading to peroxo coordination. But since completion of peroxo coordination to metal requires movement of O5 towards metal, which would occur at much slower speed on the time scale of faster protonic vibration along the reaction coordinate. Thus stabilisation of excess negative charge on O5 by readily available hydrogen bond(s) may be crucial for minimising the probability of backwards recrossing over the saddle point towards the reactants minimum.

The second proton transfer (involving H6) before the closure of peroxo–vanadium ring follows in a similar fashion, with one difference that H6 directly associates itself with valence basin of acceptor oxygen atom because no independent basin for this proton was found in transition state **8***. It is worth mentioning that populations in the core basins, and in the basins belonging to atoms not involved in bond alterations remain virtually unchanged and hence not listed here. Moreover the peroxo–vanadium bond formation by other routes exhibit the similar pattern of charge redistribution associated with each proton transfer.

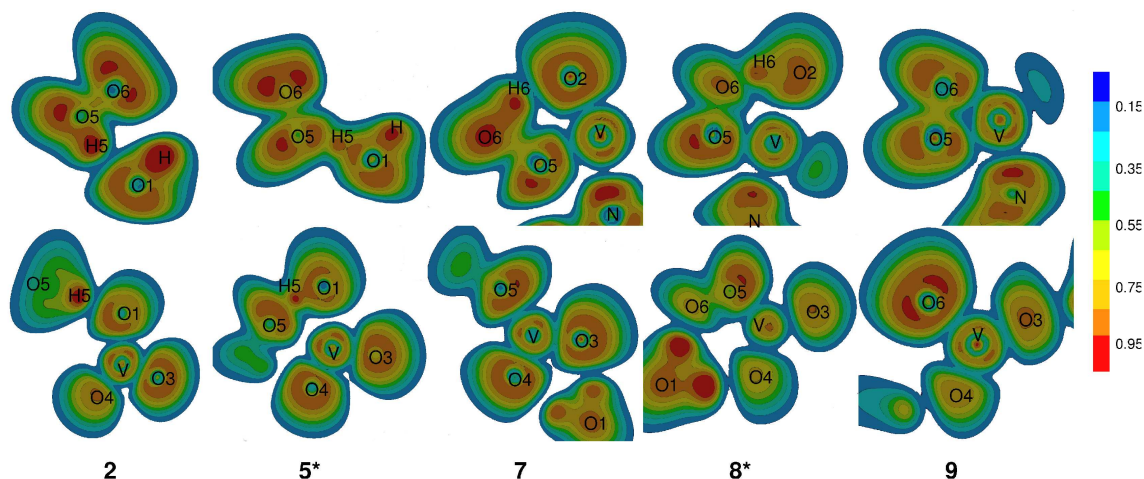


Figure 5.7: The contour diagrams of $\eta(r)$ for reaction sequence from **2** to **9**. Upper panel: plane containing peroxide O–O bond, lower panel: equatorial plane of TBP

5.3.5 Summary and Conclusions

The potential energy surface for reaction of hydrogen peroxide and imidazole bound vanadate has been explored using density functional theory in gas phase. We summarise and conclude in this section the following salient features of our findings, while focusing on Fig. 5.8. Besides, the free energies of activation and free energies of reaction for three routes leading to formation of peroxo–vanadium species are summarised in Table 5.3

1. For the reaction of hydrogen peroxide with vanadate, pentacoordination lowers the activation barrier for formation of first peroxovanadium bond. This barrier is about 5 kcal mol^{-1} higher for tetrahedral vanadate compared to that for TBP structure coordinated by imidazole.
2. Imidazole-vanadate structure in anionic form, undergoes an attack by hydrogen peroxide in equatorial plane of TBP, involving a proton transfer from peroxide to oxygen atom on vanadate. This is accompanied by peroxovanadium bond formation with water expulsion (Fig. 5.8 A) or formation of high energy octahedral species. In the former case, second peroxovanadium bond formation and expulsion of another water molecule follows in next step producing bidentate peroxovanadium species. Calculations aimed at proton transfer from hydrogen peroxide to apical oxygen of TBP did not succeed to find any stationary points. This probably shows that, for peroxide attack at apical position if possible, water expulsion from apex and peroxovanadium bond formation can not occur in concerted way.
3. Neutral TBP species with water at apical position, is attacked by hydrogen peroxide with a proton transfer from peroxide to oxygen atom in equatorial plane (Fig. 5.8 B, C). In path C, an octahedral intermediate species is formed, followed by rearrangement of metal coordination involving expulsion of two water molecules and production

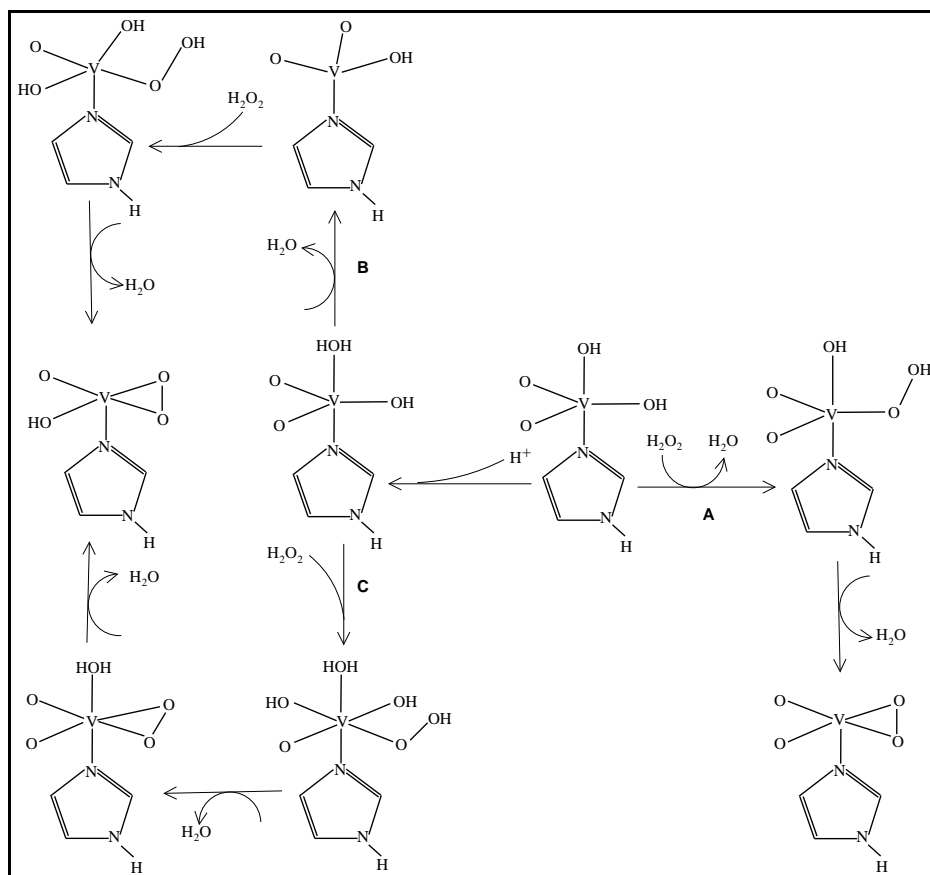


Figure 5.8: Schematic representation of reactive channels found for reaction of hydrogen peroxide with imidazole bound vanadate.

of bidentate peroxovanadium species. Alternatively apical water molecule can be first expelled (Fig. 5.8 B), forming a tetrahedral intermediate species which then undergoes an attack by hydrogen peroxide leading finally to bidentate peroxovanadium species.

- Lowest energy barrier for first peroxide–vanadium bond formation is provided by paths A and B, showing that water can be expelled from equatorial plane of TBP along with concerted peroxovanadium bond formation (path A), or both these processes can occur stepwise if a water is evicted from apical position (path B). Please compare the Gibbs free energies for reaction sequence leading from **2** to **9** with the one leading from **19** to **33** in Table 5.3.
- Inspection of CPMD trajectories calculated at 300 K for transition states show that at simulation temperature V–N bond tends to dissociate for anionic TBP structures, while a water molecule at apex of TBP (in neutral species) stabilises V–N bond.

Regarding the choice of most favourable reaction channel, the first peroxide–vanadium bond formation is energetically more demanding for which both path A and B can be equally favoured with the low energy barriers associated with them. However other considerations

Table 5.3: Gibbs free energy (of activation/reaction) in kcal mol⁻¹ at ADF-BP/TZ2P level for species involved in reactive channels (Fig. 5.8).

ΔG		ΔG		ΔG	
2 → 4*	14.18	19 → 21*	20.70	19 → 28*	2.21
2 → 5*	13.76	21* → 23	-17.16	28* → 29	-7.54
4* → 7	-21.48	23 → 24*	2.21	29 → 30*	14.23
5* → 7	-21.06	24* → 25	-10.44	30* → 31	-14.55
7 → 8*	11.11	25 → 26*	1.04	31 → 32*	2.74
8* → 9	-23.11	26* → 27	-14.27	32* → 33	-14.38
				34 → 35*	18.96

suggest that only path B may proceed fruitfully because of two reasons: One, hydrogen peroxide can approach the cofactor only through the selected entrances to active site pocket due to sterical reasons. This would limit its attack on equatorial positions of starting cofactor geometry. Two, in path A peroxide–vanadium bond formation and associated water expulsion is concerted, which would be difficult to proceed in limited available space in active site pocket. On the other hand, in path B water expulsion occurs in step wise fashion leaving enough room for subsequent peroxide attack. Specially, once the oxygen atom of apical OH in starting TBP geometry is protonated, its expulsion as water proceeds very easily as it has to overcome very low energy barrier.

Chapter 6

Reaction of Halide and Vanadium Bound Peroxide

6.1 Introduction

The primary function of vanadium containing haloperoxidase enzymes lies in the terminal catalytic phase when oxygen atom transfer is performed from metal bound peroxo group to halide ion. Present chapter deals with this phase of catalytic cycle, with the stress on the aspects that underpin the difference between active sites of VCPO and VBPO. The catalysis akin to haloperoxidase activity of VHPO in solution phase was discussed in detail in Chapter 1, and it is an accepted view that metal in the role of Lewis acid activates peroxide for nucleophilic attack. The incorporation of vanadium (Lewis acid catalyst) into VHPO active site by nature does have a greater additional advantage, and disparity of catalytic performance among VCPO and VBPO should be traced to the differences in their active sites. Some of these differences, in terms of hydrogen bonding strengths, were highlighted by results presented in Chapter 4. Since the observed crystallographic structure of the active site cavity is determined by the secondary protein environment, the contrasting hydrogen bonding patterns of two systems as determined in Chapter 4 are rather *overall* effects of differences in their respective secondary protein environments. The investigation of oxygen atom transfer step in present chapter employs models which specifically incorporate an important feature of secondary protein environment which can potentially affect the behaviour of Lys353 residue. A look at Fig. 1.1d makes it clear that residues Phe397 and His411 are the main contrasting features of two systems, and the possible hydrogen bonding between His411 and Lys may be crucial for controlling the chloroperoxidase activity of VBPO. With the models admitting this effect, the study of activation barriers for halide oxidation sheds light on different catalytic efficiency of VCPO and VBPO. Moreover the analysis of electronic character of halide oxidation allows to understand the origin of enzymatic power of VHPO active site, as opposed to Lewis acid catalysis by the bare metal in the absence of enzyme environment.

6.2 Computational Methods

The computational methods utilised to arrive at results presented in this chapter were already explained in previous chapters. The geometries optimisations were performed according to “Computational Methods” section of Chapter 5. The calculation of hydrogen bonding energies was done with supermolecular approach outlined in the Chapter 4. The aqueous solvent effects on HB energies were incorporated with COSMO approach.^{210–213} Additionally, the stationary points of some structures involved geometrical constraints which are explained here. The internal coordinates of structures in Fig. 6.1 were optimised without any constraints. The orientation of additional moieties (Lys and His) in structures given in Fig. 6.2 was constrained with reference to atoms of vanadium coordinated imidazole moiety. The constrained values of corresponding angles and dihedrals for **4** and **5***, were chosen from relative orientation of Lys353 and His496 as found in x-ray crystal structure of VCPO. For **6** and **7***, the same were chosen from relative orientation of His411, Lys341 and His486 as found in VBPO x-ray crystal structure. Same constraining strategy was also applied for optimisation of **8**, **9**, **10**, **11** and **13** (Fig. 6.3). For structure **PERCPO** (Fig. 6.3), positions of non-hydrogen atoms of amino acid residues Lys353, Arg360, Ser402, Gly403, His404, and Arg490 were fixed to crystallographic coordinates reported in x-ray crystal structure of peroxy form of VCPO, while the positions of remaining atoms were fully optimised at ADF-BP/TZP level. The analysis of $\rho(\mathbf{r})$ and $\nabla^2\rho(\mathbf{r})$ distribution and calculation of QTAIM critical points was done by using XAIM program,²¹⁴ and natural populations were calculated with NBO program.²¹⁵

6.3 Results and Discussion

6.3.1 Potential energy surface and catalysis

Description of model structures

In this section results about formation of hypohalous species in the reaction of halide ion with metal coordinated peroxide are presented. The molecular models utilised to study this reaction step are chosen to mimic the situation in VCPO active site. The crystal structure of VCPO with peroxide coordinated vanadate species in its active site shows side on coordination of bidentate peroxide ligand to metal, and reaction leading to its formation was discussed in last chapter.

Naturally this species along with halide ion is taken in present chapter as a starting point of reaction step involving oxidation of later to form hypohalous product. In this regard, three models of the reaction are presented. First, the stationary points encountered in the simplest non-enzymatic scenario are presented in Fig. 6.1. The structure **1** is starting point in which halide ion is forming a van der Waal complex with peroxy vanadate species. This is followed by transition state **2*** in which halide ion attacks one of oxygen atoms belonging

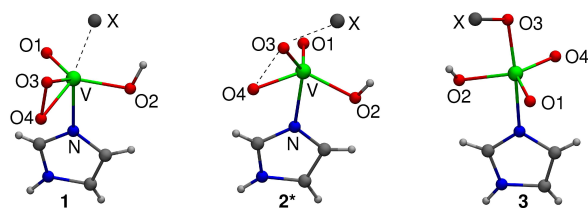


Figure 6.1: The stationary points on the potential energy surface, *non-enzymatic* model of halide oxidation. * denotes transition state. See Table 6.1 for optimised geometrical parameters of these structures.

to peroxo ligand, and finally the product represented by minimum **3** showing hypohalous ion coordinated to metal atom. The energy barrier between **1** and **2*** is taken as non-enzymatic benchmark against which influence of catalytic environment of VCPO or VBPO active site (as in the two remaining models described below) is measured. Second, based on crystal structure of peroxo form of VCPO, Lys353 residue in active site is considered to play important catalytic role in this reaction step. As mentioned in the introduction to this chapter, this is due to its donation of hydrogen bond to one of the oxygen atoms in metal bound O–O.

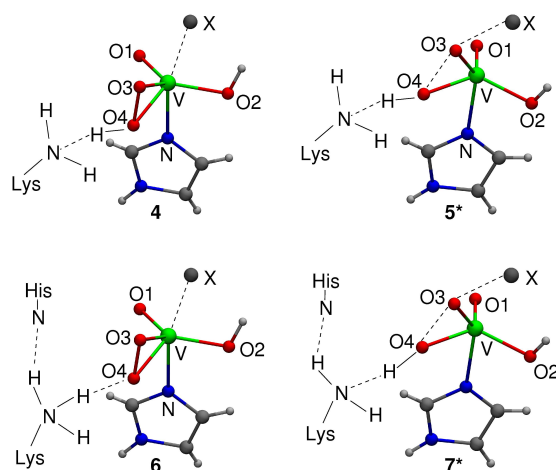


Figure 6.2: The stationary points on the potential energy surface, *VCPO-catalytic* model (**4**, **5***), and *VBPO-catalytic* model (**6**, **7***) of halide oxidation. See Table 6.1 for optimised geometrical parameters.

Inclusion of this hydrogen bond in the calculations to the simple non-enzymatic model above, for estimating catalytic role of Lys353, resulted in starting minimum **4** and transition state **5*** as shown in Fig. 6.2. Third, in VBPO which has an active site pocket identical to one in VCPO, but the corresponding hydrogen bond donating Lys residue is a member of triad composed of His411...Lys341...Vanadate forming a hydrogen bonding cascade (Fig. 6.2). Naturally Lys341 in VBPO can be expected to have an amended catalytic role in comparison to that of Lys353 in VCPO. With this situation

taken into account in calculations, gave rise to optimised geometries **6** and **7*** (Fig. 6.2). In brief, **4**, **5*** on one hand and **6**, **7*** on the other are respective analogues of **1** and **2***, with inclusion of distinctive environmental effects imparted by VCPO (**4**, **5***) or VBPO (**6**, **7***) active sites, thus allowing to compare the barrier heights of the reaction for all three cases.

Geometries: Non-enzymatic halide oxidation

The change in geometry during the reaction step under discussion can be observed by looking at calculated geometrical parameters for atoms in vanadium coordination shell for

Table 6.1: Geometries of structures **1–7** optimised at ADF/BP-TZ2P level of theory (distances in pm, angles in degrees.)

X = Br [−]							
	1	2*	3	4	5*	6	7*
r _{V–O1}	162.1	162.8	164.7	159.8	159.8	160.7	160.1
r _{V–O2}	188.3	187.2	195.1	186.3	185.3	184.9	183.9
r _{V–O3}	185.2	177.9	194.3	185.8	179.5	185.9	179.5
r _{V–O4}	185.8	178.8	164.5	197.1	198.7	193.3	197.1
r _{V–N}	223.8	222.5	228.5	222.8	217.6	221.6	216.5
r _{V–X}	271.5	317.7	323.9	258.6	268.1	266.3	278.2
r _{O3–O4}	144.4	183.8	285.7	148.0	171.8	146.3	179.1
r _{X–O3}	302.8	238.6	185.4	281.6	236.6	289.5	229.3
∠ _{X–O3–V}	62.2	98.4	117.1	63.4	78.8	133.8	84.8
∠ _{O3–V–O4}	45.8	62.0	105.3	45.4	53.7	45.3	56.6
X = Cl [−]							
r _{V–O1}	162.4	164.4	164.9	159.9	159.8	160.1	160.1
r _{V–O2}	188.7	186.1	194.8	186.7	185.1	185.2	183.6
r _{V–O3}	185.6	177.4	194.7	186.7	178.7	186.4	179.3
r _{V–O4}	185.7	176.8	164.3	197.1	197.6	193.5	195.6
r _{V–N}	225.1	224.1	227.4	223.9	217.2	222.6	216.5
r _{V–X}	250.0	306.5	310.4	238.7	254.7	245.8	265.7
r _{O3–O4}	144.3	185.1	285.6	147.1	180.6	145.9	184.9
r _{X–O3} ³	288.3	225.6	171.3	272.2	214.2	276.5	210.7
∠ _{X–O3–V}	59.0	98.3	115.8	59.3	80.3	60.5	85.5
∠ _{O3–V–O4}	45.7	62.9	105.1	44.9	57.1	45.1	58.9

structures **1**, **2***, and **3**. This can be readily observed from the values listed in Table 6.1, with substrate X being either bromide or chloride. The sequence **1**, **2***, and **3** reveals the general trend of geometrical change during the halide oxidation by vanadium bound peroxide. There are differences between geometrical parameters for chloride and bromide substrate in starting minimum **1**. The approach of Cl[−] to vanadium atom is closer compared to that of Br[−] by 21.5 pm in **1**, which may be due to larger size of Br[−] but it signals relatively larger interaction between chloride and metal. Similarly the distance between halide ion and oxygen atom belonging to peroxo ligand (O3) is larger by 14.5 pm for bromide compared to one for chloride in **1**. Formation of transition state **2*** from **1** leaves the geometrical parameters belonging to atoms not involved in bond making or breaking (O1, O2, N) unchanged, while the positions of halide (X), and peroxo oxygen atoms (O3, O4) are shifted showing O3–O4 bond breaking and X–O3 bond formation. Going to transition state **2*** from **1**, involves elongation of O3–O4 bond, shortening of X–O3 distance and elongation of V–X distance, which are given in this order for Br[−] : (39.4 pm, 64.2 pm, 46.2 pm) and for Cl[−] : (40.8 pm, 62.7 pm, 56.5 pm).

Settling of **2*** into product basin (**3**), involves changes in which O3–O4 bond is completely broken and X–O3 bond is formed resulting in TBP geometry in which oxygen atom

of hypohalous species O-X^- is apically coordinated to vanadium as can be seen in **3**. Transformation to **3** is also accompanied by slight changes in bond distances of atoms O1, O2 and N to vanadium.

Geometries: VCPO catalytic model (4 and 5*)

The trend of transformation from starting species to transition state is mimicked in model with hydrogen bond $\text{N(Lys)} \cdots \text{O(peroxo)}$ albeit with some modifications. These modifications may be helpful for understanding the catalytic role of Lys residue in case of VCPO. Presently considering **4**, the presence of aforementioned hydrogen bond causes this structure to differ from **1** in significant ways. First, O3–O4 ligand is changed to O3–O4H, because of proton transfer from positive Lys during optimisation. This feature will be discussed in detail later when hydrogen bonding geometries and energies will be discussed. Second, due to this proton transfer, V–O4 bond is elongated in **4** (by 11.3 pm for bromide substrate and 11.4 pm for chloride substrate). Also the O3–O4 bond undergoes a minor elongation (3.6 pm for bromide substrate and 2.8 pm for chloride substrate). Third, the halide ion shows closer interaction with metal and O3 in **4**. The V–Br distance is 12.9 pm shorter, while V–Cl distance is shorter by 11.3 pm in **4** compared to those in **1**. Similarly Br–O3 distance is 21.2 pm shorter, and Cl–O3 is 16.1 pm shorter in **4** compared to their respective counterparts in **1**. All these changes may be positively important for catalytic enhancement of halide oxidation by metal coordinated O3–O4 moiety. From this consideration following factors are listed for better overview, although these can also be argued as different aspects of same factor,

1. As observed for non-enzymatic case (**1** and **2***), formation of transition state requires elongation of O3–O4 distance, and closing up of halide ion to O3 atom. In presence of hydrogen bond this already happens to some extent in reactant species, thus making it more identical to geometry of transition state.
2. The $\text{O3-O4H} \cdots \text{N(Lys)}$ can be expected to have more polarised O3–O4 bond, with facilitated electron flow from halide to O3 during oxidation step.
3. The closer interaction of halide with positively charged metal atom may mediate in reducing electrostatic repulsion between negative charges of halide and atom O3 of oxidant.

This closer X–V interaction can also be argued to be counterproductive for oxidation of halide by O3–O4 moiety in case if halide to metal charge transfer causes an enhanced electrophilicity on X. But as long as halide–metal interaction remains purely electrostatic, it can be expected to play a positive role by reducing electrostatic repulsion among (O3,X) oxidant/reductant pair, which is indeed observed as shown by short X–O3 distances discussed above.

The cursory look into geometrical transformation of **4**→**5***, shows following notable changes in distances :- (a) O3–O4 is elongated by 23.8 pm for bromide complexes and by 33.5 pm for chloride complexes. (b) X–O3 distance is shortened by 45.0 pm for bromide substrate and by 58.0 pm for chloride substrate. (c) Elongation of V–X distance by 9.5 pm in case of Br[–] and by 16.0 pm in case of Cl[–]. (d) V–N distance is shortened by 5.2 pm and 6.7 pm respectively for bromide and chloride complexes.

Geometries: VBPO-catalytic model (6 and 7*)

Inclusion of His···Lys···Vanadate triad into the model, as opposed to Lys···Vanadate as was discussed above, brings into the discussion the modified catalytic role of Lys in presence of His. Consideration of reactant species **6** makes it clear that extent of changes brought by N(Lys)···O(peroxo) alone (in **4** compared to **1**) are diminished by additional N(His)···Lys(N) hydrogen bond. These are listed as follows :-

1. The proton transfer from positive Lys to O3 atom of vanadium bound peroxide is inhibited. This issue will be taken again in a subsequent section.
2. Consequently V–O4 bond elongation over its value in **1** is reduced to 7.5 pm for bromide substrate in comparison to same in **4** which was earlier reported to have a value 11.3 pm. For chloride substrate, this elongation for **6** and **4** is respectively 7.8 pm and 11.4 pm.
3. The V–X distance shortening over its value in **1** for bromide is 5.2 pm in **6** while it has a value of 12.9 pm for **4**. The same values for chloride in **6** and **4** are 4.2 pm and 11.3 pm respectively.
4. Similarly shortening of X–O3 distance over its value in **1** for bromide complex is 13.3 pm in **6** and 21.2 pm in **4**. For chloride complexes these values are 11.8 pm and 16.1 pm in **6** and **4**, respectively.

In other words, the geometrical changes brought about by N(Lys)···O(peroxo) hydrogen bond in reactant species are offset by hydrogen bond between His and Lys.

The formation of transition state **7*** from **6** occurs with similar general trend of partial cleaving of O3–O4 bond and approach of halide to O3 atom of peroxo moiety. Transition state **7*** also witnesses proton transfer from Lys, which was reported above as inhibited in starting species **6**. The delayed proton transfer (i.e. at oxygen atom transfer stage of the reaction and not prior to it, unlike in **4**→**5***) in presence of hydrogen bond of Lys with His, indicates the difficulty of its occurrence and may partly explain the inferior chloroperoxidase activity of VBPO.

The **6**→**7*** transformation takes place featured by some changes in geometrical parameters which are summarised as follows :- (a) O3–O4 distance is elongated by 32.8 pm for

bromide complexes and 39.0 pm for chloride complexes. (b) X–O3 distance is reduced by 60.2 pm and by 65.8 pm for chloride. (c) V–X is elongated by 11.9 pm for bromide and 19.9 pm for chloride. (d) V–N distance shortening, which is 5.1 pm and 6.1 pm for bromide and chloride complexes, respectively.

(Reactant)→(transition state) geometry change and catalysis

It is common to read in literature about the catalytic origin of enzymes, which is often explained on the basis that enzymes are able to stabilise the transition state involved in rate determining step better than starting reactants (misleadingly called “ground state” in literature on enzyme kinetics). A milder version of this statement would be to say that enzymes derive their catalytic power from their ability to force starting reactants in a geometry which is relatively identical to transition state. Strictly speaking the term “transition state” in such discourse corresponds to a statistical ensemble in sense of transition state theory and the single point saddle points of present work (also called transition state) are just the qualified members of such ensembles. Nevertheless it would be insightful to analyse the geometry of saddle points (**2***, **5***, **7***) described in present chapter in relation to their respective starting points in light of above mentioned statement regarding the catalytic origin of enzymes. The change in some geometrical parameters while going from starting reactant species to transition were reported for three models previously. It may seem redundant but useful to have a bird eye view of these changes for geometrical parameters corresponding to reaction coordinate, which is done as following in terms of difference (δ , pm) between their reactant and transition state values, whereas positive and negative sign indicate elongation and contraction of distance, respectively :–

	1→2*		4→5*		6→7*	
	$\delta_{\text{rO3-O4}}$	$\delta_{\text{rX-O3}}$	$\delta_{\text{rO3-O4}}$	$\delta_{\text{rX-O3}}$	$\delta_{\text{rO3-O4}}$	$\delta_{\text{rX-O3}}$
Br [–]	+39.4	–64.2	+23.8	–45.0	+32.8	–60.2
Cl [–]	+40.8	–62.7	+33.5	–58.0	+39.0	–65.8

By considering δ values in the case of bromide substrate, the non-enzymatic **1→2*** case shows the largest movement along reaction coordinate that relevant atoms have to undergo. In the instance of **4→5***, i.e. with the catalytic assistance of hydrogen bonding (and proton donating) Lys residue, reaction path in direction from reactant to transition state is cut short considerably (roughly by order of tens of pm). This catalytic advantage is curtailed if proton donating power of Lys is deteriorated because of its additional hydrogen bond with His residue, as shown by δ values for **6→7*** case.

This also applies to case of chloride substrate, but with difference. The catalytic effect of Lys in **4→5*** is much smaller compared to that for bromide oxidation and disappears almost completely in **6→7*** as δ values for this and **1→2*** cases are nearly identical.

Table 6.2: Energies (kcal mol⁻¹) for three catalytic models of halide oxidation at ADF/BP-TZ2P level of theory. Where available, values reported by Zampella *et al.*²⁵⁵ are produced for comparison.

	1→2*			2*→3		4→5*		6→7*
	ΔG	ΔE	$\Delta E, \text{ref}^{255}$	ΔG	ΔE	ΔE	$\Delta E, \text{ref}^{255}$	ΔE
Br ⁻	16.4	19.1	40.6	-18.1	-18.7	2.6	6.7	9.4
Cl ⁻	20.3	24.0	-	-19.2	-19.4	6.3	11.3	13.6

Energies along the reaction coordinate

The free energy changes ΔG , in going from **1** to **3** via **2*** are listed in Table 6.2, for the oxidation of both bromide and chloride. Expectedly chloride oxidation offers a higher free energy barrier. The comparison of activation potential energy ΔE , for three mechanistic models is also presented. The catalytic role of Lys becomes obvious by comparing barrier heights in **1→2*** and **4→5***. The ΔE for activation is reduced by nearly seven and four folds for bromide and chloride oxidation in **4→5*** respectively. In **6→7*** this catalytic benefit is reverted, i.e. barrier becomes higher in comparison to that in **4→5***, by more than three times for bromide and by two times for chloride substrates.

The relative height of activation barriers **1→2*** and **4→5*** for bromide oxidation is in line with lowering of barrier height due to Lys⁺ obtained by Zampella *et al.*²⁵⁵ with similar models. Similarly relative barrier height for bromide and chloride in **4→5*** also agrees as reported. However the absolute values of ΔE of Zampella *et al.* do not agree, being about two times larger than values reported here. This is apparently because of different reference reactant minima. Since, unfortunately Zampella *et al.* did not explicitly show the reference reactant adducts in their report, it is presently impossible to tell the detailed difference between their reference structures to ours.

6.3.2 Hydrogen Bonding Geometries, QTAIM parameters and Energies

The three mechanistic models presented in previous section operate differently because of differences in hydrogen bonding (see Figs. 6.1 and 6.2). These and other active site hydrogen bonds revealed in crystal structure of peroxo form of VCPO are the topic of present section. The Fig. 6.3 presents the optimised structures of hydrogen bonded complexes. Structures **9** and **11** are similar to **4** and **6** but were optimised without halide ion. The two other structures **8** and **10** differ in protonation state of peroxovanadate moiety. The structures **12** and **13**, along with **8** were envisioned to look into combined effects of hydrogen bonds of Lys and Arg490 with peroxovanadate. Finally the peroxo form of VCPO active site, presented in Fig. 6.3 as **PERCPO** was optimised to investigate the combined effect of all active site residues.

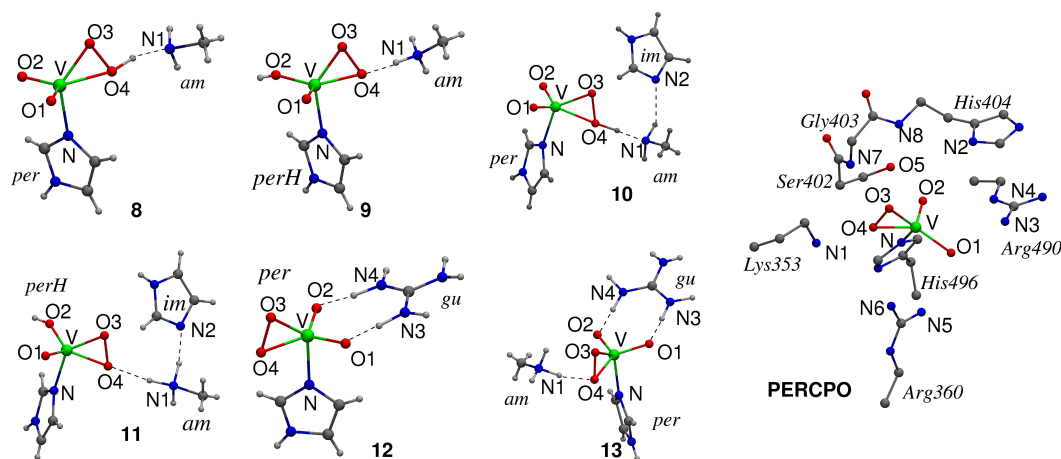


Figure 6.3: Optimised structures of HB complexes of peroxovanadate species.

Hydrogen bond geometrical and QTAIM parameters

The description of hydrogen bond geometries and QTAIM parameters at (3,−1) HB critical points (Table 6.3) is carried in two categories: The general trends in hydrogen bonding of peroxovanadate moiety with groups representing active site residues and combined effects of these HB partners. And the changes in hydrogen bonds taking place during the previously described proceeding of halide oxidation. The discussion of later will be taken first.

The changes in N(Lys)⋯O(peroxo) hydrogen bonds during the evolution of halide oxidation process to the point of formation of transition state can be observed by considering sequences (9, 4, 5*) and (11, 6, 7*). Please note that former sequence presents the reaction taking place in hydrogen bonding environment modelled after VCPO active site and later that after VBPO active site (see Sec. 6.3.1). In the former sequence the halide complexation (9→4) triggers proton transfer from N1 to O4, apparently the result of modified relative basicity of these two atoms. The proton transfer can be easily observed by inspecting the shift in N1⋯H and O4⋯H distances. Complexation to peroxovanadium is also accompanied by shortening of N1⋯O4 distance by about 10 pm. It is worth mentioning that in both 9 and 4, HB geometrical parameters indicate very strong interaction between donors and acceptors as shown by very long A–H distance and short A⋯B, H⋯B distances. In the formation of transition state 5* from 4, mentioned proton transfer achieves completion as seen by further shrinking of O4–H distance and elongation of H–N1 distance. Furthermore, N1⋯O4 distance is elongated in 5* by 12.4 pm and 16.5 pm for oxygen atom transfer to bromide and chloride respectively, over its value in 4. The inspection of QTAIM parameters for N1⋯O4 HB along the sequence (9, 4, 5*) reveals a situation interestingly in conformation with above described geometrical trends and recalling of the Popelier criteria (cf. page 56) would be useful for the description which follows. The proton transfer during 9→4 process results into a hydrogen bond (O4–H⋯N1) with (3,−1) HB critical point

Table 6.3: Calculated HB (geometrical and (3,−1) QTAIM) parameters at ADF/BP-TZ2P and B3LYP/6-311G** levels respectively, for (A,B) pairs in A–H···B hydrogen bonds (distances in pm, angles in degrees, QTAIM quantities in a.u.). Numbering scheme for atoms according to Fig. 6.3.

			$R_{A\cdots B}$	$r_{A\cdots H}$	$r_{H\cdots B}$	\angle_{AHB}	ρ_C	$\nabla^2\rho_C$	G_C	V_C	H_C
4	Br [−]	N1,O4	249.3	137.9	113.6	164.7	0.124	−0.042	0.062	−0.113	−0.051
4	Cl [−]	N1,O4	249.5	138.6	113.3	164.1	0.122	−0.034	0.061	−0.114	−0.053
5*	Br [−]	N1,O4	261.7	168.2	102.8	148.9	0.058	0.103	0.039	−0.104	−0.065
5*	Cl [−]	N1,O4	266.0	177.7	101.3	143.4	0.047	0.104	0.033	−0.092	−0.059
6	Br [−]	N1,O4	263.7	110.1	154.2	172.2	0.072	0.142	0.055	−0.146	−0.091
6	Br [−]	N2,N1	278.4	178.6	107.1	153.2	0.042	0.010	0.031	−0.086	−0.055
6	Cl [−]	N1,O4	263.4	110.3	153.8	171.9	0.073	0.141	0.056	−0.147	−0.091
6	Cl [−]	N2,N1	279.6	180.1	106.9	153.2	0.043	0.099	0.030	−0.084	−0.054
7*	Br [−]	N1,O4	263.2	157.0	106.6	173.2	0.077	0.080	0.047	−0.114	−0.067
7*	Br [−]	N2,N1	300.4	206.2	103.6	149.9	0.024	0.074	0.017	−0.052	−0.035
7*	Cl [−]	N1,O4	265.7	160.8	105.3	173.2	0.070	0.088	0.044	−0.111	−0.067
7*	Cl [−]	N2,N1	301.5	207.6	103.6	149.6	0.023	0.072	0.016	−0.051	−0.035
8		N1,O4	261.5	163.1	103.8	156.3	0.066	0.099	0.045	−0.117	−0.072
9		N1,O4	259.3	110.0	149.8	172.5	0.075	0.154	0.060	−0.159	−0.099
10		N1,O4	252.5	136.4	116.4	173.7	0.129	−0.077	0.061	−0.102	−0.041
10		N2,N1	330.0	234.2	103.7	153.0	0.013	0.038	0.008	−0.026	−0.018
11		N1,O4	304.3	104.4	201.2	168.8	0.021	0.072	0.016	−0.051	−0.035
11		N2,N1	278.0	171.5	110.4	160.4	0.053	0.089	0.034	−0.089	−0.055
12		N3,O1	256.9	111.2	145.8	178.4	0.085	0.142	0.065	−0.165	−0.100
12		N4,O2	257.8	110.4	147.4	147.4	0.081	0.145	0.063	−0.162	−0.099
13		N1,O4	254.0	115.1	141.2	164.4	0.102	0.116	0.072	−0.173	−0.101
13		N3,O1	266.8	106.2	160.7	179.6	0.056	0.148	0.047	−0.131	−0.084
13		N4,O2	272.6	105.4	167.4	176.1	0.048	0.137	0.040	−0.114	−0.074

exhibiting atypical QTAIM parameters. In **4**, ρ_C is raised significantly and $\nabla^2\rho_C$ becomes negative, showing that accumulation of charge density occurs in the H···N1 interatomic region, and HB interaction is more of covalent rather than electrostatic in nature. This is expected in the view of very short O4···N1, and H···N1 distances. A look at the values of energy densities show that V_C is slightly decreased in **4**. A relatively complete proton transfer in **4**→**5*** is characterised by **5*** assuming the values of QTAIM parameters more typical of hydrogen bonds, although a negative H_C value is an indication that some covalent character is still retained.

The trend described above, is repeated in reduced fashion in the evolution of N1···O4 hydrogen bond along the sequence (**11**, **6**, **7***). This change (explained below) is not surprising, as N1···O4 HB in **11** is weaker than the one in **9** to begin with, as shown by 45.0 pm longer N···O distance in the former. Consequently, now halide attack has to induce much larger N1···O4 shrinking in order to accomplish the required catalytic act of Lys→Peroxo proton transfer. The N1···O4 shrinking in **11** is about 40 pm for its complexation with both bromide and chloride to form **6**. Accompanying shift in position of proton relative to N1 is small and proton transfer does not happen at this stage, in contrast to one observed in **9**→**4** change reported above. The formation of transition state **7*** from

Table 6.4: Calculated HB (geometrical and (3,−1) QTAIM) parameters for (A,B) pairs in A–H...B hydrogen bonds in peroxo VCPO active site model **PERCPO**, at ADF/BP-TZP and B3LYP/6-311G** levels respectively (distances in pm, angles in degrees, QTAIM parameters in a.u.). Numbering scheme for atoms according to Fig. 6.3.

	$R_{A\cdots B}$	$r_{A\cdots H}$	$r_{H\cdots B}$	\angle_{AHB}	ρ_C	$\nabla^2\rho_C$	G_C	V_C	H_C
N1,O4	270.6	107.5	163.2	176.8	0.054	0.143	0.044	−0.125	−0.081
N2,O2	293.5	102.9	219.8	126.9	0.014	0.050	0.011	−0.035	−0.024
N3,O1	309.7	103.5	206.3	177.7	0.018	0.059	0.013	−0.041	−0.028
N4,O2	286.1	104.4	184.9	162.2	0.033	0.107	0.027	−0.080	−0.053
N5,O1	278.4	104.3	176.6	164.4	0.039	0.124	0.032	−0.096	−0.064
N6,O1	325.4	104.4	242.1	137.9	0.011	0.035	0.008	−0.024	−0.016
N7,O3	364.6	102.1	273.7	148.4	-	-	-	-	-
N7,O4	303.4	102.1	202.2	170.7	0.023	0.081	0.019	−0.058	−0.039
N8,O2	354.5	102.3	266.7	143.9	0.006	0.018	0.004	−0.013	−0.009

6 witnesses no further shortening of any note whatsoever in N1...O4 distance for both bromide and chloride attack, however this does induces proton transfer as can be easily noted from large shifts in H...O4 and N1...H distances. This is also accompanied by large elongation in N2...N1 distance in His...Lys i.e., the hydrogen bond responsible for inhibition of Lys→Peroxo proton transfer. The QTAIM parameters at (3,−1) HB critical point show that N1...O4 HB gets stronger in **11**→**6** step as indicated by higher ρ_C and $\nabla^2\rho_C$, and more negative H_C . The value of $\nabla^2\rho_C$ becomes more positive, instead of becoming negative as was noted for **9**→**4**, showing that greater HB strength is attained because of greater depletion of density at critical point, i.e. larger electrostatic pull from the nuclei connected to the critical point. The more negative H_C , however, signals that partial covalent character is also increased along. This is due more to reduction in destabilising G_C , than to increase in negative V_C as shown by the values of these quantities for **11** and **6**. To summarise the striking contrast exhibited by (halide:peroxovanadium) complexation in VCPO and VBPO models, while N1...O4 in former gets stronger by accumulating greater shared electron density at HB critical point, in later this is done by greater electrostatic interaction. The **6**→**7*** step involves decreased HB strength in terms of values of $\nabla^2\rho_C$ and H_C for the hydrogen bond under consideration.

Discussion of hydrogen bonds so far concentrated on the HB interaction of Lys353 with peroxovanadate species in context of its central place in oxygen atom transfer step. In enzyme active site, however, the role of HB interactions is not limited to Lys and other residues also play supportive role. Presently it is intended to look into general features of hydrogen bonds of peroxovanadate species by again referring to Table 6.3. Description of hydrogen bond strengths offered in Chapter 4 in terms of charge assistance and relative proton affinities of HB donor and acceptor atoms is applicable here as well. The observation of hydrogen bonds of peroxovanadate species in different protonation states makes this fact clear. Complexes **8** and **9** differ in extra proton on oxo oxygen atom, and as a result the proton involved in hydrogen bond shifts from peroxo to Lys in **9**. This effect can also be seen

in **10** and **11**. Guanidinium cation (Arg490) as an additional hydrogen bonding partner in **13** induces reverse proton transfer to Lys from peroxo group (as opposed to **8**), because it is able to sufficiently stabilise the negative charge on peroxo cofactor. The QTAIM parameters at (3,−1) HB critical points present mostly a similar picture for hydrogen bonds listed in second part of Table 6.3, except for N1...O4 hydrogen bond, which shows a negative $\nabla^2\rho_C$.

The optimised hydrogen bonding parameters for active site of VCPO in peroxo form are described in Table 6.4 according to atom numbering scheme given for **PERCPO** in Fig. 6.3. The optimised structure is based on crystallographic positions of heavy atoms in active site and care was taken to preserve the structural information available in crystal structure (see Sec. 6.2). The amino acid residues which seem to play supportive role to primary catalytic function of Lys353 are those which are in hydrogen bonding proximity to oxygen atoms in vanadium coordination shell.

Of these the most important appear to be Arg490 and Arg360, both of which hydrogen bond with oxo groups of cofactor. As seen above in **13**, hydrogen bonds of Guanidinium (analogue of Arg490 in **PERCPO**) with oxo groups tune the basicity of peroxo oxygen atoms with effect to reduce the necessity of proton transfer from Lys353. This proton transfer inevitably happens in **8** and in complexes of halide ions like **4** to **7** at certain stage of oxygen atom transfer process. This supportive role of Arg490 is present in **PERCPO** and is further augmented by Arg360 residue. The N7 atom belonging to Gly403 is within hydrogen bonding distance directly with peroxo group, and is expected to play similar role. The case of His404 on the basis of geometrical parameters of (N2,O2) pair is somewhat ambiguous: though N2...O2 distance is short enough to form a hydrogen bond, the $\angle N_2HO_2$ angle is far from linear, so geometrical parameters alone are not sufficient to predict the existence of hydrogen bond. The bond critical point for this hydrogen bond is however detected and its QTAIM parameters signal a fairly strong hydrogen bond. Same is not true for (N7,O3) pair, which despite having a relatively linear arrangement of atoms does not exhibit bond critical point due to long N7...O3 distance. The donor atom (N7) is found to donate hydrogen bond to O4 peroxy oxygen atom as bond critical point for it is detected.

Hydrogen bonding energies

The hydrogen bonding interaction energies of the pentacoordinated peroxovanadate species with enzyme environment are the subject of present section. This is started with small model complexes, and interaction of Lys residue with peroxovanadate species (Table 6.5) is considered in the sequences **9**, **4**, **5*** and **11**, **6**, **7***.

The interaction energy for N1...O4 hydrogen bond in **9** is $-35.3 \text{ kcal mol}^{-1}$ and $-4.5 \text{ kcal mol}^{-1}$ in gaseous and aqueous (COSMO, dielectric constant = 78.34) phases respectively. The large difference of values in two phases is because this hydrogen bond involves ionic attraction between cationic Lys donor and peroxo group. Low COSMO value is a reflection

Table 6.5: HB energies (kcal mol⁻¹) at ADF/PBE-TZ2P level of theory. For (1 : 1) complexes **4**, **5*** and **9**, listed values are also their total HB energy. For **6**, **7***, and **11**, total HB energy $\Delta E^{V,X}$ is split into terms (with i =Lys, labelled as *am* for **9**, **11**) according to Eq. 4.6.

		Gas phase				Aqueous (COSMO) phase			
		$\Delta E^{V,i}$	$\Delta E^{V+i,X-i}$	$\Delta E^{i,X-i}$	$\Delta E^{V,X}$	$\Delta E^{V,i}$	$\Delta E^{V+i,X-i}$	$\Delta E^{i,X-i}$	$\Delta E^{V,X}$
4	Br ⁻	-31.5	-	-	-31.5	-37.6	-	-	-37.6
4	Cl ⁻	-30.9	-	-	-30.9	-36.9	-	-	-36.9
5*	Br ⁻	-14.3	-	-	-14.3	-15.4	-	-	-15.4
5*	Cl ⁻	-11.3	-	-	-11.3	-11.4	-	-	-11.4
6	Br ⁻	-106.4	-25.9	-26.8	-105.4	-7.7	-3.7	-5.4	-6.1
6	Cl ⁻	-108.3	-25.0	-26.6	-106.7	-7.8	-3.6	-5.3	-6.2
7*	Br ⁻	-16.1	-12.4	-3.2	-25.3	-17.7	-2.0	-1.2	-18.6
7*	Cl ⁻	-14.6	-11.8	-3.3	-23.2	-16.0	-1.8	-1.2	-16.7
9		-35.3	-	-	-35.3	-4.5	-	-	-4.5
11		-26.6	-26.6	-29.2	-24.0	-3.3	-5.1	-6.9	-1.5

of the fact that a high dielectric constant is expected to neutralise the ionic character of interaction between one or both charged HB partners.

Complexation of **9** with halide ion generates **4**, in which HB energies for N1...O4 do not show above mentioned large difference between two phases. This is apparently because of change of HB character. As reported earlier (Table 6.3) the **9**→**4** step involves a proton transfer from positive lysine to peroxo group, and swapping of donor acceptor atoms neutralises opposite charges on them. This is expected to diminish ionic character of hydrogen bond. On the other hand more closer look at geometrical parameters for this hydrogen bond in **4** (Table 6.3) reveals that N1...O4 and H...N1 distances are very short (around 249 pm and 138 pm respectively) and it would not be an overestimation to assume a good deal of covalent character involved in this hydrogen bond. Indeed it was discovered in the study of HB critical point that **9**→**4** involves change of $\nabla^2\rho_C$ sign to negative. These two factors (diminishing of ionic character and enhancement of covalent character) together produce steep rise in COSMO interaction energy and relatively invariant gas phase interaction energy during **9**→**4** change.

The attack of halide on O3 in **4** results in **5***. In the later structure N1...O4 hydrogen bond energy is reduced by more than half compared to that in former, both in gas and aqueous (COSMO) phases. This is again explained in terms of shift in HB geometrical parameters during **4**→**5*** change. Referring once again to Table 6.3, it becomes obvious:— (1) proton transfer in **5*** is more complete in terms of distance of proton from oxygen and nitrogen atoms, i.e. N1...O4 is further stripped of any reminiscent ionic character. (2) N1...O4 and H...N1 distances are longer in **5*** compared to those in **4**, meaning less covalent character of hydrogen bond.

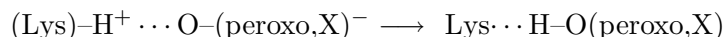
The N1...O4 hydrogen bond is weaker in **11** than in **9**, as comparison of $\Delta E^{V,i}$ values for both shows. Complexation of **11** with halide results in **6**, in which $\Delta E^{V,i}$ for N1...O4 hydrogen bond assumes a value of more than 100 kcal mol⁻¹ in gas phase but remains

Table 6.6: HB energies (kcal mol⁻¹) at ADF/PBE-TZ2P level of theory. Split according to Eq. 4.6 for complexes **10** and **13**.

	Gas phase				Aqueous (COSMO) phase			
	$\Delta E^{V,i}$	$\Delta E^{V+i,X-i}$	$\Delta E^{i,X-i}$	$\Delta E^{V,X}$	$\Delta E^{V,i}$	$\Delta E^{V+i,X-i}$	$\Delta E^{i,X-i}$	$\Delta E^{V,X}$
8 ^a	-16.7	-	-	-16.7	-18.2	-	-	-18.2
10 ^a	-28.9	-13.6	-4.1	-38.5	-36.7	-1.2	-1.8	-36.1
12 ^b	-133.2	-	-	-133.2	-15.5	-	-	-15.5
13 ^a	-130.9	-55.5	46.6	-233.0	-11.8	-9.7	-0.6	-20.8
13 ^b	-122.0	-64.4	46.6	-233.0	-11.4	-10.1	-0.6	-20.8

Amino acid residue *i* given as: ^a Lys353 (labelled *am* in Fig. 6.3) ^b Arg490 (labelled *gu* in Fig. 6.3)

less than 8 kcal mol⁻¹ in COSMO environment. This again is in line with HB critical point characteristics, which earlier revealed that greater electrostatic character is assumed in going to **6** from **11**. This is because **11**→**6** change involves transformation of hydrogen bond from +CAHB, (Lys)-H⁺⋯O-(peroxo) to ±CAHB in an ion pair: (Lys)-H⁺⋯O-(peroxo,X)⁻. Since the aqueous (COSMO) phase neutralises the ionic attraction between opposite charges, interaction energy $\Delta E^{V,i}$ adopts a lower value. Oxygen atom transfer step through the process **6**→**7*** is accompanied by Lys→peroxo proton transfer with the consequence of depriving the hydrogen bond in **7*** of its charge assisted and ionic character according to :-



As a result $\Delta E^{V,i}$ for **7*** assumes similar value in both gas and aqueous phases.

The HB interaction energies in **8**, **10**, **12**, and **13** are reported in Table 6.6, which show same general features: i.e. wherever charge assistance and ionic attraction is involved in charged HB partners, gas and aqueous phase values show large contrast, but if HB partners are neutral this contrast vanishes. It is possible to see the effects of protonation state of peroxovanadate species on interaction strength of N1⋯O4 hydrogen bond. Comparison of **8** and **9** shows that charge assisted/ionic nature of N1-H⁺⋯O4 bond in **9** makes it 18.6 kcal mol⁻¹ more stable than neutral N1⋯H-O4 in **8**. On the other hand this effect seems to be dissipated in case of **10** and **11**. The structure **11** does have a positively charged Lys donor, but energy of its N1-H⁺⋯O4 bond is slightly lower than in neutral N1⋯H-O4 hydrogen bond of **10**. This is because of closer interaction in later as is clear from its geometrical parameters (Table 6.3) which can certainly enhance covalent character of H⋯O contact. The effect of guanidinium (labelled *gu* in **13**) donor on the N1⋯O4 hydrogen bond is obvious from comparison of HB energies for **8** and **13**. Again the ionic character of this hydrogen bond in later makes it more than 100 kcal mol⁻¹ stronger than one in former. On the other hand Lys residue (labelled as *am*) in **13** makes interaction of *gu* with oxo oxygen atoms about 11 kcal mol⁻¹ weaker in it compared to that in **12**. This is probably because of less negative charge available on oxo groups, due to neutralisation of peroxovanadate by positive Lys residue.

Table 6.7: HB energies (kcal mol⁻¹) of peroxo form of cofactor with active site residues, in **PERCPO** model at ADF/PBE-TZ2P level of theory. Split according to Eq. 4.6

<i>i</i>	Gas phase				Aqueous (COSMO) phase			
	$\Delta E^{V,i}$	$\Delta E^{V+i,X-i}$	$\Delta E^{i,X-i}$	$\Delta E^{V,X}$	$\Delta E^{V,i}$	$\Delta E^{V+i,X-i}$	$\Delta E^{i,X-i}$	$\Delta E^{V,X}$
SGH	-104.3	-110.4	144.4	-359.1	-6.4	-9.3	11.1	-26.8
Lys353	-103.4	-124.3	131.4	-359.1	-8.1	-13.5	5.2	-26.8
Arg360	-102.6	-117.9	138.6	-359.1	-5.2	-19.2	2.4	-26.8
Arg490	-110.7	-98.7	149.7	-359.1	-9.3	-9.6	7.9	-26.8

Interaction energies of peroxo cofactor with different VCPO active site residues in (**PERCPO**) are listed in Table 6.7. This is to shed light on relative importance of these residues in their stabilising role with respect to peroxo form of cofactor. The two-body terms $\Delta E^{V,i}$, for the interaction between peroxovanadate cofactor and *i*th amino acid residue, show Arg490 to have strongest interaction in both gas and aqueous phases. It would be interesting to compare these $\Delta E^{V,i}$ values with those for vanadate in native enzyme active site already reported in an Chapter 4. The interaction of SGH fragment with peroxovanadate as reported in Table 6.7 is 25.2 kcal mol⁻¹ less than that with vanadate in native active site (see Table 4.11) while other residues interact in comparably identical way with both VO(O)₂OH and VO₂(OH)₂. Nevertheless interaction of SGH with cofactor in **PERCPO** remains a significant contribution in stabilisation of peroxovanadate, given the fact that Ser402 side chain is not involved in any interaction with peroxovanadate. Of special note is the direct interaction of N7 atom of Gly403 backbone with peroxo oxygen atoms (see Table 6.4) which would be of importance for tuning the charge on peroxo group for halide attack step. In aqueous (COSMO) phase, SGH fragment exhibits 10.9 kcal mol⁻¹ weaker interaction with peroxovanadate than with vanadate (Table 4.12), while other residues maintain a similar level of interaction with both forms of cofactor.

6.3.3 QTAIM Analysis of Reaction Step

The oxygen atom transfer from metal bound peroxide to halide in three model systems was discussed in terms of geometrical and energetic variations. Since ultimately all chemical changes are manifestation of rearrangement of charge density and realignment of forces associated with charges, it is necessary to find a rationale in these terms. Pursuit of this end is tried in present section by means of quantum theory of atoms in molecules (QTAIM). To find a reasonable answer it is first necessary to frame a sensible question, and we may start by asking — does oxygen atom transfer from metal bound peroxide to halide occur through nucleophilic or electrophilic attack? Actually this question has been asked and answered for epoxidation of olefin by metal bound peroxide (see Sec. 1.2.3). It would not be without conceptual advantage to draw parallels between these two oxygen atom transfer reactions, although care must be taken for one contrasting features of both

systems: While olefins are soft nucleophiles due to availability of delocalised π electron density, halide (specially chloride) is hard Lewis base, due to their high electronegativity. This makes oxidation of halides more difficult, requiring that oxidant (peroxide) acts as even harder electrophile if reaction is to proceed through nucleophilic attack of halide. Since the catalytic apparatus furnished in VHPO active site employs dual facilities in conjunction to increase the electrophilic character of peroxide i.e. Lewis acid (V^{+5}), and Brønsted acid (positive Lys), it makes sense to anticipate that halide attack inside enzyme active site is nucleophilic. One question about the role of metal centre remains to be answered. Does the metal centre operate as a passive Lewis acid for peroxide or does it also provide an electronic pathway during halide oxidation? In later case nucleophilic attack of halide is expected to be significantly different regarding the identity of potential electrophilic centre which would be predominantly vanadium ion. In the following pages, the electronic character of chloride oxidation will be discussed to outline the catalytic nature of enzyme active site.

Properties of (3,−1) bond critical points in metal coordination sphere

The extrema in electron density along the line connecting bonded atoms (bond critical points) in vanadium coordination shell were obtained, and these give preliminary information about bond formation and bond breaking processes during oxygen atom transfer. Electron density $\rho(r)$ is a scalar field and its gradient a vector field, the extrema in $\rho(r)$ being the points where vector field of its gradient vanishes according to $\nabla\rho(r) = 0$. The quantity called Laplacian ($\nabla^2\rho(\mathbf{r})$) is the sum of three eigen values of Hessian matrix (the matrix comprised of second partial derivatives of $\rho(r)$ with respect to three spatial dimensions). This quantity gives the information about the curvature of electron density, and critical points denoted by (3,−1) in literature are characterised by one positive eigen value (a minimum along bond line) and two negative eigen values (maxima in two directions perpendicular to bond line) of Hessian. The existence of a (3,−1) extremum or “bond critical point (BCP)” between two atoms is considered a proof of chemical bonding, and the sign of $\nabla^2\rho(\mathbf{r})$ at its location tells whether bonding is between closed shell atoms (if positive eigen value of Hessian determine the overall sign of Laplacian, and $\nabla^2\rho(\mathbf{r}) > 0$) or bonding is shared interaction between the atoms (negative eigen values of Hessian determine the overall sign of Laplacian and $\nabla^2\rho(\mathbf{r}) < 0$). Other quantities related to Laplacian of electron density are, local potential energy density $V(r)$, local kinetic energy density $G(r)$, and their sum or (local) total energy density $H(r)$ (see page 57 for relation of $\nabla^2\rho(\mathbf{r})$ with these quantities).

The (3,−1) critical points found between bonded atom pairs in vanadium coordination shell (i.e. V–O, V–N, O–O, X–V, and X–O bonds) and their properties at ADF/BP-TZ2P and B3LYP/6-311G** levels of theory are listed in Tables C.1 and C.2, and comparison of different quantities at both levels of theory yields similar trends. Here B3LYP/6-311G**

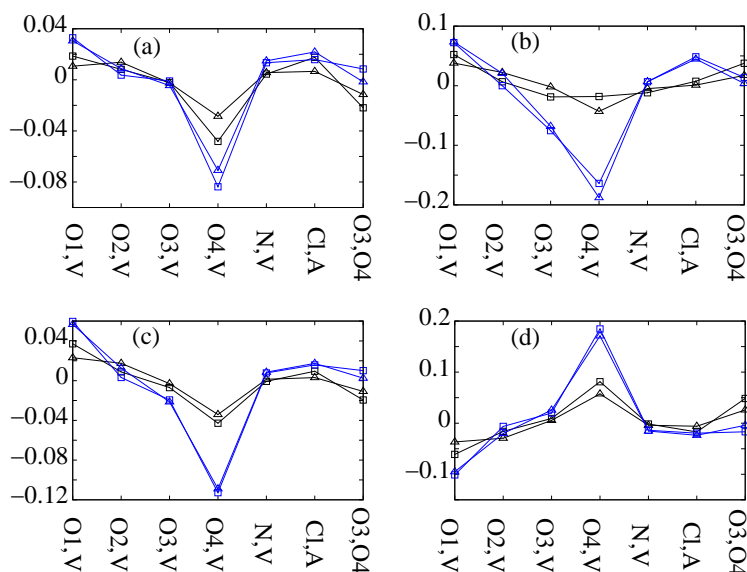


Figure 6.4: Difference (a.u.) between enzyme-catalyzed and non-enzymatic models for oxidation of chloride at B3LYP/6-311G** level, of following QTAIM parameter at (3,-1) BCP for the atom pairs in x-axis: (a) ρ_C (b) $\nabla^2\rho_C$ (c) G_C (d) V_C . “A” in pair Cl,A denotes atom V in minima and atom O3 in transition states. (□) difference between **4** and **1**, (△) difference between **6** and **1**, (□) difference between **5*** and **2***, (△) difference between **7*** and **2***.

values are chosen as basis for the discussion. The bond critical points for the listed interactions show positive $\nabla^2\rho(\mathbf{r})$ values, indicating that all interactions are closed shell or ionic in nature as far as curvature of electron density at BCP is concerned. However the negative sign of total energy density (H_C), because of dominating potential energy density at critical points gives a hint about some covalent contribution (Please refer to Chapter 4 for relation of H_C with covalent character). This is understandable in case of bonds of vanadium with other coordinated oxygen atoms, which can be expected to behave as electrostatic attraction between oppositely charged vanadium and oxygen atoms. What is surprising is that peroxo bond (O3–O4) also shows a positive $\nabla^2\rho_C$ in minima **1**, **4**, and **6**, meaning that electron density is depleted from the region of BCP, and two oxygen atoms are bonded together by electrostatic attraction rather than by shared charge density. This result may seem unexpected but not unprecedented, as peroxo bond was earlier reported to have positive $\nabla^2\rho(\mathbf{r})$ at BCP, both in metal coordinated peroxo group and hydrogen peroxide.²⁵⁶ This depletion of charge density in BCP region may be the reason why peroxo group acts a potent oxygen atom donor. The relatively larger (negative) H_C values for O3–O4 BCP in above mentioned structures, as an indication of covalent contribution, show that (negative valued) potential energy density still has a dominant presence at BCP of this bond, unmatched in this respect by ‘truly’ ionic O–V bonds with the exception of O1–V bond.

The development of the values of listed QTAIM parameters (Tables C.1, C.2) for different bonds in going from a minimum to corresponding transition states in all models, present a common trend: Disappearance of X–V BCP, appearance of X–O3 BCP, some change in O3–V and O4–V bonds, and large change in O3–O4 BCP. The last mentioned change is indicative of a destabilised O3–O4 bond involving reduction in ρ_C , increase in $\nabla^2\rho_C$ and decrease in H_C at BCP region of O3–O4 bond. In the following discussion in this subsection,

QTAIM values for chloride oxidation are taken into consideration, though discussion also applies to bromide substrate. For non-enzymatic model (**1**→**2***), ρ_C very slightly increases for both O3–V and O4–V, $\nabla^2\rho_C$ increases by around 0.1 a.u. and there is also slight accumulation of negative H_C . That Laplacian becomes more positive implying increased depletion of charge, while H_C becomes more negative implying larger increase in potential energy density than in kinetic energy density, means that there is interplay of opposite effects during the process. But there is net increase in value of ρ_C at the bond critical points. In case of enzymatic models (VCPO model, **4**→**5*** and VBPO model, **6**→**7***) the equivalence of O3–V and O4–V bonds is destroyed in reactant minima **4** and **6** because of interaction of O4 with Lys353 residue. Therefore QTAIM parameters signal weakened O4–V interaction in **4** and to lesser extent in **6** in comparison to that in **1**. Consequently, aforementioned change in O4–V in **1**→**2*** transformation, is also diminished in cases of **4**→**5*** and **6**→**7*** to varying extent. The mentioned change in O3–V bond accompanying **1**→**2*** transformation, is though maintained for corresponding transformations in both VCPO and VBPO models.

The effect of Lys353 hydrogen bond with O4 in VCPO, and VBPO models in terms of disparity in the QTAIM parameters for minima or transition states of VCPO/VBPO model from corresponding minimum or transition state of non-enzymatic model are given in Fig. 6.4. In this regard, the most affected properties would be of O3–O4 and O4–V bonds which are under the direct influence of Lys353 interaction. In conjunction with absolute values in Table C.2, from which plots in Fig. 6.4 are derived, the bond O4–V merits special attention as it appears to be affected most as a result of Lys353 hydrogen bonding with O4, while O3–O4 bond shows very small effects in comparison. This implies that weakening of O4–V bond caused by Lys353...O4 interaction, as previously noted by elongation of this bond (Table 6.1), essentially involves decrease in usual O4→V ligand to metal charge transfer, and consequent enhancement of Lewis acidity of metal centre. In other words, this role of Lys353...O4 interaction is in addition to its anticipated role in polarisation of O3–O4 bond, and may actually be more important in catalytic act. This becomes important if Lys353 not only diverts charge density in O3–O4 bond away from O4 atom, but also fine tunes the Lewis acidity of the vanadium centre in order to cope with increase of charge on O3 as a result of O3–X bonding. Further evidence for this point of view appears in next subsection which takes the issue of identifying the centres of charge accumulation and depletion in the valence shell of peroxo oxygen atoms.

Concept of valence shell charge concentration (VSCC) and depletion (VSCD)

The Laplacian of a scalar field like electron density has the property to predict where the field is locally concentrated or depleted.²⁵⁷ In enzymatic oxidation of a substrate, which is essentially catalytically assisted transfer of electronic charge, $\nabla^2\rho(\mathbf{r})$ is a useful quantity to

identify the pockets in valence shell of atoms in enzyme-oxidant complex (i.e. metal coordinated peroxo group in present context), where electronic charge can be transiently stored before the full accomplishment of reaction. The concepts involving use of $\nabla^2\rho(\mathbf{r})$ distribution in identifying areas of charge concentration or depletion are reviewed in this section. The electron density distribution in an isolated atom, as a radial function shows a maximum at nucleus and decays with increasing radial distance (r) in all directions. Due to this reason, electron density distribution does not reflect the electronic shell structure of atom as it shows no maxima corresponding to principle quantum numbers along the radial distance away from nucleus. The gradient of electron density $-\frac{\partial\rho(r)}{\partial r}$, however is not uniform and diminishing of this quantity, meaning a negative second partial derivative of $\rho(r)$ with respect to r , yields local charge concentration.

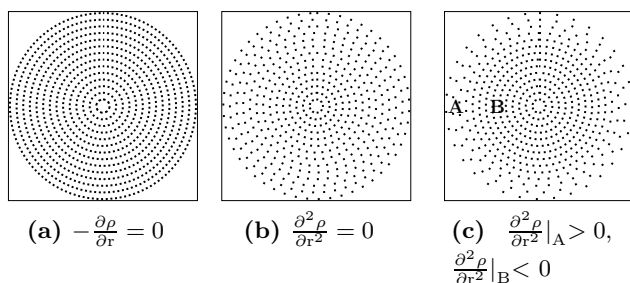


Figure 6.5: Simplified one dimensional model demonstrating local concentration or depletion of a scalar field $\rho(r)$, the value of which on any of concentric circles is proportional to number of dots per unit circumferential length.

successive circle witnesses a reduced value of the field. On the other hand a variable decay $-\frac{\partial\rho(r)}{\partial r}$ results in regions of charge concentration and depletion (Fig. 6.5c). In the region B, at each successive outlying circle, $-\frac{\partial\rho(r)}{\partial r}$ assumes lower and lower value, below its constant value in Fig. 6.5b. As a consequence of negative sign of quantity $\frac{\partial^2\rho}{\partial r^2}$ in this region, build up of the field over its values in corresponding spatial region in Fig. 6.5b is generated. The opposite happens in region A which witnesses diminished $\rho(r)$ field.

In generalisation to three dimensional space the second partial derivative $\frac{\partial^2\rho}{\partial r^2}$ is replaced by a 3×3 matrix known as Laplacian $\nabla^2\rho(\mathbf{r})$, with all second partial derivatives of $\rho(\mathbf{r})$ as elements. This function has a property that at the points where $\nabla^2\rho(\mathbf{r}) < 0$, local build up of charge occurs and at the points where $\nabla^2\rho(\mathbf{r}) > 0$, charge is locally diminished. It has been shown^{258–260} that a shell of local charge concentration and another of depletion in three dimensional space, is associated with each principle quantum shell of electronic wave function of an isolated atom, thus making it possible to recover the shell structure of atoms. Such two shells associated with electronic valence shell of atoms has been termed valence shell charge concentration (VSCC) and depletion (VSCD), respectively. More in-

Similarly increase in $-\frac{\partial\rho(r)}{\partial r}$ (or having $\rho(r)$ with positive second partial derivative) leaves local depletion in charge distribution. This one dimensional consideration is demonstrated in Fig. 6.5, where a hypothetical model (Fig. 6.5a) shows a uniform scalar field donated as $\rho(r)$, which remains constant at every point on all radial distances away from centre. In Fig. 6.5b, $\rho(r)$ decays at a constant rate ($\frac{\partial^2\rho}{\partial r^2} = 0$) starting from the origin and each

terestingly the extrema in $\nabla^2\rho(\mathbf{r})$ distribution naturally define the bound regions of charge concentration or depletion in real space. In this respect, the definitions concerning these extrema are briefly described for the purpose of later discussion of results. An extremum in $\nabla^2\rho(\mathbf{r})$, also known as critical point, is defined by $\nabla(\nabla^2\rho(\mathbf{r})) = 0$, whereas charge concentration reaches a maximum at the point where $\nabla^2\rho(\mathbf{r})$ is minimum, and *vice versa*. Three eigen values of $\nabla^2(\nabla^2\rho(\mathbf{r}))$ matrix correspond to three principle curvatures along following three coordinates: the radial distance (r) from nucleus, and two spherical angles, zenith (θ) and azimuth (ϕ). The radial curvature of $\nabla^2\rho(\mathbf{r})$ at the surface of a sphere of charge concentration is positive. If at a point on such sphere both angular curvatures are also positive, it is labelled as (3, 3). If one of the angular curvature is negative and other positive at this, it is called a (3, 1) point. Finally if both of the angular curvatures are positive the designation of point is given as (3, -1)*. A (3, 3) critical point is a minimum in $\nabla^2\rho(\mathbf{r})$, or maximum in charge concentration along all three dimensions, while (3, 1) critical point corresponds to maximum charge concentration in two dimensions and minimum in remaining dimension. Similarly at a (3, -1) critical point, charge concentration reaches maximum along one coordinate, while passes through a minimum in remaining two. As mentioned earlier, extrema in $\nabla^2\rho(\mathbf{r})$ distribution reside in the bound regions of real space with net build up or diminution of charge concentration, and the number of positive principle curvatures of $\nabla^2\rho(\mathbf{r})$ (or negative if $-\nabla^2\rho(\mathbf{r})$ is considered) at an extremum determines the number of dimensions in which charge concentration reaches maximal value on the extremum. Similarly number of negative curvatures in $\nabla^2\rho(\mathbf{r})$ at an extremum is indicative of number of dimensions in which charge concentration reaches minimum at its location. It is worth mentioning that (3, 3) critical points in valence shell, resembling definite lobes of maximum charge concentration in all three dimensions, have been regarded as physical counterparts of non-bonded (lone)/bonded electron pairs of Lewis and valence shell electron repulsion (VSEPR) models.²⁵⁷ The topology of valence shell $\nabla^2\rho(\mathbf{r})$ distribution is generally different in isolated and bonded atoms in terms of number and types of extrema. Moreover the charge rearrangement in valence shell during the chemical reaction, if reflected in its $\nabla^2\rho(\mathbf{r})$ topology, can be in principle detected by monitoring the properties like $\nabla^2\rho_C$ and ρ_C at $\nabla^2\rho(\mathbf{r})$ critical points, and change in shape of VSCC/VSCD regions centred around these critical points.

Observed VSCC/VSCD extrema at peroxo group of 1 during chloride oxidation

The oxygen atom transfer from vanadium coordinated peroxide to chloride ion in the three models of VHPO catalysis is compared by studying evolution of $\nabla^2\rho(\mathbf{r})$ distribution in

* In literature,²⁵⁷ $-\nabla^2\rho(\mathbf{r})$ instead of $\nabla^2\rho(\mathbf{r})$ distribution is often considered. In such case designations of points encountered in literature are inverse to those presently stated. So (3, 3) point becomes (3, -3), (3, 1) point gets (3, -1) label, and (3, -1) is assigned as (3, 1).

valence shell of peroxide oxygen atoms (O3 and O4) during formation of a transition state from corresponding energy minimum. The $\nabla^2\rho(\mathbf{r})$ distribution for non-enzymatic and VCPO models is produced side by side for comparison in Fig. 6.6, while the properties of critical points detected therein are listed in Table 6.8. By focusing on $\nabla^2\rho(\mathbf{r})$ distribution for **1**, it can be seen that in VSCC of each of O3 and O4 atoms, there are six critical points (lower case *italic* labels in the figure), two each of the following topology: (3, 3), (3, 1) and (3, -1). The following relative positioning of these critical points holds for both O3 and O4: The (3, 3) and (3, 1) critical points surround O–O axis alternately in a fashion that two (3, 3) points lie on two sides of oxygen nucleus perpendicularly to O–V bond while two (3, 1) critical points lie on two sides of oxygen nucleus coaxially with O–V bond. On the other hand two (3, -1) critical points are located on two sides of oxygen nucleus at the O–O axis. This formation can be described in terms of VSCC variation in valence shell of any of peroxy oxygen atoms. There are three spherical coordinates with an oxygen nucleus at origin: the radial distance r , and two spherical angles ϕ and θ . For present purpose ϕ is taken as coordinate corresponding to a rotation around O–O axis and θ as another around the axis which passes at right angles to O–O bond through either of oxygen nuclei. It is to be noted that the such a definition of axis (for rotation θ) includes an infinite number of axis, while for our purpose any one of these in arbitrary orientation around O–O would suffice. In the VSCC region, a minimum in $\nabla^2\rho(\mathbf{r})$ occurs at certain r , forming a sphere. The $\nabla^2\rho(\mathbf{r})$ distribution on the surface of this sphere is not uniform as it varies with angles ϕ and θ . The points on the sphere where $\nabla^2\rho(\mathbf{r})$ reaches minimum along both angles are (3, 3) critical points (points *c, d* for O3 and *i, j* for O4) each surrounded by a region resembling the lobe of a ion pair lying away from both O–O and O–V axis. The points on the sphere where $\nabla^2\rho(\mathbf{r})$ passes through a minimum along ϕ (rotation around O–O axis) but reaches minimum along θ are (3, 1) critical points (*a, b* for O3 and *g, h* for O4), located away from O–O axis and along O–V axis. And finally the (3, -1) critical points (*e, f* for O3 and *k, l* for O4) on which $\nabla^2\rho(\mathbf{r})$ passes through a minimum along both ϕ and θ , lying along the O–O axis and away from O–V axis.

Some characteristics of observed peroxy VSCC/VSCD extrema in 1 during chloride oxidation

After having performed spatial description of $\nabla^2\rho(\mathbf{r})$ extrema, attention is turned to properties at these extrema, starting with structure **1**. Two (3, 3) critical points on both O3 and O4 (*c, d* on O3 and *i, j* on O4) reside into pockets of non-bonded electron density. Similarly two (3, 1) critical points (*a, b* on O3 and *g, h* on O4) are aligned coaxially with respective O–V bonds. Of these *a* and *g* are clearly sites of charge density pockets involved in ionic attraction towards vanadium cation. On the other hand at (3, -1) critical points, which lie coaxially with O–O bond (*e, f* on O3 and *k, l* on O4), charge concentration is

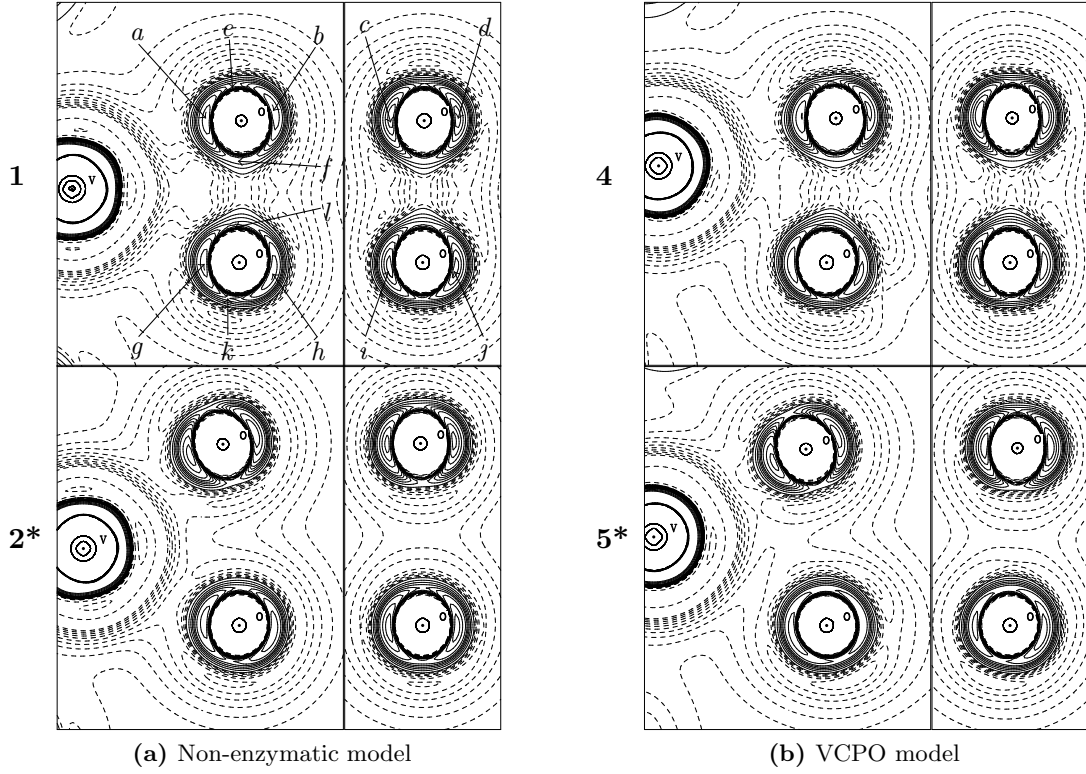


Figure 6.6: $\nabla^2\rho(\mathbf{r})$ function distribution in non-enzymatic and VCPO-catalyzed models for chloride oxidation. Dashed lines: VSCD, full lines: VSCC. Extrema labelled with *italic* letters for **1** apply to other structures as well. For each structure, left hand panel: contours in V-O3-O4 plane with atom order directed clockwise, right hand panel: contours after rotating V-O3-O4 plane at right angles around O3-O4 bond. Contours drawn at $\nabla^2\rho(\mathbf{r})$ values of $-5.0, -4.0, -3.0, -2.0, -1.5, -1.2, \dots, -0.3, 0, 0.1, 0.2, \dots, 1.0, 2.0, 3.0$ a.u.

		1			2*			4			5*		
		r_C	ρ_C	$\nabla^2\rho_C$	r_C	ρ_C	$\nabla^2\rho_C$	r_C	ρ_C	$\nabla^2\rho_C$	r_C	ρ_C	$\nabla^2\rho_C$
<i>a</i>	(3, 1)	35.7	0.81	-3.68	35.1	0.88	-4.62	35.5	0.84	-4.09	35.3	0.86	-4.43
<i>b</i>	(3, 1)	34.7	0.86	-3.97	34.1	0.92	-4.90	34.5	0.88	-4.36	34.2	0.90	-4.72
<i>c</i>	(3, 3)	33.7	0.99	-5.85	33.9	0.96	-5.52	33.5	1.02	-6.18	33.5	1.00	-6.07
<i>d</i>	(3, 3)	33.7	0.99	-5.86	33.8	0.97	-5.61	33.6	1.01	-6.13	33.7	0.99	-5.99
<i>e</i>	(3, -1)	37.1	0.63	-1.05	38.9	0.52	-0.31	37.7	0.58	-0.59	39.2	0.51	-0.20
<i>f</i>	(3, -1)	40.2	0.54	-0.77	39.6	0.50	-0.18	41.5	0.48	-0.36	39.8	0.49	-0.01
<i>g</i>	(3, 1)	35.8	0.81	-3.59	35.8	0.82	-3.61	35.2	0.85	-3.83	35.3	0.83	-3.42
<i>h</i> \star	(3, 1)	34.8	0.85	-3.85	34.8	0.85	-3.92	35.8	0.81	-3.40	36.9	0.77	-3.28
<i>i</i>	(3, 3)	33.6	0.98	-5.64	34.3	0.92	-4.75	33.6	1.01	-5.85	34.1	0.95	-5.10
<i>j</i>	(3, 3)	33.9	0.98	-5.63	34.5	0.91	-4.66	34.3	0.97	-5.07	34.9	0.87	-4.23
<i>k</i>	(3, -1)	36.9	0.65	-1.22	37.0	0.65	-1.47	37.2	0.65	-1.10	36.8	0.69	-1.76
<i>l</i> $\star\star$	(3, -1)	39.6	0.56	-0.93	38.1	0.60	-1.14	39.0	0.59	-1.29	37.0	0.68	-1.85

\star (3, 3) in **5*** $\star\star$ (3, 1) in **4**

Table 6.8: Properties at extrema in $\nabla^2\rho(\mathbf{r})$ function distribution in Fig. 6.6. (critical points in $\nabla^2\rho(\mathbf{r})$, i.e. where $\nabla\nabla^2\rho(\mathbf{r}) = 0$). Second column gives labels of $\nabla^2\rho(\mathbf{r})$ curvatures at extrema, r_C in pm is distance of an extremum from its respective atomic nucleus. Other quantities in a.u.

maximum only along radial dimension, while it is minimum at these points along any line perpendicular to O–O axis. The comparative look at ρ_C and $\nabla^2\rho_C$ of (3,–1) extrema on one hand and those for (3, 3) or (3, 1) extrema on the other, show that at (3,–1) ρ_C is smaller and $\nabla^2\rho_C$ has much lower negative value. The lower negative value of $\nabla^2\rho_C$ being an indication of much diminished charge concentration. This relative scarcity of charge makes the tips of O–O bond likely sites of charge injection into peroxo group during a nucleophilic attack. Another aspect, a reaffirmation of positive Laplacian at O–O BCP as reported in previous subsection, is the maximum (*unlabelled* in Fig. 6.6) of positive $\nabla^2\rho(\mathbf{r})$ midway between O3 and O4 atoms at O–O bond, surrounded by a basin of charge depletion. In other words, cleaving of O–O bond may not mean homolysis of shared σ electron density, in the usual understanding of homolytic cleavage of a covalent bond. It can rather be understood as an enforcement of the already ionic charge distribution between the oxygen atoms with a shift of charge from the region of charge depletion. It follows that the rise in negative charge on O3 due to the attacking nucleophile may be required to be more efficiently handled than that resulting from O–O cleavage.

Non-enzymatic (1 \rightarrow 2*) chloride oxidation model

VSCCs of O3 are profoundly affected during the non-enzymatic chloride attack (1 \rightarrow 2*) on peroxo group, as shown by comparison of $\nabla^2\rho(\mathbf{r})$ distribution in both species (Fig. 6.6a). The chloride attack on O3 in essence is alignment of chloride ion with O3 at charge deficient pocket surrounding (3,–1) critical point *e* on O3. As a result of repulsive push of approaching chloride, both charge density (ρ_C) and charge build-up ($-\nabla^2\rho_C$) are reduced at *e*, as recorded by change from 0.62 to 0.52 a.u. of ρ_C , and from –1.05 to –0.31 a.u. of $\nabla^2\rho_C$. By looking carefully, this effect can be visibly seen in the region surrounding this critical point for 2* as compared to same for 1, as shrunken VSCC area (contours with full line). This is accompanied by slight decrease of ρ_C and $\nabla^2\rho_C$ at (3, 3) critical points *c* and *d* in 2* showing that mentioned repulsive effect penetrates deeper than at critical point *e*. Coincidentally charge accumulation increases at (3, 1) critical points *a* and *b* as seen by higher ρ_C and lower $\nabla^2\rho_C$ at these critical points, along with denser negative $\nabla^2\rho(\mathbf{r})$ contours surrounding these. Since charge concentration pockets around these critical points are aligned coaxially with O3–V bond, it can be concluded that due to repulsive push of chloride ion, charge flows into O3 orbitals involved in attractive interaction with vanadium. Other source of charge inflow in *a* and *b* VSCCs may be due to O–O cleavage, but (3,–1) critical point *f* located at O–O bond, records increased charge depletion in 1 \rightarrow 2* process, though ρ_C and $\nabla^2\rho_C$ changes on it are much smaller compared to those on (3,–1) critical point *e*. This could as well be result of loss of O3–O4 interatomic charge density to O4 atom. What has been definitely observed, as noted above, is rearrangement of O3 valence shell charges with build up along O3–V bond. Obviously any such prospects result in an

increased interaction of charge on O3 with the valence shell of metal, with the implication that metal needs to be made a better Lewis acid towards O3. As the Lewis acidity of a metal cation increases with its effective proton number Z_{eff} , the reduction of negative charge in valence shell of vanadium cation may achieve this, if it can be done by reducing the negative charge acquired by metal due to donation from other coordinated atoms.

On O4 atom, the charge accumulation resulting from O–O cleavage (in **1** \rightarrow **2*** process) is observed. In fact the (3, -1) critical points (k and l) lying on the O–O axis do record a decrease in $\nabla^2\rho_C$ (increased charge concentration) and an increase in ρ_C . And so do, to diminished extent, (3, 1) critical points g and h . The (3, 3) critical points i and j , however undergo large decrease in charge concentration, which may be due to more diffusive nature of charge spreading which is a result of charge coming from the O–O interatomic region. As it was noted for O3 atom, the increased charge on O4 would result in an enhanced interaction between charge on O4 and the valence shell of the vanadium cation. Hence the deposition of charge on O4 atom due to O3–O4 cleavage, can be counterproductive from catalytic point of view by risking the Lewis acid role of vanadium towards O3 atom, the centre of chloride attack.

VCPO (**4** \rightarrow **5***) *chloride oxidation model*

Comparison of above discussed non-enzymatic model with VCPO model (**4** \rightarrow **5***) for chloride oxidation shows that interaction of Lys353 with O4 seems to impose some of the transition state $\nabla^2\rho(\mathbf{r})$ features on O3 atom (as highlighted for **2*** above) in starting minimum **4**. This can be immediately observed by having a comparative look at $\nabla^2\rho(\mathbf{r})$ contours for **1**, **2*** (Fig. 6.6a) and **4** (Fig. 6.6b), in the regions involving extrema a , b , e , and f . The corresponding values of ρ_C and $\nabla^2\rho_C$ confirm the fact that these critical points in **4** show a resemblance to their counterparts in transition state **2***, actually more than shown by those in structure **1**. This clearly indicates that valence shell of O3 is preconditioned to receive the chloride attack in VCPO model. One exception are however the (3, 3) critical points c and d , which unlike in both **1** and **2*** have larger charge build up with larger values of ρ_C and more negative $\nabla^2\rho_C$. Together these observations mean: decreased charge build up at extrema e , f and increased charge accumulation at the extrema a , b , c , d in the starting structure **4**. By looking at the geometrical location of these points, it can be concluded that preconditioning of O3 atom towards chloride attack includes suppression of charge accumulation along O3–O4 axis (points e , f), and its enhancement around the O3–O4 axis in the regions corresponding to non-bonded lone pairs (c , d) and O–V axis (points a , b).

The $\nabla^2\rho(\mathbf{r})$ distribution in valence shell of O4 in **4** is different from that in **1** in a little more complicated way, albeit with some general pattern. One member of each of critical point pairs (g , h), (i , j), and (k , l) in **4** shows enhanced charge concentration, while the other member of pair exhibits reduced charge concentration in comparison to corresponding

points in **1**. The critical points witnessing higher charge concentration in **4** are g , i , and l . Of these, g is at centre of a charge concentration pocket pointing towards vanadium and l lies on O3–O4 bond and hence closest to receive charge from O3,O4 interatomic density. This later point also gains one more negative $\nabla^2\rho(\mathbf{r})$ curvature and becomes (3, 1). Among the critical points which appear with reduced charge concentration in **4**, h apparently does so because it is at the centre of charge concentration pocket pointing towards proton of O4...Lys353 interaction.

An attempt to make a unified picture out of these observations is made as following. Lys353...O4 interaction operates in a two fold way: First, by offering a proton to drain negative charge from O3–O4 axis towards O4, thus making region surrounding e critical point on O3, the site of chloride attack, more electron deficient while that surrounding l on O4 more electron rich. Second, by weakening O4–V bond, it shifts O4 atom away from vanadium atom and hence reduces the donation of negative charge on O4 to valence shell of vanadium cation. This may induce increased Lewis acid–base interaction between vanadium and O3, as obvious from enhanced charge concentration in VSCC pocket surrounding a , even without electrostatic repulsive push of chloride as it would be in transition state. Another manifestation of this aspect is a shorter Cl–V distance in **4** (compared to that **1**) as was noted in discussion of geometrical parameters.

The transformation **4**→**5*** proceeds on similar pattern as was presented for non-enzymatic model **1**→**2***, as far as O3 atom of peroxo group is concerned, i.e. alignment of chloride on O3 side of O3–O4 bond, and pushing of electron density from (3, –1) and (3, 3) critical points to (3, 1) points which are coaxial with O3–V bond. The VSCC of O4 behaves in slightly different way than it was noted in non-enzymatic model. It is to be recalled that proton transfer to O4 from Lys353 is more complete in **5*** in comparison to **4**. The main contrasting feature of VSCC evolution at O4 in **4**→**5*** is that critical points g , and h behave in reverse way to that in non-enzymatic model by undergoing reduction in charge concentration. It is to be noted that g resides in VSCC pocket pointing towards vanadium and h in another one pointing towards proton donated from Lys353. The decrease in charge accumulation at both these points may be a consequence of Lys353→O4 proton transfer, and in case of g may be caused by subsequent loosening of O4–V bond. Notably g observes a change in curvature of $\nabla^2\rho(\mathbf{r})$ as it converts to (3, 3) in **5*** from (3, 1) in **4**.

VBPO(6→7*) chloride oxidation model

The $\nabla^2\rho(\mathbf{r})$ distribution for VBPO model presented in Fig. 6.7 and properties of extrema therein in Table 6.9, show an already discussed pattern of going to transition state geometry from a minimum. In this respect $\nabla^2\rho(\mathbf{r})$ distribution for VBPO model appears to differ from that for VCPO model, not in form but in the degree of catalytic improvement gained over non-enzymatic model. It was mentioned previously that in VCPO-catalytic model,

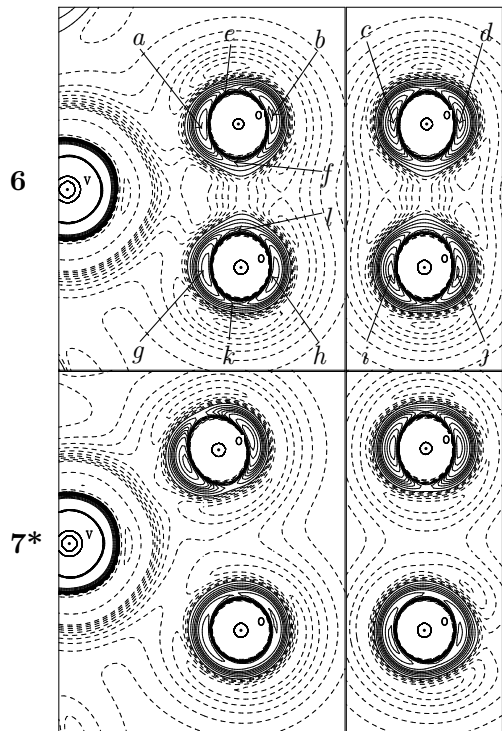


Figure 6.7: $\nabla^2\rho(\mathbf{r})$ function distribution for VBPO model of chloride oxidation. Details similar to those given in caption of Fig. 6.6.

		6			7*		
		r_C	ρ_C	$\nabla^2\rho_C$	r_C	ρ_C	$\nabla^2\rho_C$
<i>a</i>	(3, 1)	35.6	0.83	-3.88	35.2	0.86	-4.47
<i>b</i>	(3, 1)	34.6	0.87	-4.17	34.2	0.91	-4.78
<i>c</i>	(3, 3)	33.7	0.99	-5.86	33.7	0.98	-5.86
<i>d</i>	(3, 3)	33.8	0.98	-5.71	33.7	0.98	-5.81
<i>e</i>	(3, -1)	37.3	0.62	-0.93	39.3	0.51	-0.26
<i>f</i>	(3, -1)	40.4	0.53	-0.69	39.4	0.51	-0.18
<i>g</i> ★	(3, 1)	35.5	0.83	-3.85	35.5	0.83	-3.74
<i>h</i>	(3, 1)	34.9	0.85	-3.85	35.9	0.78	-2.94
<i>i</i>	(3, 3)	34.3	0.99	-5.73	34.2	0.93	-4.72
<i>j</i>	(3, 3)	33.7	0.94	-5.23	36.5	0.79	-3.55
<i>k</i>	(3, -1)	37.0	0.65	-1.18	36.5	0.72	-2.05
<i>l</i>	(3, -1)	39.7	0.55	-0.93	36.9	0.69	-1.93

★ (3,3) in 7*

Table 6.9: Properties at extrema in $\nabla^2\rho(\mathbf{r})$ function distribution shown in Fig. 6.7 (critical points in $\nabla^2\rho(\mathbf{r})$, i.e. where $\nabla\nabla^2\rho(\mathbf{r}) = 0$). The listed critical point labels in *italic* letters are according to those utilised in Fig. 6.6. Details of quantities and their units same as in Table 6.8.

O3 atom in starting reactant minimum **4** is preconditioned to receive chloride attack, as its VSCC was found to resemble the transition state **2*** of non-enzymatic model. Primarily the contrasting feature between VCPO and VBPO model turns out to be the extent of this preconditioning. While it can be directly observed by comparing $\nabla^2\rho_C$ values for each critical point in Table 6.8 and Table 6.9, it is worth pointing out that critical points in **6** assume $\nabla^2\rho_C$ values shifted from those in **1**, but not to the extent as in **4**. To take two examples, the reduction of charge concentration at critical point *e* can be very important for receiving a nucleophile, and while in **4**, $\nabla^2\rho_C$ increases by 0.46 a.u. over its value in **1**, in **6** this increase is 0.12 a.u. This kind of reasoning is also true for other $\nabla^2\rho(\mathbf{r})$ critical points lying on O–O bond. Similarly, the charge accumulation along O3–V bond, in the region centred around *a* critical point can enhance the efficiency of nucleophilic attack. The $\nabla^2\rho_C$ at this critical point is -3.68, -4.09, and -3.88 in **1**, **4**, and **6** respectively, showing that this is done most efficiently in **4**. One more interesting difference between VCPO and VBPO models is orientation of O4...Lys353 hydrogen bond. It is well known that hydrogen bonds tend to orient themselves along so called lone pairs of acceptor atom. The proton transfer from Lys353 to O4 also occurs on pocket of charge concentration associated with one of $\nabla^2\rho(\mathbf{r})$ extremum. While in VCPO model this occurs on (3, 1) extremum *h*, in VBPO model it is on (3, 3) extremum *j*. Needless to say that former lies along O4–V bond,

	1	2*	4	5*	6	7*
Van	-0.43	-0.55	-0.32	-0.48	-0.39	-0.51
Cl ⁻	-0.70	-0.57	-0.55	-0.31	-0.64	-0.31
His496	0.13	0.12	0.17	0.21	0.17	0.22
Lys353	-	-	0.70	0.58	0.82	0.59
His411	-	-	-	-	0.04	0.01
V	1.42	1.51	1.44	1.46	1.42	1.49
O1	-0.56	-0.65	-0.43	-0.42	-0.50	-0.47
O2	-0.96	-0.94	-0.92	-0.91	-0.89	-0.89
O3	-0.37	-0.39	-0.35	-0.37	-0.40	-0.41
O4	-0.42	-0.53	-0.54	-0.72	-0.50	-0.70

Table 6.10: Natural population analysis, for structures corresponding to three enzymatic models. *Upper block:* Total NPA charge on the individual fragments of each model, *lower block:* Charges on vanadium and oxygen atoms bonded to it.

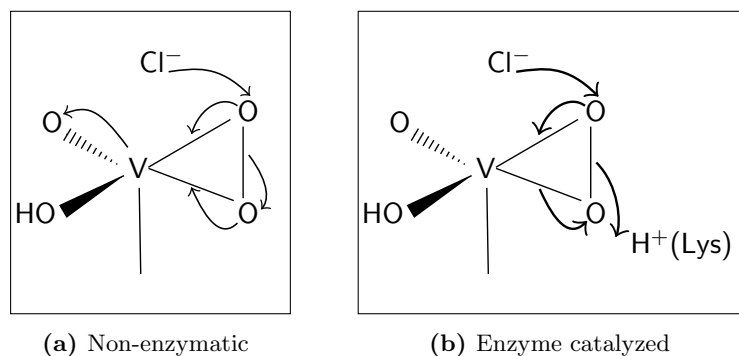
and hence can better influence it, while later is perpendicular to O4–V bond. This is also reflected in O4–V bond distance which is 3.6 pm longer in **4** compared to **6**. Perhaps the orientation imposed on O4···Lys353 hydrogen bond by a second Lys hydrogen bonding partner (His in case of VBPO) in second protein shell of enzyme active site is one aspect of subtle differences between both systems. It is to be recalled that two back bone carboxylic oxygen atoms in the vicinity of Lys residue in both enzymes (Fig. 1.1d) can also interfere with O4···Lys hydrogen bond, but the relative position of His may be vital in current considerations.

6.3.4 The Mechanistic Outlook

In this chapter the question of halide attack on vanadium bound peroxide was taken, and it was found that oxygen atom transfer to halide results in a TBP structure with hyphalite ion at apical position. The energy barrier to this process was calculated in three catalysis models and it was found that unhindered proton transfer to O4 atom of side-on bound peroxide from hydrogen bonding Lys residue brings the barrier considerably down. The electronic character of this process was studied by the analysis of $\nabla^2\rho(\mathbf{r})$ distribution in relevant stationary points on the reaction potential energy surface.

The picture presented by $\nabla^2\rho(\mathbf{r})$ distribution sheds light on local charge shifts inside atomic VSCC during the activation of reactant minima, reconciliation of which with net charge transfer between atoms and moieties of atoms is presently intended to attempt. For this purpose charges derived from natural population analysis (NPA) are utilised, as presented in Table 6.10 for chloride oxidation. The sum of the charges on all atoms in a unit, are given for following moieties: vanadium with its oxo, hydroxo, and peroxo ligands (Van), chloride ion, His496, Lys353, and His411 (the latter is only present in VBPO). All three catalytic models show that formation of transition states is accompanied by the loss

Figure 6.8: Schematic of charge flow in oxygen atom transfer to chloride ion in non-enzymatic and enzyme-catalyzed models. The thickness of arrowed lines qualitatively represent the relative intensity of charge flow.



of negative charge on chloride. The chloride negative charge in structures corresponding to enzyme-catalyzed models (**4**, **5*** and **6**, **7***) is smaller than that in non-enzymatic case (**1**, **2***), showing the fruitfulness of catalytic models. In order to judge the true catalytic significance of each model, the collective amount of charge transferred from moiety composed of chloride, Van, and His496 units to the rest of the system (Lys353 or Lys353/His411) is to be considered. This, as given by change over formal charge of +1 of Lys353 or Lys353/His411, is 0.30 a.u. in **4** and an additional 0.12 a.u. in **5***, i.e. a total of 0.42 a.u. of negative charge is neutralised by Lys353 prior to and during chloride attack in VCPO-catalyzed model. On the other hand a total of 0.40 a.u. negative charge is neutralised by Lys353/His411 in VBPO model, of which 0.14 a.u. is achieved in **6** and 0.26 a.u. in **7***. The fact that in VCPO model greater amount of negative charge is shifted to Lys353 prior to chloride attack, is indication of better preparedness of the system for oxidation of chloride. The charges on individual atoms within the Van unit, as given in second part of Table 6.10, further reveal the difference of enzyme-catalyzed models from non-enzymatic one. The increase of negative charge on O1 during **1**→**2***, along with an increase of positive charge on vanadium centre, are both notably absent in **4**→**5***, while being very moderately present in **6**→**7***. It should be pointed out that O1–V bond in **1**→**2*** does not undergo elongation, hinting that gain of charge by O1 is of back donation type without undergoing loss of bond strength. Besides, O4 atom is able to collect larger amount of negative charge in later two processes. These two facts can be reconciled by our earlier hypothesis based on observations on VSCC rearrangements, that weakening of O4–V bond due to hydrogen bonding interaction of O4 with Lys, fine tunes the Lewis acidity of vanadium by reduction of O4 to metal charge donation. When O4–V weakening is not possible to happen, like in our non-enzymatic model, the halide attack on peroxo group causes vanadium to loose some charge to O1 oxo atom. When this O4–V weakening is possible to happen, like VCPO and VBPO models, there is no need for vanadium to gain stabilisation by back donating to O1, despite the fact that O4 is now able to accommodate larger charge.

On the basis of evidence taken from various results so far discussed a charge flow scheme of contrast between the enzyme-catalyzed and non-enzymatic model is presented in Fig. 6.8. The O3–V and O4–V bonds are strengthened during **1**→**2*** process as shown by shortened

bond distances (Table 6.1), and slightly increased ρ_C at bond critical points (Appendix, Table C.2). The critical points in $\nabla^2\rho(\mathbf{r})$ distribution *a*, *b*, *g*, *h*, *k*, and *l*, record increase in charge build-up to varying degrees (Fig. 6.6 and Table 6.8). Moreover, NPA charges also show that O1 gains net negative charge during this process. All these observations furnish the rationale for direction of arrows for the non-enzymatic charge flow scheme in Fig. 6.8a. On the other hand the trend of similar quantities for VCPO and VBPO enzymatic models allow to depict the charge flow as in Fig. 6.8b. In other words, the catalytic role of Lys353 residue is in diverting the charge density from the interatomic region of not only O3–O4 and O3–V bonds.

Another aspect is the supportive catalytic role of residues other than Lys353 in the enzyme active site. It was argued that reduced charge donation from ligands to vanadium can enhance the Lewis acid performance of later due to its improved Z_{eff} . As seen from the increased NPA charge on O1 atom of **2***, there is a tendency on part of vanadium to loose the charge to oxo ligand when encountered with increased charges on peroxo group due to halide attack. Moreover, in presence of positively charged Lys353 in the vicinity of side-on bound peroxide (e.g. in **5***), vanadium does not loose charge to oxo ligand, meaning that need for O1 to act as charge withdrawing centre is reduced. Nevertheless, enzyme active site is equipped with additional HB donors like Arg490 and Arg360 to enhance the charge withdrawing capacity of non-peroxide oxygen atoms in vanadium coordination shell (cf. model **PERCPO** in Fig. 6.3), which can help vanadium in improving its performance as even better Lewis acid.

References

1. J. J. R. F. da Silva, R. J. P. Williams, *The Biological Chemistry of the elements*, Oxford University Press, Oxford, second edition **2001**.
2. S. J. Lippard, J. M. Berg, *Principles of Bioinorganic Chemistry*, University Science Books, Mill Valley, California **1994**.
3. W. Kaim, B. Schwederski, *Bioinorganic Chemistry: Inorganic Elements in the Chemistry of Life*, Wiley, New York **1994**.
4. L. Vaska, *Acc. Chem. Res.* **1976**, *9*, 175.
5. K. A. Jørgensen, *Chem. Rev.* **1989**, *89*, 431.
6. A. Butler, M. J. Clague, G. E. Meister, *Chem. Rev.* **1994**, *94*, 625.
7. M. H. Dickman, M. T. Pope, *Chem. Rev.* **1994**, *94*, 569.
8. H. Mimoun, I. S. de Roch, L. Sajus, *Bull. Soc. Chem. Fr.* **1969**, 1481.
9. H. Mimoun, I. S. de Roch, L. Sajus, *Tetrahedron* **1970**, *26*, 37.
10. W. A. Hermann, R. W. Fischer, D. W. Marz, *Angew. Chem. Int. Ed. Engl* **1991**, *30*, 1838.
11. C. Venturello, E. Alneri, M. A. Ricci, *J. Org. Chem.* **1983**, *48*, 3831.
12. W. A. Hermann, F. E. Kühn, *Acc. Chem. Res.* **1997**, *30*, 169.
13. W. Adam, W. Malisch, K. J. Roschmann, C. R. Saha-Möller, W. A. Schenk, *J. Organomet. Chem.* **2002**, *661*, 3.
14. H. Vitler, *Phytochemistry* **1984**, *23*, 1387.
15. E. de Boer, Y. van Kooyk, M. G. M. Tromp, H. Plat, R. Wever, *Biochim. Biophys. Acta* **1986**, *869*, 48.
16. J. W. P. M. van Schijndel, E. G. M. Vollenbroek, R. Wever, *Biochim. Biophys. Acta* **1993**, *1161*, 249.
17. J. H. Clark, J. C. Ross, D. J. Macquarrie, S. J. Barlow, T. W. Bastock, *Chem. Comm.* **1997**, 1203.
18. T. Moriuchi, M. Yamaguchi, K. Kikushima, T. Hirao, *Tetrahedron Lett.* **2007**, *48*, 2667.
19. C. Chiappe, E. Leandri, M. Tebano, *Green Chem.* **2006**, *8*, 742.

20. U. Bora, M. K. Chauduri, D. Dey, S. S. Dhar, *Pure Appl. Chem.* **2001**, *73*, 93.
21. G. Rothenberg, J. H. Clark, *Org. Proc. Res. & Dev.* **2000**, *4*, 270.
22. A. Messerschmidt, R. Wever, *Proc. Natl. Acad. Sci. USA* **1996**, *93*, 392.
23. M. Weyand, H. J. Hecht, M. Kiess, M. F. Liaud, H. Vitler, D. Schomburg, *J. Mol. Biol.* **1999**, *293*, 595.
24. M. N. Isupov, A. R. Dalby, A. A. Brindley, Y. Izumi, J. L. T Tanabe, G.N. Murshudov, *J. Mol. Biol.* **2000**, *299*, 1035.
25. A. Messerschmidt, L. Prade, R. Wever, *Biol. Chem.* **1997**, *378*, 309.
26. J. W. P. M. van Schijndel, P. Barnett, J. Roelse, E. G. M. Vollenbroek, R. Wever, *Eur. J. Biochem.* **1994**, *225*, 151.
27. A. Butler, *Coord. Chem. Rev.* **1999**, *187*, 17.
28. E. de Boer, K. Boon, R. Wever, *Biochemistry* **1988**, *27*, 1629.
29. J. M. Aber, E. de Boer, C. D. Garner, S. S. Hasnain, R. Wever, *Biochemistry* **1989**, *28*, 7968.
30. R. Renirie, W. Hemrika, S. R. Piersma, R. Wever, *Biochemistry* **2000**, *39*, 1133.
31. W. Hemrika, R. Renirie, S. Machedo-Ribeiro, A. Messerschmidt, R. Wever, *J. Biol. Chem.* **1999**, *274*, 23820.
32. R. Renirie, W. Hemrika, R. Wever, *J. Biol. Chem.* **2000**, *275*, 11650.
33. N. Tanaka, Z. Hasan, R. Wever, *Inorg. Chim. Acta* **2003**, *356*, 288.
34. A. Messerschmidt, R. Wever, *Inorg. Chim. Acta* **1998**, *273*, 160.
35. K. Ishikawa, Y. Mihara, K. Gondoh, E. Suzuki, Y. Asano, *EMBO* **2000**, *19*, 2412.
36. R. Renirie, *Peroxidase and Phosphatase Activity of Vanadium Chloroperoxidases from the Fungus Curvularia inaequalis*, Ph.D. thesis, Univerity of Amsterdam. (**2000**).
37. H. Taube, H. Myers, R. L. Rich, *J. Am. Chem. Soc.* **1953**, *75*, 4118.
38. H. Taube, H. Myers, *J. Am. Chem. Soc.* **1954**, *76*, 2103.
39. H. Taube, *Angew. Chem. Intl. Ed. Engl.* **1984**, *23*, 329.
40. R. H. Holm, *Chem. Rev.* **1987**, *87*, 1401.
41. L. K. Woo, J. A. Hays, *Inorg. Chem.* **1993**, *32*, 2228.
42. L. K. Woo, *Chem. Rev.* **1993**, *93*, 1125.
43. G. J. J. Chen, J. W. McDonald, W. E. Newton, *Inorg. Chim. Acta.* **1976**, *19*, L67.
44. J. M. Mayer, *Comments Inorg. Chem.* **1988**, *8*, 125.
45. B. S. Tovrog, S. E. Diamond, F. Mares, *J. Am. Chem. Soc.* **1979**, *101*, 270.
46. A. L. Feig, S. J. Lippard, *Chem. Rev.* **1994**, *94*, 759.

47. D. T. Sawyer, in A. Martell, D. Sawyer (Editors) *Oxygen Complexes and Oxygen Activation by Transition Metals.*, 131, Plenum Press, New York **1988**.
48. D. T. Sawyer, J. S. Valenitine, *Acc. Chem. Res.* **1981**, *14*, 393.
49. R. D. Jones, D. A. Summerville, F. Basolo, *Chem. Rev.* **1979**, *79*, 139.
50. F. A. Cotton, G. Wilkinson, C. A. Murillo, M. Bochmann, *Advanced Inorganic Chemistry.*, John Wiley Asia, Singapore, 6th edition **2004**.
51. H. Sigel, A. Sigel (Editors) *Vanadium and Its Role in Life*, volume 31 of *Metal Ions in Biological Systems*, Marcel Dekker, New York **1995**.
52. C. J. Ballhausen, H. B. Gray, *Inorg. Chem.* **1962**, *1*, 111.
53. A. K. Rappè, W. A. G. III, *J. Am. Chem. Soc.* **1982**, *104*, 3287.
54. J. Baes, F. Charles, R. E. Mesmer, in J. Baes, F. Charles, R. Mesmer (Editors) *The Hydrolysis of Cations*, John Wiley, New York **1976**.
55. F. Secco, *Inorg. Chem.*, **1980**, *19*, 2722.
56. J. S. Jaswal, A. S. Tracey, *Inorg. Chem.* **1991**, *30*, 3718.
57. T. J. Won, C. L. Barnes, E. O. Schlemper, R. C. Thompson, *Inorg. Chem.* **1995**, *34*, 4499.
58. W. P. Griffith, T. D. Wickins, *J. Chem. Soc. A* **1968**, 397.
59. de la Rosa, M. J. Clague, A. Butler, *J. Am. Chem. Soc.* **1992**, *114*, 760.
60. M. J. Clague, A. Butler, *J. Am. Chem. Soc.* **1995**, *117*, 3475.
61. M. J. Clague, N. L. Keder, A. Butler, *Inorg. Chem.* **1993**, *32*, 4754.
62. G. E. Meister, A. B. and, *Inorg. Chem.* **1994**, *33*, 3269.
63. J. H. Espenson, O. Pestovsky, P. Hansen, S. Staudt, *J. Am. Chem. Soc.* **1994**, *116*, 2869.
64. P. Hansen, J. H. E. and, *Inorg. Chem.* **1995**, *34*, 5839.
65. A. Butler, A. H. B. and, *Struct. and Bond.* **1997**, *89*, 109.
66. R. H. Holm, P. Kennepohl, E. I. S. and, *Chem. Rev.* **1996**, *96*, 2239.
67. R. D. Shannon, *Acta Crystallogr.* **1976**, *A32*, 576.
68. J. C. Slater, *Phys. Rev.* **1930**, *36*, 57.
69. M. Fiore, S. Orecchio, V. Romano, R. Zingales, *J. Chem. Soc. Dalton Trans.* **1993**, 799.
70. D. Rehder, in Sigel & Sigel⁵¹ **1995**.
71. O. Bortolini, V. Conte, F. D. Furia, G. Modena, *Nouv. J. Chim.* **1985**, *9*, 147.
72. V. Conte, F. D. Furia, G. Modena, *J. Org. Chem.* **1988**, *53*, 1665.

73. H. Mimoun, L. Saussine, E. Daire, M. Postel, J. Fischer, R. Weiss, *J. Am. Chem. Soc.* **1983**, *105*, 3101.
74. H. Mimoun, in S. Patai (Editor) *Chemistry of Peroxides*, chapter 15, 463, Wiley, Chicester **1983**.
75. K. B. Sharpless, J. M. Townsend, D. R. Williams, *J. Am. Chem. Soc.* **1972**, *94*, 295.
76. H. Kwart, D. H. Hoffmann, *J. Org. Chem.* **1966**, *31*, 419.
77. B. P. car, M. Tasevski, A. A. zman, *J. Am. Chem. Soc.* **1978**, *100*, 743.
78. S. Yamabe, C. Kondou, T. M. and, *J. Org. Chem.* **1996**, *61*, 616.
79. D. A. Singleton, S. R. Merrigan, J. Liu, K. N. H. and, *J. Am. Chem. SOc.* **1997**, *119*, 3385.
80. W. Sander, K. Schroeder, S. Muthusamy, A. K. W. Kappert, R. Boese, E. Kraka, C. Sosa, D. Cremer, *J. Am. Chem. Soc.* **1997**, *119*, 7265.
81. J. Liu, K. N. Houk, A. Dinoi, C. Fusco, R. Curci, *J. Org. Chem.* **1998**, *63*, 8565.
82. M. Freccero, R. Gandolfi, M. Sarzi-Amadè, A. Rastelli, *J. Org. Chem.* **1999**, *64*, 3853.
83. D. V. Deubel, G. Frenking, P. Gisdakis, W. A. Herrmann, N. Rösch, J. Sundermeyer, *Acc. Chem. Res.* **2004**, *37*, 645.
84. D. V. Deubel, J. Sundermeyer, G. Frenking, *J. Am. Chem. Soc.* **2000**, *122*, 10101.
85. P. Gisdakis, S. Antonczak, S. Köstlmeier, W. A. Herrmann, N. Rösch, *Angew. Chem. Intl. Ed. Engl.* **1998**, *37*, 2211.
86. F. R. Sensato, R. Custodio, E. Longo, V. S. Safont, J. Andres, *J. Org. Chem.* **2003**, *68*, 5870.
87. C. D. Valentin, P. Gisdakis, I. V. Yudanov, N. Rösch, *J. Org. Chem.* **2000**, *65*, 2996.
88. M. Bühl, M. Schurhammer, P. Imhof, *J. Am. Chem. Soc.* **2004**, *126*, 3310.
89. D. V. Deubel, J. Sundermeyer, G. Frenking, *Eur. J. Inorg. Chem* **2001**, 1819.
90. I. A. Yudanov, C. D. Valentin, P. Gisdakis, N. Rösch, *J. Molecular Catalysis A: Chemical*, **2000**, *158*, 189.
91. F. R. Kühn, A. M. Santos, P. W. Roesky, E. Herdtweck, W. Scherer, P. Gisdakis, I. Yudanov, C. Valentin, N. Rösch, *Chem. Eur. J.* **1999**, *5*, 3603.
92. I. V. Yudanov, P. Gisdakis, C. D. Valentin, N. Rösch, *Eur. J. Inorg. Chem.* **1999**, 2135.
93. D. V. Deubel, J. Sundermeyer, G. Frenking, *Org. Lett.* **2001**, *3*, 329.
94. P. Hohenberg, W. Kohn, *Phys. Rev.* **1964**, *136*, B864.
95. M. Levy, *Proc. Natl. Acad. Sci. USA* **1979**, *76*, 6062.
96. W. Kohn, L. J. Sham, *Phys. Rev.* **1964**, *140*, A1133.

97. K. Burke, J. W. Werschnik, E. K. U. Gross, *J. Chem. Phys.* **2005**, *123*, 62206.
98. E. Runge, E. K. U. Gross, *Phys. Rev. Lett.* **1984**, *52*, 997.
99. H. Appel, E. K. U. Gross, in J. Grotendorst, D. Marx, A. Muramatsu (Editors) *Quantum Simulations of Complex Many-Body Systems: From Theory to Algorithms*, NIC Series 10, 255, John von Neumann Institute of Computing, Jülich, Germany **2002**.
100. P. Elliot, K. Burke, F. Furche **2007**, arXiv:cond-mat/0703590v1.
101. R. Bauernschmitt, R. Ahlrichs, *Chem. Phys. Lett.* **1996**, *256*, 454.
102. T. Grabo, M. Petersilka, E. K. U. Gross, *J. Mol. Str. (THEOCHEM)* **2000**, *501*, 353.
103. J. Villa, A. Warshel, *J. Phys. Chem. B* **2001**, *105*, 7887.
104. A. Warshel, *Proc. Natl. Acad. Sci. USA* **1978**, *75*, 5250.
105. A. Warshel, M. Levitt, *J. Mol. Biol.* **1976**, *103*, 227.
106. T. C. Bruice, S. J. Benkovic, *Biochemistry* **2000**, *39*, 6267.
107. T. C. Bruice, *Acc. Chem. Res.* **2002**, *35*, 139.
108. F. C. Lightstone, T. C. Bruice, *J. Am. Chem. Soc.* **1996**, *118*, 2595.
109. T. C. Bruice, F. C. Lightstone, *Acc. Chem. Res.* **1999**, *32*, 127.
110. E. Z. Eisenmesser, D. A. Bosco, M. Akke, D. Kern, *Science* **2002**, *295*, 1520.
111. S. J. Benkovic, S. H-Schiffer, *Science* **2003**, *301*, 1196.
112. M. Garcia-Viloca, J. Gao, M. Karplus, D. G. Truhlar, *Science* **2004**, *303*, 186.
113. H. S. Soedjak, J. V. Walker, A. Butler, *Biochemistry* **1995**, *34*, 12689.
114. A. Butler, R. A. Tschirret-Guth, M. T. S. and, in A. Tracey, D. Crans (Editors) *Vanadium Compounds: Chemistry, Biochemistry, and Therapeutic Applications*, volume 711 of *ACS Symposium Series*, 202, American Chemical Society **1998**.
115. A. Butler, in J. Reedijk, E. Bouwman (Editors) *Bioinorganic Catalysis*, 55, Marcel Dekker, Inc., New York, 2nd edition **1999**.
116. A. Butler, *Curr. Opin. Chem. Biol.* **1998**, *2*, 279.
117. A. K. Rappè, W. A. G. III, *J. Am. Chem. Soc.* **1982**, *104*, 448.
118. A. R. Rossi, R. Hoffmann, *Inorg. Chem.* **1975**, *14*, 365.
119. E. Shustorovich, *Inorg. Chem.* **1978**, *17*, 2648.
120. W. Plass, *Z. Anorg. Allg. Chem.* **1994**, *620*, 1635.
121. W. Plass, *J. Inorg. Biochem.* **1995**, *59*, 587.
122. W. Plass, *Inorg. Chim. Acta* **1996**, *244*, 221.
123. W. Plass, *Z. Anorg. Allg. Chem.* **1997**, *623*, 461.
124. W. Plass, A. Pohlmann, H. Yozgatli, *J. Inorg. Biochem.* **2000**, *80*, 181.

125. A. Pohlmann, W. Plass, *J. Inorg. Biochem.* **2001**, *86*, 381.
126. W. Plass, H. Yozgatli, *Z. Anorg. Allg. Chem.* **2003**, *629*, 65.
127. A. Pohlmann, S. Nica, W. Plass, *Inorg. Chem. Comm.* **2005**, *8*, 289.
128. W. Plass, *Coord. Chem. Rev.* **2003**, *237*, 205.
129. A. Pohlmann, S. Nica, T. Luong, W. Plass, *Inorg. Chem. Comm.* .
130. G. te Velde, F. M. Bickelhaupt, S. J. A. van Gisbergen, C. Fomesca, C. Guerra, E. B. adf J.G. Snijders T. Ziegler, *J. Comput. Chem.* **2001**, *22*, 931.
131. C. F. Guerra, J. Snijders, G. te Velde, E. Baerends, *Theor. Chem. Acc.* **1998**, *99*, 391.
132. S. C. . Modelling, ADF *Versions 2004-07*, Theoretical Chemistry, Virje University, Amsterdam, <http://www.scm.com>.
133. A. J. H. Wachters, *J. Chem. Phys.* **1970**, *52*, 1033.
134. P. J. Hay, *J. Chem. Phys.* **1977**, *66*, 4377.
135. M. Bühl, *J. Comp. Chem.* **1999**, *20*, 1254.
136. M. Bühl, M. Parrinello, *Chem. Eur. J.* **2001**, *7*, 20.
137. M. Bühl, F. A. Hamprecht, *J. Comp. Chem.* **1998**, *19*, 113.
138. M. J. Frisch, G. W. Trucks, H. B. Schlegel, G. E. Scuseria, M. Robb, J. Cheese-
man, J. Montgomery, Jr., T. Vreven, K. Kudin, J. Burant, J. Millam, S. Iyengar,
J. Tomasi, V. Barone, B. Mennucci, M. Cossi, G. Scalmani, N. Rega, G. Pe-
tersson, H. Nakatsuji, M. Hada, M. Ehara, K. Toyota, R. Fukuda, J. Hasegawa,
M. Ishida, T. Nakajima, Y. Honda, O. Kitao, H. Nakai, M. Klene, X. Li, J. Knox,
H. Hratchian, J. Cross, V. Bakken, C. Adamo, J. Jaramillo, R. Gomperts, R. Strat-
mann, O. Yazyev, A. Austin, R. Cammi, C. Pomelli, J. Ochterski, P. Ayala,
K. Morokuma, G. Voth, P. Salvador, J. Dannenberg, V. Zakrzewski, S. Dap-
prich, A. Daniels, M. Strain, O. Farkas, D. Malick, A. Rabuck, K. Raghavachari,
J. Foresman, J. Ortiz, Q. Cui, A. Baboul, S. Clifford, J. Cioslowski, B. Stefanov,
G. Liu, A. Liashenko, P. Piskorz, I. Komaromi, R. Martin, D. Fox, T. Keith,
M. Al-Laham, C. Peng, A. Nanayakkara, M. Challacombe, P. Gill, B. Johnson,
W. Chen, M. Wong, C. Gonzalez, J. Pople, Gaussian 03, Revision C.02 **2004**.
139. R. G. Parr, W. Yang, *Density Functional Theory of Atoms and Molecules*, Oxford
Univ. Press, New York **1994**.
140. E. K. U. Gross, J. F. Dobson, M. Petersilka, *Topics in Current Chemistry*, **1996**, *181*,
81.
141. B. O. Roos, K. Andersson, M. P. Fülscher, L. A. P A Malmqvist, K. Pierloot,
M. Merchán, in S. R. I. Prigogine (Editor) *New Methods in Computational Quan-*

- tum Mechanics*, volume XCIII of *Advances in Chemical Physics*, 219, John Wiley and Sons, New York **1996**.
142. S. J. A. van Gisbergen, F. Kootstra, P. R. T. Schipper, O. Gritsenko, J. Snijders, E. Baerends, *Phys. Rev.* **1998**, *A57*, 2556.
 143. C. Jamorski, M. E. Casida, D. R. Salahub, *J. Chem. Phys.* **1996**, *104*, 5134.
 144. S. J. A. van Gisbergen, J. G. Snijders, E. J. Baerends, J. Groeneveld, F. Kootstra, V. Osinga, RESPONSE, Extension of the ADF program for linear and nonlinear response calculations. **1999**.
 145. S. J. A. van Gisbergen, J. G. Snijders, E. J. Baerends, *Comp. Phys. Commun.* **1999**, *118*, 119.
 146. M. Grüning, O. V. Gritsenko, S. J. A. van Gisbergen, E. J. Baerends, *J. Chem. Phys.* **2001**, *114*, 652.
 147. S. J. A. van Gisbergen, J. A. Groeneveld, A. Rosa, J. Snijders, E. Baerends, *J. Phys. Chem. A* **1999**, *103*, 6835.
 148. P. R. T. Schipper, O. V. Gritsenko, S. J. A. van Gisbergen, E. J. Baerends, *J. Chem. Phys.* **2000**, *112*, 1344.
 149. O. V. Gritsenko, P. R. T. Schipper, E. J. Baerends, *Chem. Phys. Lett.* **1999**, *302*, 199.
 150. A. Müller, E. Diemann, *Chem. Phys. Lett.* **1971**, *9*, 369.
 151. T. Ziegler, A. Rauk, E. J. Baerends, *Chem. Phys.* **1976**, *16*, 209.
 152. A. Carrington, M. C. R. Symons, *Chem. Rev.* **1963**, *63*, 443.
 153. W. J. Ray, Jr, C. B. Post, *Biochemistry* **1990**, *29*, 2779.
 154. S. I. Gorelsky, SWizard program, <http://www.sg-chem.net>.
 155. T. Borowski, W. Szczepanik, M. Chruszcz, E. Broclawik, *Intl. J. Quant. Chem.* **2004**, *99*, 864.
 156. G. Zampella, J. Y. Kravitz, C. E. Webster, P. Fantucci, M. B. Hall, H. Carlson, V. Pecoraro, L. D. Gioia, *Inorg. Chem.* **2004**, *43*, 4127.
 157. G. A. Jeffrey, *An Introduction to Hydrogen Bonding*, Oxford University Press, New York **1997**.
 158. S. Scheiner, *Hydrogen Bonding. A Theoretical Perspective*, Oxford University Press, New York **1997**.
 159. C. L. Perrin, J. B. Nielson, *Annu. Rev. Phys. Chem.* **1997**, *48*, 511.
 160. T. Kar, S. Scheiner, *J. Phys. Chem. A* **2004**, *108*, 9161.
 161. H. Tan, W. Qu, G. Chen, R. Liu, *J. Phys. Chem. A* **2005**, *109*, 6303.

162. H. S. Soedjak, A. Butler, *Inorg. Chem.* **1990**, *29*, 5015.
163. L. Pauling, *The Nature of Chemical Bond*, Cornell University Press, Itacha, New York, 3rd edition **1960**.
164. G. A. Jeffrey, W. Saenger, *Hydrogen Bonding in Biological Structures*, Springer-Verlag, Berlin **1991**.
165. A. I. Kitaigorodskii, *Molecular Crystals and Molecules*, Academic Press, New York **1972**.
166. G. R. Desiraju, *Crystal Engineering. The Design of Organic Solids*, Elsevier, Amsterdam **1989**.
167. J. Emsley, *Chem. Soc. Rev.* **1980**, *9*, 91.
168. L. Sobczyk, S. J. Grabowski, T. M. Krygowski, *Chem. Rev.* **2005**, *105*, 3513.
169. G. R. Desiraju, T. Steiner, *The Weak Hydrogen Bond in Structural Chemistry and Biology*, Oxford University Press, New York **1999**.
170. G. R. Desiraju, *Acc. Chem. Res.*, **2002**, *35*, 565.
171. A. van Vaart, K. M. Merz, Jr, *J. Chem. Phys.*, **2002**, *116*, 7380.
172. S. J. Grabowski, *J. Phys. Chem. A*, **2001**, *105*, 10739.
173. P. Huyskens, T. Zeegers-Huyskens, *J. Chem. Phys.* **84.**, (1964).
174. P. J. Desmeules, L. C. Allen, *J. Chem. Phys.* **1980**, *72*, 4731.
175. T.-H. P.L. Huyskens, W.A.P. Luck (Editor) *Intermolecular Forces*, Springer, Berlin **1991**.
176. L. Sobczyk, B. Bunsenges, *Phys. Chem.* **1998**, *102*, 377.
177. G. Gilli, P. Gilli, *J. Mol. Str.*, **2000**, *552*, 1.
178. W. W. Cleland, *Biochemistry* **1992**, *31*, 317.
179. G. A. Gerlt, P. G. Gasman, *J. Am. Chem. Soc.* **1993**, *115*, 11552.
180. G. A. Gerlt, P. G. Gasman, *Biochemistry* **1993**, *32*, 11943.
181. W. W. Cleland, *Science* **1994**, *264*, 1887.
182. P. A. Frey, S. A. Whitt, J. B. Tobin, *Science* **1994**, *264*, 1927.
183. A. Warshel, A. Papazyan, P. A. Kollman, *Science* **1995**, *269*, 102.
184. P. Hobza, *Annu. Rep. Prog. Chem. Sect. C*, **2004**, *100*, 3.
185. S. J. Grabowski, *Annu. Rep. Prog. Chem. C*, **2006**, *102*, 131.
186. B. Jeziorski, R. Moszynski, K. Szalewicz, *Chem. Rev.* **1994**, *94*, 1887.
187. U. Koch, P. L. A. Popelier, *J. Phys. Chem.* **1995**, *99*, 9747.

188. B. P. Hay, D. A. Dixon, J. C. Bryan, B. A. Moyer, *J. Am. Chem. Soc.* **2002**, *124*, 182.
189. F. B. van Duijneveldt, J. G. C. M. van Duijneveldt-van de Rijdt, J. H. van Lenthe, *Chem. Rev.* **1994**, *94*, 1873.
190. G. Chalasiński, *Chem. Rev.* **2000**, *100*, 4227.
191. S. F. Boys, F. Bernardi, *Mol. Phys.* **1970**, *19*, 553.
192. C. A. Coulson, *Valence*, Oxford University Press, Oxford **1952**.
193. C. A. Coulson, U. Danielsson, *Ark. Fysik*, **1954**, *8*, 239.
194. C. A. Coulson, U. Danielsson, *Ark. Fysik*, **1954**, *8*, 245.
195. R. F. W. Bader, *Chem. Rev.* **1991**, *91*, 893.
196. R. F. W. Bader, *Atoms in Molecules - A Quantum Theory*, Oxford University Press, Oxford **1990**.
197. O. Gálvez, P. C. Gómez, L. F. Pacios, *J. Chem. Phys.* **2001**, *115*, 11166.
198. O. Gálvez, P. C. Gómez, L. F. Pacios, *J. Chem. Phys.* **2003**, *118*, 4878.
199. L. F. Pacios, *J. Phys. Chem. A* **2004**, *108*, 1177.
200. E. Espinosa, I. Alkorta, J. Elguero, W. Molins, *J. Chem. Phys.* **2002**, *117*, 5529.
201. A. Ranganathan, G. U. Kulkarni, C. N. R. Rao, *J. Phys. Chem. A* **2003**, *107*, 6073.
202. E. Espinosa, E. Molins, C. Lecomte, *Chem. Phys. Lett.* **1998**, *285*, 170.
203. E. Espinosa, C. Lecomte, E. Molins, *Chem. Phys. Lett.* **1999**, *300*, 745.
204. S. Jenkins, I. Morrison, *Chem. Phys. Lett.* **2000**, *317*, 97.
205. D. Cremer, E. Kraka, *Angew. Chem. Intl. Ed. Engl.* **1984**, *23*, 627.
206. S. J. Grabowski, M. Malecka, *J. Phys. Chem. A* **2006**, *110*, 11847.
207. A. E. Reed, F. Weinhold, *J. Chem. Phys.* **1983**, *78*, 4066.
208. A. E. Reed, R. B. Weinstock, F. Weinhold, *J. Chem. Phys.* **1985**, *83*, 735.
209. A. E. Reed, L. A. Curtiss, F. Weinhold, *Chem. Rev.* **1988**, *88*, 899.
210. A. Klamt, G. Schüürmann, *J. Chem. Soc.: Perkin Transactions* **1993**, *2*, 799.
211. A. Klamt, *J. Phys. Chem.* **1995**, *99*, 2224.
212. A. Klamt, V. Jones, *J. Chem. Phys.* **1996**, *105*, 9972.
213. C. C. Pye, T. Ziegler, *Theor. Chem. Acc.* **1999**, *101*, 396.
214. J. C. O. Alba, C. B. Jané, Xaim, <http://www.quimica.urv.es/XAIM>.
215. E. D. Glendening, J. K. Badenhoop, A. E. Reed, J. E. Carpenter, F. Weinhold, NBO 4.M **1999**, Theoretical Chemistry Institute, University of Wisconsin, Madison.

216. I. Rozas, P. E. Kruger, *J. Chem. Theory Comput.* **2005**, *1*, 1055.
217. A. G. J. Ligtenbarg, R. Hage, B. L. Feringa, *Coord. Chem. Rev.* **2003**, *237*, 89.
218. S. M-Ribeiro, W. Hemrika, R. Renirie, R. Wever, A. Messerschmidt, *J. Biol. Inorg. Chem.* **1999**, *4*, 209.
219. N. Kitajima, M. Akita, Y. Moro-Oka, in W. Ando (Editor) *Organic Peroxides*, 535, Wiley, Chicester **1992**.
220. V. Conte, F. D. Furia, G. Modena, in W. Ando (Editor) *Organic Peroxides*, 559, Wiley, Chicester **1992**.
221. R. A. Sheldon, J. K. Kochi, *Metal Catalyzed Oxidations of Organic Compunds*, Academic Press, New York **1981**.
222. A. Sigel, H. Sigel (Editors) *Molybdenum and Tungsten: Their Roles in Biological Processes*, volume 39 of *Metal Ions in Biological Systems*, Marcel Dekker, New York **2002**.
223. E. de Boer, R. Wever, *J. Biol. Chem.* **1988**, *263*, 12326.
224. V. Conte, F. D. Furia, S. Moro, *J. Mol. Catal. A: Chemical* **1997**, *120*, 93.
225. A. Bagno, V. Conte, F. D. Furia, S. Moro, *J. Phys. Chem. A* **1997**, *101*, 4637.
226. V. Conte, F. D. Furia, G. Licini, *Appl. Catal. A: Gen.* **1997**, *157*, 335.
227. M. Bonchio, O. Borotolini, V. Conte, S. Moro, *Eur. J. Inorg. Chem.* (**2001**), 2913.
228. W. Plass, *Z. Anorg. Allg. Chem.* **1997**, *623*, 997.
229. S. Nica, A. Pohlmann, W. Plass, *Eur. J. Inorg. Chem.* **2005**, 2032.
230. M. Bangesh, W. Plass, *J. Mol. Struc.:THEOCHEM* **2005**, *725*, 163.
231. S. Rauegi, P. Carloni, *J. Phys. Chem. B.* **2006**, *110*, 3747.
232. L. Fan, T. Ziegler, *J. Chem. Phys.* **1992**, *96*, 9005.
233. L. Fan, T. Ziegler, *J. Phys. Chem.* **1992**, *96*, 6937.
234. L. Versluis, T. Ziegler, *J. Chem. Phys.* **1988**, *88*, 322.
235. L. Fan, T. Ziegler, *J. Chem. Phys.* **1991**, *95*, 7401.
236. L. Fan, T. Ziegler, *J. Am. Chem. Soc.* **1992**, *114*, 10890.
237. A. Berces, R. M. Dickson, L. Fan, H. Jacobsen, D. Swerhone, T. Ziegler, *Comput. Phys. Commun.* **1997**, *100*, 247.
238. H. Jacobsen, A. Berces, D. P. Swerhone, T. Ziegler, *Comput. Phys. Commun.* **1997**, *100*, 263.
239. S. K. Wolf, *Intl. J. Quantum Chem.* **2005**, *104*, 645.
240. R. Car, M. Parrinello, *Phy. Rev. Lett.* **1985**, *55*, 2471.

241. D. Marx, J. Hutter, in J. Grotendorst (Editor) *Modern Methods and Algorithms of Quantum Chemistry*, NIC Series 1, 301, John von Neumann Institute of Computing, Jülich, Germany **2000**.
242. J. Hutter, A. Alavi, T. Deutch, M. Bernasconi, S. Goedecker, D. Marx, M. Tuckerman, M. Parrinello, CPMD **1995–1999**.
243. CPMD, Copyright IBM Corp 1990-2004, Copyright MPI für Festkörperforschung Stuttgart **1997–2001**.
244. S. Goedecker, M. Teter, J. Hutter, *Phys. Rev. B* **1996**, *54*,, 1703.
245. N. Troullier, J. L. Martins, *Phys. Rev. B* **1991**, *43*,, 1993.
246. B. Silvi, A. Savin, *Nature* **1994**, *371*,, 683.
247. A. Savin, B. Silvi, F. Colona, *Can. J. Chem.* **1996**, *74*,, 1088.
248. S. Noury, F. Colona, A. Savin, B. Silvi, *J. Mol. Struct.* **1998**, *450*,, 59.
249. A. D. Becke, K. E. Edgecombe, *J. Chem. Phys.* **1990**, *92*,, 5397.
250. M. Kohout **2006**.
251. J. Y. Kravitz, V. L. Pecoraro, H. A. Carlson, *J. Chem. Theory Comput.* **2005**, *1*, 1265.
252. M. Calatayud, B. Silvi, J. Andres, A. Beltran, *Chem. Phys. Lett.* **2001**, *333*,, 493.
253. S. Chiodo, O. Kondakova, M. d C Michelini, N. Russo, E. Sicilia, *Inorg. Chem.* **2003**, *42*,, 8773.
254. M. Calatayud, J. Andres, B. Silvi, *Theor. Chem. Acc.* **2001**, *105*,, 299.
255. G. Zampella, P. Fantucci, V. L. Pecoraro, L. D. Gioia, *J. Am. Chem. Soc.* **2005**, *127*, 953.
256. P. Macchi, A. J. Schultz, F. K. Larsen, B. B. Iversen, *J. Phys. Chem. A* **2001**, *105*, 9231.
257. R. F. W. Bader, P. J. M. R J Gillespie, *J. Am. Chem. Soc.* **1988**, *110*, 7329.
258. R. F. W. Bader, P. M. Beddall, *J. Chem. Phys.* **1972**, *56*, 3320.
259. R. F. W. Bader, H. Essén, *J. Chem. Phys.* **1984**, *80*, 1943.
260. R. P. Smith, A. C. T. Ku, V. H. Smith, A. M. Simas, *J. Chem. Phys.* **1988**, *88*, 4367.

Erklärung

Ich erkläre,

dass mir die geltende Promotionsordnung der Fakultät bekannt ist;

dass ich die Dissertation selbst angefertigt und alle von mir benutzten Hilfsmittel, persönlichen Mitteilungen und Quellen in meiner Arbeit angegeben habe;

dass mich folgende Personen bei der Auswahl und Auswertung des Materials sowie bei der Herstellung des Manuskripts unterstützt haben;

dass die Hilfe eines Promotionsberaters nicht in Anspruch genommen wurde und dass Dritte weder unmittelbar noch mittelbar geldwerte Leistungen von mir für Arbeiten erhalten haben, die im Zusammenhang mit dem Inhalt der vorgelegten Dissertation stehen;

dass ich die Dissertation noch nicht als Prüfungsarbeit für eine staatliche oder andere wissenschaftliche Prüfung eingereicht habe;

dass ich nicht die gleiche, eine in wesentlichen Teilen ähnliche oder eine andere Abhandlung bei einer anderen Hochschule als Dissertation eingereicht habe

(Masroor Ahmad Khan Bangesh)

Jena, January 2, 2008

Curriculum Vitae

Masroor Ahmad Khan Bangesh

<i>09.03.1971</i>	Born in Balakot (NWFP), Pakistan.
<i>1977—1984</i>	Primary and middle schools (Balakot).
<i>1984—1986</i>	Secondary school (Balakot).
<i>1986</i>	Secondary school certificate (Matriculation).
<i>1986—1988</i>	Intermediate College (Balakot).
<i>1988</i>	Higher secondary school certificate.
<i>1988—1990</i>	Study of Chemistry, Zoology and Botany at Govt. College Abbottabad.
<i>1990</i>	Bachelor of Science (B.Sc.), University of Peshawar.
<i>1990—1992</i>	Study of Chemistry.
<i>1992</i>	Master of Science (M.Sc.) in chemistry, Gomal University.
<i>1994—1998</i>	Study of physical chemistry.
<i>1998</i>	Master of Philosophy (M.Phil.) in physical chemistry, Quaid-i-Azam University, Islamabad.
<i>1998—2001</i>	Scientific fellow at Chemistry Department, Quaid-i-Azam University, Islamabad.
<i>2001—2002</i>	Scientific coworker at Siegen University.
<i>2002—2007</i>	Scientific coworker at Friedrich-Schiller University, Jena.

Publications

- M. Bangesh, W. Plass, TD-DFT studies on the electronic structure of imidazole bound vanadate in vanadium containing haloperoxidases (VHPO), *J. Mol. Struc. THEOCHEM*, **2005**, 725, 153.
- W. Plass, M. Bangesh, S. Nica, A. Buchholz, Model studies of vanadium dependent haloperoxidation: Structural and functional lessons, In “*Vanadium the Versatile Metal* ” Ed. K. Kustin, J. C-Pessoa, D. C. Crains, ACS Symposium Series, **2007**, 974.
- M. Bangesh, W. Plass, DFT studies on reaction of hydrogen peroxide with imidazole bound vanadate, (*ready to submit*).
- M. Bangesh, W. Plass, Theoretical studies on supramolecular hydrogen bonding network in VHPO active site, (*to be submitted*).
- M. Bangesh, W. Plass, DFT studies on halide oxidation by vanadium bound peroxide in vanadium haloperoxidases, (*to be submitted*).

Appendix A

Supplement to Chapter 3

The data presented in this appendix shows the composition of the excitations (at ADF-SAOP/TZ2P-TZP theory level for **HPO1** and ADF-SAOP/ET-QZ3P1D for others) and involving Kohn-Sham orbitals for some structures. The data for **HPO1** include only the selected part of spectrum. In general each excitation is a mixture of several transitions and only the most predominant contributing electronic transitions and (their weights) are listed for each excitation. The sum of the weights of all contributing transitions to an excitation is unity (not all transitions and weights are listed). The composition of Kohn-Sham orbitals involved in excitations is given as percentage of contribution from atomic basis. Energy levels are labelled according to their position relative to highest occupied and lowest unoccupied molecular orbitals (*homo* and *lumo* respectively).

Table A.1: Structure 2

Excitation	(eV)	Oscillator strength	Transition	Weight
1	3.78	0.0008	<i>homo</i> \rightarrow <i>lumo</i>	0.9745
2	3.90	0.0001	<i>homo</i> \rightarrow <i>lumo+1</i>	0.9984
3	4.02	0.0002	<i>homo</i> \rightarrow <i>lumo+2</i>	0.9766
4	4.10	0.0224	<i>homo-1</i> \rightarrow <i>lumo</i>	0.8578
5	4.17	0.0065	<i>homo-1</i> \rightarrow <i>lumo+1</i>	0.9628
6	4.24	0.0058	<i>homo</i> \rightarrow <i>lumo+3</i>	0.9133
7	4.29	0.0006	<i>homo-1</i> \rightarrow <i>lumo+2</i>	0.9079
8	4.42	0.0064	<i>homo-2</i> \rightarrow <i>lumo</i>	0.9349
9	4.57	0.0058	<i>homo-2</i> \rightarrow <i>lumo+1</i>	0.7933
			<i>homo-1</i> \rightarrow <i>lumo+3</i>	0.1347
10	4.60	0.0125	<i>homo-1</i> \rightarrow <i>lumo+3</i>	0.5302
			<i>homo-2</i> \rightarrow <i>lumo+1</i>	0.1852
			<i>homo-3</i> \rightarrow <i>lumo</i>	0.1371
11	4.67	0.0005	<i>homo-2</i> \rightarrow <i>lumo+2</i>	0.9380
12	4.75	0.0057	<i>homo-3</i> \rightarrow <i>lumo</i>	0.5954
			<i>homo-1</i> \rightarrow <i>lumo+3</i>	0.1082
13	4.78	0.0008	<i>homo-3</i> \rightarrow <i>lumo+1</i>	0.9100
14	4.82	0.0007	<i>homo</i> \rightarrow <i>lumo+4</i>	0.7744
			<i>homo-2</i> \rightarrow <i>lumo+3</i>	0.1078
15	4.85	0.0014	<i>homo-2</i> \rightarrow <i>lumo+3</i>	0.3829
			<i>homo-4</i> \rightarrow <i>lumo</i>	0.2743
			<i>homo</i> \rightarrow <i>lumo+4</i>	0.1386
16	4.89	0.0077	<i>homo-3</i> \rightarrow <i>lumo+2</i>	0.3877
			<i>homo-2</i> \rightarrow <i>lumo+3</i>	0.3785
			<i>homo-4</i> \rightarrow <i>lumo</i>	0.1049
17	4.93	0.0049	<i>homo-3</i> \rightarrow <i>lumo+2</i>	0.4437
			<i>homo-4</i> \rightarrow <i>lumo+2</i>	0.1688
			<i>homo-4</i> \rightarrow <i>lumo</i>	0.1646
18	4.94	0.0003	<i>homo</i> \rightarrow <i>lumo+5</i>	0.9716
19	4.96	0.0014	<i>homo-4</i> \rightarrow <i>lumo+1</i>	0.8973
20	5.04	0.0031	<i>homo-5</i> \rightarrow <i>lumo</i>	0.4675
			<i>homo-4</i> \rightarrow <i>lumo+2</i>	0.3471

Table A.2: Structure 2

Orbital	Composition
<i>homo-4</i>	12.15% (V); 69.97% (O)
<i>homo-3</i>	3.54% (V); 89.82% (O)
<i>homo-2</i>	90.38% (O)
<i>homo-1</i>	91.96% (O)
<i>homo</i>	1.06% (V); 98.73% (O)
<i>lumo</i>	65.25% (V); 13.45% (O)
<i>lumo+1</i>	100.0% (Im)
<i>lumo+2</i>	10.79% (V); 2.96% (O); rest (Im)
<i>lumo+3</i>	56.60% (V); 20.26% (O); 6.37% (Im)

Table A.3: Structure 4

Excitation	(eV)	Oscillator strength	Transition	Weight
1	3.17	0.0004	<i>homo</i> \rightarrow <i>lumo</i>	0.9800
2	3.38	0.0006	<i>homo</i> \rightarrow <i>lumo</i> +1	0.8547
			<i>homo</i> \rightarrow <i>lumo</i> +2	0.1348
3	3.53	0.0010	<i>homo</i> \rightarrow <i>lumo</i> +2	0.8258
			<i>homo</i> \rightarrow <i>lumo</i> +1	0.1171
4	3.54	0.0025	<i>homo</i> -1 \rightarrow <i>lumo</i>	0.9502
5	3.73	0.0002	<i>homo</i> -1 \rightarrow <i>lumo</i> +1	0.9099
6	3.78	0.0011	<i>homo</i> -2 \rightarrow <i>lumo</i>	0.9128
7	3.84	0.0004	<i>homo</i> \rightarrow <i>lumo</i> +3	0.5388
			<i>homo</i> -1 \rightarrow <i>lumo</i> +2	0.4038
8	3.87	0.0020	<i>homo</i> -1 \rightarrow <i>lumo</i> +2	0.5002
			<i>homo</i> \rightarrow <i>lumo</i> +3	0.3663
9	3.99	0.0235	<i>homo</i> -2 \rightarrow <i>lumo</i> +1	0.6896
			<i>homo</i> -2 \rightarrow <i>lumo</i> +2	0.2501
10	4.08	0.0014	<i>homo</i> -3 \rightarrow <i>lumo</i>	0.9467
11	4.13	0.0004	<i>homo</i> -2 \rightarrow <i>lumo</i> +2	0.5513
			<i>homo</i> -1 \rightarrow <i>lumo</i> +3	0.2323
			<i>homo</i> -2 \rightarrow <i>lumo</i> +1	0.1234
12	4.23	0.0013	<i>homo</i> \rightarrow <i>lumo</i> +4	0.5872
			<i>homo</i> -1 \rightarrow <i>lumo</i> +3	0.2876
13	4.28	0.0007	<i>homo</i> -4 \rightarrow <i>lumo</i>	0.3681
			<i>homo</i> -3 \rightarrow <i>lumo</i> +1	0.2513
			<i>homo</i> \rightarrow <i>lumo</i> +4	0.2320
14	4.29	0.0046	<i>homo</i> -4 \rightarrow <i>lumo</i>	0.4912
			<i>homo</i> -3 \rightarrow <i>lumo</i> +1	0.4032
15	4.35	0.0118	<i>homo</i> -3 \rightarrow <i>lumo</i> +2	0.2637
			<i>homo</i> -1 \rightarrow <i>lumo</i> +3	0.2024
			<i>homo</i> \rightarrow <i>lumo</i> +4	0.0978
			<i>homo</i> -4 \rightarrow <i>lumo</i>	0.0871
			<i>homo</i> -2 \rightarrow <i>lumo</i> +3	0.0828
16	4.44	0.0078	<i>homo</i> -3 \rightarrow <i>lumo</i> +2	0.4945
			<i>homo</i> \rightarrow <i>lumo</i> +5	0.2179
			<i>homo</i> -3 \rightarrow <i>lumo</i> +1	0.1198
			<i>homo</i> -2 \rightarrow <i>lumo</i> +3	0.0972
17	4.45	0.0012	<i>homo</i> \rightarrow <i>lumo</i> +5	0.7618
			<i>homo</i> -3 \rightarrow <i>lumo</i> +2	0.1057
18	4.51	0.0009	<i>homo</i> -4 \rightarrow <i>lumo</i> +1	0.7604
			<i>homo</i> -4 \rightarrow <i>lumo</i> +2	0.1983
19	4.61	0.0044	<i>homo</i> -2 \rightarrow <i>lumo</i> +3	0.3665
			<i>homo</i> -1 \rightarrow <i>lumo</i> +4	0.2482
			<i>homo</i> \rightarrow <i>lumo</i> +6	0.2015
20	4.64	0.0035	<i>homo</i> \rightarrow <i>lumo</i> +6	0.7183
			<i>homo</i> -2 \rightarrow <i>lumo</i> +3	0.1424

Table A.4: Structure 4

Orbital	Composotion
<i>homo-4</i>	89.42 (O)
<i>homo-3</i>	90.52% (O)
<i>homo-2</i>	84.73% (O)
<i>homo-1</i>	94.18% (O)
<i>homo</i>	99.03% (O)
<i>lumo</i>	7.43% (V) ; 71.69% (Im)
<i>lumo+1</i>	33.67% (V); 44.16% (Im)
<i>lumo+2</i>	22.02% (V); 70.53% (Im)
<i>lumo+3</i>	52.08% (V); 19.52% (O); rest (Im)
<i>lumo+4</i>	22.5% (V); 3.94% (O); rest (Im)
<i>lumo+5</i>	90% (Im)
<i>lumo+6</i>	23.35% (V) ; rest (Im)

Table A.5: Structure **HPO1**

Excitation	(eV)	Oscillator strength	Transition	Weight
10	2.67	0.0093	<i>homo-4</i> \longrightarrow <i>lumo</i>	0.9773
50	4.28	0.0268	<i>homo-9</i> \longrightarrow <i>lumo+1</i>	0.2274
			<i>homo-10</i> \longrightarrow <i>lumo</i>	0.1982
			<i>homo-12</i> \longrightarrow <i>lumo</i>	0.1332
			<i>homo-8</i> \longrightarrow <i>lumo+1</i>	0.1079

Table A.6: Structure **HPO1**

Orbital	Composition
<i>homo-12</i>	52.46% (O)
<i>homo-10</i>	61.56% (O); 17.85% (Im)
<i>homo-9</i>	82.62% (O)
<i>homo-8</i>	27.81% (O); 55.49% (protein)
<i>homo-4</i>	85.75% (His496)
<i>lumo</i>	73.71% (V); 16.15% (O)
<i>lumo+1</i>	69.75% (V); 22.46% (O)

Table A.7: Structure 5

Excitation	(eV)	Oscillator strength	Transition	Weight
1	2.86	0.0008	<i>homo</i> \rightarrow <i>lumo+1</i>	0.9910
2	3.18	0.0002	<i>homo</i> \rightarrow <i>lumo+2</i>	0.9882
3	3.25	0.0184	<i>homo-1</i> \rightarrow <i>lumo+1</i>	0.9872
4	3.57	0.0152	<i>homo-1</i> \rightarrow <i>lumo+2</i>	0.8643
			<i>homo-2</i> \rightarrow <i>lumo</i>	0.1037
5	3.75	0.0060	<i>homo-2</i> \rightarrow <i>lumo</i>	0.8422
			<i>homo-1</i> \rightarrow <i>lumo+2</i>	0.0753
			<i>homo-4</i> \rightarrow <i>lumo</i>	0.0595
6	3.86	0.0037	<i>homo-3</i> \rightarrow <i>lumo+1</i>	0.9639
			<i>homo-3</i> \rightarrow <i>lumo+2</i>	0.0140
7	3.99	0.0002	<i>homo</i> \rightarrow <i>lumo+5</i>	0.9666
			<i>homo-4</i> \rightarrow <i>lumo</i>	0.0162
8	4.08	0.0009	<i>homo-2</i> \rightarrow <i>lumo+3</i>	0.9334
9	4.18	0.0095	<i>homo-3</i> \rightarrow <i>lumo+2</i>	0.9236
10	4.25	0.0058	<i>homo-1</i> \rightarrow <i>lumo+5</i>	0.4656
			<i>homo-4</i> \rightarrow <i>lumo</i>	0.3915
			<i>homo-2</i> \rightarrow <i>lumo+4</i>	0.0599
11	2.88	0.0001	<i>homo</i> \rightarrow <i>lumo</i>	0.9953
12	3.28	0.0000	<i>homo</i> \rightarrow <i>lumo+3</i>	0.9571
13	3.48	0.0086	<i>homo-1</i> \rightarrow <i>lumo</i>	0.7244
			<i>homo-1</i> \rightarrow <i>lumo+3</i>	0.1267
			<i>homo</i> \rightarrow <i>lumo+4</i>	0.0784
14	3.63	0.0002	<i>homo-1</i> \rightarrow <i>lumo+3</i>	0.7960
			<i>homo</i> \rightarrow <i>lumo+4</i>	0.1395
			<i>homo-1</i> \rightarrow <i>lumo</i>	0.0505
15	3.64	0.0000	<i>homo-2</i> \rightarrow <i>lumo+1</i>	0.9928
16	3.76	0.0102	<i>homo</i> \rightarrow <i>lumo+4</i>	0.7085
			<i>homo-1</i> \rightarrow <i>lumo</i>	0.0866
			<i>homo-1</i> \rightarrow <i>lumo+3</i>	0.0641
			<i>homo</i> \rightarrow <i>lumo+6</i>	0.0601
17	3.84	0.0003	<i>homo-3</i> \rightarrow <i>lumo</i>	0.9491
18	3.97	0.0016	<i>homo-2</i> \rightarrow <i>lumo+2</i>	0.8752
			<i>homo-1</i> \rightarrow <i>lumo+4</i>	0.0670
19	4.01	0.0000	<i>homo-1</i> \rightarrow <i>lumo+4</i>	0.8976
			<i>homo-2</i> \rightarrow <i>lumo+2</i>	0.0522
20	4.05	0.0002	<i>homo-4</i> \rightarrow <i>lumo+1</i>	0.9619

Table A.8: Structure 5

Orbital	Composition
<i>homo-4</i>	7.10% (V); 83.97% (O)
<i>homo-3</i>	95.09% (O)
<i>homo-2</i>	3.24% (V); 89.98% (O)
<i>homo-1</i>	1.14% (V); 91.39% (O)
<i>homo</i>	98.91% (O)
<i>lumo</i>	70.98% (V); 21.98% (O)
<i>lumo+1</i>	12.59% (V); 6.70% (O); rest (Im)
<i>lumo+2</i>	25.71% (V); 11.50% (O); rest (Im)
<i>lumo+3</i>	28.42% (V); 4.34% (O); rest (Im)
<i>lumo+4</i>	46.82% (V); 9.86% (O); rest (Im)
<i>lumo+5</i>	30.46% (V); 7.26% (O); rest (Im)
<i>lumo+6</i>	57.4% (V); 23.02% (O)

Table A.9: Structure 6

Excitation	(eV)	Oscillator strength	Transition	Weight
1	3.07	0.0017	<i>homo</i> \rightarrow <i>lumo</i>	0.9989
2	3.58	0.0013	<i>homo</i> \rightarrow <i>lumo+1</i>	0.9945
3	3.95	0.0074	<i>homo-1</i> \rightarrow <i>lumo</i>	0.7402
			<i>homo-2</i> \rightarrow <i>lumo</i>	0.1702
4	4.13	0.0044	<i>homo-1</i> \rightarrow <i>lumo+1</i>	0.7979
			<i>homo-2</i> \rightarrow <i>lumo</i>	0.1191
5	4.22	0.0141	<i>homo-2</i> \rightarrow <i>lumo</i>	0.5867
			<i>homo-1</i> \rightarrow <i>lumo+1</i>	0.1839
			<i>homo-1</i> \rightarrow <i>lumo</i>	0.0746
6	4.44	0.0013	<i>homo-3</i> \rightarrow <i>lumo</i>	0.6154
			<i>homo-4</i> \rightarrow <i>lumo</i>	0.2348
			<i>homo-2</i> \rightarrow <i>lumo+1</i>	0.1192
8	4.51	0.0039	<i>homo-2</i> \rightarrow <i>lumo+1</i>	0.7410
			<i>homo-4</i> \rightarrow <i>lumo</i>	0.0508
			<i>homo-2</i> \rightarrow <i>lumo</i>	0.0441
			<i>homo-3</i> \rightarrow <i>lumo</i>	0.0402
9	4.62	0.0058	<i>homo-4</i> \rightarrow <i>lumo</i>	0.6094
			<i>homo-3</i> \rightarrow <i>lumo</i>	0.2739
10	4.85	0.0002	<i>homo-5</i> \rightarrow <i>lumo</i>	0.7211
			<i>homo-6</i> \rightarrow <i>lumo</i>	0.1350
			<i>homo-3</i> \rightarrow <i>lumo+1</i>	0.0674
11	4.98	0.0083	<i>homo-3</i> \rightarrow <i>lumo+1</i>	0.5928
			<i>homo-4</i> \rightarrow <i>lumo+1</i>	0.1332
			<i>homo-5</i> \rightarrow <i>lumo</i>	0.1127
12	5.03	0.0003	<i>homo-7</i> \rightarrow <i>lumo</i>	0.6884
			<i>homo-6</i> \rightarrow <i>lumo</i>	0.1596
			<i>homo-4</i> \rightarrow <i>lumo+1</i>	0.0834
13	5.04	0.0009	<i>homo</i> \rightarrow <i>lumo+3</i>	0.8285
			<i>homo</i> \rightarrow <i>lumo+4</i>	0.0857
14	5.13	0.0210	<i>homo-4</i> \rightarrow <i>lumo+1</i>	0.4396
			<i>homo-7</i> \rightarrow <i>lumo</i>	0.1749
			<i>homo-6</i> \rightarrow <i>lumo</i>	0.0974
15	5.16	0.0008	<i>homo-6</i> \rightarrow <i>lumo</i>	0.4036
			<i>homo-5</i> \rightarrow <i>lumo+1</i>	0.1948
			<i>homo-7</i> \rightarrow <i>lumo</i>	0.0785
			<i>homo-3</i> \rightarrow <i>lumo+1</i>	0.0722
			<i>homo-4</i> \rightarrow <i>lumo+1</i>	0.0696
16	5.29	0.0088	<i>homo-1</i> \rightarrow <i>lumo+2</i>	0.7493
			<i>homo-5</i> \rightarrow <i>lumo+1</i>	0.1010
17	5.41	0.0001	<i>homo-6</i> \rightarrow <i>lumo+1</i>	0.5992
			<i>homo-5</i> \rightarrow <i>lumo+1</i>	0.2587
18	5.46	0.0049	<i>homo-2</i> \rightarrow <i>lumo+2</i>	0.8196
19	5.53	0.0020	<i>homo</i> \rightarrow <i>lumo+5</i>	0.4549
			<i>homo</i> \rightarrow <i>lumo+4</i>	0.1960
			<i>homo-7</i> \rightarrow <i>lumo+1</i>	0.0904
20	5.55	0.0040	<i>homo-5</i> \rightarrow <i>lumo+1</i>	0.2258
			<i>homo-6</i> \rightarrow <i>lumo+1</i>	0.1689
			<i>homo-7</i> \rightarrow <i>lumo+1</i>	0.1667

Table A.10: Structure 6

Orbital	Composition
<i>homo-7</i>	48.58% (O); 29.17% (Im)
<i>homo-6</i>	77.79% (O)
<i>homo-5</i>	52.03% (O); 33.22% (Im)
<i>homo-4</i>	59.46% (O); 23.97% (Im)
<i>homo-3</i>	69.19% (O); 17.67% (Im)
<i>homo-2</i>	86.73% (O); 5.20% (Im)
<i>homo-1</i>	95.59% (O)
<i>homo</i>	89.65% (Im)
<i>lumo</i>	76.47% (V); 12.79% (O)
<i>lumo+1</i>	66.50% (V); 18.54% (O)
<i>lumo+2</i>	66.54% (V); 21.42% (O)
<i>lumo+3</i>	58.20% (V); 15.08% (O)
<i>lumo+4</i>	14.6% (V); 62.06% (Im)
<i>lumo+5</i>	41.97% (V); 10.85% (O); 23.29% (Im)

Table A.11: Structure 7

Excitation	(eV)	Oscillator strength	Transition	Weight
1	3.67	0.0006	<i>homo</i> \rightarrow <i>lumo</i>	0.9950
2	4.07	0.0001	<i>homo-1</i> \rightarrow <i>lumo</i>	0.9660
3	4.17	0.0022	<i>homo</i> \rightarrow <i>lumo+1</i>	0.9877
4	4.4	0.0056	<i>homo-3</i> \rightarrow <i>lumo</i>	0.9380
5	4.48	0.0085	<i>homo-2</i> \rightarrow <i>lumo</i>	0.7421
			<i>homo-1</i> \rightarrow <i>lumo+1</i>	0.0910
6	4.58	0.0109	<i>homo-1</i> \rightarrow <i>lumo+1</i>	0.8434
7	4.75	0.0003	<i>homo</i> \rightarrow <i>lumo+2</i>	0.8619
8	4.77	0.0030	<i>homo-2</i> \rightarrow <i>lumo+1</i>	0.4808
			<i>homo-3</i> \rightarrow <i>lumo+1</i>	0.1908
			<i>homo-4</i> \rightarrow <i>lumo</i>	0.1079
			<i>homo</i> \rightarrow <i>lumo+2</i>	0.1058
9	4.84	0.0006	<i>homo-3</i> \rightarrow <i>lumo+1</i>	0.7382
			<i>homo-4</i> \rightarrow <i>lumo</i>	0.1155
10	4.98	0.0002	<i>homo</i> \rightarrow <i>lumo+3</i>	0.9831
11	5.09	0.0032	<i>homo-4</i> \rightarrow <i>lumo</i>	0.5467
			<i>homo-2</i> \rightarrow <i>lumo+1</i>	0.1624
12	5.28	0.0005	<i>homo-5</i> \rightarrow <i>lumo</i>	0.4104
			<i>homo-2</i> \rightarrow <i>lumo+2</i>	0.2321
			<i>homo-6</i> \rightarrow <i>lumo</i>	0.2266
13	5.3	0.0013	<i>homo-2</i> \rightarrow <i>lumo+2</i>	0.6693
			<i>homo-5</i> \rightarrow <i>lumo</i>	0.1085
14	5.41	0.0002	<i>homo-1</i> \rightarrow <i>lumo+3</i>	0.9282
15	5.43	0.0003	<i>homo-3</i> \rightarrow <i>lumo+2</i>	0.9041
16	5.53	0.0083	<i>homo-4</i> \rightarrow <i>lumo+1</i>	0.4745
			<i>homo</i> \rightarrow <i>lumo+4</i>	0.1535
			<i>homo-3</i> \rightarrow <i>lumo+3</i>	0.1278
			<i>homo-5</i> \rightarrow <i>lumo</i>	0.0963
17	5.56	0.0063	<i>homo</i> \rightarrow <i>lumo+4</i>	0.3790
			<i>homo-6</i> \rightarrow <i>lumo</i>	0.2072
			<i>homo-5</i> \rightarrow <i>lumo+1</i>	0.1949
18	5.59	0.0034	<i>homo</i> \rightarrow <i>lumo+4</i>	0.4383
			<i>homo-6</i> \rightarrow <i>lumo</i>	0.2179
			<i>homo-3</i> \rightarrow <i>lumo+3</i>	0.1090
19	5.62	0.0506	<i>homo-2</i> \rightarrow <i>lumo+3</i>	0.9439
20	5.74	0.0012	<i>homo-7</i> \rightarrow <i>lumo</i>	0.8069

Table A.12: Structure 7

Orbital	Composition
<i>homo-7</i>	19.94% (V); 73.47% (O)
<i>homo-6</i>	10.76% (V); 79.46% (O)
<i>homo-5</i>	17.19% (V); 69.93% (O)
<i>homo-4</i>	15.90% (V); 63.76% (O); 13.21% (Im)
<i>homo-3</i>	91.94% (O)
<i>homo-2</i>	85.84% (O)
<i>homo-1</i>	84.13% (Im)
<i>homo</i>	96.03% (O)
<i>lumo</i>	69.65% (V); 19.38% (O)
<i>lumo+1</i>	56.99% (V); 24.32% (O); 10.79% (Im)
<i>lumo+2</i>	6.08% (V); 80.01% (Im)
<i>lumo+3</i>	68.55% (V); 10.28% (O)
<i>lumo+4</i>	9.55% (V); 75.69% (Im)

Table A.13: Structure 8

Excitation	(eV)	Oscillator strength	Transition	Weight
1	1.62	0.0076	<i>homo</i> \rightarrow <i>lumo</i>	0.9333
2	1.69	0.0018	<i>homo</i> \rightarrow <i>lumo</i> +1	0.9356
3	3.20	0.0105	<i>homo-1</i> \rightarrow <i>lumo</i>	0.8881
4	3.28	0.0104	<i>homo-1</i> \rightarrow <i>lumo</i> +1	0.9002
5	3.7	0.0021	<i>homo-2</i> \rightarrow <i>lumo</i>	0.5526
			<i>homo-2</i> \rightarrow <i>lumo</i> +1	0.4094
6	3.88	0.0079	<i>homo-2</i> \rightarrow <i>lumo</i> +1	0.3360
			<i>homo-2</i> \rightarrow <i>lumo</i>	0.2337
			<i>homo-3</i> \rightarrow <i>lumo</i>	0.2264
7	3.91	0.0072	<i>homo-3</i> \rightarrow <i>lumo</i>	0.7058
			<i>homo-2</i> \rightarrow <i>lumo</i> +1	0.1401
8	3.97	0.0004	<i>homo</i> \rightarrow <i>lumo</i> +4	0.9912
			<i>homo-3</i> \rightarrow <i>lumo</i>	0.0056
			<i>homo</i> \rightarrow <i>lumo</i> +5	0.0015
9	4.09	0.0031	<i>homo-4</i> \rightarrow <i>lumo</i>	0.5523
			<i>homo-3</i> \rightarrow <i>lumo</i> +1	0.3678
10	4.18	0.0013	<i>homo-1</i> \rightarrow <i>lumo</i> +2	0.9524
11	4.36	0.0131	<i>homo-3</i> \rightarrow <i>lumo</i> +1	0.2338
			<i>homo-4</i> \rightarrow <i>lumo</i>	0.2291
			<i>homo-5</i> \rightarrow <i>lumo</i>	0.2203
12	4.38	0.0036	<i>homo-4</i> \rightarrow <i>lumo</i> +1	0.7742
13	4.55	0.0017	<i>homo-5</i> \rightarrow <i>lumo</i>	0.5054
			<i>homo-2</i> \rightarrow <i>lumo</i> +2	0.3510
14	4.58	0.0028	<i>homo-1</i> \rightarrow <i>lumo</i> +3	0.6352
			<i>homo-5</i> \rightarrow <i>lumo</i> +1	0.2983
15	4.63	0.0006	<i>homo-5</i> \rightarrow <i>lumo</i> +1	0.6156
			<i>homo-1</i> \rightarrow <i>lumo</i> +3	0.2346
16	4.65	0.0024	<i>homo-2</i> \rightarrow <i>lumo</i> +2	0.4137
			<i>homo-6</i> \rightarrow <i>lumo</i>	0.2229
			<i>homo-5</i> \rightarrow <i>lumo</i>	0.1495
17	4.71	0.0002	<i>homo-6</i> \rightarrow <i>lumo</i> +1	0.4666
			<i>homo-6</i> \rightarrow <i>lumo</i>	0.3181
			<i>homo-2</i> \rightarrow <i>lumo</i> +2	0.1109
18	4.9	0.0093	<i>homo-7</i> \rightarrow <i>lumo</i>	0.2199
			<i>homo-6</i> \rightarrow <i>lumo</i> +1	0.2081

Table A.14: Structure 8

Orbital	Composition
<i>homo-7</i>	56.11% (O); 19.55% (Im)
<i>homo-6</i>	82.95% (O)
<i>homo-5</i>	80.47% (O)
<i>homo-4</i>	66.93% (O); 13.05% (Im)
<i>homo-3</i>	81.77% (O)
<i>homo-2</i>	58.89% (O); 24.42% (Im)
<i>homo-1</i>	17.40% (O); 75.27% (Im)
<i>homo</i>	94.59% (Im)
<i>lumo</i>	70.93% (V); 16.38% (O)
<i>lumo+1</i>	70.61% (V); 16.54% (O)
<i>lumo+2</i>	66.95% (V); 20.30% (O)
<i>lumo+3</i>	66.86% (V) ; 16.25% (O)
<i>lumo+4</i>	64.06% (V); 12.06% (O); 8.33% (Im)
<i>lumo+5</i>	91.50% (Im)

Appendix B

Supplement to Chapter 5

Time evolution of atomic positions in vanadium coordination shell simulated with CPMD, with transition state geometries as starting point.

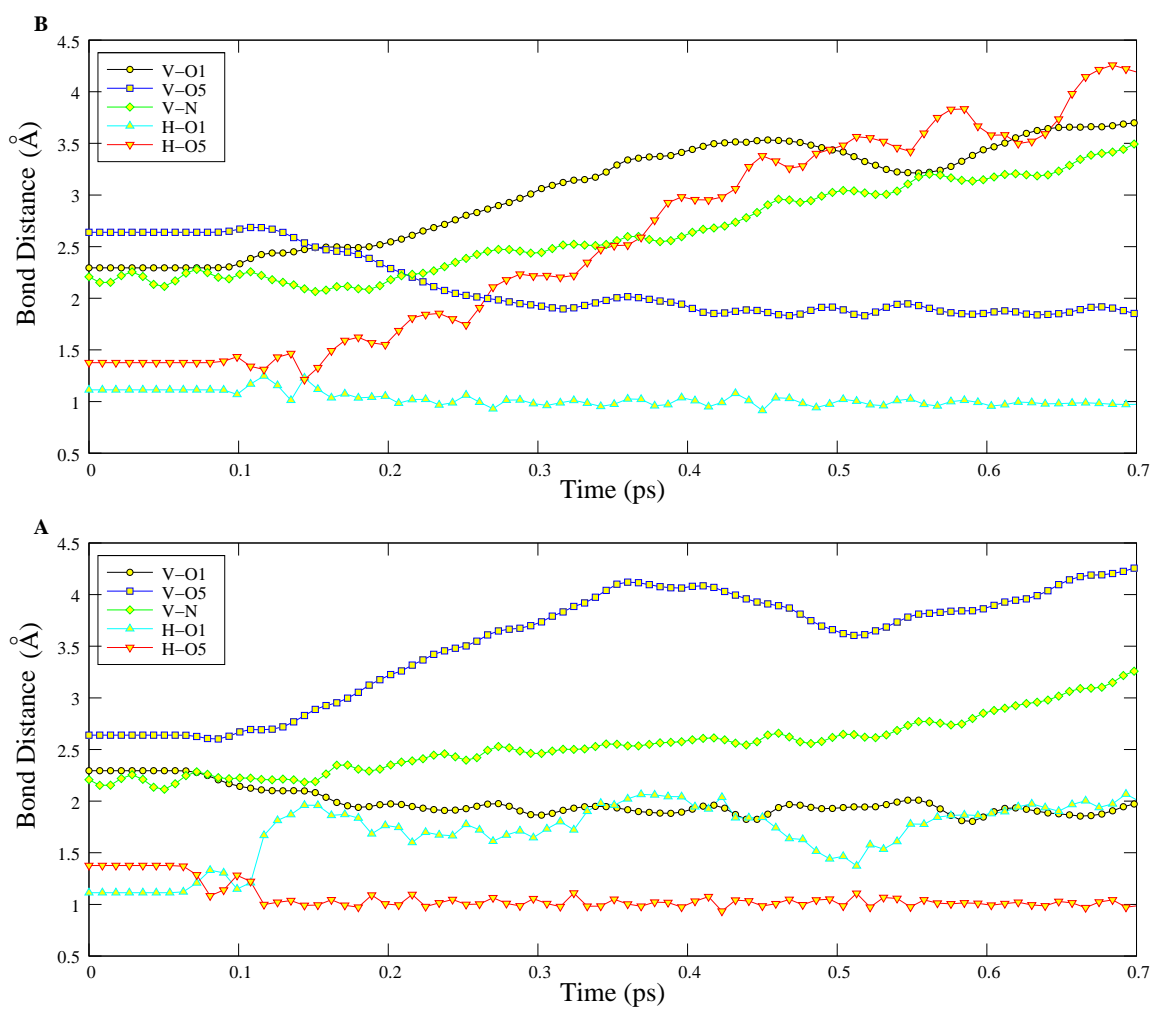


Figure B.1: CPMD trajectories of atoms in vanadium coordination sphere with **4*** as starting point

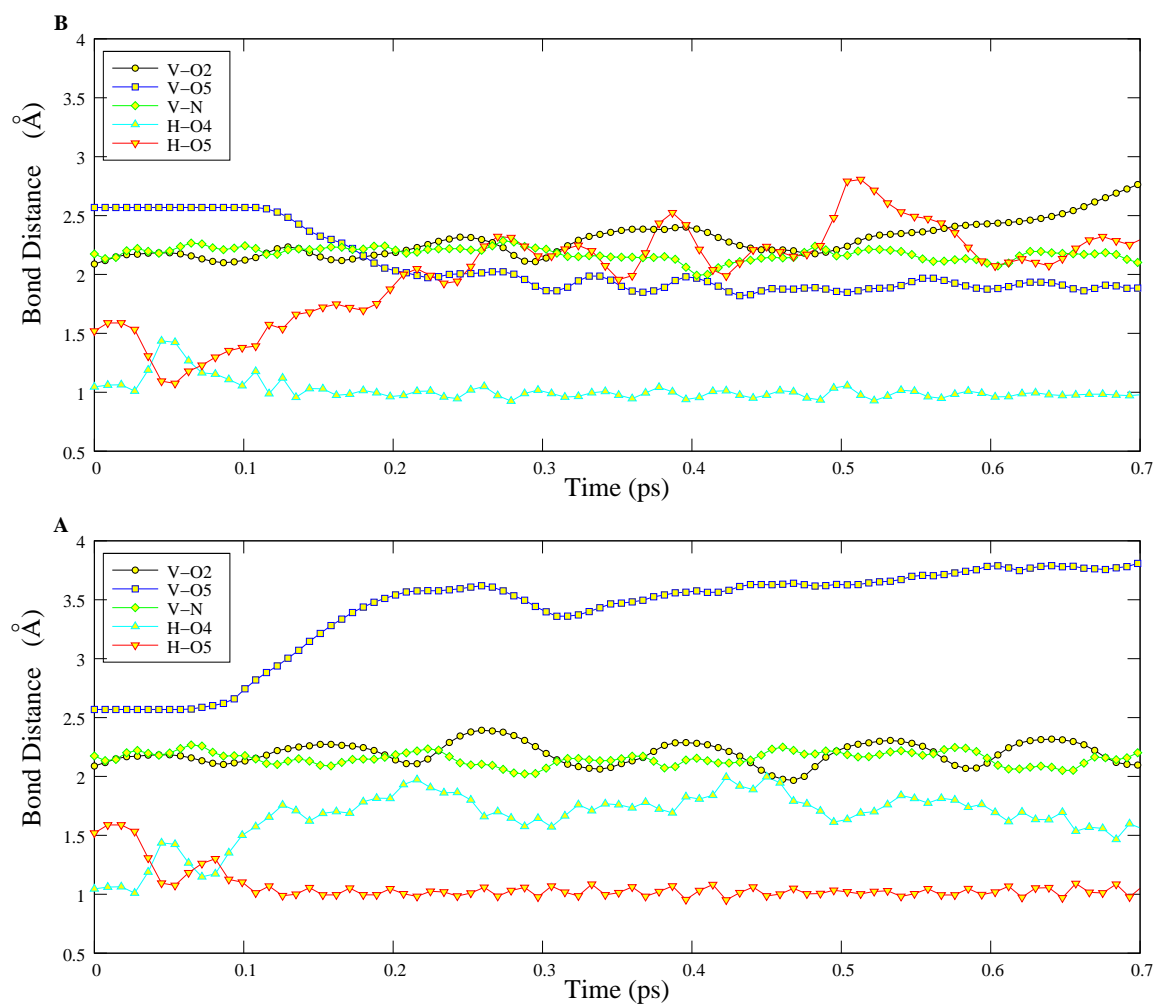


Figure B.2: CPMD trajectories of atoms in vanadium coordination sphere with **21*** as starting point

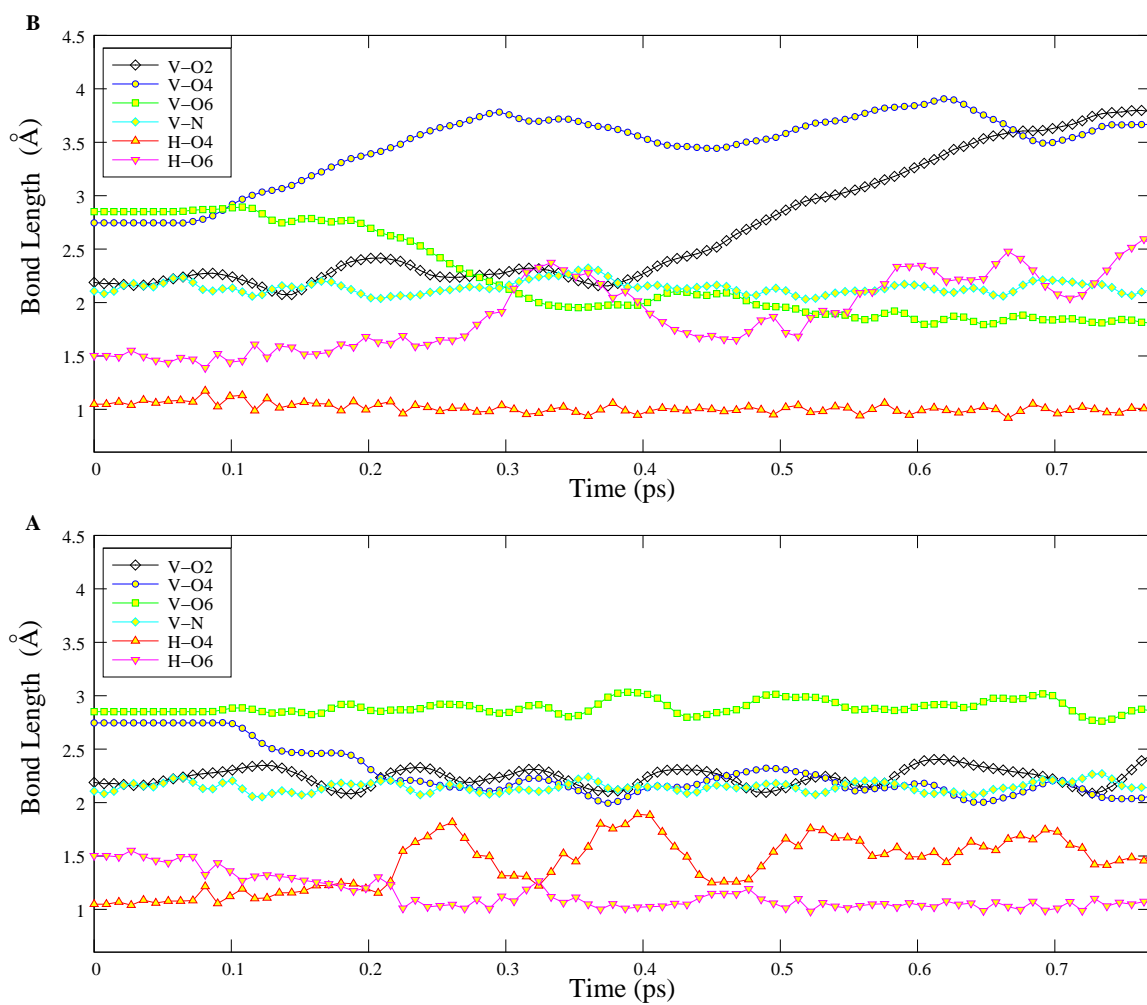


Figure B.3: CPMD trajectories of atoms in vanadium coordination sphere with **24*** as starting point

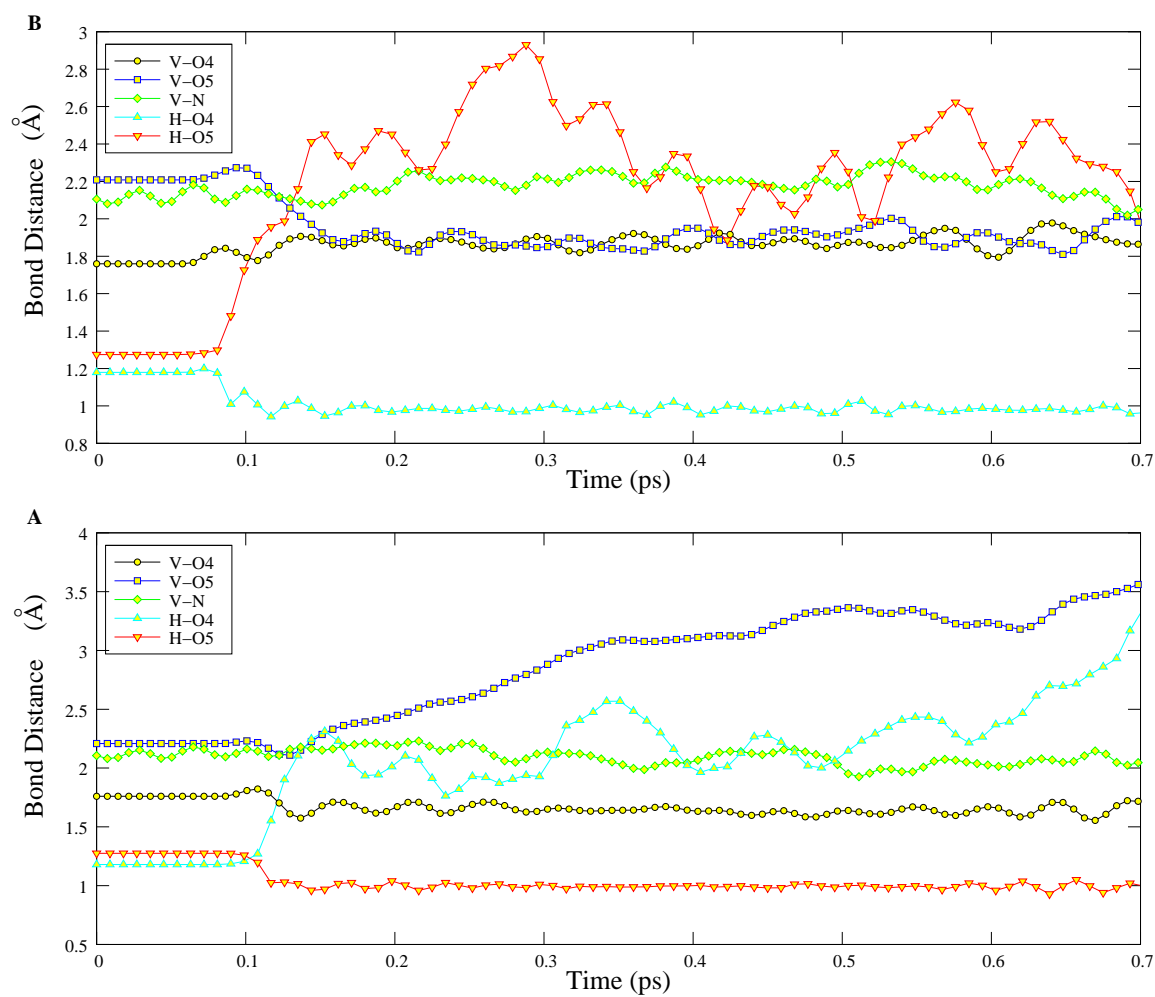


Figure B.4: CPMD trajectories of atoms in vanadium coordination sphere with **30*** as starting point

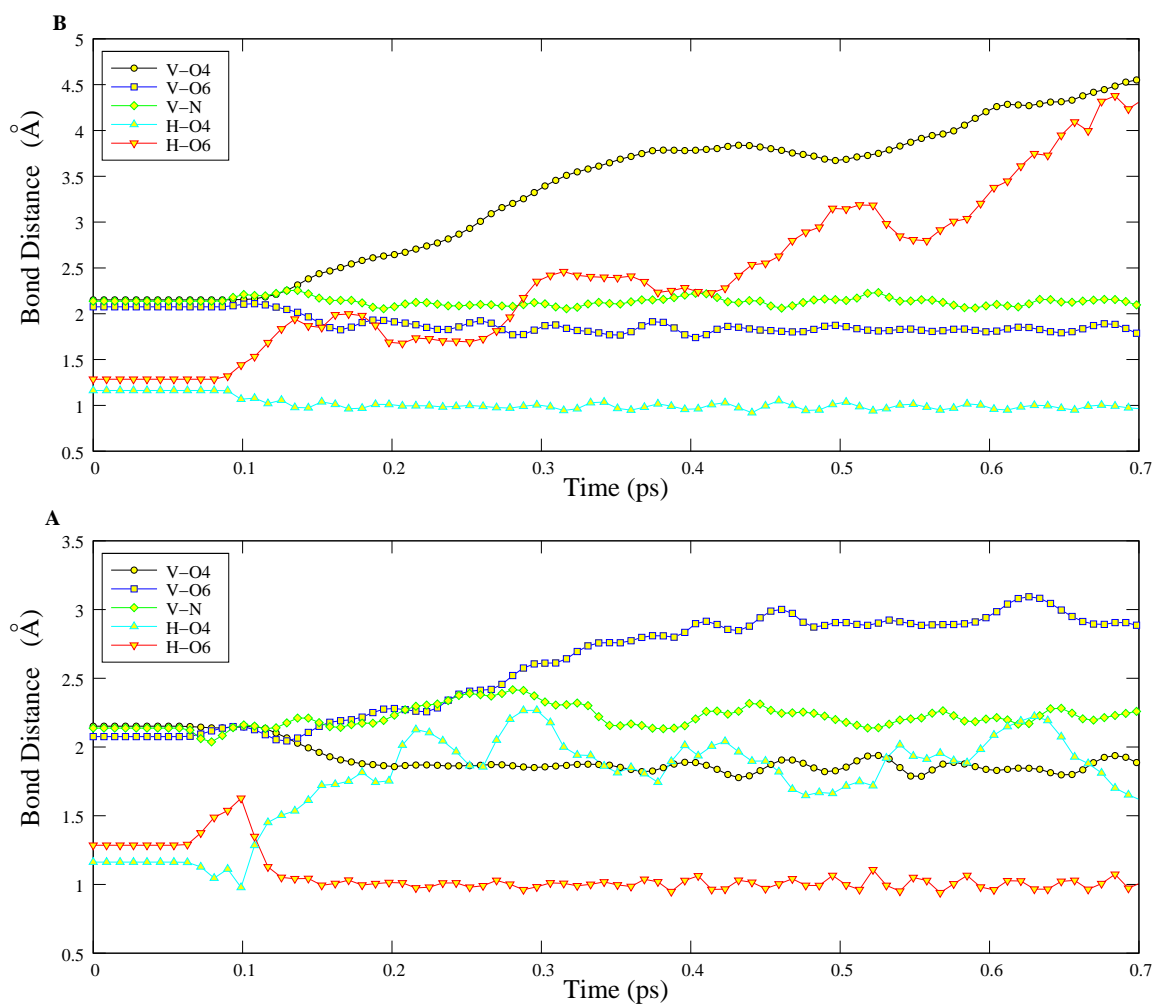


Figure B.5: CPMD trajectories of atoms in vanadium coordination sphere with **32*** as starting point

Appendix C

Supplement to Chapter 6

The QTAIM parameters at bond critical points between relevant atom pairs, for the optimised structures.

Table C.1: QTAIM parameters (a.u.) at bond critical points at ADF-BP/TZ2P level.

		Br^-					Cl^-				
		ρ_C	$\nabla^2\rho_C$	G_C	V_C	H_C	ρ_C	$\nabla^2\rho_C$	G_C	V_C	H_C
1	O1—V	0.247	0.98	0.377	-0.508	-0.132	0.245	0.973	0.373	-0.503	-0.13
	O2—V	0.125	0.468	0.154	-0.192	-0.037	0.124	0.453	0.151	-0.19	-0.038
	O3—V	0.134	0.506	0.172	-0.218	-0.046	0.132	0.504	0.169	-0.213	-0.043
	O4—V	0.131	0.524	0.168	-0.205	-0.037	0.131	0.526	0.169	-0.206	-0.037
	N—V	0.053	0.21	0.055	-0.058	-0.003	0.051	0.205	0.053	-0.056	-0.002
	X—V	0.037	0.076	0.023	-0.027	-0.004	0.048	0.124	0.036	-0.041	-0.005
	O3—O4	0.271	0.262	0.226	-0.387	-0.161	0.272	0.26	0.227	-0.389	-0.162
2*	O1—V	0.242	0.969	0.37	-0.499	-0.128	0.232	0.935	0.352	-0.469	-0.118
	O2—V	0.128	0.506	0.162	-0.198	-0.036	0.132	0.491	0.167	-0.212	-0.044
	O3—V	0.163	0.649	0.222	-0.282	-0.06	0.165	0.68	0.228	-0.285	-0.058
	O4—V	0.16	0.608	0.211	-0.27	-0.059	0.168	0.635	0.227	-0.295	-0.068
	N—V	0.055	0.213	0.056	-0.059	-0.003	0.053	0.207	0.054	-0.057	-0.003
	X—V	0.051	0.129	0.035	-0.038	-0.003	0.059	0.164	0.044	-0.048	-0.003
	O3—O4	0.106	0.343	0.104	-0.123	-0.019	0.104	0.342	0.102	-0.119	-0.017
4	O1—V	0.263	1.039	0.411	-0.562	-0.151	0.262	1.036	0.41	-0.56	-0.151
	O2—V	0.133	0.464	0.164	-0.211	-0.048	0.131	0.462	0.161	-0.206	-0.045
	O3—V	0.087	0.465	0.126	-0.135	-0.01	0.131	0.5	0.161	-0.197	-0.036
	O4—V	0.134	0.511	0.166	-0.204	-0.038	0.087	0.461	0.125	-0.135	-0.01
	N—V	0.057	0.199	0.055	-0.059	-0.005	0.056	0.195	0.053	-0.057	-0.004
	X—V	0.051	0.083	0.029	-0.038	-0.009	0.064	0.142	0.047	-0.058	-0.011
	O3—O4	0.246	0.3	0.206	-0.336	-0.13	0.252	0.288	0.209	-0.345	-0.137
5*	O1—V	0.263	1.042	0.41	-0.56	-0.15	0.263	1.039	0.41	-0.559	-0.15
	O2—V	0.135	0.5	0.17	-0.214	-0.045	0.136	0.503	0.171	-0.215	-0.045
	O3—V	0.16	0.562	0.204	-0.267	-0.063	0.163	0.584	0.21	-0.274	-0.064
	O4—V	0.085	0.424	0.115	-0.124	-0.009	0.09	0.42	0.117	-0.129	-0.012
	N—V	0.065	0.222	0.062	-0.069	-0.007	0.066	0.223	0.063	-0.07	-0.007
	X—V	0.054	0.146	0.041	-0.045	-0.004	0.076	0.205	0.061	-0.071	-0.01
	O3—O4	0.137	0.393	0.132	-0.166	-0.034	0.112	0.366	0.111	-0.131	-0.02
6	O1—V	0.256	1.021	0.397	-0.539	-0.142	0.255	1.017	0.395	-0.536	-0.141
	O2—V	0.137	0.504	0.172	-0.218	-0.046	0.137	0.483	0.17	-0.219	-0.049
	O3—V	0.132	0.498	0.168	-0.211	-0.043	0.13	0.505	0.165	-0.204	-0.039
	O4—V	0.106	0.45	0.136	-0.159	-0.023	0.105	0.446	0.135	-0.158	-0.023
	N—V	0.058	0.208	0.057	-0.062	-0.005	0.057	0.203	0.055	-0.06	-0.004
	X—V	0.043	0.079	0.026	-0.031	-0.006	0.054	0.13	0.04	-0.047	-0.007
	O3—O4	0.259	0.279	0.216	-0.362	-0.146	0.261	0.274	0.217	-0.366	-0.149
7*	O1—V	0.261	1.035	0.406	-0.554	-0.147	0.261	1.035	0.406	-0.553	-0.147
	O2—V	0.14	0.539	0.179	-0.223	-0.044	0.14	0.501	0.18	-0.236	-0.055
	O3—V	0.159	0.586	0.206	-0.266	-0.06	0.16	0.608	0.208	-0.264	-0.056
	O4—V	0.097	0.391	0.117	-0.137	-0.02	0.102	0.409	0.122	-0.141	-0.02
	N—V	0.067	0.226	0.064	-0.072	-0.008	0.067	0.224	0.064	-0.072	-0.008
	X—V	0.063	0.152	0.045	-0.052	-0.007	0.082	0.203	0.063	-0.076	-0.012
	O3—O4	0.116	0.374	0.116	-0.138	-0.022	0.102	0.352	0.103	-0.118	-0.015

Table C.2: QTAIM parameters (a.u.) at bond critical points at B3LYP/6-311G** level.

		Br ⁻					Cl ⁻				
		ρ_C	$\nabla^2\rho_C$	G_C	V_C	H_C	ρ_C	$\nabla^2\rho_C$	G_C	V_C	H_C
1	O1—V	0.26	0.798	0.38	-0.56	-0.18	0.258	0.792	0.376	-0.554	-0.178
	O2—V	0.128	0.446	0.152	-0.191	-0.04	0.127	0.438	0.148	-0.187	-0.039
	O3—V	0.138	0.463	0.167	-0.217	-0.051	0.137	0.458	0.164	-0.213	-0.049
	O4—V	0.135	0.46	0.163	-0.21	-0.048	0.136	0.458	0.163	-0.211	-0.048
	N—V	0.053	0.213	0.055	-0.057	-0.002	0.052	0.208	0.053	-0.055	-0.001
	X—V	0.038	0.075	0.023	-0.027	-0.004	0.048	0.114	0.034	-0.04	-0.006
	O3—O4	0.277	0.161	0.224	-0.407	-0.183	0.278	0.157	0.224	-0.409	-0.185
2*	O1—V	0.254	0.796	0.373	-0.548	-0.174	0.244	0.77	0.354	-0.515	-0.161
	O2—V	0.131	0.468	0.16	-0.202	-0.043	0.136	0.472	0.164	-0.211	-0.047
	O3—V	0.168	0.585	0.223	-0.3	-0.077	0.17	0.602	0.229	-0.308	-0.079
	O4—V	0.166	0.538	0.21	-0.286	-0.076	0.175	0.568	0.227	-0.312	-0.085
	N—V	0.056	0.215	0.056	-0.058	-0.002	0.053	0.211	0.054	-0.056	-0.001
	X—V	0.05	0.142	0.035	-0.035	0	0.055	0.181	0.044	-0.043	0.001
	O3—O4	0.1	0.387	0.101	-0.105	-0.004	0.098	0.382	0.098	-0.101	-0.003
4	O1—V	0.277	0.847	0.414	-0.617	-0.203	0.276	0.844	0.413	-0.615	-0.202
	O2—V	0.136	0.453	0.16	-0.207	-0.047	0.135	0.445	0.157	-0.203	-0.046
	O3—V	0.138	0.449	0.162	-0.211	-0.05	0.134	0.439	0.157	-0.204	-0.047
	O4—V	0.087	0.443	0.121	-0.13	-0.01	0.087	0.44	0.12	-0.13	-0.01
	N—V	0.058	0.201	0.054	-0.058	-0.004	0.056	0.197	0.053	-0.056	-0.004
	X—V	0.053	0.076	0.029	-0.038	-0.01	0.066	0.121	0.044	-0.057	-0.013
	O3—O4	0.25	0.213	0.201	-0.349	-0.148	0.256	0.195	0.205	-0.361	-0.156
5*	O1—V	0.277	0.844	0.414	-0.616	-0.203	0.277	0.842	0.413	-0.616	-0.203
	O2—V	0.139	0.47	0.167	-0.216	-0.049	0.139	0.472	0.168	-0.217	-0.05
	O3—V	0.165	0.514	0.203	-0.277	-0.074	0.169	0.526	0.21	-0.288	-0.078
	O4—V	0.086	0.41	0.112	-0.122	-0.01	0.091	0.404	0.114	-0.128	-0.013
	N—V	0.066	0.217	0.061	-0.069	-0.007	0.067	0.217	0.062	-0.069	-0.008
	X—V	0.04	0.087	0.027	-0.032	-0.005	0.071	0.23	0.06	-0.062	-0.002
	O3—O4	0.131	0.408	0.128	-0.154	-0.026	0.106	0.396	0.108	-0.118	-0.009
6	O1—V	0.269	0.833	0.401	-0.594	-0.193	0.268	0.83	0.399	-0.59	-0.192
	O2—V	0.141	0.468	0.168	-0.219	-0.051	0.14	0.46	0.166	-0.217	-0.051
	O3—V	0.136	0.461	0.163	-0.211	-0.048	0.134	0.456	0.161	-0.207	-0.047
	O4—V	0.107	0.419	0.13	-0.155	-0.025	0.107	0.415	0.129	-0.154	-0.025
	N—V	0.059	0.208	0.056	-0.061	-0.004	0.057	0.204	0.055	-0.059	-0.004
	X—V	0.044	0.075	0.025	-0.031	-0.006	0.055	0.115	0.037	-0.046	-0.009
	O3—O4	0.264	0.182	0.212	-0.378	-0.166	0.266	0.175	0.213	-0.383	-0.17
7*	O1—V	0.274	0.844	0.41	-0.609	-0.199	0.274	0.843	0.41	-0.61	-0.211
	O2—V	0.144	0.489	0.176	-0.229	-0.053	0.145	0.493	0.177	-0.231	-0.123
	O3—V	0.165	0.526	0.206	-0.279	-0.074	0.166	0.534	0.208	-0.282	-0.133
	O4—V	0.099	0.375	0.114	-0.134	-0.02	0.104	0.38	0.118	-0.141	-0.095
	N—V	0.068	0.219	0.063	-0.071	-0.008	0.068	0.217	0.063	-0.071	-0.008
	X—V	0.061	0.168	0.045	-0.047	-0.003	0.077	0.226	0.062	-0.066	-0.057
	O3—O4	0.11	0.404	0.113	-0.125	-0.012	0.096	0.386	0.101	-0.105	-0.096